Ph.D. Thesis

Université de Limoges

University of Limoges

ED 653 - Sciences et Ingénierie (SI)

Institute of Research for Ceramics (IRCER)

A thesis submitted to University of Limoges
in partial fulfillment of the requirements of the degree of

Doctor of Philosophy

Ceramic Materials and Surface Treatments

Presented and defensed by

Harikeshava Ranganathan

On May 6, 2026

Discrete element modelling to refine heterogeneous refractory microstructure for enhancing thermomechanical properties governed by CTE mismatch induced microcracking

Thesis supervisor:

M. Marc Huger, M. Damien Andre, M. Ratana Soth, M. Christoph Wöhrmeyer

JURY:

President of jury

M. Ferenc Kun, Full professor, University of Debrecen (Hungary)

Reporters

M. Vladimir Buljak, Full professor, University of Belgrade (Serbia)

M. Gael Combe, Full professor, University of Grenoble (France)

Examiners

M. Marc Huger, Full professor, University of Limoges (France)

M. Damien Andre, Associate professor, University of Limoges (France)

M. Ratana Soth, Senior scientist, Imerys Technology Centre (France)

M. Christoph Wöhrmeyer, Refractory director, Imerys Technology Centre (France)

Guests

M. Jérémie Girardot, Chercheur HDR, ENSAM bordeaux (France)

To my family and myself

I am so clever that sometimes I don't understand a single word of what I am saying.

Oscar Wilde

Acknowledgements

This PhD was funded by the *CESAREF project*, supported by the European Union's Horizon Europe Research and Innovation Programme (Grant Agreement No. 101072625). I am grateful for this support, which provided both the resources and a unique scientific-industrial framework for my research. The project was conducted in collaboration between the Thermomechanics of Ceramics (TMC) Group at IRCER (Université de Limoges) and the Imerys Technology Centre (ITC) in Lyon, offering an exceptional opportunity to connect academic research with industrial applications in refractory materials.

I sincerely thank the CESAREF consortium for their trust and for selecting me for this PhD. Beyond funding, CESAREF offered a platform to explore the circular economy of refractory materials, engage with academic and industrial partners, and participate in stimulating discussions across the refractory value chain. I am also grateful for the opportunity to work alongside my *CESAREF colleagues*; the in-person meetings were always productive, inspiring, and enjoyable.

I am especially grateful to *Dr. Damien* for his dedication and guidance, which were instrumental in developing my computational skills. I will always remember the *Occam's razor* principle he taught me, which refined my approach to visualisation and helped me navigate the "black-box" aspects of this project. His mentorship, feedback, and introduction to the GranOO software framework, within which my contributions have been integrated, greatly strengthened my computational expertise and contributed to a long-term research tool. I also sincerely thank *Prof. Marc* for his dynamic working style and scientific vision. He facilitated collaborations, particularly with *Dr. Mouiya*, and encouraged my participation in international conferences, which enhanced my confidence, visibility, and professional network. I am grateful for the resources and opportunities he provided, which broadened my knowledge in refractory materials. A special mention goes to *Dr. Mouiya*, who generously provided the experimental data to validate my numerical tools and was always available for guidance. I also thank the *University of Limoges* for providing the essential resources and facilities to carry out this PhD.

I warmly acknowledge my industrial supervisors, *Dr. Ratana, Dr. Christoph, and Dr. Chris Parr*, for their invaluable support during my 18 months at ITC Lyon. Their hospitality, encouragement, and confidence created a friendly and motivating environment that made my PhD journey enjoyable. I am grateful for the time, resources, and industrial expertise they provided.

Finally, I wish to express my deepest gratitude to my *parents (Mr Ranganathan & Mrs Lavanya) and my brother (Mr. Lakshmikant)*. Their unwavering moral and emotional support has been invaluable throughout my journey. I especially thank my *father (Mr. Ranganathan)* for his financial support during my education, which allowed me to pursue my master's in Germany and acquire the knowledge that ultimately enabled me to reach CESAREF. I am also profoundly grateful to my *wife (Mrs Aishwarya)*, who, despite being newly married, provided immense emotional and mental support, patience, and encouragement throughout this journey.

Lastly, I sincerely thank all the *members of the jury* for accepting the invitation to participate in my thesis defence. I deeply appreciate their feedback, thoughtful comments, and the time and expertise they dedicated to evaluating this work.

Rights

This creation is available under a Creative Commons contract:
« Attribution-Non Commercial-No Derivatives 4.0 International »
online at https://creativecommons.org/licenses/by-nc-nd/4.0/

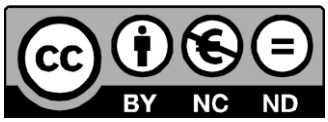

Table of Contents

General Introduction 1
Chapter I. State of art about refractory material and thermomechanical approaches 6
I.1. Introduction 6
I.2. Thermal shock resistance of industrial refractory materials 6
I.2.1. Illustration of microstructure complexity to face thermal shocks 7
I.2.2. Theoretical framework about thermal shock 11
I.2.3. Microstructure design to improve thermal shock resistance 13
I.2.4. Models for the effective properties of heterogeneous and microcracked materials 21
I.3. Full field continuum approach to simulate fracture initiation and propagation 26
I.3.1. Finite Element Method 27
I.3.2. Boundary Element Method 37
I.4. Particle-based approach to simulate fracture initiation and propagation 39
I.4.1. Material Point Method 40
I.4.2. Peridynamics 44
I.4.3. Lattice models 47
I.4.4. Discrete Element Method 52
I.5. Appropriate numerical approach for refractory materials 57
I.6. Scope and Objectives of the present study 58
Chapter II. About Distinct Lattice Spring Method and its enhancement 60
II.1. Overview on improved Distinct Lattice Spring Method 60
II.1.1. Generation of iDLSM numerical sample 61
II.1.2. Main steps in computing the reaction forces in iDLSM approach 62
II.1.3. Crack management in iDLSM numerical sample 63
II.2. Enhancements to the original iDLSM model 64
II.2.1. Periodic boundary condition 64
II.2.2. Anisotropic thermal expansion 72
II.2.3. Crack opening and closing management in iDLSM numerical sample 75
II.3. Conclusion 77
Chapter III. Overview of the reference refractory materials 79
III.1. Industrial refractory microstructure design - thermomechanical property relationship under thermal expansion effects 79
III.1.1. Cordierite-mullite refractories 80

III.1.2. Polycrystalline alumina with large grain 82
III.1.3. Andalusite based castable 85
III.2. Aluminum titanate model material 88
III.2.1. Key general aspects about Aluminum Titanate materials 89
III.2.2. AT based materials studied by TMC group for understanding microcrack effects 91
III.2.3. From real polycrystalline microstructures to virtual ones 96
III.3. Composite model material 97
III.3.1. Monocrystal AT aggregates 98
III.3.2. Alumina-AT composite microstructure 98
III.3.3. Macroscopic thermomechanical response 99
III.3.4. From real composite microstructures to virtual ones 101
III.4. Expected Outputs and Workflow using Different Model Microstructure 105
Chapter IV. iDLSM modelling of microcracking induced by anisotropic thermal expansion: polycrystalline case study 108
IV.1. Introduction 108
IV.2. Virtual DEM lab development for polycrystalline AT model material 109
IV.2.1. Polycrystalline microstructure digitalization strategy 109
IV.2.2. Evaluation of apparent CTE and Young's modulus 114
IV.2.3. Convergence study 117
IV.3. Numerical modelling of thermomechanical damage in a model material 119
IV.3.1. Thermal stress study 119
IV.3.2. Analyses of the micro-crack network 124
IV.3.3. Apparent stress-strain response of microcracked numerical sample 132
IV.3.4. Factors promoting non-linear stress-strain response 133
IV.3.5. Numerical vs experimental: microcracked sample response under cyclic loading 139
IV.4. Conclusion 141
Chapter V. iDLSM modelling of microcracking induced by anisotropic thermal expansion: porous polycrystalline case study 142
V.1. Introduction 142
V.2. Porous polycrystalline model 143
V.2.1. Porous polycrystalline microstructure digitalization strategy 144
V.2.2. Anisotropic thermal expansion of porous polycrystalline elastic domain 146
V.2.3. Mechanical response of porous polycrystalline domain 148

V.3. Apparent behavior of porous polycrystalline aluminum titanate 149
V.3.1. Dilatometry 149
V.3.2. Young's modulus 150
V.4. Micromechanical investigations 152
V.5. Mechanical study 157
V.5.1. Monotonic uniaxial tensile loading 157
V.5.2. Cyclic uniaxial tensile loading 159
V.6. Conclusion 160
Chapter VI. iDLSM modelling of microcracking induced by anisotropic thermal expansion: composite case study 164
VI.1. Introduction 164
VI.2. Microstructure digitalization strategy 165
VI.2.1. A first strategy: random positioning of inclusion 165
VI.2.2. A second strategy: regular positioning of inclusion 168
VI.3. Validation of the numerical sample 170
VI.3.1. Impact of inclusion positioning methods on apparent Young's modulus 170
VI.3.2. Impact of volume fraction on apparent Young's modulus 172
VI.4. Micromechanics study 174
VI.4.1. Thermal stress study 174
VI.4.2. Analyses of the micro-crack network 178
VI.5. Mechanical response 183
VI.5.1. Monotonic uniaxial tensile loading 183
VI.5.2. Cyclic uniaxial tensile loading 185
VI.6. Conclusion 186
Conclusion and perspective 189
Bibliography 196

List of Figures

Figure I-1: Illustration of heterogeneous refractory microstructure used in refractory component 7

Figure I-2: Application of magnesia-spinel lining in cement rotary kiln (Grasset-Bourdel, 2011; Khlifi, 2019) 9

Figure I-3: Application of alumina-carbon refractory in the ladle shroud for continuous caster (Peruzzi, 2000) 10

Figure I-4: Illustration of different individual mechanisms which could allow to enhance energy dissipation during crack propagation within refractories microstructure (Miyaji et al., 2014; Steinbrech, 1992) 14

Figure I-5: Thermal stresses promotion in a single particulate-reinforced material (Mouiya, 2024; Tessier-Doyen et al., 2006). 15

Figure I-6: Illustration of impact of aggregate nature on the CTE mismatch and thermal defects 16

Figure I-7: Overview on the microstructure-macroscopic response of andalusite based castable (Kakroudi, 2007) 18

Figure I-8: Mini-WST set-up and its load-displacement results for the alumina-AT composites 20

Figure I-9: Overview on the Voigt and Reuss approach to determine effective properties (Tessier-Doyen, 2003) 22

Figure I-10: Overview on the HS model for two constituent system 23

Figure I-11: Illustration of Katchanov penny shaped crack model (Kachanov, 1992; Yuan et al., 2021) 24

Figure I-12: Schematic stress-strain relation and its corresponding damage growth (Öchsner, 2016) 26

Figure I-13: Key representation of CZM framework 28

Figure I-14: Illustration of the virtual microstructure generation technique (Espinosa & Zavattieri, 2003b) 29

Figure I-15: Stress state before and after crack growth in a polycrystalline sample under tension (Lin et al., 2017) 29

Figure I-16: Overview on different results obtained in a thermal or thermomechanical study 30

Figure I-17: Schematic of XFEM discontinuity representation compared to conventional FEM 31

Figure I-18: Overview on the studies related polycrystalline model material 32

Figure I-19: Illustration of XFEM for tracking crack paths and analysing multiple cracks 33

Figure I-20: Illustration of thermal stress promotion and microcracks in a thermal study (Zhang et al., 2020) 33

Figure I-21: Illustration of a material body in PF framework (Muneton Lopez, 2023) 34

Figure I-22: Complex crack evolution in a polycrystalline material in PF modelling 35

Figure I-23: Multiscale pores effects on the crack patterns and stress-strain response (Cavuoto et al., 2024) 35

Figure I-24: Overview of the results based on thermal stress induced microcrack studies .. 36

Figure I-25: Illustration of different strategy of discretisation with BEM and FEM (Shiah & Tan, 2016) 37

Figure I-26: Illustration of impact of the pre-cracked sample on the macroscopic properties 38

Figure I-27: Illustration of 3D BEM model with polycrystalline micro-model in a macro-model (Benedetti & Aliabadi, 2015) 38

Figure I-28: Overview on the thermomechanical study based on Geraci & Aliabadi (2018) . 39

Figure I-29: Fundamental iterative steps present in the MPM numerical solution (Sun et al., 2024) 41

Figure I-30: Illustration of tearing of material under gravity using MPM simulation (Wretborn, 2016) 42

Figure I-31: Overview on different brittle fracture studies related to MPM approach 42

Figure I-32: MPM thermal shock simulation and results for the circular disc (Sun et al., 2024) 43

Figure I-33: Material points shown under different PD formulations, each with its own horizon (Javili et al., 2019) 44

Figure I-34: Monitoring the crack propagation speed versus time in polycrystalline material (De Meo et al., 2016) 45

Figure I-35: Overview of the study of Yang and co-workers (Z. Yang et al., 2022) 46

Figure I-36: Experimental and numerical thermal shock test on the alumina circular ceramic (Bazazzadeh et al., 2020) 47

Figure I-37: Examples of lattice model to discretise a domain (Nikolić et al., 2018) 48

Figure I-38: Illustration of spring as a cohesive connector between two nodes (A and B) (Wang et al., 2020) 48

Figure I-39: Comparison of crack paths obtained in experimental and simulation approach (Wang et al., 2020) 49

Figure I-40: Illustration of four-point bending using CSL approach (Cusatis et al., 2003) 49

Figure I-41: Illustration of the fracture of quasi-brittle material using site-model approach ... 50

Figure I-42: 4D-LSM Mode-I Failure Criterion and Uniaxial Compression test result 51

Figure I-43: Illustration of modelling thermal induced microcrack using LSM approach (Sridhar et al., 1994) 51

Figure I-44: Snapshot of an hourglass flow simulation, with interaction pair using linear spring model (From Pöschel & Schwager, 2005) 52

Figure I-45: Illustration of numerical procedure for the DEM approach 53

Figure I-46: Illustration of the popular BPEM contact models 54

Figure I-47: Microstructure digitization and apparent stress-strain curve under cyclic loading (Longchamp et al., 2024) 54

Figure I-48: Overview of the models and obtained results from different thermomechanical studies 55

Figure I-49: Illustration of stress-strain response of the hypothetical sample under uniaxial loading 57

Figure II-1: Illustration of iDLSM sample generation (Ranganathan et al., 2025) 62

Figure II-2: illustration of basic iDLSM problem in 2D (Ranganathan et al., 2025) 63

Figure II-3: Crack-facet representation in iDLSM numerical sample (Ranganathan et al., 2025) 64

Figure II-4: Central and periodic cells with master and slave elements in a 2D PBC sample. 65

Figure II-5: Procedure to generate PBC-iDLSM box from initial spherical domain to polyhedral bonded domain without ‘‘useless’’ periodic elements (Ranganathan et al., 2025) 66

Figure II-6: The 2D central periodic cell together with its associated boundary regions 68

Figure II-7: Stress and Poisson’s ratio responses versus strain in a PBC-iDLSM tensile test 71

Figure II-8: Schematic representation of anisotropic thermal expansion management in iDLSM framework 73

Figure II-9:Iteration versus temperature during cooling simulation (Ranganathan et al., 2025) 74

Figure II-10: Evolution of strain versus temperature for a PBC-iDLSM cooling test.(Ranganathan et al., 2025) 75

Figure II-11: 3D Illustration of the crack opening and closing (Ranganathan et al., 2025) ... 76

Figure II-12: Numerical sample under shear loading 76

Figure II-13: Snippets of numerical sample under shear loading 77

Figure III-1: Cordierite - mullite microstructure with decohesion between matrix and grains (Chotard et al., 2008) 80

Figure III-2: Young’s modulus variation, thermal expansion behavior as well as acoustic emission recording during a thermal cycle up to 1215 ℃ with heating-cooling rate 5 ℃ min^{-1}. Interfacial decohesion which occur during cooling is highlighted by the decrease in Young’s modulus, a strong reduction in CTE as well as an important acoustic emission below 710 ℃ (Chotard et al., 2008) 81

Figure III-3: Young’s modulus evolution versus temperature for different polycrystalline samples (Case et al., 1981) 83

Figure III-4: Polycrystalline alumina microstructure with equiaxed grains (Yousef et al., 2005) 84

Figure III-5: Illustration of modified Youngs modulus and ΔE versus ΔT plots for different samples (Yousef et al., 2005)..... 84

Figure III-6: Andalusite-cementitious microstructure design (Kakroudi, 2007) 86

Figure III-7: Thermomechanical properties evolution vs temperature for andalusite-based castable (Huger et al., 2007) 87

Figure III-8: AT's lattice mode and associated octahedral distortions and cation displacements 90

Figure III-9: AT's Lattice dilation (Fei, 2013) 90

Figure III-10: Microstructures of the different grades of AT and its corresponding stress-strain response under uniaxial tensile cyclic loading 93

Figure III-11: Representation of Ceramtec AT's microstructural information's 94

Figure III-12: CERAMTEC microstructural changes effects on the thermomechanical properties versus temperature (Mouiya, 2024) 95

Figure III-13: Schematic sketch of strategy to generate simplified polycrystalline model 96

Figure III-14: AT monocrystal (Mouiya et al., 2026) 98

Figure III-15: Composite microstructure design (Mouiya, 2024) 99

Figure III-16: AT volume fraction effects on the composite microstructure-property relationship (Mouiya, 2024) 100

Figure III-17: Schematic sketch of the strategy to generate composite model 102

Figure III-18: Analytical equations used to describe thermomechanical property evolution versus temperature for alumina matrix 104

Figure III-19: Crack extension identification mechanisms in iDLSM framework 105

Figure III-20: Thermomechanical analysis framework 106

Figure III-21: Overview of the workflow considering different model material and microstructure 107

Figure IV-1: Illustration of polycrystalline domain generation 110

Figure IV-2: Evolution of mean CTE versus temperature for a PBC-PGB-iDLSM cooling test 112

Figure IV-3: Stress state snippets of polycrystalline numerical sample at two temperatures 113

Figure IV-4: Snippets of the AT numerical samples at 20 °C 114

Figure IV-5: Experimental and numerical dilatometry results of AT 116

Figure IV-6: Evolution of microcrack network 116

Figure IV-7: Experimental and numerical results of AT's Young's modulus vs temperature 117

Figure IV-8: Apparent Young's modulus of aluminum titanate as a function of temperature for numerical samples with 10k, 20k, and 30k discrete elements 118

Figure IV-9: Microstructural changes in a 2D numerical sample in two case studies 120

Figure IV-10: Microstructural changes in the 3D numerical sample in two case studies 120

Figure IV-11: Thermal stress distribution versus temperature for the “no-crack” study 121
Figure IV-12: Thermal stress distribution versus temperature for the “crack” study 121
Figure IV-13: Temperature-dependent evolution of the mean thermal stress 122
Figure IV-14: Temperature-dependent evolution of thermal stress standard deviation 123
Figure IV-15: Recording of crack count and damage states versus temperature 124
Figure IV-16: Bonded polyhedral DE pair under mode-I failure 125
Figure IV-17: Representation of the n in relation to the local grain orientation 125
Figure IV-18: Orientation angle distributions of microcrack “n ” in different local grain planes 1000 ℃ 126
Figure IV-19: Orientation angle distributions of microcrack “n ” in different planes of local grain’s orientation versus temperature 127
Figure IV-20: Standard deviation of the microcracks n distribution angle versus temperature 128
Figure IV-21: Microcrack n count in relation to the local crystallographic axes versus temperature 129
Figure IV-22: Schematic representation of bulk and interface cracks along with their corresponding bonds in a 2D polycrystalline sample 129
Figure IV-23: Evolution of the interface and bulk cracks versus temperature 130
Figure IV-24: Monitoring of crack surface distribution at different temperature 132
Figure IV-25: Evolution of apparent stress-strain versus the temperature 133
Figure IV-26: Thermal effects impact on the stress-strain behaviour in [1200-1100 ℃] range 134
Figure IV-27: Thermal effects impact on the stress-strain behaviour in [1000-800 ℃] range 135
Figure IV-28: Thermal effects impact on the stress-strain behaviour in [700-20 ℃] range . 136
Figure IV-29: Progression of microcracks in the model material as a function of temperature 137
Figure IV-30: Evolution of the applied cyclic stretch over successive iterations 138
Figure IV-31: Monitoring irreversible strain development under uniaxial cyclic loading 139
Figure IV-32: Cyclic uniaxial stress-strain response of AT under cyclic loading at 20 ℃.... 140
Figure V-1: Illustration of the strategy to generate the PBC-PMI sample 145
Figure V-2: Illustration of porous polycrystalline domain generation 145
Figure V-3: Evolution of mean CTE vs temperature during cooling of porous polycrystalline domain 147
Figure V-4: Evolution of stresses versus strain for a dense and porous sample 149
Figure V-5: Evolution of thermal strain versus temperature for dense and porous AT 150

Figure V-6: Evolution of Youngs modulus results of dense and porous aluminum titanate material 151

Figure V-7: Relative representation of Youngs modulus versus temperature 152

Figure V-8: Mean and standard deviation of the thermal stress distribution versus temperature 153

Figure V-9: Relative microcrack number as a function of temperature 154

Figure V-10: Absolute evolution of interface and bulk crack versus temperature 155

Figure V-11: Relative evolution of interface and bulk crack versus temperature 156

Figure V-12: Crack n angles distribution's standard deviation vs temperature 157

Figure V-13: Thermal effects influence on apparent stress-strain in [1200-20 ℃] range 158

Figure V-14: Irreversible strains captured during uniaxial cyclic loading in [1200-20℃] range 161

Figure VI-1: Illustration of generating 2D composite domain with randomly positioned inclusion 167

Figure VI-2: Illustration of matrix, interface and inclusion bonds in a 2D sample snippet ... 167

Figure VI-3: Illustration of the 2D composite sample with local orientations assigned to the inclusions 167

Figure VI-4: Unit central cell of the 3D composite sample 168

Figure VI-5: Illustration of generating 2D composite domain with regular positioned inclusion 169

Figure VI-6: Illustration of the 2D composite sample with local orientations assigned to the inclusions 169

Figure VI-7: Illustrates the 3D composite sample with regularly positioned inclusions 170

Figure VI-8: Experimental and numerical results of alumina - aluminum titanate composite Young's modulus evolution versus temperature 172

Figure VI-9: illustration "Regular" samples with 5.6% and 11.2% inclusion volume fractions 172

Figure VI-10: Volume fraction effects on Young's modulus vs temperature (experiment from Mouiya et al., 2026vs. simulation) 173

Figure VI-11: Stress states of the sample during cooling 175

Figure VI-12: Micro-crack visualization in relation to the sample's stress state during cooling 175

Figure VI-13: Thermal stress distribution versus temperature for the "crack" study 176

Figure VI-14: Stress distribution's mean and standard deviation evolution versus temperature 177

Figure VI-15: Recording of crack count and damage states of numerical sample vs temperature 178

Figure VI-16: 3D linear microcracks n orientation vs temperature 179

Figure VI-17: Crack n count in relation to inclusion's local crystallographic axes vs temperature 180
Figure VI-18: Evolution of cracks in matrix, at interface and in inclusion versus temperature 181
Figure VI-19: Monitoring of crack surface density distribution at different temperature 182
Figure VI-20: Evolution of apparent stress-strain response and cracks in [1200 - 20 ℃] range 184
Figure VI-21: Evolution of apparent stress-strain versus the temperature 184
Figure VI-22: Evolution of the microcrack of the modal material versus temperature 185
Figure VI-23: Irreversible strain recording during uniaxial cyclic loading in [1200 - 20 ℃] range 187

List of Tables

Table I-1: Key analytical relationships in HS model for a two-constituent system 22

Table I-2: A comparison between various numerical methods to model quasi-brittle material 58

Table II-1: Hypothetical material properties for elastic tensile test (Ranganathan et al., 2025) 71

Table II-2: Hypothetical material properties for thermal test (Ranganathan et al., 2025)..... 74

Table II-3 : Hypothetical material properties for thermal test..... 76

Table III-1:Input data, assuming to be representative of local properties of each AT grain at initial temperature $T0$ = 1200 ℃ (Mouiya, 2024) and used in DEM simulation 97

Table III-2 :Input data, assuming to be representative of local properties of the alumina matrix and of the AT inclusions used in DEM simulation 104

Table IV-1: Apparent mean CTE values obtained from nine samples, all using identical material parameters 113

Table IV-2: Numerical samples with different polycrystalline structure for convergence study 118

Table V-1: Apparent mean CTE values for 9 different samples 147

Table VI-1: List of input parameters for the “Generate Inclusion” algorithm 166

Table VI-2: List of “Random” samples employed for the statistical study 170

General Introduction

Refractory materials are multiphase ceramics often composed of a matrix, aggregates, and discontinuities in the form of pores or cracks (da Luz A et al., 2015). They are specifically engineered for high-temperature industrial applications, including steelmaking and glass production. Their high chemical stability, combined with excellent thermal and mechanical performance, enables them to withstand extreme temperatures, aggressive environments, and severe thermal loading conditions (Biswas & Sarkar, 2020; Cabezas-Rodriguez et al., 2022; Huger et al., 2007; Sarkar, 2023). Among the various degradation mechanisms encountered during service, thermal shock remains one of the primary factors limiting refractory lifetime (Alekseeva et al., 2022; Mouiya, 2024; Tessier-Doyen, 2003). In fact, temperature variations generate significant internal stresses which, if not adequately accommodated through appropriate microstructural design, can lead to macrocracking, spalling, and catastrophic failure, thereby posing substantial safety and operational risks (Biswas & Sarkar, 2020; Huger et al., 2007; Mouiya, 2024).

Beyond these technical challenges, refractory materials must also adapt to the ongoing industrial transition driven by decarbonization strategies (Ribeiro Gomes et al., 2024). In Europe, this transition aims to reduce carbon dioxide and greenhouse gas emissions in energy-intensive sectors such as steel, glass, and cement production through the adoption of more sustainable and low-carbon manufacturing routes (Huger, 2023; Huger et al., 2024; Ribeiro Gomes et al., 2024). These evolving technologies impose new and often more severe operating conditions, raising critical questions regarding the long-term performance and sustainability of refractory materials, particularly under increasingly demanding thermal shock environments (Huger, 2023).

To address these challenges, the FIRE network (Federation for International Refractory Research and Education) (Rigaud et al., 2006) has, over the past fifteen years, brought together academic and industrial partners to promote collaborative research and to train researchers and engineers in the field of refractories. Building upon this foundation, and in response to challenges arising from decarbonization-driven industrial transformations, the Concerted European Action on Sustainable Applications of Refractories (CESAREF) consortium was established in 2022 (Huger, 2023). CESAREF is a Marie Skłodowska-Curie Industrial Doctoral Network (Verbanac, 2023) supported by the European Commission (Huger et al., 2024), uniting seven European universities, including the University of Limoges, and thirteen industrial partners such as Imerys, Safran, and Tata Steel. This project aims to train fifteen Doctorate Candidates through PhD programs while advancing both fundamental and applied research on the sustainability of refractory materials. It focuses on the responsible management of mineral resources and the promotion of recycling, microstructure design for enhanced sustainability, the anticipation of hydrogen-based steelmaking routes, and improvements in energy efficiency and material durability (Huger, 2023; Huger et al., 2024). In this context, the present PhD work directly contributes to CESAREF's objectives by addressing the optimisation of microstructure design of refractory materials under industrial operating conditions, particularly under severe thermal shock environments.

Historically, refractory specific design for thermal shocks has been guided by two principal theoretical frameworks. Kingery's thermoelastic criterion (Kingery, 1955) emphasises minimising thermal expansion and elastic modulus to delay crack initiation, thereby favouring high-strength materials. In contrast, Hasselman's mechanical energetic approach (Hasselman, 1969) promotes fracture energy by controlled microcracking as a means of relaxing thermal stresses and limiting crack propagation. Industrial practice in refractory area has largely adopted Hasselman's strategy (Chotard et al., 2008; Grasset-Bourdel et al., 2012; Huger et al., 2007, 2011), as it enhances fracture energy of the material through controlled energy dissipation (via microcracks) rather than

License CC BY-NC-ND 4.0

relying solely on high-strength but brittle behaviour. Indeed, such an approach also offers cost-effective solutions. Consequently, deliberate microstructural tuning, particularly through the controlled introduction of microcracking, has become a central strategy in the design of thermal-shock-resistant refractory materials (Huger et al., 2011; Kakroudi, 2007; Mouiya, 2024; Tessier-Doyen, 2003).

Numerous studies have investigated approaches to promote controlled microcracking, with particular emphasis on introducing mismatches in the coefficient of thermal expansion (CTE) between the matrix and aggregates (Boateng et al., 2025; Grasset-Bourdel et al., 2012; Joliff et al., 2007; Lemaistre, 1998; Mouiya, 2024; Peruzzi, 2000). Such mismatches generate localized internal stresses (Mouiya, 2024) that induce local microcracking, as observed in andalusite-based castable (Kakroudi, 2007; M. G. Kakroudi et al., 2009), or promote interfacial decohesion, as in cordierite-mullite systems (Boccaccini et al., 2005; Chotard et al., 2008). More recently, embedding coarse monocrystalline aggregates (Kakroudi, 2007) exhibiting a huge anisotropy in CTE values (for example aluminum titanate monocrystalline grains) within a fine-grained matrix (for example polycrystalline alumina) has proven to be especially effective in generating a complex microcrack network (Mouiya et al., 2026). This dense network, by promoting macrocrack deflection(Miyaji et al., 2014), crack bridging (Steinbrech, 1992), and stable crack growth, thereby dissipating elastic energy (Mouiya, 2024), act as efficient toughening mechanisms.

The promotion of such microcracked microstructures is closely linked to the thermal processing route (de Carvalho Bonaldo, 2022; Kakroudi et al., 2008; Terzić & Pavlović, 2009). After powder/grains compaction, refractory materials undergo a firing cycle consisting of heating, dwelling at high temperature for sintering, and subsequent cooling (da Luz A et al., 2015; Kakroudi, 2007; Mouiya, Tessier-Doyen, et al., 2023). Typically, materials are heated from room temperature to temperatures in the range of 1000-1600 °C, held for several hours to ensure densification and pertinent phase development, and then cooled back to ambient conditions (Kakroudi, 2007; Mouiya et al., 2019; Shan et al., 2022). The resulting microcracked microstructure therefore emerges as a direct consequence of internal stresses resulting from CTE mismatch between constituents during cooling (Huger et al., 2007; Mouiya et al., 2026; Tessier-Doyen, 2003).

Experimental observations further indicate that microcracking is responsible for the characteristic quasi-brittle, nonlinear mechanical response of industrial refractory materials (Ghassemi Kakroudi et al., 2009; Grasset-Bourdel et al., 2012; Kakroudi et al., 2009; Mouiya et al., 2023; Shan et al., 2022). This response manifests as an enhanced fracture energy (Mouiya et al., 2026), a high strain-to-failure (Mouiya et al., 2023), a significant irreversible deformation after unloading, as well as a significant hysteresis between unloading and reloading (Kakroudi, 2007). While macroscopic constitutive behaviour can be characterised experimentally through extensive mechanical testing, such investigations are time-consuming and experimentally demanding (Chotard et al., 2008; Fruhstorfer & Gruber, 2023; Harmuth, 1995; Mouiya, 2024; Shan et al., 2022). In contrast, numerical approaches that can explicitly resolve microstructural microcracking mechanisms, such as crack initiation, propagation, branching, closure, and friction, offer a powerful alternative for visualisation/understanding of precise damage evolution within the microstructure of a given material, thus offering a promising route for the optimisation of refractory microstructures (Buljak & Bruno, 2018; Espinosa & Zavattieri, 2003a; Fasching et al., 2015; Jebahi et al., 2015; Nguyen et al., 2014).

Within this framework, the present PhD project, carried out under the CESAREF program, is a collaborative effort between the Thermomechanics of Ceramics (TMC) Group at IRCER (Limoges) and the Imerys Technology Centre (ITC) in Lyon. The project aims to leverage advanced numerical

License CC BY-NC-ND 4.0

modelling tools to simulate key microstructural damage mechanisms occurring during thermomechanical loading, with a particular emphasis on the cooling stage (André et al., 2017). By linking microstructural crack evolution to macroscopic thermomechanical response (Asadi, 2021; Nguyen, 2019), the study seeks to quantify the role of an anisotropic CTE of the aggregates in promoting microcracking and to assess its impact on thermomechanical properties (Kakroudi, 2007; Mouiya, 2024). In addition, since porosity is an inherent feature of refractory materials (Bruno & Kachanov, 2013; Tessier-Doyen, 2003), the contribution of pores under thermomechanical loading conditions, still largely unexplored numerically, is also investigated here.

To achieve these objectives, the Discrete Element Method (DEM) is employed, as it is particularly well suited to capture multiple crack initiations, propagations, branching, closures, and frictional interactions, while naturally representing complex heterogeneous microstructures (André et al., 2017; Asadi, 2021; Nguyen, 2019). Although previous works using DEM have been conducted at TMC for materials exhibiting isotropic CTE (André et al., 2017; Nguyen, 2019), the behaviour of materials with anisotropic CTE remains unexplored. Addressing this gap constitutes a central focus of the present study.

The DEM framework adopted in this work is the improved Distinct Lattice Spring Model (iDLSM) (André et al., 2019; André & Celigueta, 2023; Ranganathan et al., 2025), implemented quite recently within the GranOO workbench (André et al., 2015) developed at IRCER. The iDLSM offers a continuum-equivalent description through advanced contact laws while naturally incorporating fracture processes in quasi-brittle materials, thereby reducing the need for extensive parameter calibration typical of classical DEM approaches (André et al., 2019; André & Celigueta, 2023).

In this context, the present dissertation is organised into six chapters, whose structure and content are briefly outlined below.

Chapter I is dedicated to the state of the art relevant to the present PhD research. It first introduces refractory materials, with emphasis on their applications and in-service thermomechanical behaviour. The chapter then highlights the importance of microstructural optimisation and reviews microstructural design strategies that can be adopted to experimentally develop refractory materials with enhanced thermal shock resistance. Subsequently, an overview of numerical approaches used to investigate the thermomechanical behaviour of refractory materials at the microstructural scale is presented, focusing on two main classes: full-field continuum-based methods and particle-based methods. The capabilities and limitations of these approaches are critically discussed with respect to their ability to represent key physical mechanisms relevant to refractory materials. Finally, the chapter concludes with a comparative assessment of the reviewed numerical methods, leading to the selection of the most suitable modelling framework for the present study. A particular attention is given to the ability of the chosen approach to account for thermal expansion mismatch, multiple crack initiation, opening and closure, the representation of heterogeneous and damaged microstructures, and the linkage between microstructural evolution and macroscopic thermomechanical response.

Chapter II is dedicated to the improved Distinct Lattice Spring Model (iDLSM), which constitutes the advanced modelling framework employed in this PhD research. The chapter first introduces the fundamental principles of the iDLSM, including the strategy used to generate iDLSM samples, the key steps involved in reaction force computation, which differ from those of classical Discrete Element Method (DEM) approaches, and the crack management strategy inherent to this formulation. The chapter then details the methodological enhancements developed within the scope of this work, namely crack closure management, anisotropic thermal expansion, and

License CC BY-NC-ND 4.0

thermomechanical coupling. These developments are further integrated with Periodic Boundary Conditions (PBCs) to enable two-scale analyses. Since a PBC framework is employed, the strategies used to impose mechanical and thermal loading under such conditions are also discussed. Finally, the chapter presents the validation of the enhanced iDLSM framework using a hypothetical model material, where macroscopic responses, including apparent Young's modulus, Poisson's ratio, thermal strain, CTE, and stress-strain behaviour, are evaluated.

Chapter III is primarily dedicated to the review of industrial refractory materials and their corresponding thermomechanical behaviour, with the aim of identifying the key characteristic features that must be captured in numerical models. This overview provides essential insight into the typical responses of refractory materials under service conditions and helps define the modelling requirements relevant to the objectives of the present PhD. Based on this analysis, the chapter identifies suitable model materials for the numerical investigations. In particular, aluminium titanate-based refractories are described in detail to familiarise the reader with their characteristic macroscopic thermomechanical behaviour under thermal and mechanical loading. In accordance with the selected model materials, the chapter then discusses the strategy adopted to generate a simplified refractory microstructure that realistically represents the essential features of the chosen system. Finally, the chapter concludes by presenting the expected outputs, the thermomechanical modelling framework, and the overall workflow adopted for analysing the different model microstructures considered in this study.

Chapter IV addresses the primary objective of the present PhD, namely to investigate the role of anisotropic CTE in the generation of microcracks and the consequent impact of microcracking on the thermomechanical behaviour of refractory model materials. To this end, polycrystalline aluminium titanate (AT) is employed as a first model material throughout this chapter. The chapter first focuses on validating the numerical framework by comparing simulation results with available experimental data for polycrystalline AT, including dilatometry measurements and the evolution of Young's modulus. To this purpose, a strategy for generating representative polycrystalline microstructures is proposed, and the thermomechanical framework introduced in **Chapter III** is applied to compute apparent dilatometric response and elastic properties. Once validated, the modelling framework is used to perform detailed micromechanical analyses of microcracked samples. Novel strategies are proposed to represent local stress distributions and crack statistics, enabling identification of preferred crack orientations, locations, propagation modes, and the evolution of crack surface area. In addition, mechanical simulations under monotonic and cyclic tensile loading conditions are presented to capture brittle and quasi-brittle (nonlinear) stress-strain responses, as well as irreversible (pseudo-plastic) strains observed experimentally. This chapter thus constitutes a first step toward the development of a virtual DEM laboratory for a better understanding of the thermomechanical behaviour of such complex industrial refractory materials.

Chapter V is dedicated to investigate the role of pores and their contribution to the thermomechanical behaviour of refractory materials. For this purpose, the previously investigated polycrystalline AT model is enriched by the introduction of certain number of spherical pores. The chapter begins by describing the strategy used to generate such porous microstructures. Since the pore volume fraction is known to significantly influence mechanical behaviour, a preliminary study is conducted to assess its impact on elastic properties, with results compared to analytical predictions to validate the numerical trends. To isolate the specific role of porosity, a comparative study is then performed between the porous AT model and the dense AT model investigated in **Chapter IV**. Thermomechanical characterisation of the porous samples, including apparent Young's modulus and dilatometry, is carried out, followed by micromechanical and mechanical analyses. The results are compared with those of the dense samples to assess the influence of

License CC BY-NC-ND 4.0

pores on local stress distribution, preferred crack orientation, crack propagation mechanisms, and macroscopic stress-strain response.

Chapter VI focuses on composite refractory systems containing coarse monocrystalline AT aggregates exhibiting anisotropic CTE embedded within a fine-grained alumina matrix. This chapter addresses the third objective of the present PhD, namely the investigation of the effect of monocrystalline aggregate volume fraction on microcracking and the resulting thermomechanical behaviour. The strategy used to generate such composite microstructures is first presented. The numerical framework is then validated by computing the apparent Young's modulus for different aggregate volume fractions and comparing the results with available experimental data on similar materials. Subsequently, micromechanical and mechanical analyses, similar to those performed in **Chapter IV** and **Chapter V**, are conducted to investigate the influence of anisotropic aggregates on local stress distribution, crack orientation and propagation, crack surface area evolution, and macroscopic stress-strain response under monotonic and cyclic loading.

Finally, the dissertation concludes with a synthesis of the main scientific contributions of this work, along with perspectives for future research based on the experience gained and the results obtained using the iDLSM approach.

License CC BY-NC-ND 4.0

Chapter I. State of art about refractory material and thermomechanical approaches

I.1. Introduction

Industrial refractory materials used in kilns, continuous casters, Furnace etc, in the steel, cement and glass applications, are routinely exposed to severe thermal gradients and rapid temperature fluctuations (Guthrie & Isac, 2022; Khlifi, 2019; Peray K. E & Waddell J. J, 1986; Peruzzi, 2000). As a result, thermal shock resistance, the ability of a material to withstand sudden temperature changes without cracking or failure, constitutes a critical performance requirement (Alekseeva et al., 2022). Their behaviour under such conditions is governed by a complex and heterogeneous microstructure, as well as by the intricate coupling between thermophysical and mechanical properties (Kakroudi, 2007; Lemaistre, 1998; Mouiya, 2024; Peruzzi, 2000; Tessier-Doyen, 2003). This chapter first examines how microstructural complexity, encompassing aggregates, matrix, porosity, and inherent or induced microcracks, contributes to the accommodation of thermally induced stresses. It then revisits the principal theoretical frameworks of thermal shock, with particular emphasis on Kingery's thermoelastic theory (Kingery, 1955) and Hasselman's energetic approach (Hasselman, 1969) which provide fundamental relationships between material properties, and crack initiation and propagation. Building on this theoretical background, the chapter discusses microstructural design strategies aimed at enhancing thermal shock resistance. These include approaches to increase fracture energy (Steinbrech, 1992) as well as strategies that deliberately promote microcracking through thermal expansion mismatch (Huger et al., 2007), aggregate anisotropy (Mouiya et al., 2026), and tailored processing routes (Boateng et al., 2025; Kakroudi et al., 2008). The resulting microcracked states are characterized in terms of their macroscopic mechanical response under cyclic tensile loading (Kakroudi et al., 2008) and wedge splitting tests (Grasset-Bourdel et al., 2013). Finally, analytical (Hill, 1952) and damage-mechanics-based models (Öchsner, 2016) for the effective properties of heterogeneous (Hashin & Shtrikman, 1963) and microcracked materials (Kachanov, 1992) are presented, providing a link between microstructural features and the effective thermo-mechanical response (Tessier-Doyen, 2003). On this materials and modelling foundation, the chapter then turns to numerical strategies for simulating fracture initiation and propagation in refractory materials. Continuum, full-field approaches are first addressed, to capture crack onset and evolution within a continuum framework (Chen & Wang, 1996). In parallel, particle-based approaches, are examined as powerful alternatives for representing discontinuities, complex crack topologies, and interactions between microstructural features (André et al., 2017; De Meo et al., 2016; Rui & Zhao, 2022; Sun et al., 2024). Based on this overview, the chapter evaluates the suitability and limitations of these numerical strategies for refractory applications, leading to the definition of the specific scope and objectives of the present study. These objectives aim to establish a consistent framework for the design and numerical assessment of thermal-shock-resistant in refractory materials.

I.2. Thermal shock resistance of industrial refractory materials

This section addresses thermal shock resistance from both microstructural and mechanistic perspectives. Refractory microstructures are inherently complex, and this complexity can be exploited to accommodate thermally induced stresses (Biswas & Sarkar, 2020; da Luz A et al., 2015; Kingery et al., 1977). Classical theoretical frameworks of thermal shock (Hasselman, 1969; Kingery, 1955) are reviewed to relate material properties and loading conditions to crack initiation and damage evolution. Building on this foundation, microstructural design strategies are examined (Grasset-Bourdel et al., 2012; M. G. Kakroudi et al., 2009; Mouiya, Tessier-Doyen, et al., 2023), and the resulting key macroscopic mechanical behavior of industrial refractories is discussed (Kakroudi, 2007; Mouiya, 2024). Finally, analytical and damage-mechanics-based models for

License CC BY-NC-ND 4.0

heterogeneous (Reuss, 1929; Voigt, 1889) and microcracked refractories (Guéguen & Kachanov, 2011) are presented, linking microstructure, microcracking, and thermomechanical properties.

I.2.1. Illustration of microstructure complexity to face thermal shocks

High-temperature industrial processes are fundamental to modern manufacturing, enabling the production of metals, glass, cement, ceramics, petrochemicals, and other materials (da Luz A et al., 2015; Kingery et al., 1977; Sarkar, 2023). These processes often operate above 1000 °C under chemically aggressive environments, and involve severe thermal and mechanical loading. The performance of materials forming furnace linings, kilns, continuous casters, and other equipment largely determines operational reliability, efficiency, and safety (Kappmeyer et al., 1974; Khlifi, 2019; Peray K. E & Waddell J. J, 1986; Peruzzi, 2000). Refractory materials are thus specifically designed to maintain mechanical strength, dimensional stability, and chemical durability at elevated temperatures. Chemically, refractories include oxides (silica, alumina, magnesia, zirconia, chromia) and non-oxides (carbon, silicon carbide, boron carbide), selected for their thermal stability, chemical resistance, and high-temperature performance (da Luz A et al., 2015; Kappmeyer et al., 1974; Peray K. E & Waddell J. J, 1986).

At the microstructural scale, refractory materials are designed as heterogeneous composites, which, in most of the case, contain a significant amount of porosity (Biswas & Sarkar, 2020; da Luz A et al., 2015; Shyam et al., 2015). A first representative example is andalusite-based castable (M. G. Kakroudi et al., 2009), which are extensively used in the steel industry due to their excellent resistance to thermal shock. As illustrated in Figure I-1a, the microstructure of an andalusite-based refractory consists of a cementitious matrix embedding andalusite aggregates, providing a simplified representative view of the material architecture (Kakroudi, 2007). From a crystallographic perspective, the performance of these materials is strongly influenced by the nature of these andalusite aggregates. In fact, Andalusite is an orthorhombic mineral ($a \neq b \neq c$; $\alpha = \beta = \gamma = 90°$) that exhibits pronounced anisotropy in thermal expansion (M. G. Kakroudi et al., 2009). Its coefficients of thermal expansion differ significantly along the crystallographic axes (α_a = 12.9 × 10^{-6} K^{-1}, α_b = 9.6 × 10^{-6} K^{-1} and α_c = 3.1 × 10^{-6} K^{-1}), in contrast to the nearly isotropic thermal expansion of the castable matrix (α ≈ 7.6 × 10^{-6} K^{-1}) (Huger et al., 2007). This specific thermal expansion properties lead to a significant amount of microcracks after a given first thermal cycle that enhance the ability of the material to sustain later thermal shocks (M. G. Kakroudi et al., 2009). As a second representative example, alumina-graphite composites (Peruzzi, 2000; Pilli & Sarkar, 2020), which are extensively used in steel continuous casting due to their excellent resistance to thermal shock, could be seen as a much more complex refractory material. Figure I-1b depicts the alumina-graphite composite where alumina grains and graphite flakes constitute the aggregates, and the pyrolytic carbon (resulting from the pyrolysis of the resin used as bonding phase) constitute the matrix (Pilli & Sarkar, 2020). The contrast in thermal expansion between those different phases lead also to a significant amount of microcracks/decohesion's after firing that also enhance the ability of the material to sustain thermal shocks (Peruzzi, 2000; Pilli & Sarkar, 2020).



a) andalusite-based (Kakroudi, 2007) b) alumina-based (Peruzzi, 2000)

Figure I-1: Illustration of heterogeneous refractory microstructure used in refractory component

License CC BY-NC-ND 4.0

Typically, such refractories are produced by thermal treatment up to 1000-1600 °C, held for several hours, and subsequently cooled under controlled conditions (Biswas & Sarkar, 2020; da Luz A et al., 2015). Indeed, during such thermal treatment process, the material exhibits critical stresses due to mismatches in the coefficient of thermal expansion (CTE) between phases (Kakroudi et al., 2009, 2008). As consequences, when the material reaches locally its tensile strength, the materials exhibit microcracks, across the microstructure. As a consequence, a microcracked refractories are obtained (Case et al., 1981; Huger et al., 2011; Mouiya et al., 2026; Shan et al., 2022).

Among the various degradation mechanisms affecting refractories, thermal shock is often the most critical life-limiting factor (Alekseeva et al., 2022). On introducing such microcracked refractories as linings for high-temperature applications, the existing rapid heating and cooling generate additional thermal stresses resulting from thermal gradient within the component. New cracks may form, while pre-existing microcracks initially help relieving stresses by enabling energy dissipation and stress redistribution (Khlifi, 2019; Peruzzi, 2000). However, with continued thermal cycling, the material's capacity to accommodate new damage could diminish. In fact, when damage progress within the microstructure, at a given threshold, microcracks usually coalesce to form macroscopic cracks (localisation), ultimately leading to final rupture of the component (Peruzzi, 2000; Vakhrushev et al., 2021).

Understanding refractory performance in industrial contexts is therefore essential to evaluate their impact on equipment availability, product quality, energy efficiency, and maintenance costs, highlighting the critical role of refractory microstructure design for high-temperature processes.

I.2.1.1. Industrial context 1: Cement rotary Kiln

The cement rotary kiln is the central thermal unit in clinker production, converting finely ground and homogenized raw minerals into sintered clinker. Continuous rotation promotes efficient mixing and enhances heat and mass transfer between the gas phase, material bed, and refractory lining (Peray K. E & Waddell J. J, 1986; Szczerba et al., 2017) as shown in Figure I-2. The thermal efficiency and operational stability of the kiln directly influence clinker quality, making the performance and durability of the refractory lining a critical industrial concern (Peray K. E & Waddell J. J, 1986).

Along the kiln, distinct thermal and chemical environments impose varying demands on the refractory system, which can be divided into six operational zones. Zones 1 and 2, corresponding to drying, preheating, and calcining, experience temperatures of approximately 200-1050 °C (Figure I-2). While these temperatures are moderate compared with downstream zones, frequent thermal cycling during start-ups, shutdowns, and process fluctuations generates steep transient thermal gradients (Peray K. E & Waddell J. J, 1986). As material progresses through zones 3 (upper transition), 4 (sintering), and 5 (burning), temperatures rise to 1050-1450 °C (Figure I-2). In these zones, solid-state reactions intensify, partial melting occurs, and fluctuations in coating stability expose the refractory to combined thermal, chemical, and mechanical stresses (Khlifi, 2019; Peray K. E & Waddell J. J, 1986; Shubin, 2001). The burning zone represents the most severe environment, with refractory hot-face temperatures of 1250-1450 °C and even higher gas-phase temperatures. Intense radiative heat flux, alkali- and sulphate-rich vapors, and extreme thermal gradients act simultaneously, and sudden loss of clinker coating can abruptly expose bare refractory to flame, causing severe thermal shock (Janati, 2020; Peray K. E & Waddell J. J, 1986). In the lower kiln and discharge region (zone 6 in Figure I-2), temperatures decrease rapidly, but localized cooling and transient events, such as emergency stops, continue to impose significant thermal shock despite lower average temperatures.

License CC BY-NC-ND 4.0

In general, the kiln has two types of linings (see Figure I-2): i) working lining (the lining that is in direct contact with the clinker) and safety lining (the lining that is not in contact with the clinker) (Khlifi, 2019; Peray K. E & Waddell J. J, 1986). To protect the kiln shell and ensure stable operation, refractories are selected according to local thermal and chemical conditions (Khlifi, 2019; Peray K. E & Waddell J. J, 1986; Shubin, 2001) (see Figure I-2). In the burning and transition zones (3rd to 5th zones), basic refractories such as magnesia-spinel (where spinel aggregates are embedded in magnesia matrix) are preferred for their resistance to clinker melt corrosion and high refractoriness (Peray K. E & Waddell J. J, 1986; Szczerba et al., 2017). However, their high elastic modulus and limited fracture toughness make them inherently sensitive to thermal shock, particularly during coating loss (Janati, 2020; Khlifi, 2019; Peray K. E & Waddell J. J, 1986). In cooler and low temperature regions (1st, 2nd and 6th zones), aluminosilicate and high-alumina refractories are used; their phase composition and microstructure can be tailored to enhance strain tolerance through controlled porosity and crack-deflecting features (Peray K. E & Waddell J. J, 1986; Szczerba et al., 2017).

Refractories loss of mechanical integrity arises from the combined action of chemical, mechanical, and thermal mechanisms, with thermal shock being dominant, especially in the transition zones. Rapid temperature changes (due to the rotation of the furnace) generate differential expansion between the hot face and the cooler interior, inducing tensile stresses that can initiate microcracks at grain boundaries, pores, and phase interfaces (Khlifi, 2019; Peray K. E & Waddell J. J, 1986; Shubin, 2001). Repeated cycling could lead these microcracks to coalesce into macrocracks, typically perpendicular to the hot face, ultimately causing spalling when critical crack depths are reached. The severity of thermal shock depends on the magnitude and rate of temperature change, the refractory's thermal and mechanical properties, microstructure, and the mechanical constraints imposed by the lining and shell (Peray K. E & Waddell J. J, 1986). Understanding these factors is essential for improving lining durability and overall kiln reliability.

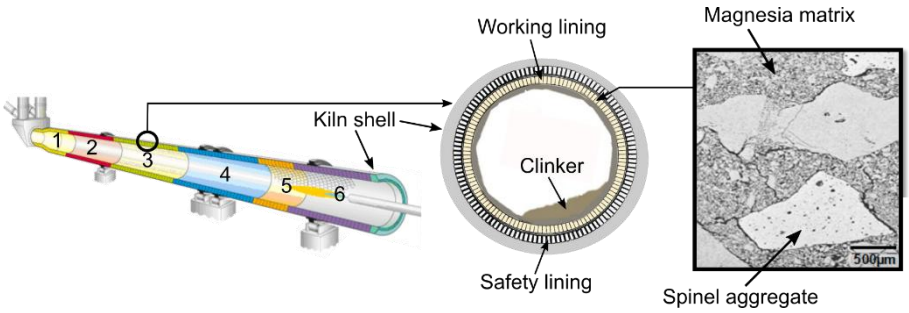

Figure I-2: Application of magnesia-spinel lining in cement rotary kiln (Grasset-Bourdel, 2011; Khlifi, 2019)

I.2.1.2. Industrial context 2: Continuous caster

Continuous casting is the dominant industrial route for producing semi-finished steel products due to its high productivity, energy efficiency, and precise control of product quality. Figure I-3 illustrates a typical continuous casting machine used in the steel industry. In this process, liquid steel is tapped from the ladle and conveyed through refractory-lined flow control components, such as the ladle shroud, which regulate steel flow while protecting it from atmospheric exposure (Guthrie & Isac, 2022; Irving, 2024; Zhang et al., 2019), as depicted in Figure I-3. This component consists of a shoulder highlighted in pink region, a liner and slag line regions with the body highlighting the pathway along which the liquid steel would flow.

The ladle shroud provides a controlled pathway for transferring molten steel from the ladle to the tundish and simultaneously functions as a structural ceramic component exposed to temperatures

License CC BY-NC-ND 4.0

approaching 1600 °C and severe thermal transients. Its thermo-mechanical integrity is therefore essential for caster reliability and operational safety (Irving, 2024; Zhang et al., 2019). To withstand chemical attack, erosion, and extreme thermal loading, ladle shrouds are lined with refractory materials specifically designed for thermal shock, corrosion, and erosion resistance (Kappmeyer et al., 1974). Alumina-carbon and alumina-graphite refractories are commonly employed, often enhanced (in some specific area) with zirconia, spinel-forming phases, or other engineered aggregates (Kappmeyer et al., 1974). Figure I-3 illustrates the application of alumina-carbon as liner in the ladle shroud (Peruzzi, 2000).

Depending on plant practice, ladle shrouds may be installed at ambient temperature or preheated to intermediate levels. As an illustration, Figure I-3 depicts the ladle shroud under in-service condition. Upon first contact with molten steel, they experience a rapid temperature rise, followed by quasi-steady high-temperature exposure and, in multi-heat sequences, repeated heating and cooling cycles due to ladle exchanges, changes in casting conditions, or unplanned interruptions (Guthrie & Isac, 2022; Irving, 2024; Kappmeyer et al., 1974). Severe thermal shocks occur during start-up, when the molten steel suddenly arrive in contact with the refractory part. These rapid temperature changes generate steep thermal gradients across the refractory wall and along the component length, inducing high radial and circumferential stresses (Guthrie & Isac, 2022; Irving, 2024; Zhang et al., 2019). As the internal stresses rise within the refractory part, geometrical discontinuities, such as shoulders, connection regions etc, act as stress concentrators and are thus common sites for crack initiation. Over repeated cycles, these cracks may propagate and coalesce, causing spalling, material loss, and, in extreme cases, macroscopic fracture (Irving, 2024; Peruzzi, 2000; Vakhrushev et al., 2021; Zhang et al., 2019). As an illustration, Figure I-3 depicts a catastrophic failure of the ladle shroud under thermal shock, where the crack path is highlighted by the white dashed line. Such critical damage compromises both mechanical integrity and functional performance, as cracks can facilitate steel penetration and air aspiration (very detrimental for the quality of steel) (Irving, 2024; Zhang et al., 2019). Given their vulnerability to extreme thermal shock, particularly during first filling, mitigation strategies must focus on the refractory material, particularly its microstructure, to enhance thermal shock resistance.

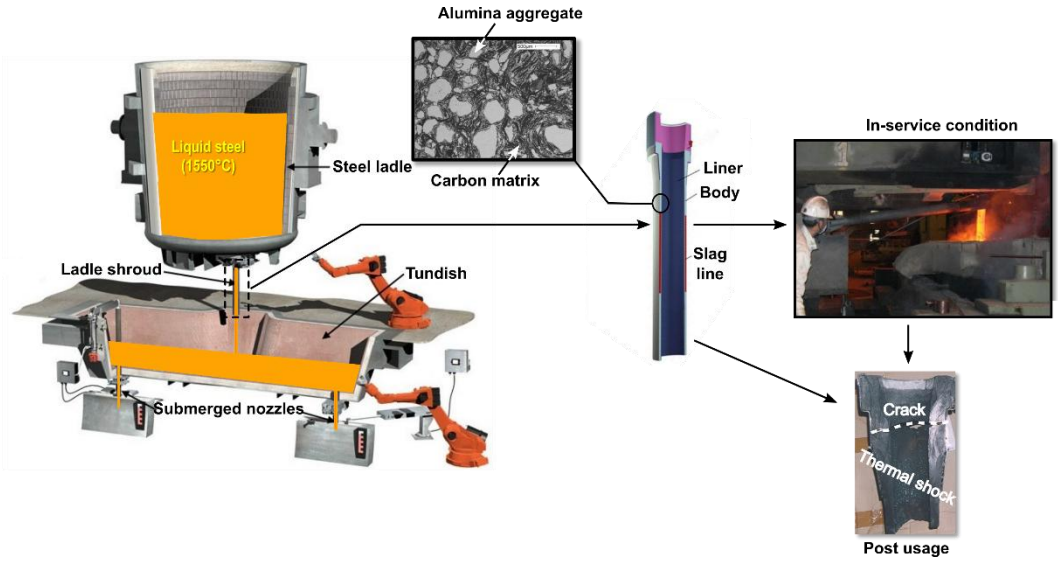

Figure I-3: Application of alumina-carbon refractory in the ladle shroud for continuous caster (Peruzzi, 2000)

License CC BY-NC-ND 4.0

Consequently, improving the sustainability of refractory materials has become an important research focus, driving efforts to identify and optimize the key material properties and microstructural parameters that govern thermal shock resistance and service life.

I.2.2. Theoretical framework about thermal shock

Refractories are often subjected to thermal shock and, consequently, it is important to improve their thermal shock resistance. Beginning in the 1950s and 1960s, two major analytical frameworks were introduced to quantify how materials (and refractories) respond under rapid temperature changes.

- Thermo-elastic approach (Kingery, 1955)**:** This method examines thermal-shock failure from a macroscopic perspective. It evaluates how temperature gradients generate internal stresses and predicts failure when those stresses exceed the material's inherent strength; Indeed, this approach is more suitable for brittle material;
- Energetic or fracture-mechanics approach (Hasselman, 1963, 1969, 1985): In contrast, this framework takes into account microstructural aspects. It describes how existing microcracks (flaws) in the material evolve and propagate under thermal loading, linking thermal-shock resistance to energy considerations and fracture mechanics. Indeed, this approach is more suitable for quasi-brittle and non-linear material.

I.2.2.1. Kingery's thermoelastic theory

The thermoelastic approach proposed by (Kingery, 1955) describes thermal-shock behavior by considering an ideal case where an infinite plate at an initial temperature T_i is suddenly exposed to a medium at temperature T_f. The analysis assumes a uniform biaxial stress field and a continuous, homogeneous, isotropic, and linearly elastic material (Glandus & Boch, 1984).

Under these assumptions, the maximum surface stress σ_T produced by an instantaneous temperature change, can be written using the two-dimensional form of Hooke's law:

$$\sigma_T = \frac{E\alpha\Delta T}{1-\nu}. \qquad \text{I-1}$$

where, E is the Young's modulus, ν is the Poisson's ratio, α is the Coefficient of Thermal Expansion (CTE) of the infinite plate material and ΔT is the temperature difference between T_i and T_f.

Crack initiation occurs when this thermal stress reaches the material's rupture stress ($\sigma_T = \sigma_R$). The corresponding temperature difference is the critical thermal shock, ΔT_c. Kingery defined a thermal-shock resistance parameter R (Kingery, 1955), equal to ΔT_c, which expresses the maximum instantaneous temperature gradient the material can tolerate without cracking:

$$R = \frac{\sigma_R(1-\nu)}{E\alpha} \qquad \text{I-2}$$

High values of R indicate good resistance, typically associated with high rupture strength and low Young's modulus and thermal expansion coefficient (Kingery, 1955).

When heat transfer is not instantaneous (a mild thermal shock), thermal conductivity λ influences the temperature profile, and a second parameter R' is used:

$$R' = \lambda R \qquad \text{I-3}$$

License CC BY-NC-ND 4.0

A high R' reflects higher thermal conductivity resulting in improved thermal shock resistance (Kingery, 1955).

I.2.2.2. Hasselman energetic theory

A few years after Kingery's work, (Hasselman, 1963, 1969, 1985) introduced an alternative framework based on the presence of pre-existing microdefects. His model assumes that defects:

- already exist before the thermal shock occurs,
- are uniformly distributed with a density number N, and
- share identical geometry and size, idealized as discs of radius a.

Interactions between the stress fields around individual defects are neglected. During a thermal shock, these defects could evolve in a manner that reduces the system's total mechanical energy (Hasselman, 1963). The applied thermal stress, denoted σ, is considered to be uniform and triaxial, corresponding to uniform cooling with constrained external surfaces (Hasselman, 1969, 1985). It can be expressed as:

$$\sigma_T = \frac{\alpha E \Delta T}{1 - 2\nu}. \quad \text{I-4}$$

where, E is the Young's modulus, ν is the Poisson's ratio and α is the CTE of the material and ΔT is the temperature difference under thermal shock.

The total energy of the system is then written as:

$$U_{\text{total}} = U_{\text{elastic}} + U_{\text{defects}} \quad \text{I-5}$$

where U_{elastic} is the elastic strain energy stored in the material and U_{defects} is the energy associated with the defect surfaces (Hasselman, 1969).

Crack growth occurs when increasing the size of pre-existing defects results in a reduction of the total energy. In this situation, part of the initial elastic energy is converted into new surface energy during crack extension (Hasselman, 1963, 1969).

When defects are small, crack propagation is abrupt once ΔT exceeds the critical value ΔT_c. The cracks increase significantly in size to dissipate the stored elastic energy, leading to a marked decrease in rupture strength (Hasselman, 1969). Hasselman therefore introduced a thermal-shock damage resistance parameter, R'''', given by (Hasselman, 1963):

$$R'''' = \frac{\gamma_s E}{\sigma_R^2 (1 - \nu)} \quad \text{I-6}$$

where γ_s is the surface free energy, E the initial Young's modulus, and σ_R the initial rupture stress. Improving this parameter requires high surface energy, high elastic modulus, and a relatively low initial rupture stress (Hasselman, 1963, 1969).

When defects are large and if a new $\Delta T_c'$ (being larger than ΔT_c) is reached, crack propagation could again take place but in a stable manner (Hasselman, 1969). Thus, Hasselman defined a corresponding resistance parameter, R_{st}:

License CC BY-NC-ND 4.0

$$R_{st} = \sqrt{\frac{\gamma_s}{\alpha^2 E}} \quad \text{I-7}$$

In this regime, enhanced resistance to crack growth is achieved by using materials with high fracture (surface) energy (Hasselman, 1969).

I.2.3. Microstructure design to improve thermal shock resistance

I.2.3.1. Strategy to improve fracture energy

Industrial refractory design strategies frequently focus on increasing fracture energy in accordance with the Hasselman approach, since it is generally more effective to develop more compliant materials than to achieve very high strengths, as emphasized in the Kingery approach. Enhancing the fracture energy of refractory materials relies on designing microstructures capable of dissipating significant energy during crack initiation and propagation (Cunha-Duncan & Bradt, 2003; Hasselman, 1969).

One effective approach is to promote cracks deflection, branching, and bridging (see Figure I-4) (Miyaji et al., 2014; Steinbrech, 1992). The introduction of coarse aggregates (example like andalusite (M. G. Kakroudi et al., 2009) or aluminum titanate (Mouiya et al., 2026) based castable), elongated grains (Mouiya, Tessier-Doyen, et al., 2023), or phases exhibiting anisotropic elastic or thermal properties forces cracks (Kakroudi, 2007) to follow tortuous paths, increasing the effective fracture surface, and so on, the energy consumption for creating this surface (Mouiya et al., 2026; Mouiya, Martynyuk, et al., 2023). In addition, interlocking grains or elongated aggregates can additionally act as bridges across cracks (see Figure I-4), where pull-out or rupture consumes further energy as shown in Figure I-4 (Miyaji et al., 2014).

Controlled weak grain boundaries and microcracks formation constitute another important toughening mechanism in refractories (Mouiya, Tessier-Doyen, et al., 2023; Steinbrech, 1992). In this context, engineered weak grain boundaries (or secondary interfaces) are interfaces whose bonding strength is deliberately reduced or tailored during processing. This is performed through suitable choices of additives (Chen et al., 2021) and bonding-phase chemistry (Sarkar, 2020), firing/sintering schedule (Kakroudi et al., 2009, 2008), liquid-phase content (Kim et al., 2007; Miyaji et al., 2014), and/or CTE mismatch between phases (Grasset-Bourdel et al., 2012; Mouiya et al., 2026). In such a way, the crack propagates in a stable and non-catastrophic manner under thermo-mechanical loading. Such tailored interfaces promote the formation of distributed microcracks around aggregates prior to macroscopic failure (see Figure I-4). These microcracks blunt advancing crack tips (see Figure I-4), redistribute local stresses, and thereby increase the energy required for further crack propagation (Huger et al., 2007; Miyaji et al., 2014; Steinbrech, 1992). Aluminum titanate-based refractories exemplify this strategy: their pronounced anisotropic thermal expansion (Bayer, 1971), combined with controlled interfacial bonding (Chen et al., 2021), generates beneficial microcrack networks that effectively enhance the apparent fracture energy of the material (Mouiya, Martynyuk, et al., 2023).

Reinforcement with fibres (Liu et al., 2024) and tough particulates (Liu et al., 2024) provides additional energy-dissipating mechanisms. Metallic or ceramic fibres bridge cracks (similar to aggregate bridging in Figure I-4) and transfer load across the fracture plane, with debonding and pull-out processes (see Figure I-4) absorbing substantial energy and imparting quasi-brittle behaviour (Miyaji et al., 2014; Steinbrech, 1992). Particulates such as mullite needle (Mocciaro et al., 2022), spinel (Mukhopadhyay & Das Poddar, 2004), SiC (Becher et al., 1991), or partially stabilized ZrO_2 (Liu et al., 2016) could also be used to enhance toughness through crack deflection, transformation toughening, and residual stress development, as depicted in Figure I-4.

License CC BY-NC-ND 4.0

Microstructural optimisation (Mouiya, 2024) and porosity management (Tessier-Doyen, 2003) are also critical for improving refractory performance. An optimized particle-size distribution reduces critical flaw sizes and promotes a heterogeneous microstructure that helps resist to crack initiation and propagation (Braulio et al., 2008; Liu et al., 2016). Large or interconnected pores tend to act as stress concentrators and crack initiation sites. In contrast, a controlled population of fine, rounded pores can blunt crack tips and relieve local stresses without significantly reducing mechanical strength (Terzić & Pavlović, 2009; Tessier-Doyen, 2003; Trostel, 1962).

Finally, matrix chemistry and bonding systems (as phase bridging in Figure I-4) can be tailored to support these mechanisms. Low-cement and sol-gel bonded matrices promote finer, more homogeneous microstructures (Sarkar, 2020), while additives that form in-situ phases (e.g., spinel or mullite) introduce residual stresses and heterogeneities that deflect cracks and generate microcracks (Braulio et al., 2008; Mukhopadhyay & Das Poddar, 2004). Lastly, careful processing, including mixing, casting, drying, and firing, is essential for improving the sustainability of refractory materials by enhancing their effective fracture energy and resistance to thermal shock damage (de Carvalho Bonaldo, 2022; Doncieux et al., 2008; Kakroudi et al., 2008; Ohin Mensan Daniel et al., 2014).

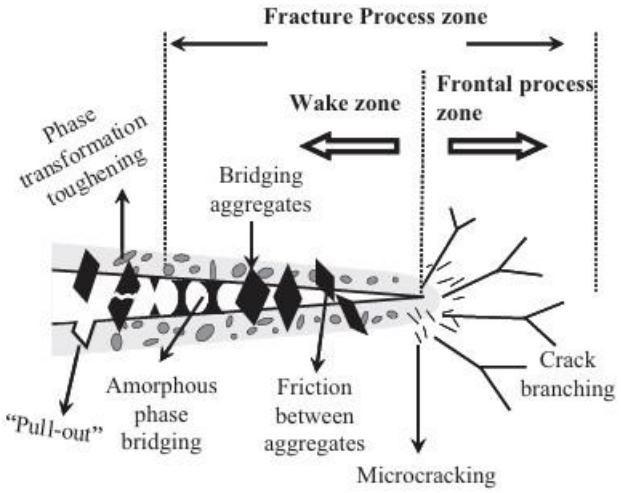

Figure I-4: Illustration of different individual mechanisms which could allow to enhance energy dissipation during crack propagation within refractories microstructure (Miyaji et al., 2014; Steinbrech, 1992)

To summarize, one effective strategy to improve the fracture energy of refractory materials is the use of coarser aggregates in combination with controlled weak interfaces and microcracks (Kakroudi, 2007; Mouiya, 2024). Numerous studies (Chotard et al., 2008; Grasset-Bourdel et al., 2012; Huger et al., 2011; Kakroudi et al., 2008; Mouiya et al., 2026) have demonstrated that promoting controlled microcracking, often induced by a CTE mismatch between the aggregate and the matrix (Kakroudi, 2007; Mouiya, 2024; Nguyen, 2019; Tessier-Doyen, 2003), is a promising approach to enhance fracture energy (Aksel & Warren, 2003; Grasset-Bourdel et al., 2013; Mouiya et al., 2026).

More recent work further highlights the dual role of coarser aggregates, which not only act as crack arresters but also promote the formation of beneficial microcrack networks (Miyaji et al., 2014). In this context, Kakroudi et al., (2008) clearly demonstrated the efficiency of the usage of coarse monocrystalline aggregates which are highly anisotropic (like andalusite). Such aggregates simultaneously act as crack arresters and promote dense, stable microcrack networks, as observed

License CC BY-NC-ND 4.0

in andalusite-(Kakroudi, 2007) and aluminum titanate-based (Mouiya, 2024) systems, ultimately leading to enhanced apparent fracture energy and improved thermal damage tolerance.

I.2.3.2. Strategies to induce microcracking via CTE mismatch

From the previous discussion, it is understood that controlled microcracking is a deliberate strategy to improve the fracture-related performance of refractories by promoting thermal defects such as microcracking during cooling from the firing temperature or under service conditions (Huger et al., 2007). Here, a particular attention is given to different microstructure configuration with a specific focus on the cooling stage (Tessier-Doyen et al., 2006), as it follows the sintering phase, which is a process commonly used for many refractories.

I.2.3.2.1. Isotropic aggregates generating microcracks by CTE mismatch with matrix

In general, by considering the schematic sketch of an isotropic aggregate embedded within an isotropic matrix (see Figure I-5), and the CTE mismatch $\Delta\alpha = \alpha_{matrix} - \alpha_{inclusion}$ during the cooling, three microstructural configurations can be developed locally (Tessier-Doyen et al., 2006):

- $\alpha_{matrix} - \alpha_{inclusion}$ = 0, perfect thermal expansion agreement: when there is perfect agreement in thermal expansion between the two phases, no stress develops since both the matrix and the inclusion have the same contraction. In this case, there is no internal stress and the initial state of the microstructure is preserved throughout the cooling process (Tessier-Doyen et al., 2006) (Figure I-5);
- $\alpha_{matrix} - \alpha_{inclusion}$ < 0, matrix contracting less than the inclusion: if the matrix contracts less than the inclusion, this results in radial tensile stress and orthoradial (also referred as circumferential) compression in the matrix (Tessier-Doyen et al., 2006). The tensile stress can lead to partial or complete interfacial decohesion/debonding of the inclusion (Figure I-5). This phenomenon is commonly seen in cordierite-mullite (Boccaccini et al., 2005; Chotard et al., 2008) industrial refractories;
- $\alpha_{matrix} - \alpha_{inclusion}$ > 0, matrix contracting more than the inclusion: conversely, when the matrix contracts more than the inclusion, the matrix experiences orthoradial (or circumferential) tension and radial compression (Tessier-Doyen et al., 2006). When the matrix can no longer accommodate the tensile stress, the orthoradial stress reaches a critical level, initiating the formation of radial microcracks (Figure I-5). This mechanism is typically observed in industrial magnesia-spinel refractories (Grasset-Bourdel, 2011).

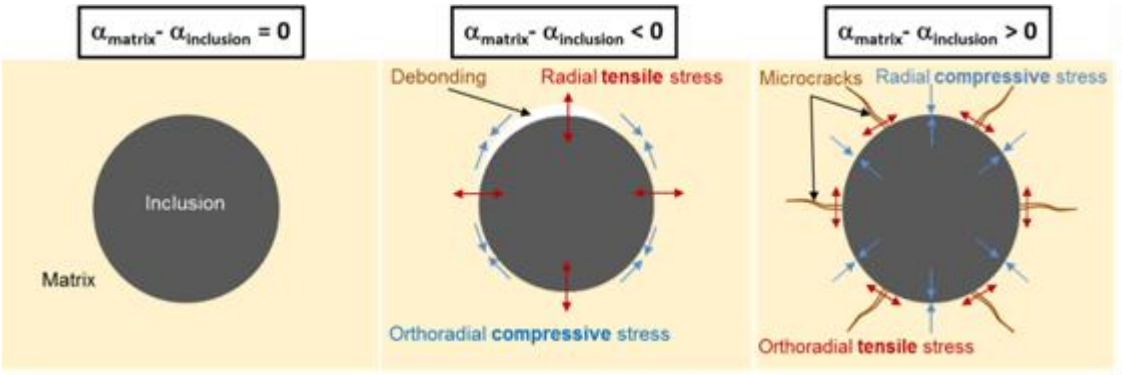

Figure I-5: Thermal stresses promotion in a single particulate-reinforced material (Mouiya, 2024; Tessier-Doyen et al., 2006).

So, for aggregates with an isotropic CTE (such as spinel), thermal expansion is uniform in all directions. A single inclusion embedded in a homogeneous matrix generates an approximately radially symmetric stress field (Eshelby, 1957). Thus, defects generally initiate as ring-like debonding along the aggregate-matrix interface (Boccaccini et al., 2005; Chotard et al., 2008) or

License CC BY-NC-ND 4.0

radial microcracks (Grasset-Bourdel et al., 2012; Tessier-Doyen, 2003) in the surrounding matrix (see Figure I-5). With increasing temperature range or repeated thermal cycles, these microcracked zones grow and may overlap, forming a statistically isotropic damage distribution at the mesoscale (Grasset-Bourdel et al., 2012; Tessier-Doyen, 2003). This relatively uniform morphology implies that microcrack density may evolve gradually with thermal cycling.

Having introduced these primary mechanisms, it becomes clear that engineers can deliberately exploit thermal-expansion mismatch to tailor the microstructure and high temperature performance of refractory materials (Huger et al., 2007). Several design levers are available, including the judicious selection of matrix and aggregate with respect to phase composition (da Luz A et al., 2015), particle size (Liu et al., 2016), morphology and quality (da Luz A et al., 2015), the magnitude and sign of the CTE mismatch (Fei, 2013), and thermal processing parameters (such as firing temperature, cooling rate, and thermal cycling) (Kakroudi et al., 2008; Mouiya, Tessier-Doyen, et al., 2023; Shan et al., 2022). Among these strategies, the incorporation of aggregates exhibiting a sufficiently large anisotropic CTE mismatch with the matrix is often the most effective means of activating controlled microcracking (Kakroudi et al., 2008; Mouiya et al., 2026). With these aspects, the resulting microcracks are fine, non-uniformly distributed, and remain subcritical, they can deflect, branch, or blunt propagating macrocracks (Hasselman, 1969; Mouiya, 2024; Steinbrech, 1992). In addition, if the aggregate is coarser, it could play the role of crack bridging (Kakroudi, 2007; Miyaji et al., 2014). Thereby, such an aggregate could contribute in enhancing thermal-shock resistance and fracture toughness without inducing a catastrophic loss of strength. Achieving this balance requires careful aggregate selection and precise process control to maximize the beneficial effects of CTE mismatch. In this context, not only the scalar value of the CTE but also its potential anisotropy at the crystal scale becomes critical, as the directional thermal-expansion behavior of aggregates strongly governs the morphology, orientation, and connectivity of the induced microcrack network (Mouiya et al., 2026).

I.2.3.2.2. Aggregate's CTE anisotropy influences on the microcracking

In contrast to the previous case, aggregates with an anisotropic CTE (such as andalusite (M. G. Kakroudi et al., 2009), or aluminum titanante (Bayer, 1971)) expand differently along each crystallographic orientation ($\alpha_a \neq \alpha_b \neq \alpha_c$), generating internal, direction-dependent thermal expansion. When embedded in an isotropic or weakly anisotropic matrix, a highly non-uniform stress fields can be generated within the surrounding region (Razavi et al., 2024). Such anisotropic and very complex stress fields promote a dense complex network of microcracks all around in the neighbouring matrix (see Figure I-6) (Kakroudi et al., 2008; Mouiya, 2024). Consequently, microcracks morphology in refractories containing anisotropic aggregates differs markedly from isotropic systems (as shown in Figure I-6). Rather than radially symmetric cracks, one observes oriented crack paths at the aggregate scale, and complex crack paths that follow the morphology/orientation of the aggregate (Bruno et al., 2010) (see Figure I-6).



a) isotropic CTE case (Mouiya, 2024) b) anisotropic CTE case

Figure I-6: Illustration of impact of aggregate nature on the CTE mismatch and thermal defects

License CC BY-NC-ND 4.0

Besides the intrinsic CTE behavior of the aggregates, several additional microstructural parameters strongly influence the formation and evolution of microcracking. These include the aggregate size, shape, and volume fraction, as well as the crystallinity of the grains (amplitude of the anisotropy) and their crystallographic orientation (da Luz A et al., 2015; Sridhar et al., 1994). Together, all these factors govern both the density and the orientation of the resulting microcrack networks within the material.

I.2.3.2.3. Thermal processing's influences on microcracking

Thermal processing of compacted powders, especially firing and sintering, strongly governs the extent and character of microcracks that develop from CTE mismatch in refractories. The processing steps involve, heating, dwell period and cooling (Kakroudi et al., 2008; Mouiya et al., 2019; Terzić & Pavlović, 2009). High firing temperatures and long dwell times promote densification (lower porosity), grain growth, and stronger interparticle bonding (Mouiya, 2024; Yousef et al., 2005). In contrast, lower firing temperatures or shorter dwells retain more porosity, finer grains, and weaker interfaces, making the microstructure more compliant (Studart et al., 2006; Terzić & Pavlović, 2009; Tessier-Doyen, 2003). As the refractory cools from the firing temperature, the creep can no longer accommodate the differential thermal contraction caused by CTE mismatch at the microstructural scale (Hasselman, 1967; Merlani et al., 2001; Terzić & Pavlović, 2009). So, these mismatches manifest as internal thermal stresses. These stresses lead to the formation of microcracks around aggregates (Kakroudi et al., 2008; Mouiya, Tessier-Doyen, et al., 2023). Thus, heating and cooling rates can have a huge influence in shaping the final thermomechanical behaviour of the material: rapid cooling amplifies thermal gradients and can promote the formation of fewer but larger cracks, whereas slow cooling favours a more diffuse population of more numerous, smaller microcracks (Kakroudi et al., 2008; Merlani et al., 2001; Mouiya, Tessier-Doyen, et al., 2023; Terzić & Pavlović, 2009).

Thermal processing can also interact with phase transformations and reaction sintering, which can introduce additional volumetric change due to phase transformation and generate new phases with distinct CTEs from the parent phases (Chotard et al., 2019; Kakroudi, 2007; Mukhopadhyay & Das Poddar, 2004). Such reactions frequently produce characteristic microcrack patterns, including reaction rims or circumferential cracks around transformed grains, with their extent directly controlled by the firing curve (Kakroudi, 2007).

The resulting microcrack network establishes the initial damage state of the refractory prior to service at room temperature. This microcrack network and its evolution under thermal loading can be indirectly characterized thanks to ultrasonic measurements (Chotard et al., 2008; Tessier-Doyen et al., 2006), dilatometric measures (Huger, 2019) or by mechanical tests such as (cyclic and monotonic) tensile tests (Mouiya, Martynyuk, et al., 2023).

I.2.3.3. Key mechanical behavior of a microcracked material

Microcracked refractories (obtained after sintering) exhibit quasi-brittle behavior and high fracture toughness. Therefore, it is interesting to explore the macroscopic mechanical response of these materials under different mechanical tests.

I.2.3.3.1. Macroscopic stress-strain response under cyclic tensile loading

In this section, it is interesting to focus on the study performed by Kakroudi (2007), where he employed an andalusite-based refractory. In this study, monocrystal andalusite (Al_2O_3-SiO_2) was employed as aggregates and a cementitious bonding phase was employed as matrix. The choice of the monocrystal andalusite as aggregate was due to its significant anisotropy that contributes to promote dense microcrack networks under CTE mismatch (M. G. Kakroudi et al., 2009). Moreover, Kakroudi et al., (2008) explored the relationships between sintering temperature, microscale

License CC BY-NC-ND 4.0

microcrack density, macroscale stress-strain response in tension. The studied microstructure was produced by drying the specimens at 110 °C for 24 h, heating them to 110 °C, 250 °C, …1100 °C at 5 °C/min with a 5h dwell, and cooling at the same rate.

Figure I-7 depicts the macroscopic stress-strain response in tension at room temperature after thermal treatment at different temperatures. These results clearly depicts that the sample just after curing at 110 °C, exhibited high Young's modulus with a brittle stress-strain response behavior. In contrast, a sample fired at 1100 °C, exhibited low Young's modulus with a strong non-linear stress-strain response (see Figure I-7a). Moreover, these pronounced non-linear behavior (see Figure I-7a) depicts that the sample is highly microcracked and could better accommodate internal thermal stresses potentially generated by thermal shock (Kakroudi et al., 2008). Additionally, the hysteresis which is clearly observed between unloading and reloading (especially on the curve after thermal treatment at 1100 °C), indicates energy dissipation mechanisms resulting from friction between microcrack surfaces (Kakroudi, 2007). As a result, macrocracks develop in a stable and distributed manner rather than unstable manner. This response allows the material to tolerate repeated thermal cycling, and maintain structural integrity under high thermal shock conditions, making non-linear mechanical behavior a key attribute for high-performance refractory materials (Huger et al., 2007). Therefore, this study demonstrates the key role of the thermal history of the material on its ability to develop non-linear behavior.

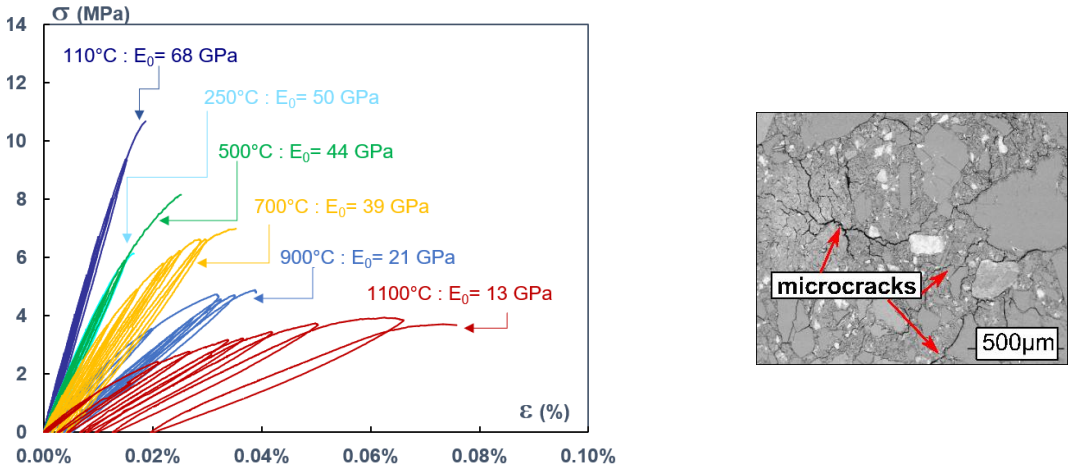

a) stress-strain response in tension at room temperature after thermal treatment at different temperatures

b) microcracked sample after thermal treatment at 900 °C

Figure I-7: Overview on the microstructure-macroscopic response of andalusite based castable (Kakroudi, 2007)

These results are achieved through the presence of a microcrack network within the material microstructure, as illustrated in Figure I-7b. Such a microcrack network enables stress relaxation and imparts a more compliant, damage-tolerant mechanical behaviour to the refractory (Kakroudi, 2007).

Consequently, these results highlight that tensile test characterization can be an effective tool for identifying non-linear mechanical behaviour and qualitatively assessing whether a material exhibits increased fracture energy and improved thermal shock resistance (Kakroudi, 2007). However, tensile tests alone do not allow for a direct or quantitative determination of the fracture energy. For this reason, more specialized fracture mechanics tests, such as wedge splitting tests (Harmuth, 1995), are commonly employed to obtain quantitative insight into the fracture energy of such materials (Grasset-Bourdel et al., 2013).

License CC BY-NC-ND 4.0

I.2.3.3.2. Macroscopic load-displacement response under wedge splitting test

Early methods for determining fracture energy in brittle materials relied on Griffith-type analyses (Griffith, 1921) for two-dimensional cracks (Irwin, 1958) or alternative techniques such as cone fracture (Roesler, 1956) and cleavage fracture (Gilman, 1960). These approaches were effective for homogeneous, purely brittle materials but did not capture the fracture processes of heterogeneous ceramics and refractories. Subsequent developments, namely the work-of-fracture method (Nakayama, 1965) and the notched-beam test (Brown & Srawley, 1966), provided tools to estimate total fracture energy (γ_{WOF}) and crack-initiation energy γ_{NBT}, respectively. However, for refractories, the WOF method often led to unstable crack propagation (because strain-softening in quasi-brittle materials, combined with slender bending geometry and a strong stress gradient), while the NBT captured only initiation behaviour and not the full non-linear fracture processes (Aksel & Warren, 2003). Recognizing these limitations, several researchers highlighted the importance of tests involving controlled, stable crack growth on pre-cracked samples (Sakai & Bradt, 1993). The (full) Wedge Splitting Test (WST), introduced by Tschegg (1986), addressed these challenges. By using larger specimens and a specialized loading device, the (full) WST ensures stable mode-I crack propagation even in coarse-grained or highly heterogeneous refractories (Harmuth, 1995). Because it provides a reliable J-integral-based fracture energy and captures a large crack-propagation process, the (full) WST has become the preferred and most relevant technique for characterizing fracture energy in refractories and civil engineering materials.

The benefits of employing the WST are that: i) now it is well established, and ii) it is regarded as a promising technique for determining the fracture energy of refractory materials (Grasset-Bourdel et al., 2013; Harmuth, 1995). However, within the scope of the present PhD work, it is evident that no studies reported in the literature have applied this method to monocrystal-aggregate-based castable to quantify their fracture energy, particularly with the aim of elucidating microstructure-thermomechanical property relationships. To date, only one study, conducted by Mouiya et al., 2026, has investigated a material containing monocrystal aggregates using a miniaturized wedge splitting test (mini-WST) approach. This methodology was inspired by the earlier works of Fruhstorfer & Gruber, (2023) from Leoben. Although this study demonstrated the feasibility of the approach, deeper insight into fracture energy requires a stochastic framework (Fruhstorfer & Gruber, 2023). Owing to the small specimen size and the limited number of aggregates involved, the observed fracture behaviour cannot be directly generalized to the underlying micromechanical mechanisms of the material. Consequently, variability must be explicitly accounted through statistical analysis. Nevertheless, the use of miniature specimens combined with optical/electron microscopy, offers a specific very interesting advantage: it allows direct characterization of the crack path within the microstructure of the sample (cracks passing through the grain boundaries or grains, real effect of large grains in crack bridging) in real-time during the test (Fruhstorfer & Gruber, 2023; Mouiya, 2024). This makes the mini-WST particularly attractive for studying fracture behaviour in relation to microstructural features.

Figure I-8a depicts the mini-WST set up in a 2D view. The key difference in the mini-WST lies with the dimensions of the sample, where the sample dimensions employed by Mouiya et al., (2026) were 35 × 25 × 4 mm^3. The analysis generates load-displacement curve following the same principle of (Full) WST. The load is transferred from the roller to the sample through the load transmission supports, resulting in the conversion of the vertical load (F_V) applied by the wedge into a horizontal load (F_H) (see Figure I-8a). It is important to mentioned that both the (full) and mini-WST measure the specific fracture energy (G_T') rather than the real fracture energy G_T as the test is stopped at 15% of the peak load. This loading situation is followed to prevent the roller from contacting the sample during downward movement. It is important to highlight that the readers can refer to (Fruhstorfer & Gruber, 2023) to get more details on the experimental set up, material

License CC BY-NC-ND 4.0

preparation etc. Indeed, such an approach was employed by Mouiya et al., (2026) to characterise an aluminum titanate-based model composite. In fact, gaining motivation from (Kakroudi, 2007), Mouiya et al., (2026) has investigated aluminum titanate monocrystals as aggregates embedded within alumina matrix, to fully take advantage of the huge anisotropy of aluminum titanate CTE to promote a dense microcrack network, as explained in section I.2.3.2.2. Thus, this study explored the relationships between the weight percentage of aluminium titanate aggregates on the load-displacement response. For this study, four different composites (0 wt%, 2.5 wt%, 5. wt% and 10 wt%) were prepared (sintered at 1600 °C). Then, these samples of four different composition were subjected to mini-WST tests to investigate the impact of the aluminum titanate fraction on the microcrack density and fracture energy.

Figure I-8b depicts the results obtained from mini-WST. For clarity, only the two extreme systems are discussed here (Mouiya et al., 2026). Consistent with the stress-strain behavior (also investigated in tension but not presented here), the pure alumina material that do not contain any microcracks, exhibited rapid load-displacement response with a brittle failure. In contrast, the composite with 10 wt% of AT displayed a complex cracking path, including crack initiation, propagation, and branching, leading to an enlarged load-displacement response corresponding to a quasi-brittle failure (Mouiya et al., 2026). As illustrated in Figure I-8b, the area under the green curve accounted to 251 J/m^2, a significantly higher fracture toughness than the pure alumina system.

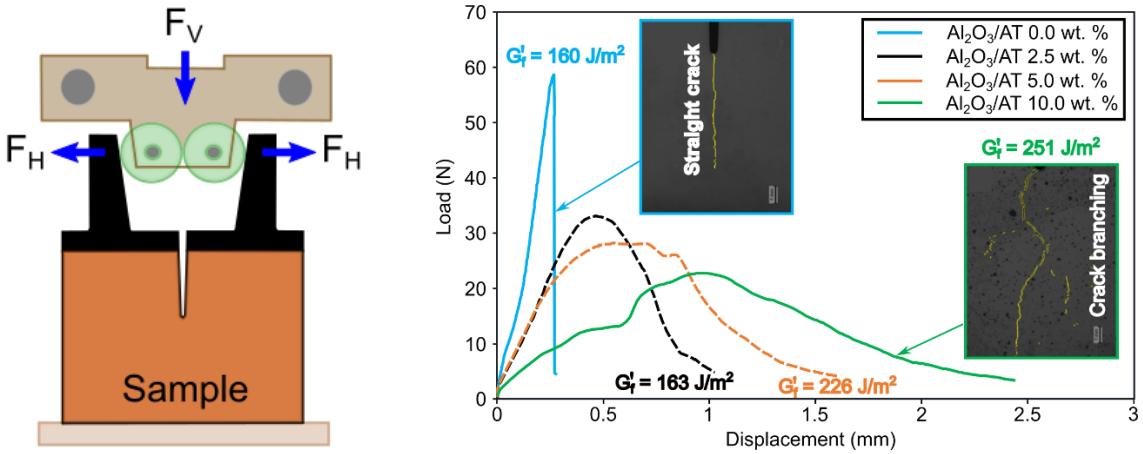

a) mini-WST set-up (Fruhstorfer & Gruber, 2023)

b) load-displacement curve (Fruhstorfer & Gruber, 2023; Mouiya et al., 2026)

Figure I-8: Mini-WST set-up and its load-displacement results for the alumina-AT composites

These findings demonstrate that, despite the relatively low content of aluminium titanate aggregates (2.5–10 wt%) embedded within the matrix (pure alumina in the present case), the aggregate weight fraction has a strong influence on the microcrack density immediately after processing. This increased microcrack density subsequently leads to a significant enhancement in fracture energy (Mouiya et al., 2026) and thus enhances the ability of the material to sustain thermal shocks. Accordingly, the present PhD work focuses on understanding the microstructure-thermomechanical property relationship, specifically how the incorporation of monocrystalline aggregates with anisotropic CTE, such as andalusite (Razavi et al., 2024), mullite (Chotard et al., 2019), and aluminum titanate (Mouiya et al., 2026), promotes the development of complex microcrack networks. In fact, quite recently, researchers have increasingly employed modelling approaches (Kachanov, 1992; Öchsner, 2016) to investigate the behavior of refractory materials, allowing for the exploration of microstructure-property relationships while reducing the time, cost, and material consumption associated with traditional trial-and-error experiments. In the following

License CC BY-NC-ND 4.0

section, different modelling strategies are explored, that could be employed to study these complex materials.

I.2.4. Models for the effective properties of heterogeneous and microcracked materials

The present section presents the analytical framework adopted to describe the effective elastic response and damage evolution of the materials. First, we recall classical micromechanical approaches for estimating the effective elastic properties of heterogeneous media (Hill, 1952, 1963), as applied to composite materials. We then extend the analysis to materials containing distributed microcracks, using the Non-Interacting Crack (NIC) approximation to relate microcrack density and orientation to the resulting reduction in elastic stiffness (Guéguen & Kachanov, 2011; Kachanov, 1992). Finally, these homogenization results are embedded within the general framework of continuum damage mechanics (Öchsner, 2016), with particular emphasis on formulations relevant for refractory materials.

I.2.4.1. Analytical approach

The present section is focused on discussing the analytical models that takes into accounting the materials microstructure to predict the macroscopic characteristics response of the material. With this in mind, first the analytical models that accounts to predict the macroscopic properties of an elastic medium (Hashin & Shtrikman, 1963; Reuss, 1929; Voigt, 1889) will be discussed and then the analytical models that account to predict the macroscopic properties of a cracked medium (Guéguen & Kachanov, 2011; Kachanov, 1992) with penny shape cracks will be presented.

I.2.4.1.1. Effective elastic properties of composite

For over a century, some models have been proposed in literature to estimate easily the elastic properties of a two-phase composite from those of the two constituents. An interesting category of models is the category of bounds models providing the extrema behavior of the composite (Hashin & Shtrikman, 1963; Reuss, 1929; Voigt, 1889). The simplest ones consider parallel and serial associations of the two phases as shown in Figure I-9a.

The Voigt (1889) and Reuss (1929) bounds are among the earliest analytical approaches. As an illustration purpose, let's assume a two-constituent sandwich composite as shown in Figure I-9a, that are perfectly bonded. The material 1 (isotropic) is assumed to exhibit elastic modulus of E_1, volume fraction of V_1 and shear modulus of G_1, while the material 2 (isotorpic) is assumed to exhibit elastic modulus of E_2, volume fraction of V_2 and shear modulus of G_2.

Now, the effective property in the parallel direction of the sandwich could be deduced using Voigt bound (Voigt, 1889). In this approach the sandwich is assumed to exhibit a uniform macroscopic strain across all phases, leading to an arithmetic average of stiffness as depicted in equation I-8.

$$E_V = V_1 E_1 + V_2 E_2 \qquad \text{I-8}$$

Therefore, the Voigt bound yields a rigorous upper bound on the effective moduli (Voigt, 1889).

In contrast, the effective property in the perpendicular direction of the sandwich could be deduced using Reuss bound (Reuss, 1929). In this approach the sandwich is assumed to exhibit a uniform macroscopic stress, giving a harmonic average of compliance as depicted in equation I-9.

$$\frac{1}{E_R} = \frac{V_1}{E_1} + \frac{V_2}{E_2} \qquad \text{I-9}$$

License CC BY-NC-ND 4.0

Therefore, this provides a rigorous lower bound (Reuss, 1929).

Using the same principle, the effective shear modulus could be deduced (Reuss, 1929; Voigt, 1889). By using the equation I-8 and I-9 the Young's modulus versus volume fraction is plotted (see Figure I-9b) to depict the upper and lower bound for the sandwich model.

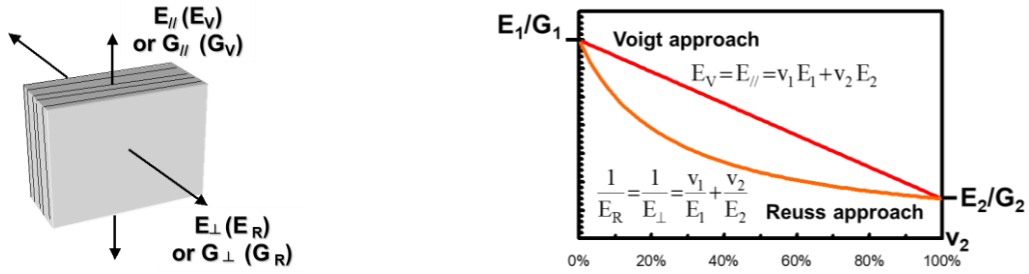

a) sandwich model b) Young's modulus vs volume fraction

Figure I-9: Overview on the Voigt and Reuss approach to determine effective properties (Tessier-Doyen, 2003)

While both bounds are simple and require only phase properties and fractions, they do not account for microstructural geometry and often yield overly conservative estimates (Hashin & Shtrikman, 1963).

A significant advance was introduced by Hashin & Shtrikman (1963) which are isotropic materials composed of a matrix (m) and inclusions (i) with perfect matrix/inclusion interfaces. In the composite spheres assemblage constructed by Hashin & Shtrikman, (1963), each composite consists of a spherical particle that is surrounded by a concentric matrix shell as shown in Figure I-10a. The volume fractions of particle and matrix material are the same in each sphere (Hashin & Shtrikman, 1963), but the spheres themselves can be of any size, as shown in Figure I-10a.

In such a case, the matrix is assumed to exhibit a shear modulus of (G_m), volume fraction of (V_m) and bulk modulus (K_m), while the inclusion is assumed to exhibit a shear modulus of (G_i), volume fraction of (V_i) and bulk modulus (K_i). When the inclusion is stiffer than matrix (example glass/alumina composite (Tessier-Doyen, 2003)), the Young's modulus could be deduced using the lower bound (HS^-) which is depicted Table I-1. In the case where matrix is stiffer than inclusion (example glass/pores composites (Tessier-Doyen, 2003)), the Young's modulus could be deduced using the upper bound (HS^+) as depicted in the Table I-1.

Table I-1: Key analytical relationships in HS model for a two-constituent system

Property	Lower bound (HS^-)	Upper bound (HS^+)
Bulk modulus	$K^- = K_m + \dfrac{V_p}{\dfrac{1}{K_p - K_m} + \dfrac{3V_m}{3K_m + 4G_m}}$	$K^+ = K_p + \dfrac{V_m}{\dfrac{1}{K_m - K_p} + \dfrac{3V_p}{3K_p + 4G_p}}$
Shear modulus	$G^- = G_m + \dfrac{v_p}{\dfrac{1}{G_p - G_m} + \dfrac{6(K_m + 2G_m) \cdot v_m}{5G_m(3K_m + 4G_m)}}$	$G^+ = G_p + \dfrac{V_m}{\dfrac{1}{G_m - G_p} + \dfrac{6(K_p + 2G_p) \cdot V_p}{5G_p(3K_p + 4G_p)}}$
Young's modulus	$E^- = \dfrac{9K^- \cdot G^-}{3K^- + G^-}$	$E^+ = \dfrac{9K^+ \cdot G^+}{3K^+ + G^+}$

License CC BY-NC-ND 4.0

Figure I-10b, depicts the experimental and analytical results obtained by Tessier-Doyen (2003) for a glass (matrix) and alumina spherical inclusion composite. This composite material corresponds to the case of inclusion stiffer than matrix. The result depicts that the experimental results are closer to the HS^- as mentioned previously.

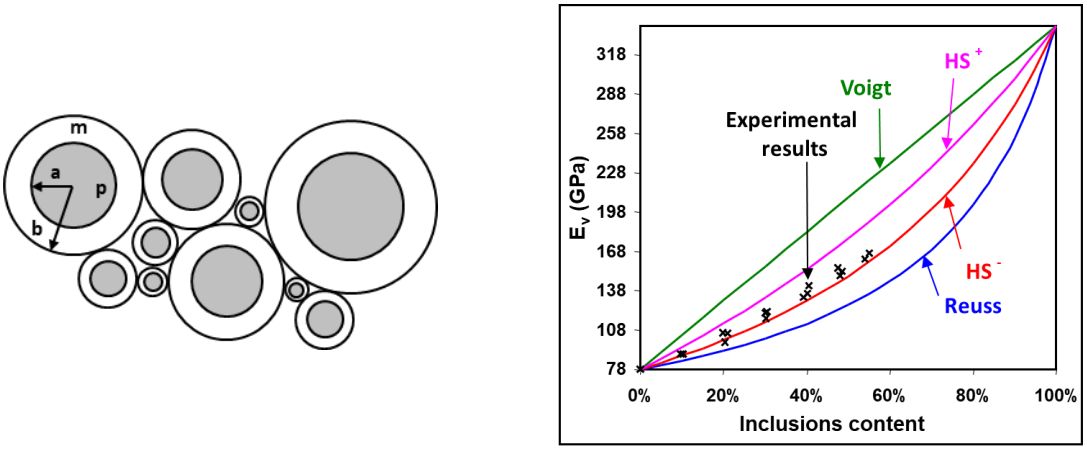

a) two-constituent model (Hashin & Shtrikman, 1963)

b) Young's modulus vs volume fraction (Hashin & Shtrikman, 1963)

Figure I-10: Overview on the HS model for two constituent system

I.2.4.1.2. Effective elastic properties of microcracked materials

The effective elastic behavior of materials containing networks of penny-shaped microcracks can be analysed using the Non-Interacting Crack (NIC) approximation (Guéguen & Kachanov, 2011; Kachanov, 1992), which assumes that cracks do not interact with each other. Despite its simplicity, this approximation provides the only universally accepted analytical solution for arbitrary crack orientation distributions in both 2-D and 3-D. Under this framework, the elastic potential of the cracked solid is derived, and the change in compliance due to cracks is expressed in terms of the average crack opening displacement, $\langle \vec{b}_i \rangle$, integrated over the crack area S_i. The matrix is assumed to be isotropic and linearly elastic (Guéguen & Kachanov, 2011).

For an isolated crack (see Figure I-11) in an infinite isotropic matrix (Kachanov, 1992), the average crack opening displacement is related to the applied traction $\bar{\bar{t}}$ through the second-rank crack compliance tensor $\bar{\bar{B}}$:

$$\langle \vec{b}_i \rangle = \bar{\bar{t}} \cdot \bar{\bar{B}} \qquad \text{I-10}$$

For a penny-shaped circular crack (with radius a) in 3-D (see Figure I-11a), the tensor $\bar{\bar{B}}$ takes the form (Kachanov, 1992):

$$\bar{\bar{B}} = \gamma(\bar{\bar{I}} - 2\nu_0 \, \vec{n} \otimes \vec{n}) \qquad \text{I-11}$$

Where $\vec{n}$ is the unit normal to the crack, $\bar{\bar{I}}$ is the identity tensor, ν_0 is the matrix Poisson's ratio, and γ is a size-dependent coefficient (Kachanov, 1992):

$$\gamma = \frac{\beta}{1 - \nu_0/2}, \beta = \frac{16a(1-\nu_0^2)}{3\pi E_0}. \qquad \text{I-12}$$

License CC BY-NC-ND 4.0

Because the normal and shear compliances of a penny-shaped crack differ ($\beta \neq \gamma$ unless $\nu_0 = 0$), $\langle \vec{b_i} \rangle$ is generally not collinear with the traction $\vec{n_i} \cdot \bar{\bar{\sigma}}$. Consequently, the effective 3-D compliance requires both the second-rank crack density tensor $\bar{\bar{\eta}}$ and an additional fourth-rank tensor term (Kachanov, 1992).

The general additional elastic potential due to non-interacting 3-D circular cracks is given by:

$$\Delta f = \frac{8(1-\nu_0^2)}{3(1-\nu_0/2)E_0}\left[(\bar{\bar{\sigma}}\cdot\bar{\bar{\sigma}}):\bar{\bar{\eta}} - \frac{\nu_0}{2}\,\bar{\bar{\sigma}}:\left(\frac{1}{V}\sum_i (a^3\,\vec{n}\otimes\vec{n}\otimes\vec{n}\otimes\vec{n})^i\right):\bar{\bar{\sigma}}\right] \qquad \text{I-13}$$

where the crack density tensor is defined as:

$$\bar{\bar{\eta}} = \frac{1}{V}\sum_i a^3\,\vec{n}\otimes\vec{n} \qquad \text{I-14}$$

In the case of cracks arranged in a random orientation (Kachanov, 1992), as shown in Figure I-11b, the second rank tensor $\bar{\bar{\eta}}$ simplifies to $\bar{\bar{\eta}} = (\rho/3)\mathrm{I}$ (where $\rho = \frac{1}{V}\sum_i a^3$) and the fourth rank tensor in equation I-13 reduces to $\nu_0/2$. Therefore, the effective Young's modulus of the cracked sample with cracks arranged randomly could be described by equation I-15.

$$E = E_o.\left[1 + \left(\frac{16}{9}\left(\frac{(1-\nu_o^2).(1-3.\nu_o/10)}{(1-\nu_o/2)}\right).\rho\right)\right]^{-1} \qquad \text{I-15}$$

In the case of cracks arranged in a constant orientation (see Figure I-11c), the effective Young's modulus of the cracked sample could be described by the equation I-16 (Kachanov, 1992).

$$E = E_o.\frac{1}{1 + k_o.\left(\frac{16}{3}\left(\frac{(1-\nu_o^2)}{(1-\nu_o/2)}\right).\rho\right)} \qquad \text{I-16}$$

Where k_o ranges between [0,1] which describes if the cracks are parallel or perpendicular to an axis (1-3) (Kachanov, 1992).

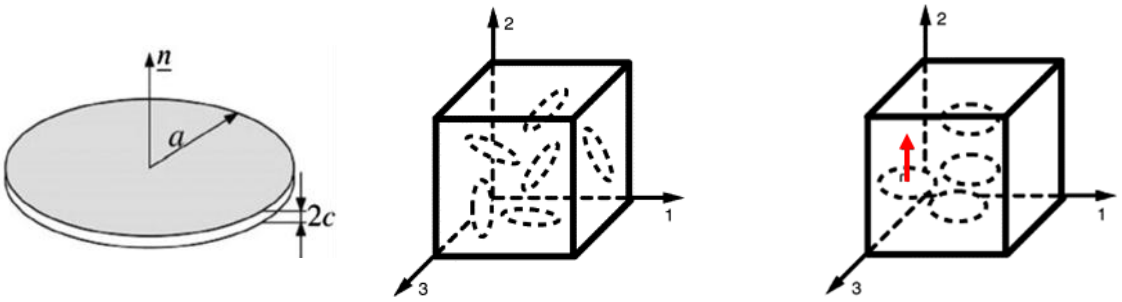

a) isolated penny crack b) random crack distribution c) constant crack distribution

Figure I-11: Illustration of Katchanov penny shaped crack model (Kachanov, 1992; Yuan et al., 2021)

License CC BY-NC-ND 4.0

Despite the analytical approach helps deduce the effective macroscopic response of the composite, its unable to directly predict stresses that led to microcrack initiation. In addition, it is not possible to dynamically depict the crack propagation, merging, branching and closure that occurs during a thermal study (Huger et al., 2007; Kachanov, 1992). Therefore, adapting to approach like damage mechanics (Öchsner, 2016) could possibly improve the understanding on the microstructure-property relationship.

I.2.4.2. Damage mechanics

From the section I.2.3.3, it was interesting to know that the refractories with thermally induced microcracks exhibit macroscopic non-linear mechanical response. Indeed, this microstructure and its related macroscopic mechanical behavior could be explained and described using the Continuum Damage Mechanics (CDM) framework (Öchsner, 2016). CDM provides a powerful framework for bridging these scales by replacing the explicit representation of individual cracks thanks to internal variables that quantify their averaged influence on the bulk response (Hütter & Tervoort, 2008; Öchsner, 2016). In doing so, CDM transforms the discrete evolution of thousands of microcracks into smooth field variables compatible with mechanical structural analysis and numerical simulation such as Finite Element Method (FEM).

CDM is built upon a thermodynamically consistent formulation of material degradation (Hütter & Tervoort, 2008). The Helmholtz free energy incorporates elastic strain, temperature, and damage, while the corresponding thermodynamic force, derived from the dissipation inequality, governs irreversible damage evolution (Hütter & Tervoort, 2008; Öchsner, 2016). Damage variables may be scalar, representing isotropic stiffness reduction, or tensorial, capturing direction-dependent cracking. Using the effective stress concept and the strain-equivalence hypothesis, the damaged solid is assumed to follow the same constitutive law as the undamaged material when expressed in terms of an effective stress acting on the remaining sound area (Öchsner, 2016). For isotropic damage, this yields the classical relation:

$$\sigma = (1 - D).E_0.\varepsilon$$
$$E_s = (1 - D).E_0. \qquad \text{I-17}$$

and the Figure I-12 depicts the schematic representations of equation I-17 in a graphical format, where D ∈ [0; 1] is the internal damage variable, E_0 is the undamaged modulus, and E_s is the degraded modulus. Coupled with a suitable damage criterion and evolution law (often driven by a damage energy-release rate), CDM provides a smooth representation of stiffness loss, softening, and the gradual approach to failure (Öchsner, 2016) as shown in Figure I-12.

License CC BY-NC-ND 4.0

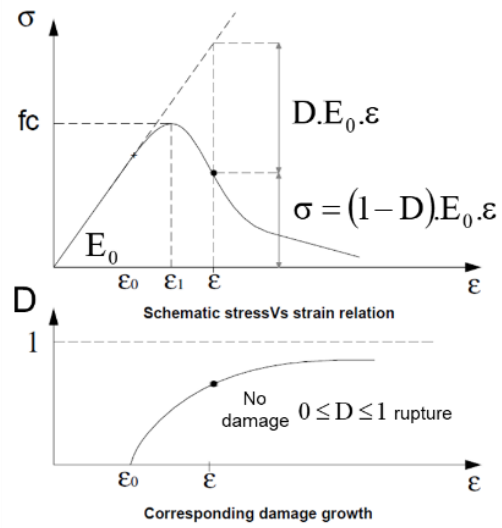

Figure I-12: Schematic stress-strain relation and its corresponding damage growth (Öchsner, 2016)

Indeed, CDM plays an essential role in multiscale modelling. At the microscale, thermal expansion mismatch and transient temperature gradients generate local tensile stresses that nucleate cracks along preferred orientations (Bruno et al., 2010). As these cracks accumulate and interact, they alter the effective stiffness ($\bar{\bar{C}}(D,T)$), thermal expansion ($\bar{\bar{\alpha}}(D,T)$), and thermal conductivity ($\bar{\bar{\lambda}}(D,T)$) of the material (Kachanov, 1992; Tessier-Doyen, 2003). Homogenization schemes translate microcrack statistics into effective tensors $\bar{\bar{C}}(D,T)$, $\bar{\bar{\alpha}}(D,T)$, and $\bar{\bar{\lambda}}(D,T)$ (Eshelby, 1957; Guéguen & Kachanov, 2011; Kachanov, 1992), allowing CDM to incorporate microstructure-induced property changes within continuum constitutive laws (Öchsner, 2016). At the macroscale, these effective tensors could be employed to determine the damage, it could reveal the insights on the crack propagation whether it is rapid or controlled crack growth, similar to the stress-strain response and completing the multiscale feedback loop (Hütter & Tervoort, 2008).

Despite its strength, it is not a preferred approach as grains, aggregates, pores, and crack fronts are not resolved explicitly; their effects enter only through effective parameter degradation. Consequently, CDM cannot predict microcrack nucleation sites, pore-controlled deflection, aggregate-induced bridging, or the influence of grain morphology on crack paths (Hütter & Tervoort, 2008; Öchsner, 2016). Different microstructural crack networks may correspond to the same macroscopic value of D, and CDM produces diffuse damage zones rather than discrete cracks, leaving out branching, bridging, and crack-microstructure interactions unless explicitly enriched by micromechanical (Öchsner, 2016). Therefore, simulations of such cracking phenomena that occur in brittle or quasi-brittle media, have become a topic of interest in the research field (Chen & Wang, 1996; Sadd, 2019), to insight on the microstructure-property relationship of refractories.

I.3. Full field continuum approach to simulate fracture initiation and propagation

The modelling strategies discussed so far provide complementary but essentially homogenized descriptions of brittle cracking. Analytical approaches idealize microcracks, often as penny-shaped defects embedded in an elastic matrix (Hütter & Tervoort, 2008; Kachanov, 1992), to derive closed-form or semi-analytical expressions for the effective stiffness tensor. These formulations reveal how crack density, orientation and aspect ratio influence macroscopic elasticity but rely on simplified crack geometries and distributions (Guéguen & Kachanov, 2011; Kachanov, 1992). CDM extends this homogenized viewpoint by introducing internal damage variables that capture the influence of microcrack nucleation and growth on the apparent stiffness and strength, thereby

License CC BY-NC-ND 4.0

linking microscopic degradation to macroscopic stress-strain behaviour without resolving individual defects (Hütter & Tervoort, 2008; Öchsner, 2016).

While such constitutive-level models are valuable for studying global material trends, indeed, they cannot explicitly describe the initiation, propagation and coalescence of discrete cracks, especially in structures with complex geometries, non-uniform loading or highly localized fracture processes (Öchsner, 2016). To analyse such scenarios, full-field numerical methods are required, where displacement and stress fields are computed across the actual domain and fracture is represented explicitly (Chen & Wang, 1996; Kuna, 2013; Sadd, 2019).

In this work, we focus on reviewing two major classes of full-field formulations. The first is the FEM, which discretizes the domain and solves the governing equations in weak form, allowing various brittle fracture models to be incorporated through appropriate constitutive laws and kinematic enrichments (Ambati et al., 2015; Khoei, 2014; Kuna, 2013). The second is the Boundary Element Method (BEM), which reformulates the problem using boundary integral equations. By discretizing only the external boundary and crack surfaces, BEM offers reduced computational cost and high accuracy in linear elastic media, making it particularly effective for evaluating crack-tip fields and energy release rates (Aliabadi & Brebbia, 2025).

I.3.1. Finite Element Method

The FEM is a general numerical framework for approximating the solutions of boundary value problems governed by partial differential equations. By discretizing a domain into finite elements and approximating the unknown fields through suitable shape functions, FEM converts a continuous problem into a system of algebraic equations solvable with standard linear or nonlinear techniques. Owing to its flexibility in handling complex geometries, heterogeneous materials, and diverse boundary conditions, FEM has become the dominant computational tool in solid engineering mechanics (Kuna, 2013).

For brittle fracture, classical displacement-based FEM provides an accurate description of the elastic response prior to crack initiation. However, once a crack nucleates and propagates, the displacement field becomes discontinuous across the crack surfaces, whereas standard FEM assumes continuity within and across elements. As a result, representing crack growth, especially when involving branching, coalescence, or non-planar trajectories, typically requires frequent remeshing or other mesh-alignment strategies, making simulations cumbersome, computationally demanding, and often mesh dependant solutions (Kuna, 2013).

To overcome these limitations, several FEM-based formulations have been developed to more effectively represent fracture processes in brittle materials. Three widely used and conceptually distinct approaches are:

- **Cohesive Zone Models (CZM):** These introduce cohesive elements or traction–separation laws along potential crack paths. The interface response governs damage initiation and evolution, enabling localized representation of fracture processes (Kuna & Roth, 2015; Wciślik & Pała, 2021).
- **Extended Finite Element Method (XFEM):** XFEM enriches the finite element approximation with additional functions to represent discontinuities and near-tip asymptotic fields. Cracks can therefore evolve independently of the underlying mesh, minimizing the need for remeshing (Khoei, 2014).
- **Phase-Field (PF) methods:** PFM regularizes the sharp crack surface by introducing a continuous phase-field variable that transitions smoothly between intact and fully fractured states. This diffuse representation allows automatic crack initiation, complex crack

License CC BY-NC-ND 4.0

trajectories, and topological changes without explicitly tracking the crack surface (Ambati et al., 2015).

The following subsections review and compare CZM, XFEM, and PFM in the context of brittle fracture modelling, with emphasis on their theoretical foundations, numerical implementation aspects, and respective strengths and limitations for simulating crack nucleation and propagation with special attention to studies related to microscopic scales in a thermomechanical context.

I.3.1.1. Cohesive Zone Modelling

The CZM is widely used in computational fracture mechanics to simulate the initiation and evolution of material failure. Its foundations trace back to Dugdale (1960) and Barenblatt (1962) models. Later, Hillerborg et al., (1976) advanced the approach by introducing a traction-crack-opening relationship for quasi-brittle materials, establishing key features of modern cohesive modelling. Figure I-13a illustrates this concept, showing the local process zone at the crack tip, which is governed by a traction-separation law. The traction-separation law enables tracking of material progressive degradation as cohesive tractions rise to a finite maximum value t_0 (Figure I-13a), avoiding the stress singularity predicted by classical linear elastic fracture mechanics (Kuna, 2013; Kuna & Roth, 2015). Figure I-13b illustrates the cohesive elements placed along the anticipated crack path (Wciślik & Pała, 2021). Numerous traction-separation laws have been proposed such as cubic, polynomial, exponential, linear softening, and bilinear laws (Kuna & Roth, 2015; Park & Paulino, 2011; Wciślik & Pała, 2021). As an illustration purpose the bilinear formulation is being depicted in Figure I-13c for mixed mode of failure using bilinear laws (Kim et al., 2011).

CZM has proven highly versatile, enabling the simulation of fracture in a wide range of engineering materials, including ceramics (Kim et al., 2011). Its conceptual simplicity, numerical robustness, and ease of implementation in FEM frameworks have contributed to its widespread adoption (Kuna, 2013). Moreover, by using a TSL as a local failure criterion, CZM eliminates the need for a separate macroscopic non-local fracture criterion such as energy balance involved in fracture mechanics (Kuna, 2013).

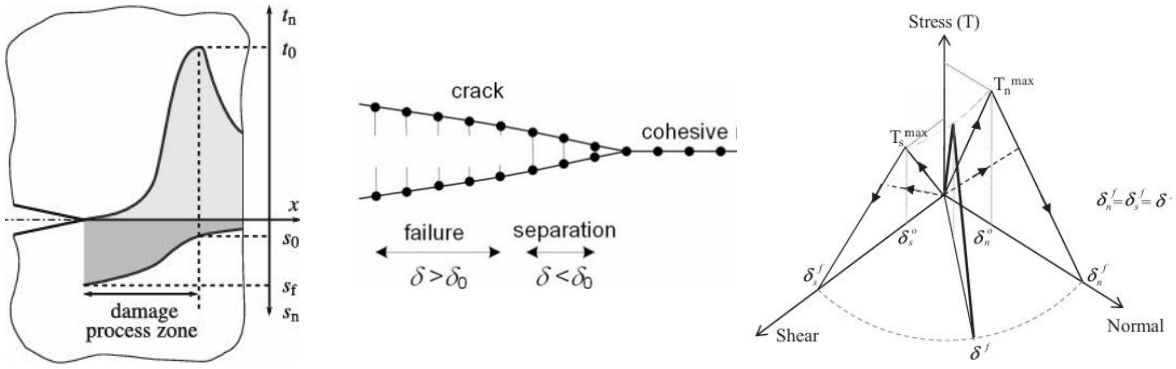

a) crack tip with CZM (Kim et al., 2011; Kuna & Roth, 2015)

b) CZM crack extension (Wciślik & Pała, 2021)

c) mixed mode bilinear law (Kim et al., 2011)

Figure I-13: Key representation of CZM framework

Several studies (Espinosa & Zavattieri, 2003b; Lin et al., 2017; Liu et al., 2023) have combined CZM with FEM to perform microstructure-informed fracture simulations, assigning different constitutive behaviors to grain boundaries and grain interiors.

License CC BY-NC-ND 4.0

For example, the work of H Espinosa & Zavattieri, (2003); Kim et al., (2011); Lin et al., (2017); Liu et al., (2023) share a common focus on investigating fracture and damage mechanisms in brittle or polycrystalline ceramics at the microstructural level using numerical simulations based on CZMs. Each study highlights the critical role of microstructural features, such as grain boundaries (Espinosa & Zavattieri, 2003b; Kim et al., 2011; Lin et al., 2017) or particle/matrix interfaces (Liu et al., 2023), in governing crack initiation, propagation, and overall reduction in elastic stiffness. FEM are employed in all cases, with microstructures either derived from real SEM images (Kim et al., 2011) or generated computationally using techniques such as Voronoi tessellation (Lin et al., 2017). For illustration, Figure I-14 shows the workflow for generating a cohesive polycrystalline model for mechanical analysis: a real ceramic microstructure is digitized to represent grain morphology as polygons, which are then meshed using Delaunay triangulation, with cohesive interface elements added along the grain facets (Espinosa & Zavattieri, 2003b; Kim et al., 2011).

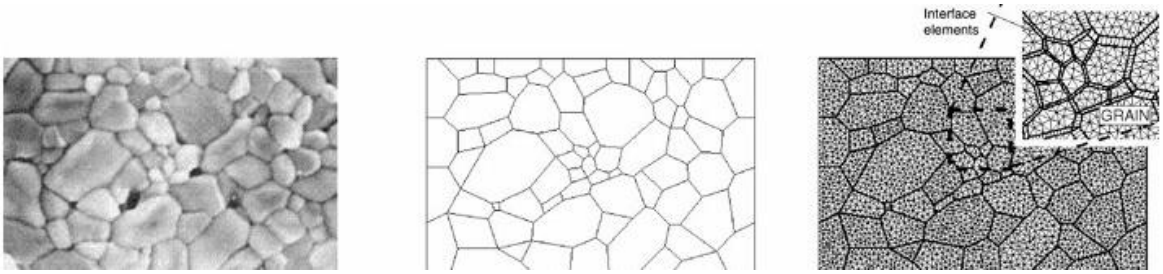

Figure I-14: Illustration of the virtual microstructure generation technique (Espinosa & Zavattieri, 2003b)

As an outcome of these studies (Espinosa & Zavattieri, 2003b; Kim et al., 2011; Lin et al., 2017; Liu et al., 2023), the simulations produce outputs such as crack patterns, stress distributions across the model microstructure, and the evolution of crack density, as exemplified in Figure I-15. For illustration, the results from Lin et al., (2017) are discussed here. The author emphasize the fracture mode transition from intergranular to transgranular in polycrystalline solids, exploring the influence of cohesive law parameters and grain size on fracture behavior. When a pre-existing cracked, polycrystalline sample was subjected to tensile loading (Figure I-15a), stress concentrations were observed at the crack tip (Figure I-15b). As the crack propagated, regions of stress relaxation appeared (depicted as zero-stress areas in green), indicating local stress redistribution as shown in Figure I-15c. Furthermore, a transition from intergranular to transgranular fracture was captured in the model, as shown in Figure I-15c.

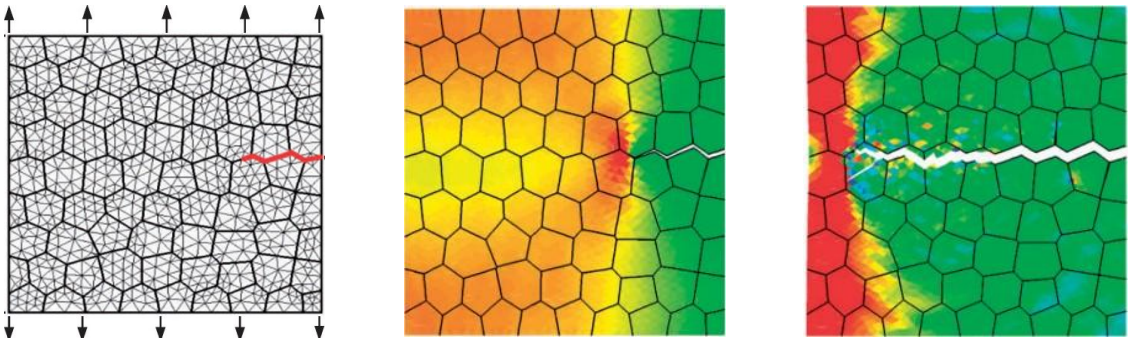

a) tensile loading b) stress state at initial stage c) stress state at final stage

Figure I-15: Stress state before and after crack growth in a polycrystalline sample under tension (Lin et al., 2017)

In addition, the studies based on thermomechanical behaviour and microcracking of ceramics, emphasizing the interplay between thermal anisotropy, residual stresses, and fracture mechanisms (Fertig & Nickerson, 2016; Ortiz & Suresh, 1993), have also been conducting using CZM. In this

License CC BY-NC-ND 4.0

line, Ortiz & Suresh (1993) present a comprehensive computational study of thermally induced residual stresses and intergranular fracture in alumina polycrystalline ceramics, with cohesive grain boundaries (similar to Figure I-14). As shown in Figure I-16a, the author represented the statistical distribution of the residual (normal and shear) stress field generated during cooling from fabrication temperatures. These stress distribution data have been examined to understand their role in microcrack initiation and growth. As an outcome, the results resembled a Gaussian-distribution (Wlodzimierz Bryc, 1995). In addition, elastic anisotropy of the polycrystalline ceramic strongly amplifying stress magnitudes. When intergranular microcracking is permitted, residual stresses are substantially reduced, demonstrating microcracking as an effective stress release mechanism. This study further highlighting the fundamental link between microstructural variability, thermal anisotropy, and the mechanical integrity of ceramics.

Later, Fertig & Nickerson (2016) introduced a modelling framework based on the underlying physical processes that predicts how small cracks form and partially close (see Figure I-16b) in porous cordierite ceramics during repeated heating and cooling. Combining sonic resonance experiments with insights from two-dimensional simulations of randomly oriented hexagonal grains, they identified statistical characteristics of grain-boundary stresses and crack opening displacements that govern microcrack evolution. These findings were used to develop a simple analytical model with three physically meaningful parameters. The model captures the thermal-history-dependent hysteresis in Young's modulus caused by microcracks opening during cooling and partially closing during heating, as shown in Figure I-16c. The study highlights the dominant role of thermally driven microcracking in stiffness degradation and recovery in porous ceramics, while emphasizing the value of statistical based models for predicting thermomechanical behaviour.

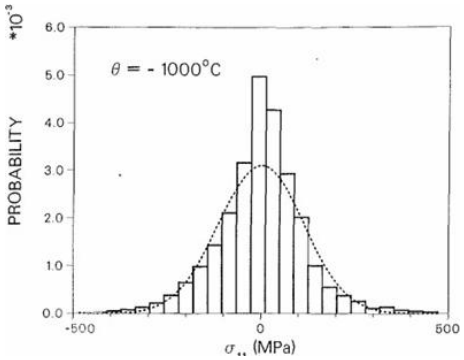

a) thermal stress distribution (Ortiz & Suresh, 1993)

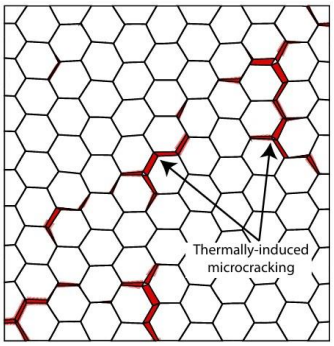

b) microcracking(Fertig & Nickerson, 2016)

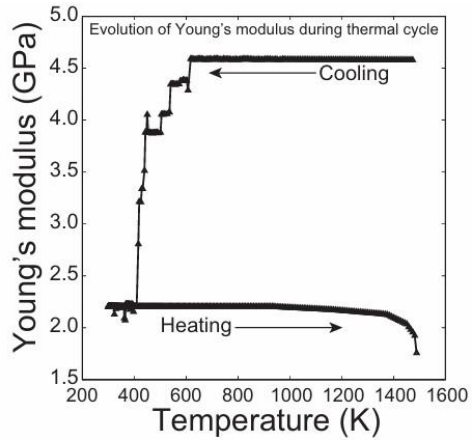

c) microcrack effects on materials Young's modulus (Fertig & Nickerson, 2016)

Figure I-16: Overview on different results obtained in a thermal or thermomechanical study

License CC BY-NC-ND 4.0

Despite their wide use, CZMs exhibit several important limitations. Although CZMs remove the need for pre-existing cracks, they still require predefined potential crack paths during fracture analyses (Espinosa & Zavattieri, 2003b; Kim et al., 2011). Also, their essentially (one-dimensional) traction-separation formulation also struggles to capture constraint and triaxiality effects (Kuna & Roth, 2015; Wciślik & Pała, 2021), and certain formulations may produce non-physical behaviours such as negative tractions, artificial elastic ranges, or inconsistent boundary conditions (Wciślik & Pała, 2021). Extending CZMs to fully three-dimensional microstructures remain challenging. Realistic crack growth, especially branching, coalescence, and interactions among multiple cracks, is difficult to represent, and assigning cohesive elements at triple or multi-junctions introduces significant computational and geometric complications (Kim et al., 2011; Lin et al., 2017; Wciślik & Pała, 2021). Furthermore, modelling unloading, reloading, and fatigue is computationally demanding (Kim et al., 2011; Kuna & Roth, 2015) and parameter identification, especially for shear-dominated behaviour, remains difficult because cohesive properties depend on factors such as element size, triaxiality, and strain rate (Kuna & Roth, 2015; Lin et al., 2017; Liu et al., 2023).

I.3.1.2. Extended Finite Element Method

The XFEM is an advanced numerical technique that models arbitrary geometric features, such as cracks (Belytschko & Black, 1999; Moes et al., 1999), voids (Daux et al., 2000), and branched flaws (Daux et al., 2000) (see Figure I-17a), independently of the finite element mesh, as illustrated in Figure I-17b. This mesh-independent representation eliminates the need for continual remeshing as cracks propagate (Khoei, 2014), as shown in Figure I-17b, which contrasts with the classical FEM approach presented in Figure I-17c. XFEM enriches the standard displacement approximation with special functions that introduce discontinuities or singular fields without modifying the mesh topology (Daux et al., 2000; Khoei, 2014). Elements are enriched when the support of their nodal shape functions intersects a crack or contains critical features such as crack tips or junctions (Khoei, 2014). For example, Figure I-17b highlights enriched elements in yellow, while standard FEM elements are shown in blue. Common enrichment functions include near-tip asymptotic fields expressed in polar coordinates (r, θ) (such as $\sqrt{r}\cos(\theta/2)$) to capture the crack-tip displacement singularity (Daux et al., 2000), and a discontinuous Heaviside function $(H(x))$ to represent the displacement jump across crack surfaces (Belytschko & Black, 1999; Daux et al., 2000; Moes et al., 1999). Together, these enrichments enable efficient and accurate simulation of crack initiation and growth, offering substantial advantages over traditional FEM for fracture analysis (Khoei, 2014).

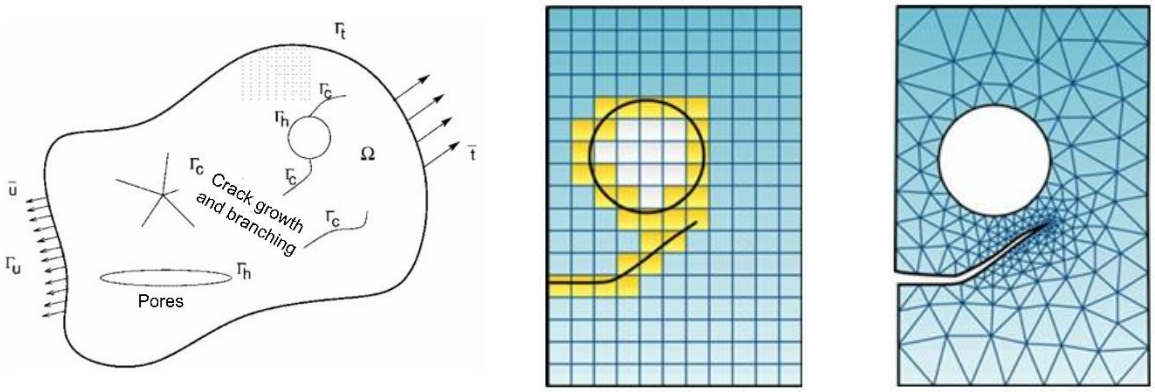

a) discontinuous material domain (Daux et al., 2000) b) XFEM discretization (Khoei, 2014) c) FEM discretization (Khoei, 2014)

Figure I-17: Schematic of XFEM discontinuity representation compared to conventional FEM

Although XFEM can represent crack initiation and propagation, studies (Sukumar et al., 2003; Sukumar & Srolovitz, 2004; Wang et al., 2013) have shown that coupling XFEM with a CZM provides significant advantages. By doing so, the grain boundaries are governed by the CZM

License CC BY-NC-ND 4.0

through specific traction-separation laws incorporating damage evolution and mixed-mode coupling, while XFEM preserves geometric flexibility and avoids mesh alignment constraints. This combined approach enables realistic, microstructure-informed fracture modelling where grain boundaries and grain interiors can be assigned different constitutive behaviors.

Figure I-18a presents a numerically generated polycrystalline microstructure, created using either the Potts model (Sukumar et al., 2003) or Voronoi tessellation (Wang et al., 2013), in which grain interiors are represented by X-FEM enrichment functions and grain boundaries are modelled using CZM. This microstructural configuration was employed by Sukumar & Srolovitz, (2004) and subsequently adapted by Wang et al., (2013) for composite materials. These studies investigate the competition between intergranular and transgranular fracture, using energy-based (Sukumar et al., 2003; Sukumar & Srolovitz, 2004) or stress-based (Wang et al., 2013) criteria to govern crack propagation. The Sukumar et al., (2003) study introduced a two-dimensional X-FEM framework for brittle polycrystalline fracture, demonstrating the influence of grain boundary and grain interior toughness on crack paths. The Sukumar & Srolovitz, (2004) work refined this approach by examining numerical convergence and systematically analysing fracture-mode transitions across different toughness ratios. The methodology was further extended by Wang et al., (2013) to incorporate additional microstructural features, including grain size, secondary-phase content, and grain boundary thickness, to evaluate their effects on fracture toughness, with particular emphasis on microstructure-property relationships and the calibration of critical energy release rates for complex ceramics. Figure I-18(b-d) illustrate the critical energy released during crack initiation and propagation as a function of grain size, grain boundary, and secondary-phase volume fraction, thereby elucidating the correlation between microstructural characteristics and fracture response.

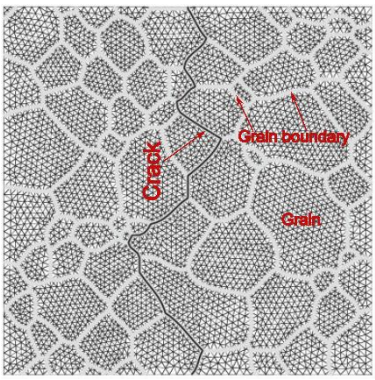

a) polycrsytalline microstructure (Sukumar et al., 2003)

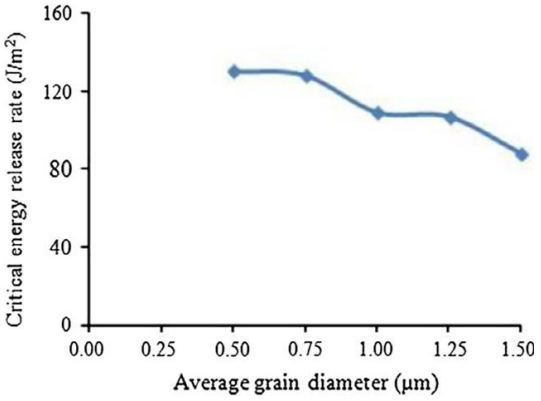

b) average grain size effects (Wang et al., 2013)

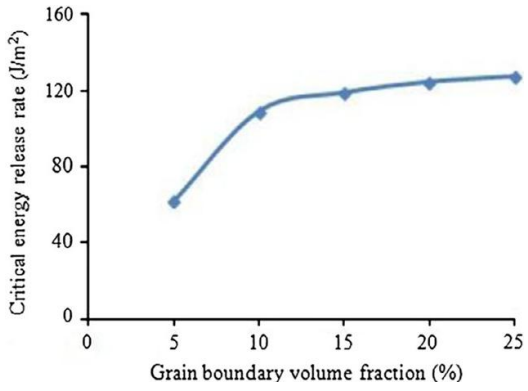

c) grain boundary volume fraction effects (Wang et al., 2013)

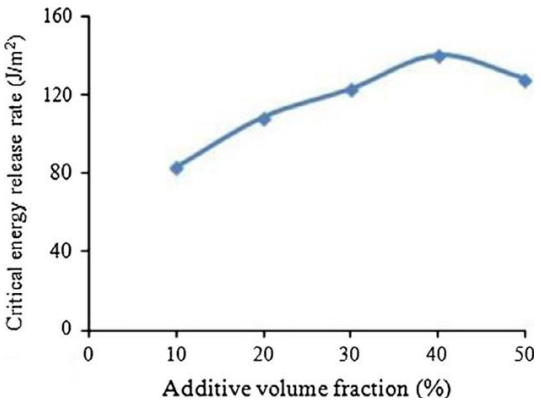

d) additive volume fraction effects (Wang et al., 2013)

Figure I-18: Overview on the studies related polycrystalline model material

License CC BY-NC-ND 4.0

Subsequently, Farukh et al., (2016) pioneered a microstructure-informed approach for low solvus high refractory nickel superalloys by integrating SEM-derived RVEs with a large-deformation, rate-dependent crystal plasticity model and XFEM. This framework accurately captured cyclic deformation, localised stress and strain heterogeneities, and grain orientation-dependent crack paths for a notched three point bending test (see Figure I-19a). Therefore, this study demonstrates the importance of microstructural fidelity in predictive modelling. Liu et al., (2018) studied the effect of micro-defects, including micro-cracks and micro-voids, on the fatigue propagation of a macro-crack using a multiscale XFEM approach. The method combined a macroscale model to capture the overall influence of micro-defects with a microscale model to resolve crack interactions and evolution. Figure I-19b shows multiple randomly distributed micro-cracks under stress. Key results indicate that only micro-defects located near the macro-crack tip significantly affect propagation, as reflected in the stress field around neighbouring micro-crack tips (see Figure I-19b), with micro-cracks generally accelerating crack growth and deflecting the crack path toward themselves.

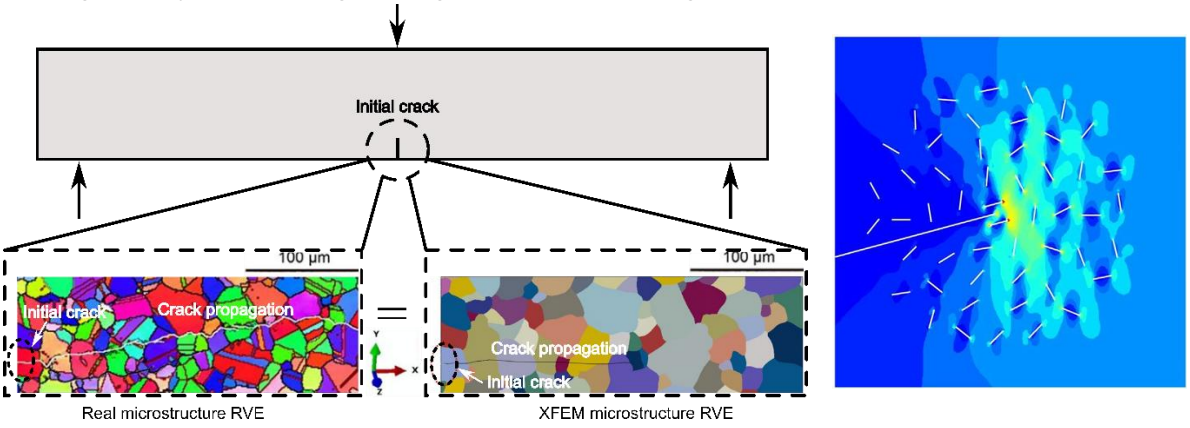

a) crack trajectory experimental vs numerical (Farukh et al., 2016)

b) multiple microcrack effects (Liu et al., 2018)

Figure I-19: Illustration of XFEM for tracking crack paths and analysing multiple cracks

Very few studies have applied XFEM to investigate microcracking induced by thermal stresses. One notable example, is the work by Zhang et al., (2020), who examined nanostructured thermal barrier coatings under thermal cycling by coupling XFEM with microstructure-resolved features, including unmelted nanoparticles (UNPs), thermally grown oxide layers, and multilayer coating architectures. By incorporating plasticity, creep, and oxide growth effects, their simulations demonstrated that UNPs (Figure I-20a, showing three UNPs) act as effective microstructural barriers, redistributing thermal stresses (Figure I-20a), localizing crack initiation, and deflecting crack propagation paths (Figure I-20b), thereby enhancing thermal shock resistance. This study highlights that microstructure-informed XFEM, combined with homogenization technic, can capture not only mechanical heterogeneity but also the macroscale consequences of the microstructure on thermomechanical failure.

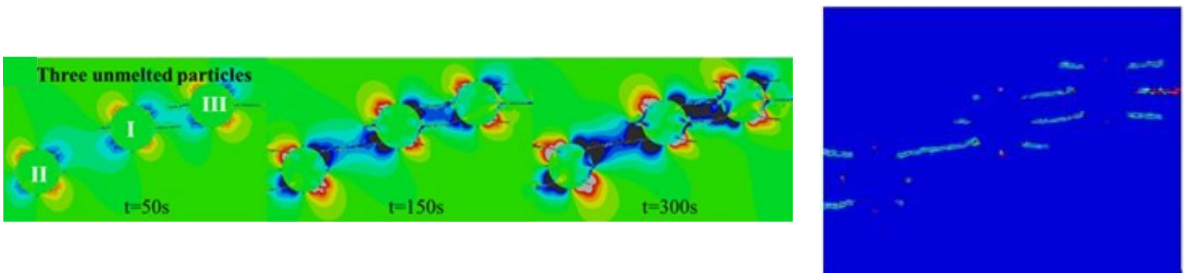

a) thermal stress (due to CTE mismatch)

b) microcracks

Figure I-20: Illustration of thermal stress promotion and microcracks in a thermal study (Zhang et al., 2020)

License CC BY-NC-ND 4.0

Despite its versatility, XFEM also presents several limitations. The use of enrichment functions increases the number of degrees of freedom, computational cost, and can adversely affect stiffness matrix conditioning, challenges that become particularly significant in large-scale 3D simulations (Khoei, 2014; Sukumar et al., 2003). Cohesive elements offer an alternative for predefined crack paths, but they are sensitive to element arrangement in complex geometries and may produce unrealistic crack trajectories when placed too close to XFEM-enriched regions (Mubashar et al., 2014). Moreover, there is no clear criterion governing the optimal proportion or spatial distribution of cohesive versus enriched elements, creating ambiguity in hybrid modelling strategies.

I.3.1.3. Phase Field modelling

Phase-Field (PF) modelling has emerged as variationally consistent framework for describing the evolution of material interfaces, such as phase, grain, and domain boundaries, whose behaviour under external stimuli follows energy-minimizing pathways (Ambati et al., 2015; Clayton & Knap, 2015). By replacing sharp boundaries with diffuse interfaces represented by continuous parameters, the method provides a unified and thermodynamically consistent description of interfacial processes. Since its introduction to brittle fracture in the late 1990s (Ambati et al., 2015), the PF approach has been extensively developed to regularise sharp cracks through a scalar crack (damage) field, as shown in Figure I-20, that smoothly transitions between intact and fully broken states, governed by a coupled system of mechanical equilibrium and gradient-type evolution equations derived from Griffith-type fracture mechanics (Ambati et al., 2015; Nguyen et al., 2017). A major advantage of this formulation, compared with approaches such as XFEM or CZM, is its ability to avoid explicit crack tracking and to naturally capture complex fracture phenomena, including nucleation, propagation, branching, and coalescence in both 2D and 3D, as crack paths emerge directly from free-energy minimisation on a fixed mesh (Ambati et al., 2015). Owing to this robustness and its strong variational foundation, the PF method is widely regarded as one of the most powerful and versatile tools for modern computational fracture mechanics.

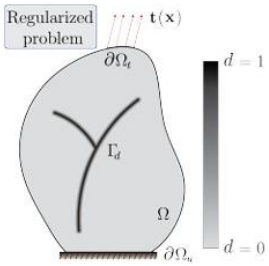

Figure I-21: Illustration of a material body in PF framework (Muneton Lopez, 2023)

Several studies have applied PF modelling to investigate fracture in polycrystalline (Clayton & Knap, 2015; Nguyen et al., 2017; Teichtmeister et al., 2017) and multi-constituent (Cavuoto et al., 2024) materials, particularly focusing on anisotropic brittle fracture as influenced by crystallographic orientation, grain-boundary structure, and material symmetry. These works share the central objective of assessing how anisotropy affects crack initiation, propagation, and path selection, leveraging the PF approach to predict complex fracture patterns without explicit crack tracking, as shown in Figure I-22. All studies consider quasi-static mechanical loading, with outputs including crack morphology, damage-field evolution, and global mechanical responses such as stress-strain curves as shown in Figure I-22a. Collectively, these approaches provide valuable insights into anisotropic fracture. Clayton & Knap, (2015); Nguyen et al., (2017) incorporated cleavage-plane-dependent fracture energy and elastic anisotropy to study the competition between intergranular and transgranular cracking (see Figure I-22a) and to investigate size effects. The methods can handle multiple cleavage systems per grain using CZM, enabling realistic simulations of grain-boundary decohesion, crack deflection, branching, and three-dimensional crack twisting (see

License CC BY-NC-ND 4.0

Figure I-22b). Building on this framework, Teichtmeister et al., (2017) incorporated structural tensors to capture material symmetries, allowing the prediction of complex anisotropic crack patterns, including helical crack paths under large deformations (Figure I-22b).

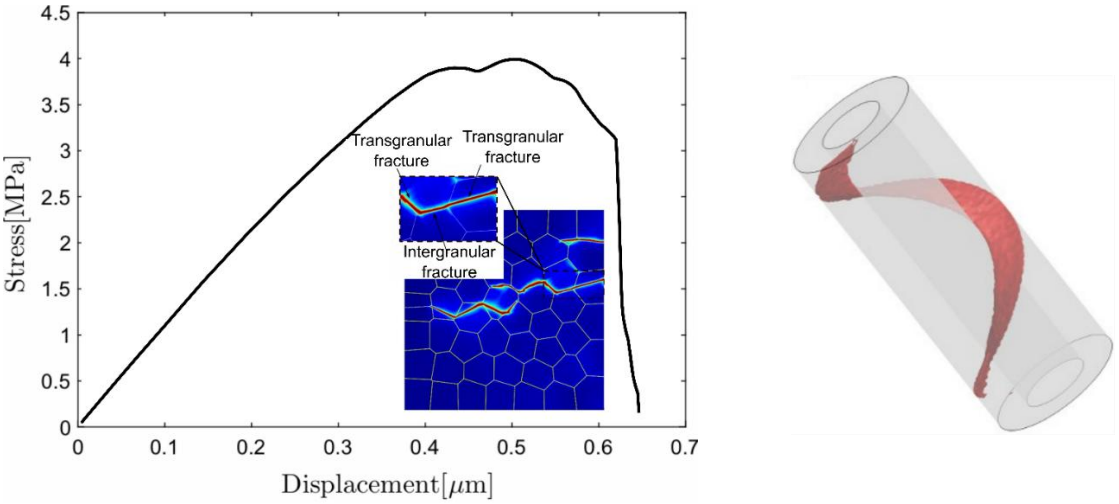

a) stress-strain response under mixed crack growth (Nguyen et al., 2017)

b) Helical and twisted cracks (Teichtmeister et al., 2017)

Figure I-22: Complex crack evolution in a polycrystalline material in PF modelling

Also, Cavuoto et al., (2024) focused on ceramics with multiscale porosity, applying phase-field model to artificial microstructures featuring macro- and meso-pore distributions, as shown in the Figure I-23a. As an outcome, the stress-strain curves and damage maps were monitored (see Figure I-23). Figure I-23a illustrates the macroscopic stress-strain response for three different microstructures with same volume fraction of pores but with different proposition of macro- and meso-pores. Indeed, from the stress-strain response it could be understood that macro-pores controlled global strength (see Figure I-23a) while meso-pores promoted damage nucleation and crack bridging (see Figure I-23b). Most recently, Adalberto Horácio de Oliveira Mendes et al., (2024) sought to accelerate fracture prediction in concrete by integrating a machine-learning surrogate into the phase-field framework; using strain measures and fracture driving forces as inputs. Indeed, the trained neural network accurately reproduced damage fields while significantly reducing computational cost.

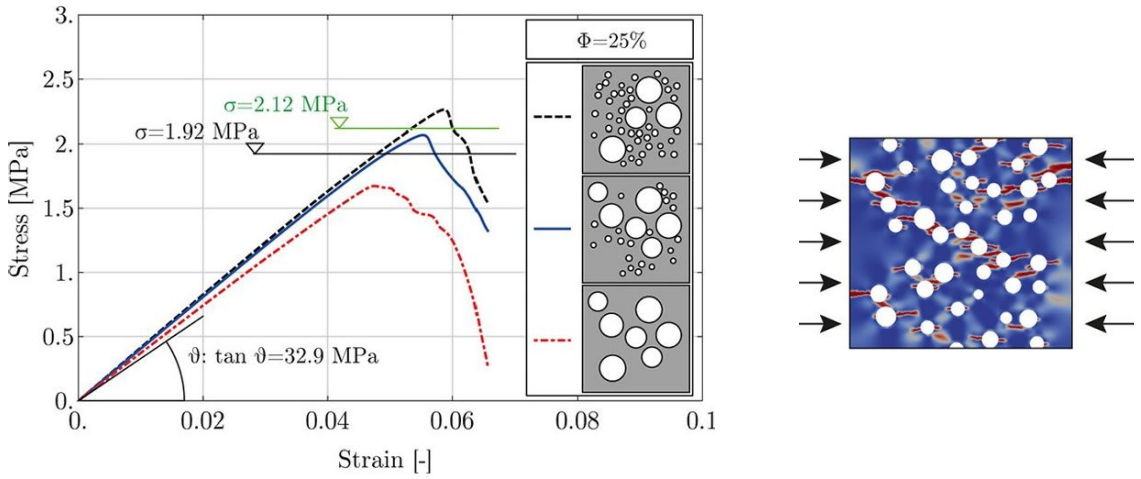

a) macroscopic stress-strain response

b) crack patterns

Figure I-23: Multiscale pores effects on the crack patterns and stress-strain response (Cavuoto et al., 2024)

License CC BY-NC-ND 4.0

PF modelling has been progressively applied to thermo-mechanical stress-induced microcrack studies, starting with Miehe et al., (2015), who developed thermoelastic PF models using elastic properties and thermal expansion coefficients to predict crack evolution under thermal stresses. Their studies tracked the development of thermal stress (Figure I-24a) and microcracks (Figure I-24b) due to CTE mismatch. Subsequently, the thermal stressed samples (Figure I-24c) were subjected to mechanical loading and it was noticed to exhibit stress relaxation along crack paths (Figure I-24d), accounting for internal residual stresses around uncracked inclusions. Building on this framework, Prakash et al., (2023) proposed a thermodynamically consistent PF model for thermo-mechanical fracture, validated through a quenching test on a ceramic specimen. A quarter of the specimen was modelled under plane stress conditions, with initial temperatures of 680 K and 880 K quenched to 300 K. The results captured temperature distribution and damage evolution, showing that higher initial temperatures led to increased crack density and deeper crack propagation as shown in Figure I-24e. Moreover, the quantitative metrics such as crack number versus normalized crack length depicted a good agreement with experimental from Shao et al., (2011) and numerical benchmarks from Tangella et al., (2022) These studies collectively demonstrate the capability of PF models to predict complex crack patterns under coupled thermal and mechanical loading.

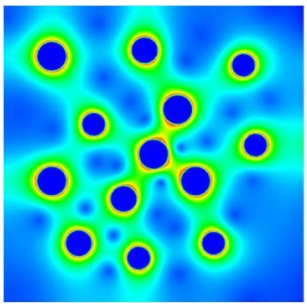

a) thermal stress (Miehe et al., 2015)

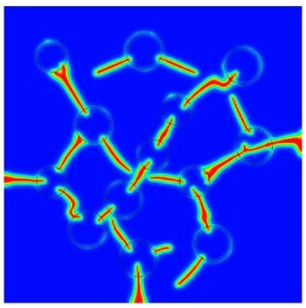

b) microcracks (Miehe et al., 2015)

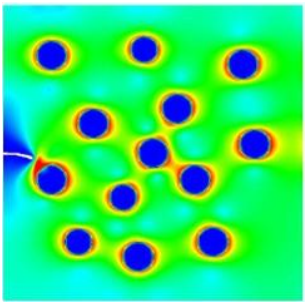

c) thermal stressed sample (Miehe et al., 2015)

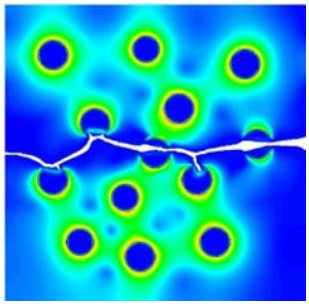

d) stress-relaxation in the crack path (Miehe et al., 2015)

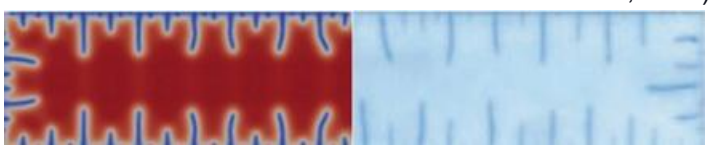

e) microcrack initiation and propagation during thermal shock (Prakash et al., 2023)

Figure I-24: Overview of the results based on thermal stress induced microcrack studies

Despite its advancements, PF modelling is generally limited for analysing material failure under compressive loads, as it cannot capture crack closure and realistic crack-lip interactions (Ambati et al., 2015). Moreover, when PF is integrated with CZM, its full advantages are not entirely realized, since the CZM imposes explicit crack propagation criteria, partially constraining the diffusive nature of PF fracture prediction (Wang et al., 2022).

License CC BY-NC-ND 4.0

I.3.2. Boundary Element Method

The BEM, developed in the 1960s (Aliabadi & Brebbia, 2025; Liu et al., 2011), offers a compelling alternative to domain-based numerical techniques such as the FEM (Kuna, 2013). Unlike FEM, which requires discretization of the entire domain (Kuna, 2013), BEM employs Green's fundamental solutions to transform partial differential equations into boundary integral equations, thereby reducing the problem's dimensionality by requiring discretization only of the boundary (Liu et al., 2011). For example, in the case of a solid sphere as shown in Figure I-25, BEM discretizes only the surface (Figure I-25a), whereas FEM and its variants demand meshing of the entire volume (Figure I-25b) (Shiah & Tan, 2016). This boundary-only approach typically results in fewer degrees of freedom and lower computational cost compared to volumetric methods (Aliabadi & Brebbia, 2025; Liu et al., 2011).

In fracture mechanics, many problems are idealised as cracks in infinite plates or elastic half-spaces (semi-infinite domains), where the body is assumed sufficiently large that external boundaries are effectively at infinity (Kuna, 2013). The BEM is particularly well suited to such problems because its fundamental solutions inherently satisfy the conditions at infinity, eliminating the need to discretize or truncate the far field (Aliabadi & Brebbia, 2025; Liu et al., 2011). Furthermore, in the boundary element method cracks are represented explicitly as internal boundaries, so only the crack surfaces and the external boundary need to be discretized. When the crack propagates, the numerical model is updated mainly by modifying the mesh along the crack front, without the need to regenerate a volumetric mesh for the surrounding domain (Aliabadi & Brebbia, 2025). This boundary-only remeshing is generally simpler and less computationally demanding than the volumetric remeshing typically required in domain-based methods such as the finite element method, especially for problems involving complex crack paths (Liu et al., 2011; Shiah & Tan, 2016).



a) BEM discretisation b) FEM discretisation

Figure I-25: Illustration of different strategy of discretisation with BEM and FEM (Shiah & Tan, 2016)

Building on these advantages, several studies (Benedetti & Aliabadi, 2013; Geraci & Aliabadi, 2017; Gulizzi et al., 2018; Gulizzi & Benedetti, 2016; Sfantos & Aliabadi, 2007) employed BEM to model micro-cracks in polycrystalline materials. In these studies, polycrystalline models (see Figure I-26a) were generated using Voronoi tessellations, with grains treated as anisotropic elastic domains (Figure I-26a) and cohesive laws (similar to Figure I-13c) applied to simulate cracking. Firstly, Benedetti & Aliabadi, (2013) and Sfantos & Aliabadi, (2007) focus on modelling intergranular cracks in polycrystalline brittle materials using the BEM. Both formulations incorporate non-linear frictional contact analysis to handle fully cracked interfaces under mechanical loading. The studies examine the effects of microstructural randomness, such as grain orientation, morphology, and pre-existing flaws, under tensile and compressive loading, highlighting shear-driven fracture patterns. This approach allows tracking of micro-crack initiation, propagation, and coalescence, capturing the resulting macroscopic stress-strain response. For example, Figure I-26a illustrates the microcracked polycrystalline sample under compressive loading and their macroscopic stress-strain response. Similarly, Geraci & Aliabadi, (2017) and Gulizzi et al., (2018)

License CC BY-NC-ND 4.0

investigated both intergranular and transgranular cracking in polycrystalline materials. They studied the effects of pre-existing cracks (single and multiple), their statistical distribution (random), and grain size on micro-crack evolution and the macroscopic stress-strain response, as illustrated in Figure I-26b.

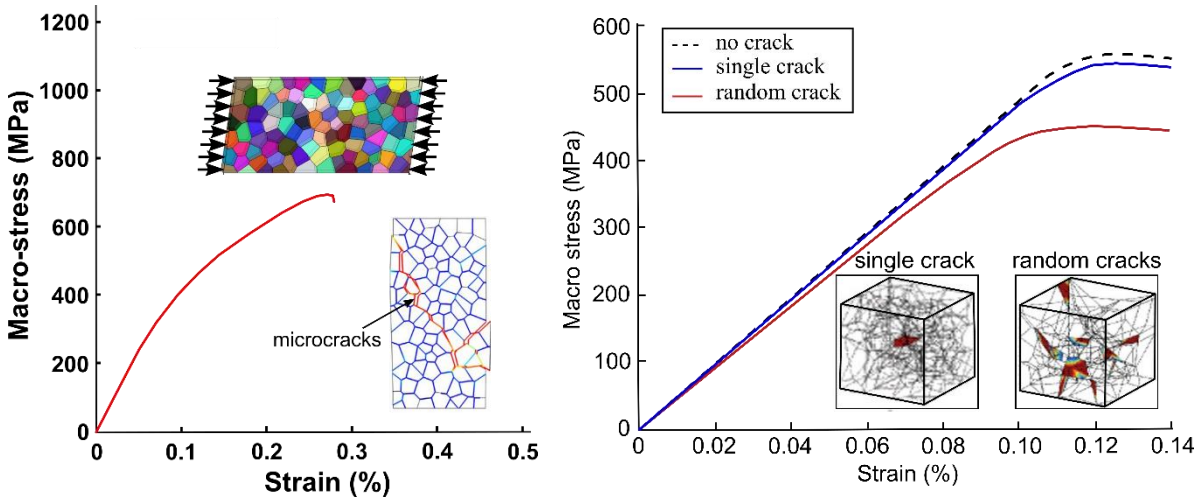

a) under compression test (Benedetti & Aliabadi, 2013)

b) under tensile test (Gulizzi et al., 2018)

Figure I-26: Illustration of impact of the pre-cracked sample on the macroscopic properties

Subsequently, few studies (Benedetti & Aliabadi, 2015; Gabriela Rezende Fernandes et al., 2024; Gulizzi et al., 2015) developed multiscale framework (as shown in Figure I-27) that used BEM at each scale to capture microscale phenomena (such as intergranular cracking, interface damage, and material heterogeneity) and link them to the macroscopic material behavior (e.g., stress-strain response), similar to previous discussed studies. These approaches employ microstructural representations such as Voronoi or RVE-based as depicted in Figure I-27 and compute homogenized or structural-scale responses by resolving detailed microscale fields.

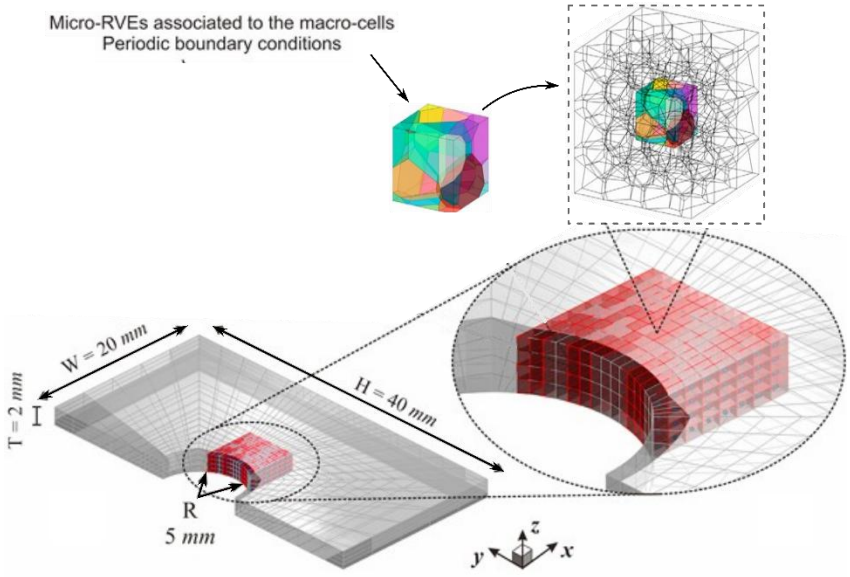

Figure I-27: Illustration of 3D BEM model with polycrystalline micro-model in a macro-model (Benedetti & Aliabadi, 2015)

License CC BY-NC-ND 4.0

In addition, the studies by Geraci & Aliabadi (2018, 2019) both focus on micromechanical modelling of thermoelastic cracking in polycrystalline materials using BEM. The study simulated cracks using cohesive laws and non-linear frictional contact to simulate separation and sliding, employing Voronoi-generated polycrystalline microstructures under thermomechanical loading. As an illustration, Figure I-28a depicts the polycrystalline model subjected to thermal loading in the study by Geraci & Aliabadi (2018), analysing Al_2O_3 and SiC. These studies investigated the influence of grain size on fracture mechanisms and identified which material exhibits higher resistance to thermally induced cracking. Again, a Voronoi-generated polycrystalline grain model (30-100 grains), shown in Figure I-28b, was employed to monitor damage metrics as a function of temperature (Figure I-28a). The results revealed that finer grains degrade faster, coarse grains favour transgranular cracking (Figure I-28a), and SiC is more resistance to thermally induced cracking than Al_2O_3 (Figure I-28b). In addition, these studies monitored the local thermal stress distribution in the sample, as shown in Figure I-28c. Moreover, Benedetti (2023) and Cascio et al., (2024) extended these frameworks to compute effective thermoelastic properties with results showing rapid convergence within classical Reuss-Voigt bounds (Reuss, 1929; Voigt, 1889) and providing a foundation for thermo-mechanical damage analysis.

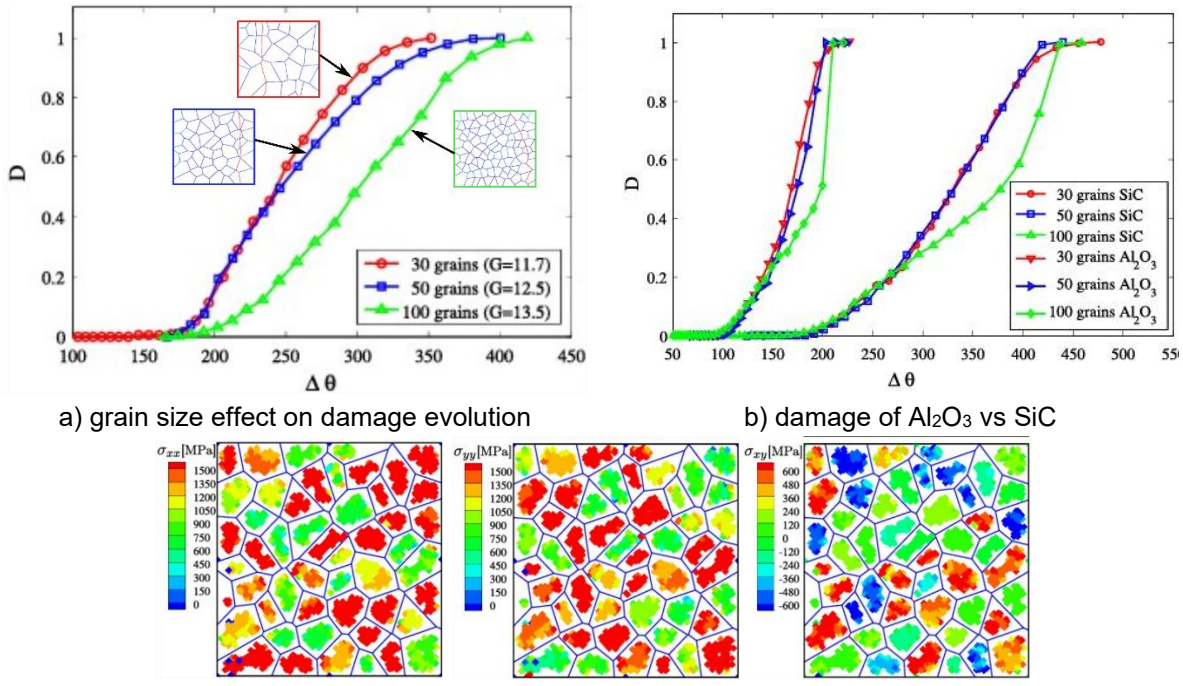

a) grain size effect on damage evolution

b) damage of Al_2O_3 vs SiC

c) thermal stress distribution

Figure I-28: Overview on the thermomechanical study based on Geraci & Aliabadi (2018)

Despite its applicability, traditional BEM formulations are limited to linear elasticity and homogeneous domains, making large-scale nonlinearities, plasticity, and complex heterogeneous behavior difficult to model. Detailed boundary discretization can be cumbersome for irregular geometries or evolving cracks (Gulizzi et al., 2018; Sfantos & Aliabadi, 2007), and fully coupled multi-physics phenomena, such as thermo-chemo-mechanical degradation, remain challenging (Benedetti, 2023; Cascio et al., 2024).

I.4. Particle-based approach to simulate fracture initiation and propagation

In full-field continuum mechanics, materials are treated as continuous media in which field quantities such as stress, strain, and displacement vary smoothly in space (Kuna, 2013). This assumption becomes invalid when the characteristic length scale of heterogeneities, defects, or discontinuities approach the scale of observation (Callister Jr & Rethwisch, 2020; Javili et al., 2019;

License CC BY-NC-ND 4.0

Z. Yang et al., 2022). Many engineering materials (including geomaterials, composites, ceramics, and refractories) exhibit inherently discontinuous behaviour due to pores, grains, interfaces, or cracks (Biswas & Sarkar, 2020; Callister Jr & Rethwisch, 2020; da Luz A et al., 2015). To capture such micro-mechanical processes, particle-based approaches have been developed as an alternative to full field continuum formulations (Javili et al., 2019; Nikolić et al., 2018; Potyondy & Cundall, 2004; Wretborn, 2016).

Particle-based methods discretize the material into interacting points or particles that carry mass, momentum, and internal state variables, evolving according to discrete equations of motion (Ladányi & Gonda, 2021; Pan et al., 2018; Potyondy & Cundall, 2004; Sun et al., 2021). Geometry is described by the whole point or particle lattice structure rather than a fixed mesh which is more suitable for large deformations, fragmentation, and complex crack patterns (Pan et al., 2018; Z. Yang et al., 2022). Particles or points can move, separate, and form new interaction networks without remeshing, and displacement discontinuities emerge naturally from their interactions (Herrmann et al., 1989; Sulsky et al., 1994).

These methods can be broadly classified into two categories. The first is discrete mechanics, where particles or points represent physical entities interacting via contact forces, bonds, or potentials. The Discrete Element Method (DEM, (Cundall & Strack, 1979)) and lattice modelling (Herrmann et al., 1989; Schlangen & Garboczi, 1996) belong to this class, treating the material as assemblies of rigid or deformable entities. The second category comprises particle discretization's of continuum theories, which retain continuum governing equations but use particles as primary carriers of state. The Material Point Method (MPM, (Sulsky et al., 1994)) and Peridynamics (Silling, 2000) reformulates solid mechanics within this theoretical background.

All these methods share a common principle: macroscopic material behaviour emerges from local interactions among discrete entities. In addition, discrete models do not require predefining crack paths or remeshing during fracture, providing a natural framework for simulating damage evolution, fragmentation, and discontinuity formation (Adibaskoro et al., 2024; De Meo et al., 2016; Mariotti et al., 2009; Morrison et al., 2014). Building on these advantages, the following section reviews recent particle-based approaches widely employed for fracture analysis.

I.4.1. Material Point Method

The Material Point Method (MPM) is a particle-grid computational framework introduced by Sulsky and co-workers (Sulsky et al., 1994) in the mid-1990s as an extension of the particle-in-cell and fluid-implicit-particle approaches originally developed for fluid dynamics. In MPM, the continuum body is represented by a collection of Lagrangian material points that store all state information (such as mass, velocity, strain, stress, and any history-dependent variables) while a stationary Eulerian background mesh is employed to evaluate gradients and to solve the governing balance laws (Liang et al., 2021; Sun et al., 2021, 2024; Wretborn, 2016). This dual representation enables the particles to track the evolving material response while the grid provides a distortion-free computational platform (Sun et al., 2021).

The numerical algorithm in MPM is built by a sequence of operations comprising both Lagrangian and Eulerian phases:

- Transfer of particle data to the grid**:** at the beginning of a time step, material point quantities (including mass, linear momentum, and internal force contributions derived from particle stresses) are mapped onto the nodes of the background mesh through finite element shape functions (see step1 in Figure I-29) (Sun et al., 2021, 2024).

License CC BY-NC-ND 4.0

- Solution of the nodal momentum equations**:** with the particle information assembled on the grid, the discrete equations of motion are solved at the grid nodes to obtain updated nodal accelerations and velocities (step2 in Figure I-29) (Sun et al., 2021, 2024).
- Interpolation of nodal updates back to the particles**:** the nodal solutions are then projected back onto the material points using the same interpolation basis, providing each particle with its updated kinematic quantities such as acceleration or velocity increments (step3 in Figure I-29) (Sun et al., 2021, 2024).
- Particle state update and grid reset**:** each material point subsequently updates its position, velocity, deformation gradient, volume, strain, stress, and any internal variables according to the interpolated values (step4 in Figure I-29). After this update, the background grid is cleared of all temporary quantities and restored to its initial undeformed configuration so that the next mapping step can begin (transition from step4 back to step1) (Sun et al., 2021, 2024).

Taken together, this algorithm forms an FEM compatible formulation in which the material points act as moving integration points. This structure enables MPM to track deformation history and material interfaces with high fidelity while avoiding many of the numerical challenges that arise in mesh-based methods, such as severe element distortion (Cheon & Kim, 2019; Kakouris & Triantafyllou, 2017; Liang et al., 2021).

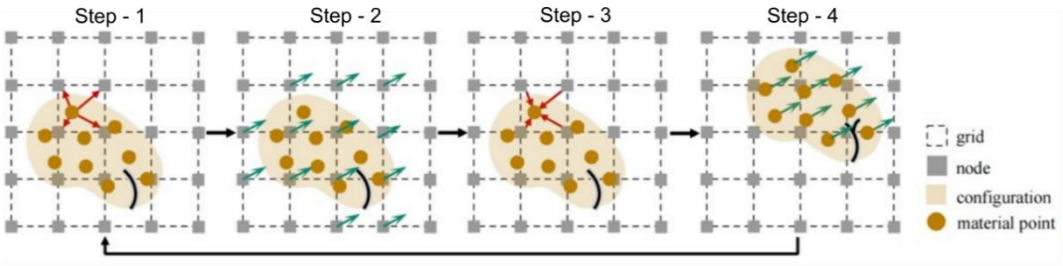

Figure I-29: Fundamental iterative steps present in the MPM numerical solution (Sun et al., 2024)

Consequently, MPM brings together the advantages of both Lagrangian and Eulerian frameworks, enabling it to handle highly nonlinear scenarios (such as extreme deformation, fragmentation, impact, contact interactions, and evolving boundaries) making it a powerful tool for a broad spectrum of problems in solid mechanics and multiphysics applications (Adibaskoro et al., 2024; Kakouris & Triantafyllou, 2017; Sun et al., 2021; Wretborn, 2016). Wretborn (2016) investigates an extension of the MPM for simulating fracture in elastic solids. The framework was applied to a rectangular brick-like sample, represented by 35,301 material points, with a small initial cut to facilitate crack initiation (Figure I-30a). The simulation was performed three times, differing only in the pre-fracturing of the material. Key inputs include material point initialization, material parameters (Lamé constants), simulation controls such as grid spacing and time step, boundary conditions, and crack failure criteria. Here, two cases are highlighted: Figure I-30b shows a sample with no pre-fractures, while Figure I-30c includes pre-existing cracks. Both samples exhibit failure, but with crack patterns (the unfractured sample breaks near the center as expected) whereas the pre-fractured sample develops a zigzag crack. The method, however, remains limited to non-branching cracks (Wretborn, 2016). Adibaskoro et al., (2024) extended MPM to simulate multiple cracks initiating, propagating, and merging under dynamic loading, successfully capturing complex crack patterns, boundary termination, and large deformations in elastic materials.

License CC BY-NC-ND 4.0

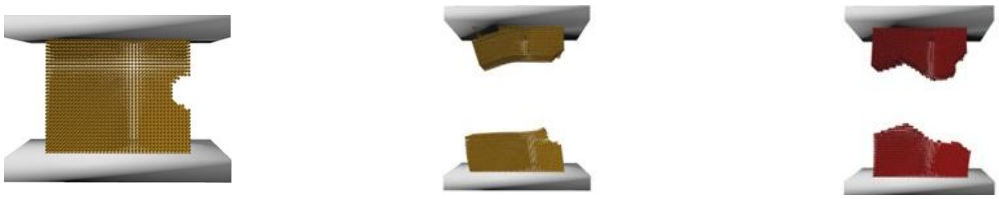

a) initial set up b) no-pe-cracked sample c) pre-cracked sample

Figure I-30: Illustration of tearing of material under gravity using MPM simulation (Wretborn, 2016)

Kakouris & Triantafyllou, (2017) and Cheon & Kim, (2019) both model brittle fracture under purely mechanical loading using the MPM combined with a Griffith-based phase-field formulation, enabling smooth, diffuse crack evolution (including initiation and branching) without explicit discontinuity tracking, and both employ staggered schemes to solve the coupled fields. Despite their shared conceptual base, work by Kakouris & Triantafyllou, (2017) demonstrated the feasibility and accuracy of PF-MPM, showing that the method eliminates mesh distortion, reproduces experimental crack paths, and matches PF-FEM load-displacement curves as shown in Figure I-31a. The obtained results (see Figure I-31a) evidently depict the potential of the model to exhibit crack patterns aligning with the experimental results and the model was successful capturing the macroscopic load-displacement curve as response of crack evolution at the microscale of the sample. In contrast, Cheon & Kim, (2019) introduce an adaptive phase-field MPM, by embedding a grid-based octree refinement strategy that automatically increases resolution only near the crack tip (see Figure I-31b), where the phase-field variable approaches a critical threshold. This refinement is coupled with material point subdivision, enabling highly localized accuracy without global refinement. Their numerical examples employed Mode I, Mode II, and mixed mode fracture, and demonstrates practical utility through 3D applications such as the brittle failure of a road wheel (see Figure I-31c). As a result, their method resolves the length scale with far greater efficiency and avoids the unrealistic crack broadening that occurs when non adaptive phase-field models lack sufficient resolution (Cheon & Kim, 2019).

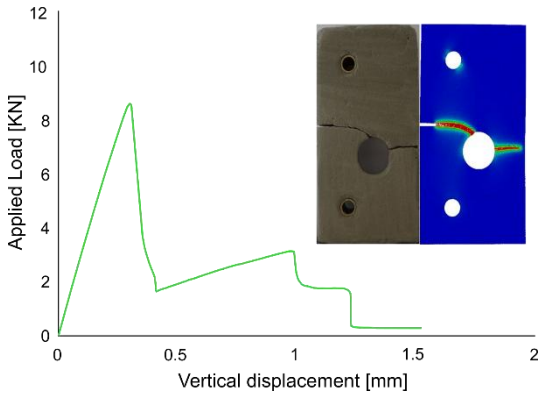

a) load-displacement curve (Kakouris & Triantafyllou, 2017)

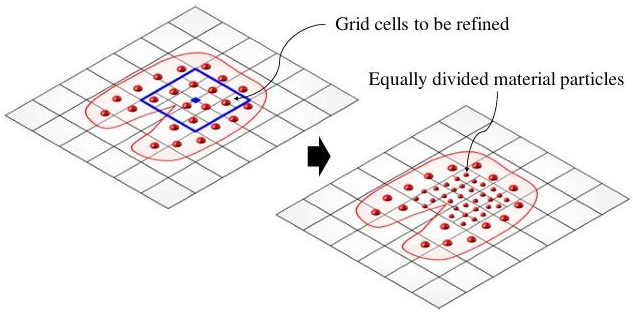

b) adaptive remeshing strategy (Cheon & Kim, 2019)

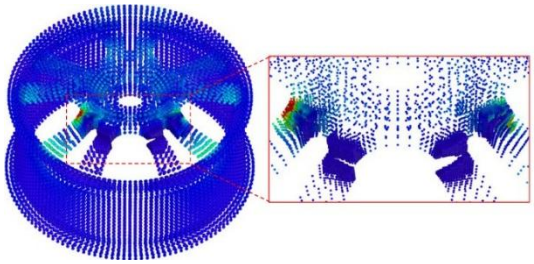

c) brittle failure of road wheel under hydraulic stress (Cheon & Kim, 2019)

Figure I-31: Overview on different brittle fracture studies related to MPM approach

License CC BY-NC-ND 4.0

Other studies shifted to explicit-discontinuity formulations, with Sun et al., (2021) introducing a 2D extended MPM using phantom nodes and particle cutting, and Liang et al., (2021) advancing this to full 3D via the XMPM framework with enrichment and level-set crack tracking, enabling more geometrically explicit fracture simulation.

Sun et al., (2024) proposed an explicit phase-field MPM to model thermally induced fractures by simultaneously coupling temperature, displacement, and phase (damage) fields in a particle-based framework. The method discretizes the domain into material points on a fixed Eulerian grid, using a phase-field variable to represent crack through a strain-history field and degradation function. It was applied to thin circular ceramic specimens (13 mm in diameter and 1 mm as shown in Figure I-32a) of stacked 99% Al_2O_3 sheets, heated to 250-500 °C and quenched in 15 °C liquid, following the experiments of Liu et al., (2015). Material heterogeneity was captured via a Weibull distributed Young's modulus, with additional properties including density 3980 kg/m³, Poisson's ratio 0.22, fracture energy 12.16 J/m², and temperature dependent thermal expansion, conductivity, and specific heat. Simulations successfully reproduced crack initiation perpendicular to the circumference, propagation toward the center, branching, and hierarchical patterns, with cracks halting dynamically where thermal strain energy was insufficient to drive the crack, as shown in Figure I-32a.

Figure I-32b presents a comparison of crack lengths from simulations (coloured bars) and experiments (black error bars) across different levels. The simulated results closely matched the experimental data, showing that higher initial temperatures led to longer cracks while shorter cracks remained small. Quantitative analyses of crack spacing and lengths further confirmed the accuracy and reliability of the method (Sun et al., 2024).

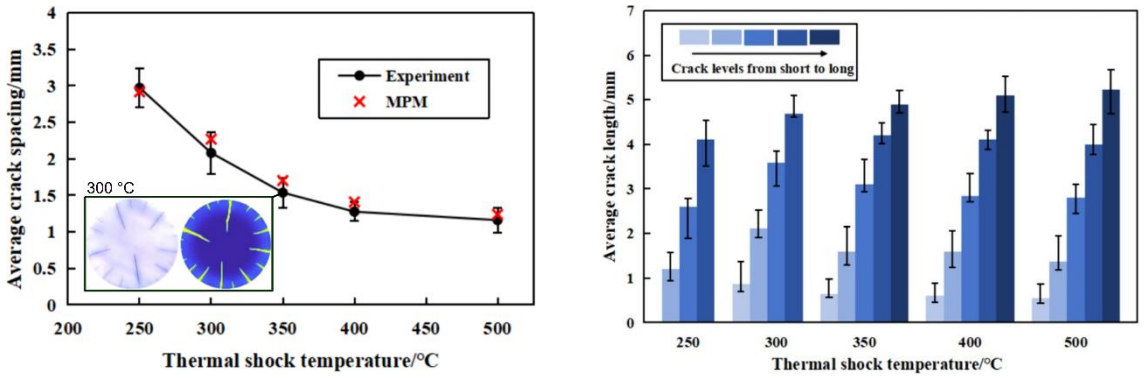

a) crack spacing vs initial temperature

b) different Crack lengths levels at different initial temperatures

Figure I-32: MPM thermal shock simulation and results for the circular disc (Sun et al., 2024)

Despite its advantages in simulating large deformations and fracture, the MPM has several inherent limitations. Its accuracy is highly sensitive to grid refinement, often requiring fine meshes to achieve results comparable to FEM, which increases computational cost (Cheon & Kim, 2019; Kakouris & Triantafyllou, 2017). Numerical artifacts such as smoothing of sharp features, premature contact (between two or multiple phase/components), spurious damping, or stick-slip behavior can occur if contact algorithms are not carefully implemented (Cheon & Kim, 2019; Kakouris & Triantafyllou, 2017). The use of explicit time integration and staggered solution schemes imposes small critical time steps, reducing computational efficiency (Sun et al., 2024). Particle-based integration sacrifices some precision relative to FEM's Gaussian quadrature, and repeated reconstruction of the background mesh further adds to overhead (Sun et al., 2024). MPM is less efficient in small-

License CC BY-NC-ND 4.0

deformation problems and usually considers only one-way thermomechanical coupling, neglecting the effect of deformation on temperature under non-extreme conditions (Sun et al., 2024).

I.4.2. Peridynamics

Peridynamics (PD) is a modern formulation of continuum mechanics (a nonlocal theory) introduced by Silling, (2000) . According to dell'Isola and co-authors (dell'Isola et al., 2016), its foundational ideas can be linked to the earlier contributions of Gabrio Piola. The approach was developed to address the high computational cost associated with mesh generation in classical continuum models, a major obstacle when simulating crack initiation and growth (Javili et al., 2019; Ladányi & Gonda, 2021). In essence, PD describes how material points interact through forces acting over a finite neighbourhood. Unlike classical continuum mechanics, its governing equations take the form of integro-differential relations, which naturally accommodate discontinuities within the material (Javili et al., 2019; Ladányi & Gonda, 2021; Nguyen et al., 2023; Z. Yang et al., 2022).

PD models are broadly classified into bond based and state based formulations, distinguished by the introduction of a state defined by an array that stores the properties of the PD bonds associated with each material point (Javili et al., 2019; Ladányi & Gonda, 2021). The state based framework is further divided into ordinary and non-ordinary types. Figure I-33 illustrates the interactions of material points under each formulation, highlighting the horizon defined by the parameter δ (Javili et al., 2019). A key feature of PD is that a material point's response depends on the collective deformation of points within its horizon, which also defines the characteristic length scale (see Figure I-33). The three formulations differ in the magnitude and direction of interaction forces (green arrows) (Ladányi & Gonda, 2021). In bond based PD, the bond force vector is parallel to the bond and symmetric as shown in Figure I-33a. In state based PD, the force magnitude can differ between $y \to y'$and $y' \to y$ (see Figure I-33b), with non-ordinary PD also allowing the force direction to deviate from the bond (see Figure I-33c). All formulations satisfy the fundamental conservation laws (Javili et al., 2019).

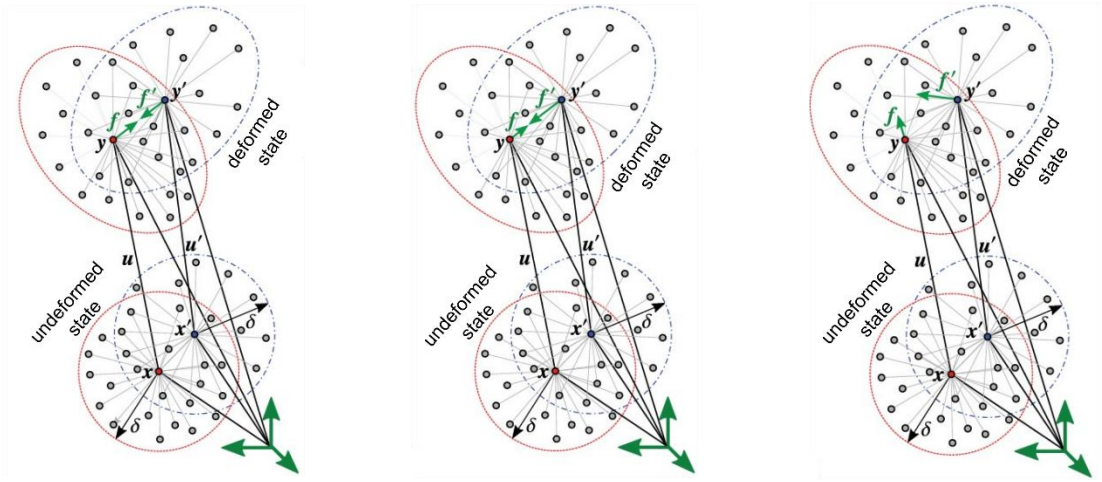

a) bond-based b) ordinary state-based c) non-ordinary state-based

Figure I-33: Material points shown under different PD formulations, each with its own horizon (Javili et al., 2019)

In recent times, a growing number of recent studies have employed PD to investigate fracture and damage due to its natural ability to accommodate discontinuities (Bazazzadeh et al., 2020; Gu et al., 2023; Ladányi & Gonda, 2021; Li et al., 2024; Nguyen et al., 2023; Z. Yang et al., 2022; Zhang et al., 2022). In peridynamics, material damage/crack is represented by the failure of bonds between pairs of particles by monitoring the stretch criteria of each bond (Javili et al., 2019; Ladányi

License CC BY-NC-ND 4.0

& Gonda, 2021). Once a bond breaks, its interaction is permanently removed from the analysis. The damage index ϕ quantifies the local damage at a material point by measuring the ratio of broken bonds to the original number interactions associated with it (Javili et al., 2019; Ladányi & Gonda, 2021).

Building on this framework, De Meo et al., (2016) developed a new PD formulation to investigate fracture in polycrystalline materials under mechanical loading. The model uses Voronoi-generated microstructures with randomly oriented grains (Figure I-34), incorporates two PD bond types, and applies a grain boundary coefficient to differentiate grain-interior and grain-boundary strength. PD material parameters are incorporated from experimental data. The simulations examine how grain boundary coefficient, grain size, fracture toughness, and loading conditions affect key failure mechanisms, including microcracking, crack-speed evolution, branching, nucleation, and time-to-failure as shown in Figure I-34. Crack-propagation results (see Figure I-34) for grain boundary coefficient values between 0.7 and 10 reveal that lower grain boundary coefficient leads to earlier crack initiation and higher crack speeds due to weaker boundary paths. All cases display rapid acceleration followed by sharp deceleration, with crack branching occurring only at grain boundary coefficient equals 0.7, which further slows propagation. In contrast, higher grain boundary coefficient values (5 and 10) reduce crack speed by increasing grain-boundary resistance, and time-to-failure becomes largely insensitive to grain boundary coefficient beyond this range (De Meo et al., 2016).

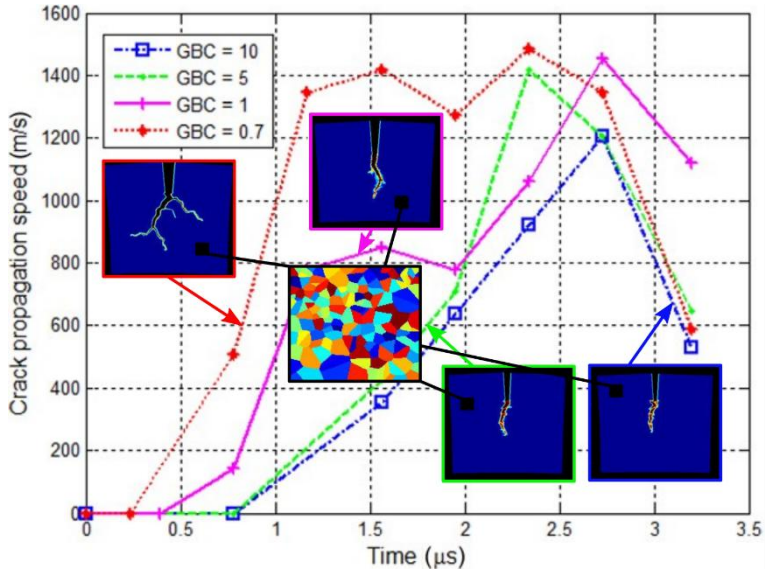

Figure I-34: Monitoring the crack propagation speed versus time in polycrystalline material (De Meo et al., 2016)

Subsequently, Yang et al., (2022) developed a PD-based statistical multiscale framework capable of efficiently modelling fracture in composites exhibiting microstructural randomness. The approach links microscale bond-based PD simulations of RVEs to a homogenized macroscale PD model using statistical homogenization theory. The present study employs two sets of 2D and 3D RVEs (see Figure I-35a) comprising matrix, inclusions (circular, elliptical, spherical, or ellipsoidal, with varying orientations and volume fractions) and interface bonds. The method couple's microscale bond-based PD analyses of RVEs with a homogenized macroscale PD model through statistical homogenization theory (Z. Yang et al., 2022). Figure I-35a illustrates the geometry and boundary conditions of the composite structures and their corresponding RVEs. This study examined the influence of RVE microstructure on macroscopic fracture behavior, including crack paths and stress-displacement responses. Figure I-35b presents the crack paths and stress-displacement

License CC BY-NC-ND 4.0

responses of the two RVEs. As shown in Figure I-35b it is understandable that the microstructure influences crack propagation. The stress-displacement curves (Figure I-35b) indicate that RVE2 exhibits slightly lower strength than RVE1. Validation against single-scale direct PD simulations shows that the PSM method accurately predicts fracture behavior while reducing computational cost by up to 80% (Z. Yang et al., 2022). In addition, Gu et al., (2023) developed a hybrid implicit-explicit bond-based PD framework to predict the mechanical behavior of porous quasi-brittle material. Again, the framework outputs stress-strain responses, macroscopic properties and detailed damage evolution (Gu et al., 2023).

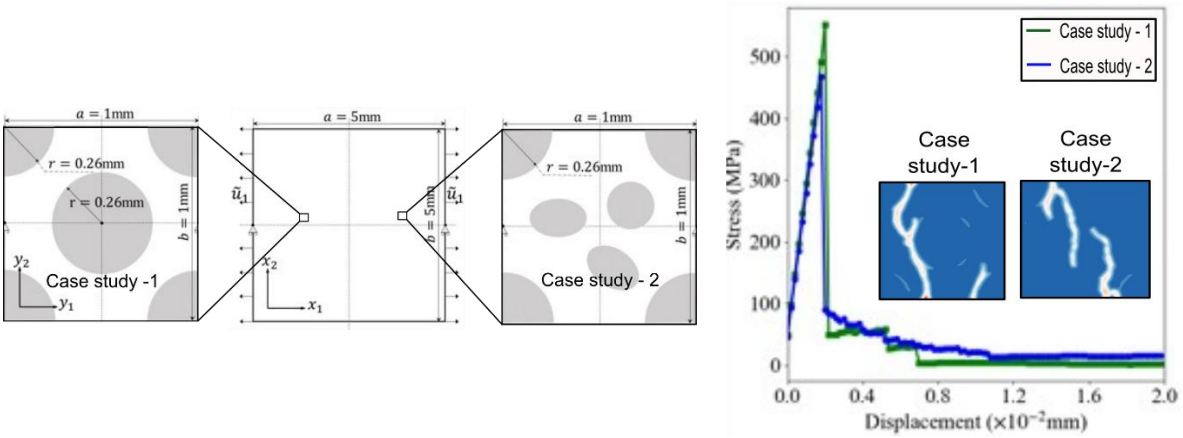

a) composite RVEs with matrix, interface and inclusion b) stress-displacement curve

Figure I-35: Overview of the study of Yang and co-workers (Z. Yang et al., 2022)

Several recent studies have advanced the application of PD models for simulating thermo-mechanical fracture in brittle and quasi-brittle materials, sharing a common goal of accurately predicting crack initiation, propagation, and post-damage behaviour under thermal or coupled thermo-mechanical loading (Bazazzadeh et al., 2020; Li et al., 2024; Zhang et al., 2022). All three studies leverage the nonlocal nature of PD to model fracture without predefining crack paths, incorporate material point discretization, and capture damage evolution through bond breaking or damage variables (Bazazzadeh et al., 2020; Li et al., 2024; Zhang et al., 2022). Despite these similarities, the approaches differ in methodology and material focus.

Bazazzadeh et al., (2020) proposed an adaptive multi-grid PD framework for ceramics under thermal shock, using fine grids only near expected crack zones to reduce computational cost. Figure I-36, depicts the simulated thermal shock in a thin circular ceramic plate (99% Al_2O_3, radius 0.065 m) using the proposed numerical method. The strategy was replicating the experiments test in reference (Liu et al., 2015b), where ceramics were heated and quenched in water (Figure I-36a). The analysis assumes plane stress, with temperature-dependent thermal conductivity, specific heat and thermal expansion. It also employs a convection boundary condition on the boundary surfaces. Contour plots show that multiple cracks initiate from the edges and propagate toward the center, closely matching experimental crack paths (Figure I-36a). Both the uniform models (Figure I-36b) and adaptive (Figure I-36c) predict 15 total cracks, with 4 long cracks exceeding half the radius (Bazazzadeh et al., 2020).

License CC BY-NC-ND 4.0

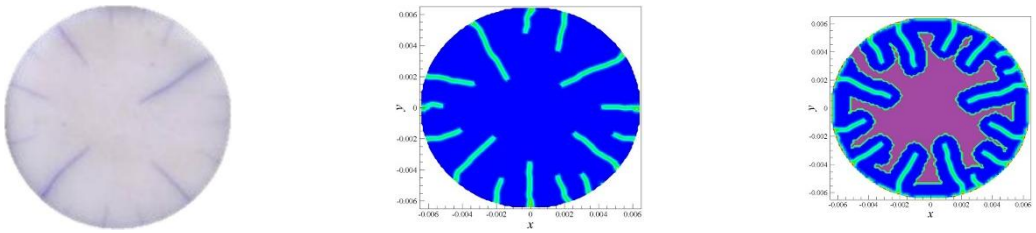

a) experimental b) uniform model c) adaptive model

Figure I-36: Experimental and numerical thermal shock test on the alumina circular ceramic (Bazazzadeh et al., 2020)

Zhang et al., (2022) developed a fully coupled thermomechanical bond-based PD model for quasi-brittle materials that accounts for both tension (brittle) and compression (plastic-softening) behaviour, including heterogeneous microstructures such as granite. In addition, Li et al., (2024) introduced a coupled non-ordinary state-based PD (NOSB-PD) model capable of simulating both brittle fracture under thermal shock, employing a unified multiaxial constitutive model with a damage-based fracture criterion and stabilization algorithms to avoid numerical oscillations while capturing dynamic thermomechanical responses. Collectively, these studies demonstrate that PD frameworks (through adaptive refinement, coupled constitutive models, and nonlocal interactions) can provide both accurate and computationally efficient predictions of complex fracture behaviour in brittle and quasi-brittle materials under sever thermomechanical conditions (Li et al., 2024).

The PD method, despite its advantages in fracture modelling, presents several significant limitations related to computational cost, theoretical formulation, and numerical robustness. A primary drawback is its high computational expense, stemming from the non-local integral formulation that requires each material point to interact with all points within a finite horizon. As a result, PD simulations are typically far more time consuming than concurrent numerical methods and achieving high accuracy often demands a large number of nodes within the horizon, further increasing computational burden (Ladányi & Gonda, 2021). In addition, the classical bond based PD formulation suffers from foundational theoretical restrictions: it enforces a fixed Poisson's ratio of 0.25 in 3D and 0.33 in 2D, which is unsuitable for many engineering materials (Javili et al., 2019; Ladányi & Gonda, 2021; Zhang et al., 2022). Numerical stability poses another challenge. In state-based PD models, the use of a non-local deformation gradient can introduce unphysical behaviours such as zero energy modes, material collapse, and interpenetration, particularly under large deformations (Javili et al., 2019; Li et al., 2024). Finally, the treatment of boundary conditions in PD is non-trivial. Because the PD variational framework does not naturally admit traction boundary conditions, the conventional notion of surface traction is incompatible with standard PD theory, requiring special techniques to approximate natural boundary conditions (Javili et al., 2019; Ladányi & Gonda, 2021).

I.4.3. Lattice models

Lattice element models (commonly referred to as lattice models) trace their origins to Hrennikoff's 1941 study (Hrennikoff, 1941), which introduced a grid-framework technique to represent two-dimensional elastic continua using truss-like assemblies, as shown in Figure I-37a. Since then, the methodology has evolved substantially, giving rise to numerous lattice formulations. In most approaches, the bulk material is idealised by interconnecting nodes with one-dimensional discrete bonding elements (Nikolić et al., 2018; Pan et al., 2018). The Lattice Beam Model (LBM) and the Lattice Spring Model (LSM) emerging as the two most widely adopted types, as illustrated in Figure I-37a and b (Pan et al., 2018). During the 1990s, the LBM was generally preferred over the LSM because of its superior ability to capture complex fracture behaviour (Nikolić et al., 2018; Pan et al., 2018). However, after the seminal contribution by Schlangen & Garboczi, (1996), developments

License CC BY-NC-ND 4.0

within the LBM framework progressed more gradually, with key refinements including adaptive meshing strategies (Bolander et al., 1996), extension to three-dimensional analyses (Lilliu & van Mier, 2003), formulation of a generalised beam element (Liu et al., 2008), and application of the spectral element method (SEM) for modal analysis (Branko Savija & Erik Schlangen, 2015). In contrast, the LSM has gained increasing prominence and has undergone substantial advancement, particularly after the year 2000 (Pan et al., 2018).



a) Lattice beam model b) Lattice spring model

Figure I-37: Examples of lattice model to discretise a domain (Nikolić et al., 2018)

The LSM, derived from the rigid body spring approach of Kikuchi et al., (1992), represents a material by connecting discrete particles with spring elements. These springs act as cohesive links between rigid particles, as illustrated in Figure I-37b. Depending on the modelling needs, different combinations of spring types such as normal (Figure I-38a), shear (Figure I-38b), and rotational (Figure I-38c) (Wang et al., 2020) were employed. The simplest LSM employs only normal springs to transfer forces between particles, while more advanced versions incorporate all three spring components.

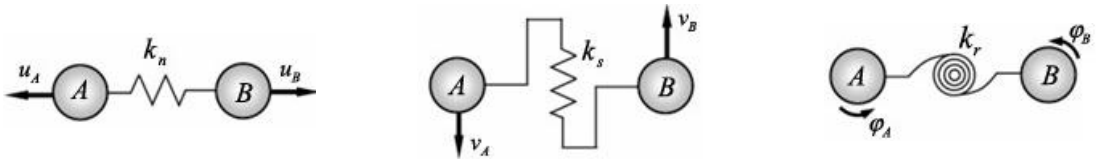

a) normal spring b) shear spring c) rotation spring

Figure I-38: Illustration of spring as a cohesive connector between two nodes (A and B) (Wang et al., 2020)

The simplicity of the LSM, combined with its ability to capture localized failure and cracking, has greatly contributed to its widespread use. In fracture simulations, crack initiation and propagation emerge naturally by removing bonds once stress, strain, or energy-based criteria are exceeded (Nikolić et al., 2018; Pan et al., 2018). The chosen spring rheology (which defines how nodes interact) strongly influences the predicted crack path and the mechanical behaviour (Wang et al., 2020). This is illustrated in Figure I-39, comparing experimental observations (Figure I-39a) with the WST simulations (Figure I-39b and c) of Wang and coworkers (Wang et al., 2020). Two numerical models were evaluated: Model 1 included normal, shear, and rotational spring components, whereas Model 2 excluded the rotational term. Consequently, Model 1 accurately reproduced the experimental crack trajectory, while Model 2 yielded an unrealistic failure pattern (Wang et al., 2020). This comparison underscores the LSM's capability to simulate crack development when an appropriate spring formulation is employed.

License CC BY-NC-ND 4.0

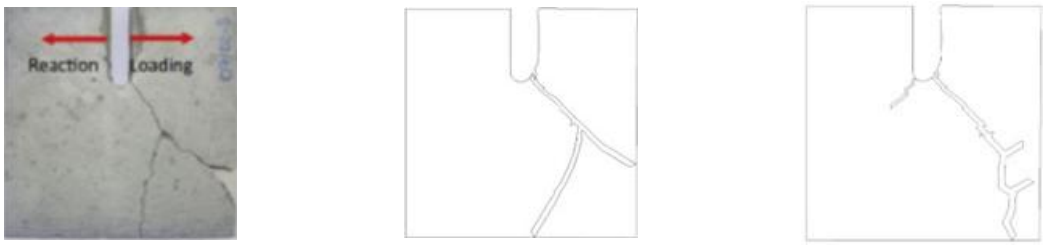

a) experimental b) with rotational spring c) without rotational spring

Figure I-39: Comparison of crack paths obtained in experimental and simulation approach (Wang et al., 2020)

A broad family of models, including the Confinement-Shear Lattice (CSL) model (Cusatis et al., 2003), Distinct Lattice Spring Model (DLSM) (Zhao et al., 2011), 3D Nonlocal LSM (Chen et al., 2016), and 4D-LSM (Fu & Zhao, 2022), falls under the general “LSM” designation and has been widely applied for multiscale analysis of brittle materials.

Cusatis et al., (2003) used the CSL model to study fracture propagation in multiphase materials such as concrete, as illustrated in Figure I-40a. In the CSL framework, lattice nodes coincide with aggregate centres (P1 and P2), and each node has five degrees of freedom (three translational and two rotational). Aggregates interact through designated contact zones, where shear behaviour is driven by nodal rotations and transverse displacements (Cusatis et al., 2003). Model inputs include geometric data (aggregate positions, granulometric distribution, lattice topology/area) and thirteen meso-level parameters governing elasticity, strength, hardening/softening, and fracture energy. This approach reproduces fracture behaviour under four-point bending, as shown by the good agreement between experimental and numerical load-displacement curves in Figure I-40b, which highlight crack initiation and propagation (Cusatis et al., 2003). Extending this concept, (Cusatis et al., 2008) introduced the Lattice Discrete Particle Model (LDPM), which retains key CSL features while incorporating long-range contact behaviour characteristic of DEM-based methods.

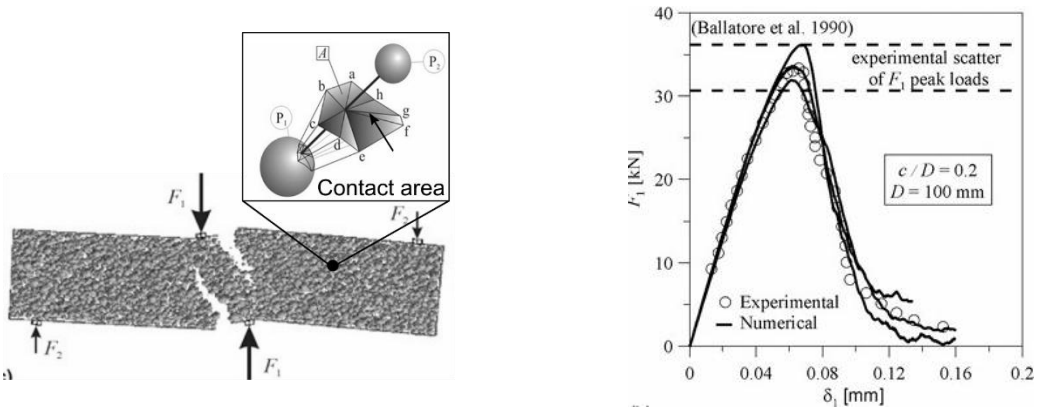

a) fracture of CSL model b) load-displacement curve

Figure I-40: Illustration of four-point bending using CSL approach (Cusatis et al., 2003)

Morrison and co-authors (Morrison et al., 2014, 2016) advanced microstructure informed lattice modelling of quasi-brittle material by employing a truncated octahedral site bond lattice enriched with experimentally derived pore statistics as shown in Figure I-41a. In their 2014 work, Morrison et al., (2014). demonstrated this behaviour using macroscopic stress-strain responses from uniaxial tensile tests (see Figure I-41b). They showed that increasing porosity leads to a transition from quasi-brittle behaviour to highly brittle, avalanche-type failure, accompanied by a significant reduction in fracture energy. This trend is consistent with ageing effects observed in reactor

License CC BY-NC-ND 4.0

graphite (Morrison et al., 2014). Despite these advances, the study reported limitations, including simplified failure assumptions, underprediction of strength, and incomplete representation of fine porosity, highlighting the need for further refinement of microstructural characterisation and bond-level mechanics (Morrison et al., 2014).

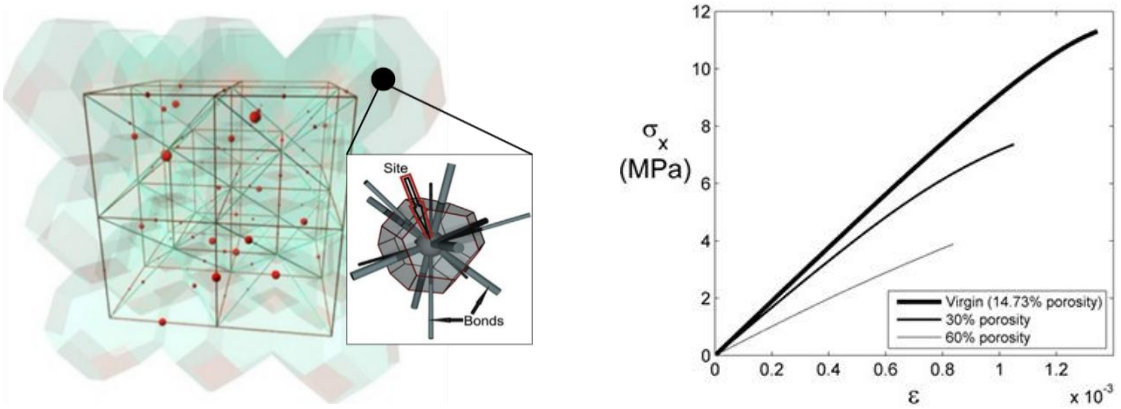

a) site-bond model representation with pores (Morrison et al., 2016)

b) stress-strain response vs pores vol. (Morrison et al., 2014)

Figure I-41: Illustration of the fracture of quasi-brittle material using site-model approach

In addition, DLSM (Zhao et al., 2011), Nonlocal LSM (Chen et al., 2016), and 4D-LSM (Fu & Zhao, 2022) are all extensions of the classical LSM, to simulate fracture via bond breakage. While DLSM achieves rotational invariance and variable Poisson's ratios using shear springs, stiffness recovery, and a least-squares strain calculation, making it efficient for large-scale dynamic simulations (Pan et al., 2018; Zhao et al., 2011), non-local LSM improves physical realism by including interactions with multiple neighbouring particles at the cost of higher computational effort (Chen et al., 2014; Pan et al., 2018). The 4D-LSM advances further by introducing a fourth-dimensional mapping, maintaining purely central interactions while covering a wide range of Poisson's ratios, preserving simplicity, robustness, and efficiency. Overall, 4D-LSM stands out by providing the most versatile and computationally efficient framework for heterogeneous, elastic deformation, dynamic fracturing (Fu & Zhao, 2022; Pan et al., 2018). The 4D-LSM approach is currently used in geomechanics to simulate rock fracture. It includes a spring stiffness recovery mechanism in which critical elements are temporarily removed and later reinstated with partially recovered stiffness when particle motions reduce their separation, as illustrated for mode-I in Figure I-42a (Fu & Zhao, 2022). The method also employs a least-squares formulation to compute local particle strains and supports large-scale parallel computation (Zhao et al., 2020). These capabilities enhance the flexibility of the approach and allow for the simulation of complex failure processes. Building on these structural and computational foundations, (Fu & Zhao, 2022) integrated a micro-macro constitutive framework into the 4D-LSM to reproduce the full nonlinear behaviour of rock under uniaxial and triaxial compression. Their approach captures key features such as crack closure, post-peak failure, and strain localization. For the uniaxial case, these mechanisms are illustrated in Figure I-42b. This was achieved by coupling micromechanical spring-bond descriptions with macroscopic failure criteria.

License CC BY-NC-ND 4.0

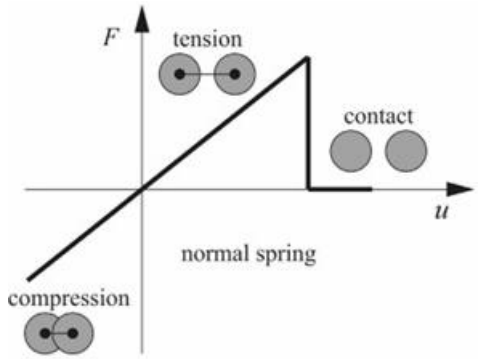

a) crack management under mode-I (Pan et al., 2018)

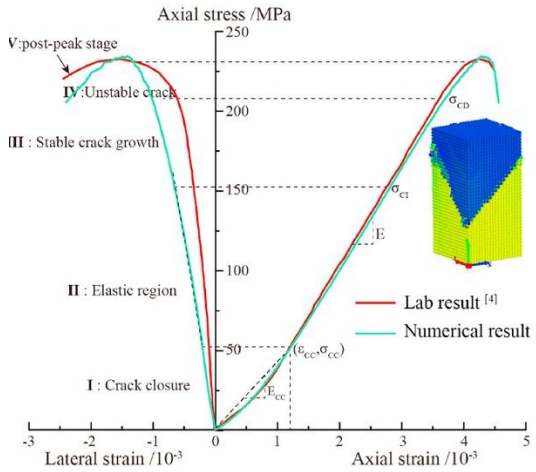

b) stress-strain response (Fu & Zhao, 2022)

Figure I-42: 4D-LSM Mode-I Failure Criterion and Uniaxial Compression test result

In addition, a key early contribution was made by Sridhar et al., (1994), who developed a two-dimensional microstructural mechanic's model to investigate anisotropic thermal expansion induced microcracking in polycrystalline materials. As shown in Figure I-43a, their polycrystalline microstructure (generated using a Monte Carlo procedure (Bauer, 1958) was mapped onto a triangular lattice of brittle elastic springs. In the present study, the same polycrystalline model is adopted with three different grain sizes to examine the influence of grain size on microcrack development. The models were subjected to incremental misfit strains to mimic thermal contraction, and fracture was tracked by irreversibly breaking bonds whose strain energy exceeded a prescribed critical value (Sridhar et al., 1994). As illustrated in Figure I-43b, the results demonstrate that larger grains initiate microcracks at lower misfit strains and tend to form longer cracks, whereas smaller grains develop higher crack densities but only at higher misfit strains; in both cases, weak grain boundaries and mechanical constraints intensify fracture evolution. Although this approach successfully captured key qualitative trends, its restriction to two dimensions, simplified anisotropy, and discrete lattice representation limited its quantitative predictive accuracy (Sridhar et al., 1994).

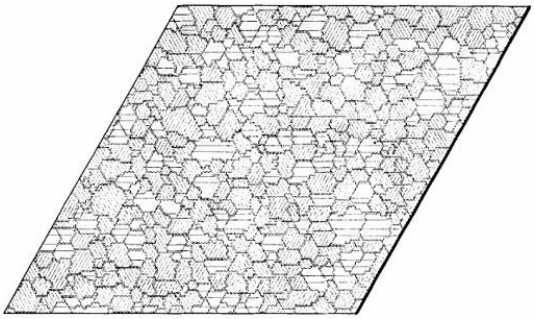

a) Polycrystalline LSM

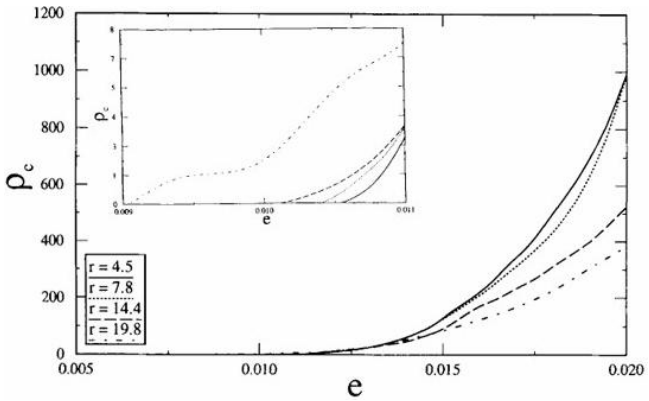

b) crack density vs strain misfit

Figure I-43: Illustration of modelling thermal induced microcrack using LSM approach (Sridhar et al., 1994)

Despite advances in LSM-based approaches, lattice modelling remains limited in microstructure-based investigations of thermal and thermomechanical behavior. While the 4D-LSM overcomes the Poisson's ratio limitation (Fu & Zhao, 2022; Wei et al., 2024; Zhao et al., 2020), its reliance on idealized lattices restricts explicit representation of critical microstructural features such as

License CC BY-NC-ND 4.0

anisotropic thermal expansion, temperature-dependent damage, grain orientation, and pore connectivity (Pan et al., 2018). Future developments should integrate high-resolution microstructural imaging with multiscale lattice formulations to capture these features more accurately. Incorporating adaptive strategies within the 4D-LSM remains an open challenge, though recent extensions indicate its potential to model plastic fracture in metals, further broadening its applicability (Wei et al., 2024). Moreover, not much studies performed to investigate refractories microstructure-property relationship.

I.4.4. Discrete Element Method

Cundall and Strack (Cundall & Strack, 1979) laid the foundation for the Discrete (or Distinct) Element Method (DEM), which is widely used to study granular systems whose behavior cannot be fully described by continuum theories or analytical models (for instance, particle packing or granular flow through an hourglass). In DEM, the material is represented as an assembly of rigid particles (often represented as disks, spheres, or clumped shapes), referred to as discrete elements (Pöschel & Schwager, 2005). For example, Figure 16a illustrates the spherical Discrete Element (DE) and is represented as “DE-1” and “DE-2”. Each DE’s motion is governed by Newton’s second law, with interaction forces continuously updated according to specified force-displacement laws (Pöschel & Schwager, 2005). The simplest interaction is often modelled using a linear spring (Figure I-44), which can be used as contact laws and to capture more complex processes, advance and complex rheology is employed (Pöschel & Schwager, 2005). While DEM has been extensively applied to rocks (Li et al., 2017), soils (Taghizadeh et al., 2017), concrete (Nitka & Tejchman, 2020), and other granular materials (Asadi, André, Emam, Doumalin, & Huger, 2022; Pöschel & Schwager, 2005), its application to ordinary refractory ceramics remains limited in literature.

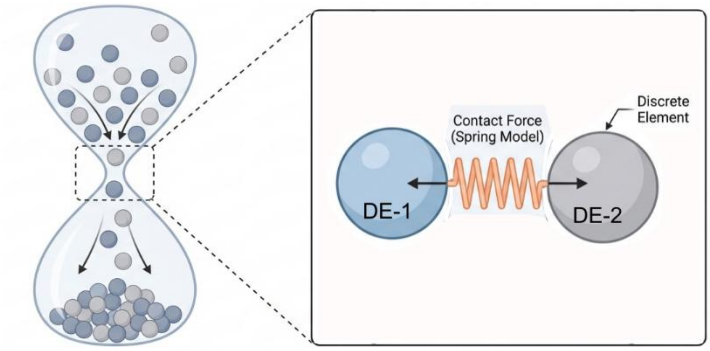

Figure I-44: Snapshot of an hourglass flow simulation, with interaction pair using linear spring model (From Pöschel & Schwager, 2005)

The DEM numerical procedure is an iterative process that repeatedly executes a sequence of operations, as illustrated in Figure I-45. An appropriate time step Δt is first selected, since a value that is too large may cause numerical instability, while an excessively small value increases computational cost (Pöschel & Schwager, 2005); for a linear spring contact, stability requires Δt to be a fraction of the contact natural period. Newton’s second law is then applied to compute translational and rotational accelerations from the forces and moments acting on each particle, and these accelerations are integrated to update particle velocities and positions (Pöschel & Schwager, 2005; Potyondy & Cundall, 2004). The simulation time is subsequently advanced by Δt. Contact detection is performed using an efficient broad-phase search to identify nearby particle pairs (employing spatial subdivision methods such as linked cells, trees, or neighbour lists) followed by a narrow-phase check to confirm actual contacts (Pöschel & Schwager, 2005). For confirmed contacts, forces and moments are computed using the selected force-displacement contact laws (Potyondy & Cundall, 2004). This sequence is repeated until a predefined stopping criterion is

License CC BY-NC-ND 4.0

satisfied, such as reaching a target simulation time, a fixed number of cycles, or a user-defined mechanical condition (Pöschel & Schwager, 2005; Potyondy & Cundall, 2004).

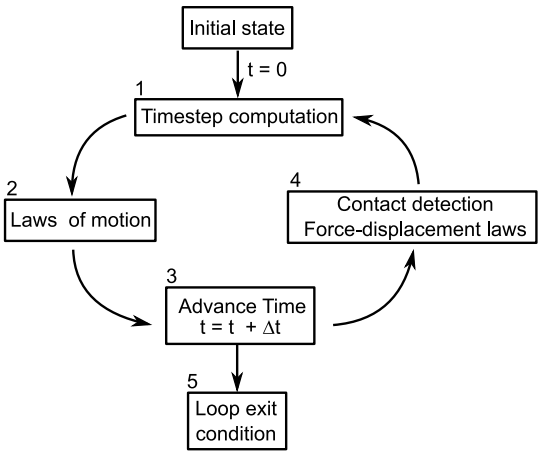

Figure I-45: Illustration of numerical procedure for the DEM approach

The literature review shows that the DEM has rapidly evolved for modelling crack initiation and propagation in brittle materials (André & Celigueta, 2023; Longchamp et al., 2024; Mariotti et al., 2009; Nitka & Tejchman, 2020; Ranganathan et al., 2026). Within this context, the Bonded Particle Element Method (BPEM) has emerged as a widely used approach, in which spherical discrete elements are connected through mechanically enriched interaction laws (André et al., 2019; Asadi, 2021; Longchamp et al., 2024; Nguyen, 2019; Potyondy & Cundall, 2004; Ranganathan et al., 2025). BPEM can be viewed as a combination of lattice modelling and DEM: particle centres are linked by lattice-like bonds (Pan et al., 2018) that transmit forces and moments and can fail (Longchamp et al., 2024). Unlike classical lattice models (Pan et al., 2018), BPEM employs volumetric particles instead of non-volumetric nodes, enabling contact interactions, and unlike classical DEM (Cundall, 1988), it incorporates an internal lattice-like bond network. As a result, BPEM effectively integrates the strengths of both lattice modelling and DEM (Alhajj Hassan et al., 2020; Asadi, André, Emam, Doumalin, & Huger, 2022; Jebahi et al., 2015; Leclerc et al., 2018; Longchamp et al., 2024).

Notably, DEs connected by flat-joint bonds (Asadi, André, Emam, Doumalin, Khlifi, et al., 2022) (see Figure I-46a) were introduced to overcome the limitations of classical parallel bonds (a pair of normal and tangential bonds (Potyondy & Cundall, 2004)), particularly their unrealistic compressive-to-tensile strength ratio in geomaterials (Potyondy, 2011). DEs connected by cohesive beam bonds (see Figure I-46b) were provided as continuum-consistent stiffness, realistic mixed-mode fracture behaviour, and improved representation of rotations and size effects (André et al., 2012, 2017; Longchamp et al., 2024). These bonds, governed by force-displacement laws, are designed to reproduce the macroscopic mechanical behaviour of the material, while bond-level failure criteria enable the simulation of crack initiation, growth, and coalescence (André et al., 2017; Longchamp et al., 2024). Thanks to these capabilities, flat-joint (Asadi et al., 2023) and cohesive beam based BPEM (André et al., 2012) frameworks have been extensively applied to investigate microstructure property relationships and quantify how microstructural features influence the apparent mechanical response of brittle materials (Asadi, 2021; Longchamp et al., 2024; Nguyen, 2019).

License CC BY-NC-ND 4.0



a) Flat-joint (Asadi, 2021) b) Cohesive beam (André et al., 2012)

Figure I-46: Illustration of the popular BPEM contact models

The recent study by Longchamp et al., (2024) provides a compelling demonstration of BPEM based approaches. The authors conducted a 3D micromechanical analysis of plasma sprayed yttria-stabilized zirconia (YSZ) coatings. High resolution FIB-SEM tomography was used to reconstruct in 3D the actual coating microstructure, enabling explicit representation of pores, microcracks, and spatially varying crack thicknesses (Figure I-47a). The reconstructed microstructure was discretized into spherical discrete elements linked by cohesive beams, while preexisting cracks were modelled via the so-called contact beams, transmitting only compressive forces (Figure I-47a). Using the macroscopic elastic properties of the dense ceramic and the extracted microstructural data, the model simulated quasi-static tensile, compressive, triaxial, and cyclic tests to predict macroscopic responses, including stress-strain behavior, crack closure (represented by the contact beams), and damage accumulation. Figure I-47b illustrates the cyclic-loading response, showing key experimentally observed features: tension compression asymmetry driven by progressive crack closure, stiffness degradation from pore crack interactions, and anisotropy induced by preferential crack orientations. The evolution of pre-existing cracks further captures the associated reduction in effective stiffness and mechanical integrity.

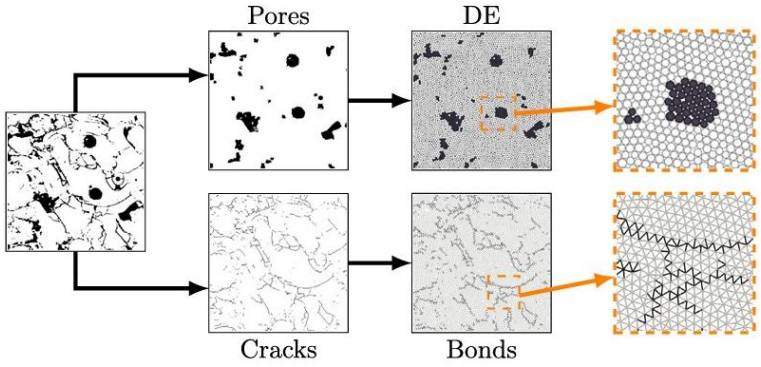

a) microstructure discretisation

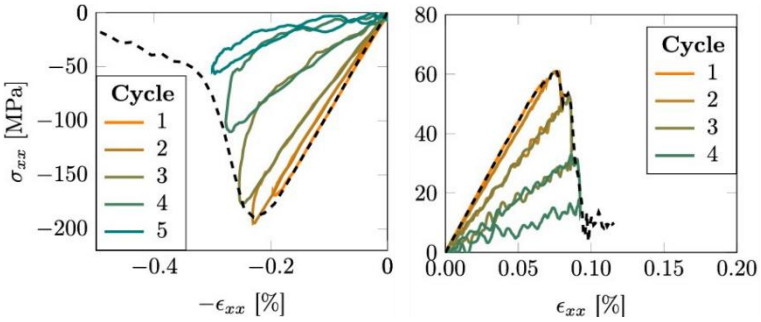

b) stress-strain response under compressive and tensile cyclic loading

Figure I-47: Microstructure digitization and apparent stress-strain curve under cyclic loading (Longchamp et al., 2024)

Similar to Longchamp et al., (2024), several studies have incorporated microstructural cracks and weak links (Du et al., 2024; Du & Jin, 2022; Zhou, 2021), often assigned using stochastic approach such as Weibull-type statistical distributions (Asadi, 2021), to evaluate their effect on the apparent

License CC BY-NC-ND 4.0

mechanical response (Asadi, 2021; Nguyen, 2019). Other works (Alhajj Hassan et al., 2020; André et al., 2017; Leclerc et al., 2018; Li et al., 2017; Nosewicz et al., 2020; Ranganathan et al., 2025) explicitly model crack opening, closure and friction through the introduction of crack surface contact, which is not considered in Longchamp et al., (2024) model. Finally, even when accounting for cracks induced by thermal stresses during sintering in the work of Longchamp et al., (2024) and Asadi, (2021), these models were unable to reproduce the irreversible strains observed experimentally.

Thermal and thermomechanical DEM studies can be grouped based on their modelling focus and microstructural complexity. The first cluster, including (Alhajj Hassan et al., 2020; André et al., 2017; Asadi, 2021; Leclerc et al., 2018; Nguyen, 2019; Nosewicz et al., 2020) focuses on thermal expansion mismatch in composite microstructures (Figure I-48a) using BPEM contact laws. These studies share micromechanical objectives such as evaluating thermal stress distributions (Nosewicz et al., 2020) (Figure I-48b), predicting temperature-induced cracking (Alhajj Hassan et al., 2020; André et al., 2017; Ma et al., 2023; Sinaie et al., 2016) (Figure I-48c), and estimating effective thermoelastic properties, including stress-strain response (Asadi, 2021; Nguyen, 2019) and Young's modulus (Asadi, 2021; Nguyen, 2019) (Figure I-48d). They differ primarily in dimensionality (2D vs. 3D) and microstructural representation (single inclusions, multi-inclusions, or fibre-reinforced composites). In contrast, Rangel et al., (2024) represents a distinct category, embedding thermal expansion effects within a multiscale, data-driven DEM continuum framework that enables the prediction of both microstructure evolution and homogenized thermomechanical responses.

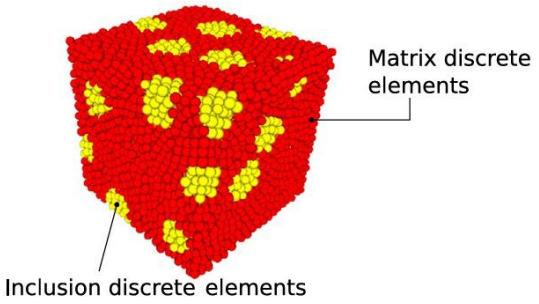

a) two constituent sample (Nguyen, 2019)

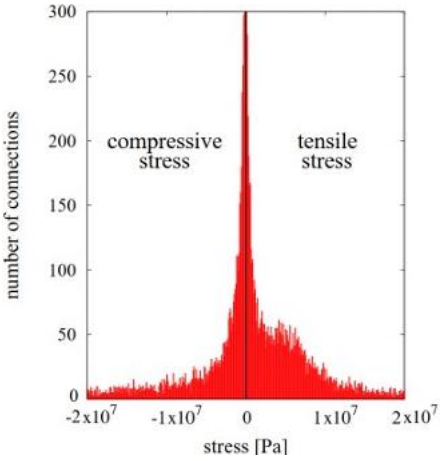

b) thermal stress distribution (Nosewicz et al., 2020)

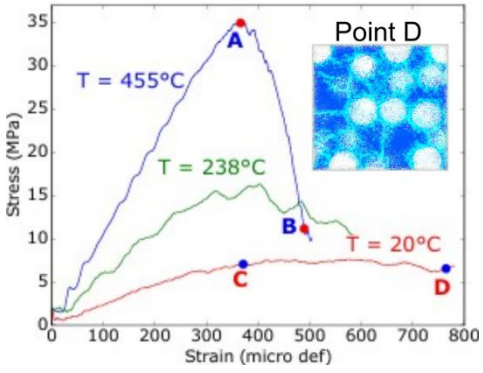

c) stress-strain curve vs temperature (Nguyen, 2019)

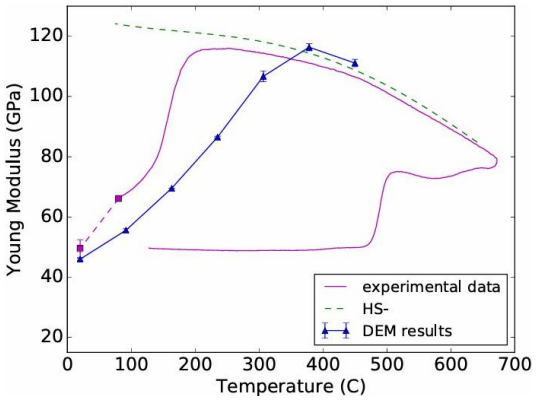

d) Youngs modulus vs temperature (Nguyen, 2019)

Figure I-48: Overview of the models and obtained results from different thermomechanical studies

License CC BY-NC-ND 4.0

Despite advances in calibration strategies (Coetzee & Katterfeld, 2023), such as direct methods accounting for the coupling between microstructural and structural parameters (Nguyen, 2019), the integration of advanced crack management mechanisms (multiple crack opening/closure, shearing, friction) (Asadi, 2021; Longchamp et al., 2024; Nguyen, 2019) and thermomechanical frameworks for CTE mismatch (André et al., 2017), BPEM models remain limited to small scale problems and require labour intensive calibration. This limitation arises because conventional DEM interaction laws are expressed in force-displacement terms rather than stress-strain relationships, making continuum equivalent behaviour challenging. To overcome this, André et al., (2019) proposed the improved Distinct Lattice Spring Model (iDLSM), originally developed by Zhao et al., (2011) for elasticity and brittle dynamic failure. iDLSM inherently reduce calibration needs because their rheological parameters can be analytically related to continuum material properties (André et al., 2019; André & Celigueta, 2023); however, classical LSMs cannot reproduce arbitrary Poisson's ratios, which depend on lattice topology rather than bond stiffness (Pan et al., 2018). iDLSM addresses this by computing Cauchy strain tensors from neighbouring particle displacements using a least squares method, enabling direct use of continuum stress-strain laws and eliminating the Poisson's ratio limitation (André et al., 2019; André & Celigueta, 2023). While the non-local strain averaging can induce numerical instabilities, especially at high Poisson's ratios, these can be fixed by introducing a numerical damping in the explicit integration time scheme (Mahéo et al., 2009). As a result, iDLSM provides a calibration free, continuum compatible framework. Indeed, it is less suited for dynamics dominated problems like high velocity impact fragmentation due to the introduction of the numerical damping stabilization (André et al., 2019; Ranganathan et al., 2025).

André & Celigueta, (2023) employed the iDLSM approach to enable the direct use of continuum stress-strain laws from FEM codes within a DEM framework, removing the calibration procedures typically required in bonded-particle models. The method couples the GranOO DEM solver with an FEM solver (Kratos Multiphysics), using its constitutive laws as interaction laws for the bonds. GranOO computes the local strain tensor for each bond and passes it to the FEM solver, which returns the corresponding stress tensor taking into account the constitutive laws; these stresses are then converted into bond level reaction forces, allowing DEM behaviour to follow established continuum constitutive relations. In the iDLSM framework, the domain is discretized into polyhedral elements via Voronoi tessellation (with bonds defined through the dual Delaunay triangulation) (see Figure I-49a) (André & Celigueta, 2023). Using standard continuum parameters, such as Young's modulus, Poisson's ratio, density, yield strength, and fracture energy, the model reproduces a wide range of mechanical behaviours, including orthotropic elasticity, plasticity, and quasi-brittle damage. As a result, the macroscopic response closely matches the prescribed constitutive inputs, capturing elastic properties (Figure I-49a), plastic localization patterns (Figure I-49a), tensile strength (Figure I-49b), and the softening behaviour associated with damage evolution (Figure I-49b).

License CC BY-NC-ND 4.0

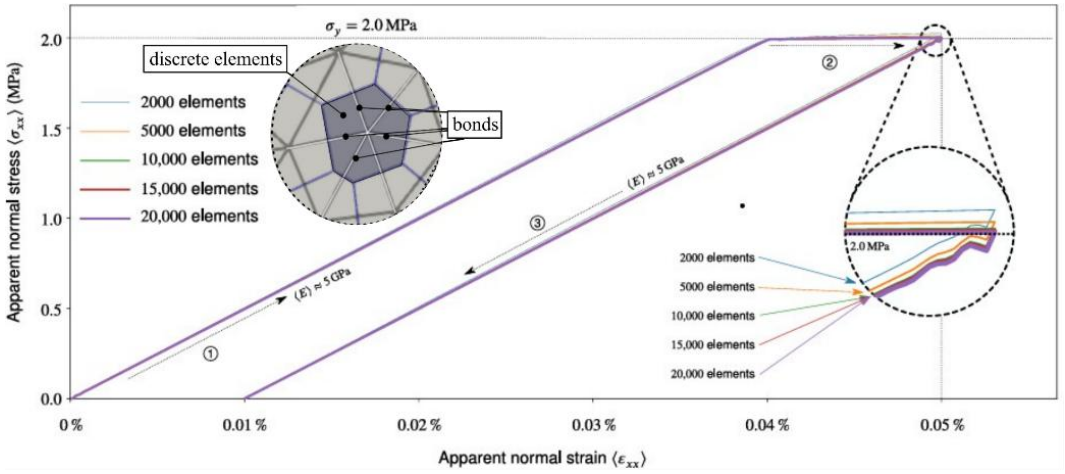

a) plastic strain recording (André & Celigueta, 2023)

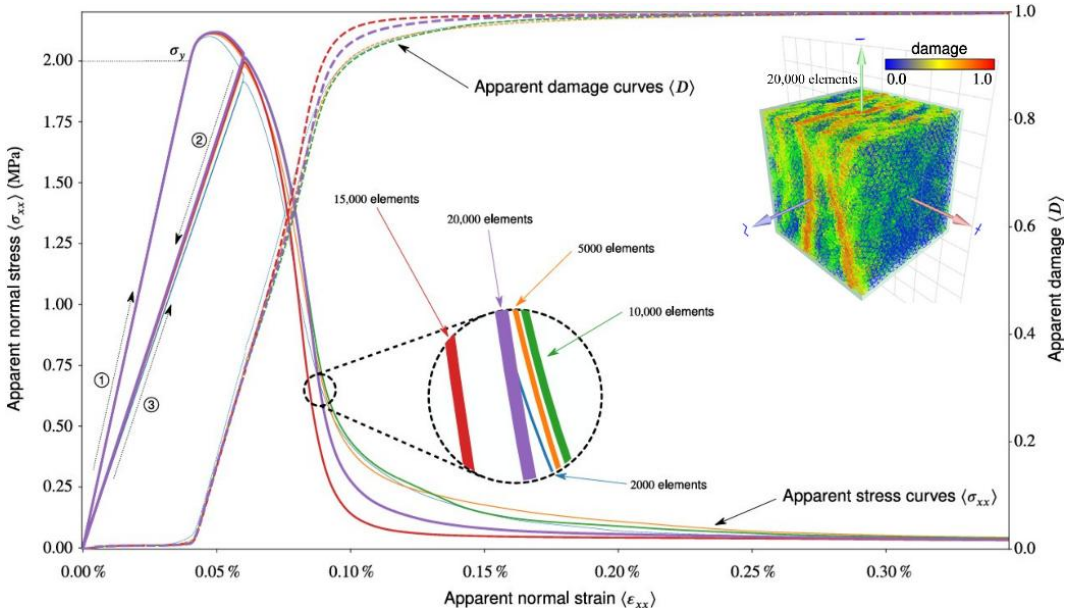

b) stress-strain-response and damage evolution (André & Celigueta, 2023)

Figure I-49: Illustration of stress-strain response of the hypothetical sample under uniaxial loading

With these advantages, the iDLSM approach could be extended to investigate the microstructural thermomechanical properties of refractory materials, an application that has not yet been explored.

I.5. Appropriate numerical approach for refractory materials

The purpose of this section is to highlight the numerical approaches that are the best suited to represent the multiscale fracture mechanisms governing the macroscopic response of refractory materials. From section I.2, it is evident that refractory materials are prone to spontaneous microcracking and consequently display a highly non-linear macroscopic mechanical response. This overall non-linearity arises directly from damage and microcrack evolution at the microstructural scale. Therefore, the objective of this work is to identify numerical strategies capable of reproducing the macroscopic behaviour of refractories as an emergent consequence of their underlying heterogeneous microstructure.

With this motivation, section I.3 and I.4 examined suitable numerical techniques for modelling crack initiation and propagation while capturing key characteristics of refractories, such as thermal-expansion mismatch, thermally induced stresses, progressive microcracking, and the resulting

License CC BY-NC-ND 4.0

non-linear mechanical response. Each candidate method was assessed against six essential criteria required for accurately modelling refractory behaviour, as summarised in Table I-2.

Table I-2: A comparison between various numerical methods to model quasi-brittle material

Criteria	Continuum				Continuum/particle		Particle	
	FEM							
	CZM	XFEM	PFM	BEM	MPM	PD	LM	DEM
Heterogeneous microstructure design	-	-	=	-	=	=	+	+
Multiple discontinuity	+	+	+	=	=	+	=	+
Crack opening	+	=	+	=	+	+	+	+
Crack closing	+	=	-	-	=	-	+	+
Homogenisation	=	-	=	=	=	=	=	=
CTE mismatch	+	-	+	=	=	+	-	+
Efficiency	-	=	-	=	-	-	-	-

-: less preferable, =: preferable and +: most preferable

Table I-2 clearly indicates that Peridynamics and DEM are the two approaches most suitable for modelling refractory materials, outperforming the other considered methods. However, there lies a slight difference in their suitable operation in different modelling regimes and reflect distinct physical philosophies.

As discussed in section I.4.2, Peridynamics following a nonlocal continuum theory, particularly powerful for simulating thermal shock, complex fracture networks, and the interaction between microcracking and the overall continuum response. Its formulation also facilitates coupling with thermal and thermo-mechanical fields, which is essential when representing CTE mismatch, distributed thermal stresses, and the emergent nonlinear behaviour of monolithic refractories (Javili et al., 2019).

DEM (see section I.4.4), in contrast, is inherently particle-based and is most effective when the refractory behaves as, or is intentionally idealised as, an assembly of grains, aggregates, blocks. It excels in scenarios dominated by contact mechanics and discontinuities. DEM is also more mature from an industrial standpoint; with the emergent of advance contact models such as iDLSM, it can represent a continuum-equivalent solid without extensive calibration, further broadening its applicability (André et al., 2019; André & Celigueta, 2023).

I.6. Scope and Objectives of the present study

The present PhD aims to advance the understanding and design of refractory materials by investigating the role of anisotropic CTE in promoting controlled microcracks within the microstructure. Specifically, the objectives of this study are to:

- understand the impact of anisotropic CTE in promoting microcrack formation at the microstructural scale.
- investigate the effect of embedding aggregates with anisotropic CTE on the sustainability and performance of composite refractory systems example in alumina-spinel castable under high-temperature and thermal shock conditions.

To achieve these goals, some numerical developments have to be provided in order to:

- develop a DEM tool that acts as a virtual laboratory to investigate microstructure-property relationships. This tool will enable virtual performance evaluation of industrial

License CC BY-NC-ND 4.0

characterizations, including acoustic emission monitoring, micromechanical analysis during cooling, dilatometry, Young's modulus measurements, stress-strain tests, and cyclic loading.

- provide an efficient and cost-effective framework for optimizing refractory microstructure design, reducing the time and resources required for experimental investigations.

This approach is expected to significantly improve the design and performance of refractory materials, providing new insights into microstructure-engineering strategies that enhance sustainability of the microstructure design by improving its fracture toughness.

License CC BY-NC-ND 4.0

Chapter II. About Distinct Lattice Spring Method and its enhancement

II.1. Overview on improved Distinct Lattice Spring Method

The aim of the Distinct Lattice Spring Model (DSLM) is to enable the usage of continuum mechanics mathematical concepts such as stress and strain Cauchy tensors into a discrete modeling framework. This allows the usage of stress strain (behavior) laws directly into the DEM modeling (André et al., 2019) which is one of the most significant challenges within the DEM community that applies DEM for studying the mechanics of brittle materials such as rocks (Li et al., 2017), ceramics (Asadi, André, Emam, Doumalin, & Huger, 2022) or concretes (Nitka & Tejchman, 2020). This chapter introduces this advanced interaction model, the improved Distinct Lattice Spring Model (iDLSM), proposed by. Andre and coworkers (André et al., 2019; André & Celigueta, 2023) to simulate brittle elastic materials without a calibration process.

As outlined in the introduction, the iDLSM is classified as a BPEM-based method within the DEM framework (André & Celigueta, 2023). It is specifically designed to model the mechanical behavior of cohesive bulk materials in a continuum-equivalent manner (André et al., 2019). Unlike traditional BPEM methods that use spherical discrete elements (Asadi et al., 2023; Longchamp et al., 2024; Nguyen et al., 2014), the iDLSM employs polyhedral discrete elements (Ranganathan et al., 2025, 2026), following the approach of Mariotti et al., (2009), to construct a continuum-like domain without voids using Voronoi tessellation (Du et al., 1999). The key main steps in sample generation are presented in the section II.1.1.

In addition to this unusual geometrical representation involving polyhedral, the iDLSM considers not only the interaction between the two bonded discrete elements but also the influence of their direct discrete elements neighbours for computing the reaction forces (André & Celigueta, 2023), similar to the work of Celigueta et al., (2017). A key improvement in the model is the way it represents the strain. Taking inspiration from the study of Zhao and his coworkers (Zhao et al., 2011), André et al., (2019) represent strain using Cauchy's strain tensors, which are obtained through least square regressions based on the displacement of surrounding elements. These strain tensors are expressed in the local frame of each DE, with the normal strain component set equal to the engineering strain directly obtained from the relative displacement of the two bonded elements. As a result, the interactions between bonded polyhedral discrete elements can be directly expressed using stress-strain relationships (André et al., 2019; André & Celigueta, 2023).

The proposed model naturally accommodates standard mechanical material parameters, namely Young's modulus (E) and Poisson's ratio (ν), in alignment with their use in established stress-strain constitutive frameworks and numerical engineering tools. This integration alleviates the reliance on the cumbersome calibration processes often encountered in BPEM, while simultaneously strengthening the framework's capacity to employ continuum mechanical theory (André & Celigueta, 2023). Finally, the iDLSM approach compute's reaction forces based on the stress by taking into account the contact surface between the 2 bonded discrete elements. Moreover, the main steps involved in reaction force calculation are explained in section II.1.2.

In contrast to the standard DLSM introduced by Zhao et al., (2011), the iDLSM also can account for the local orientation and rotation of the discrete elements (André et al., 2019). This is done using quaternions, similar to the method used by Christian et al., (2015) These local rotations allow the calculation and transmission of torques, enabling the model to incorporate rotational rigidity. This

License CC BY-NC-ND 4.0

makes the iDLSM more capable of handling non-regular geometries and to deal with large rotational rigid body displacements.

Lastly, the iDLSM employs an explicit integration scheme. The velocity Verlet algorithm is chosen for its efficiency and simplicity. However, the model encounters instabilities after several thousand iteration steps. High-frequency vibrations gradually build up, eventually causing the simulation to diverge. A small numerical damping factor is added to the integration scheme to address this issue, following the decentered explicit method proposed by Mahéo et al., (2009). This approach enables the dissipation of high-frequency vibrations, thereby enhancing the stability of the simulation. Dissipation is regulated through a single parameter, φ. with modifications applied exclusively to the second time-derivative equation (André et al., 2019). This leads to the following Velocity Verlet expression:

$$\dot{\vec{\boldsymbol{p}}}(t + \Delta t) = \dot{\vec{\boldsymbol{p}}}(t) + \varphi \Delta t \, (\ddot{\vec{\boldsymbol{p}}}(t) + \ddot{\vec{\boldsymbol{p}}}(t + \Delta t)) \qquad \text{II-1}$$

where $\vec{\boldsymbol{p}}$ is the position vector, t is the time variable and Δt is the time step. The same approach is applied to quaternions:

$$\dot{\boldsymbol{q}}(t + \Delta t) = \dot{\boldsymbol{q}}(t) + \varphi \Delta t \, (\ddot{\boldsymbol{q}}(t) + \ddot{\boldsymbol{q}}(t + \Delta t)) \qquad \text{II-2}$$

where $\boldsymbol{q}$ is related to a quaternion. Value of φ higher than 1 contributes to a stable simulation. The value between [1 - 1.3] is a stable range for φ. Now, having all the highlighting information's about iDLSM model (André et al., 2019; André & Celigueta, 2023), the next step is to understand the process of generating the polyhedral samples and the additional enhancements developed, to simulate brittle elastic materials.

II.1.1. Generation of iDLSM numerical sample

The procedure followed to generate the samples is depicted in two dimensions in Figure II-1a, b and c (the two-dimensional views are provided only as pedagogical illustrations). In addition, the corresponding 3D view of each step for sample generation is illustrated in Figure II-1d, e and f.

The generation of a random yet well-controlled sphere arrangement begins with a packing procedure based on the Cooker algorithm, as implemented in the open-source discrete element code GranOO (André et al., 2015). The resulting sphere centers are then extracted and used as scattered points, often referred to as germs, for constructing the Voronoi tessellation (Du et al., 1999). During this process, spherical discrete elements with radii selected from a prescribed size range are inserted into a confining domain, as illustrated in Figure II-1a (the corresponding 3D view is depicted in Figure II-1d). The filling process goes on as long as some free place is found to add a new spherical discrete element (Ranganathan et al., 2025). Indeed, the packing process is controlled by a targeted coordination number and ensures an acceptable level of contact isotropy by ensuring non regular arrangement thanks to adequate random picking of sphere radii. For more information about the packing algorithms, the readers can refer to the reference (Jebahi et al., 2015).

The centers of the spherical discrete elements are subsequently taken as seed points (input germs) for constructing the Voronoi tessellation producing polyhedral elements (Ranganathan et al., 2025) as shown in Figure II-1b (the corresponding 3D view is depicted in Figure II-1e that perfectly fill the boundary volume without voids. The Voro++ library is used to implement these tessellations (Rycroft, 2009). The Voro++ library was chosen as it could deal with many surface boundaries

License CC BY-NC-ND 4.0

(such as boxes, cylinders, or spheres). In the current study, a (3D) numerical sample is a cubical box, as shown in Figure II-1e.

In the final step, bonds are established between the polyhedral discrete elements, shown as white lines in Figure II-1c. These connections are created using a Delaunay tessellation (Ranganathan et al., 2025), which systematically detects neighboring polyhedral element that share a common contact face (see Figure II-2). Once these pairs are identified, bonds are formed between their centroids to represent the interactions. For a detailed description of the method used to generate polyhedral discrete elements, as well as the numerical libraries applied for tessellation in constructing iDLSM domains, refer to (André et al., 2019).

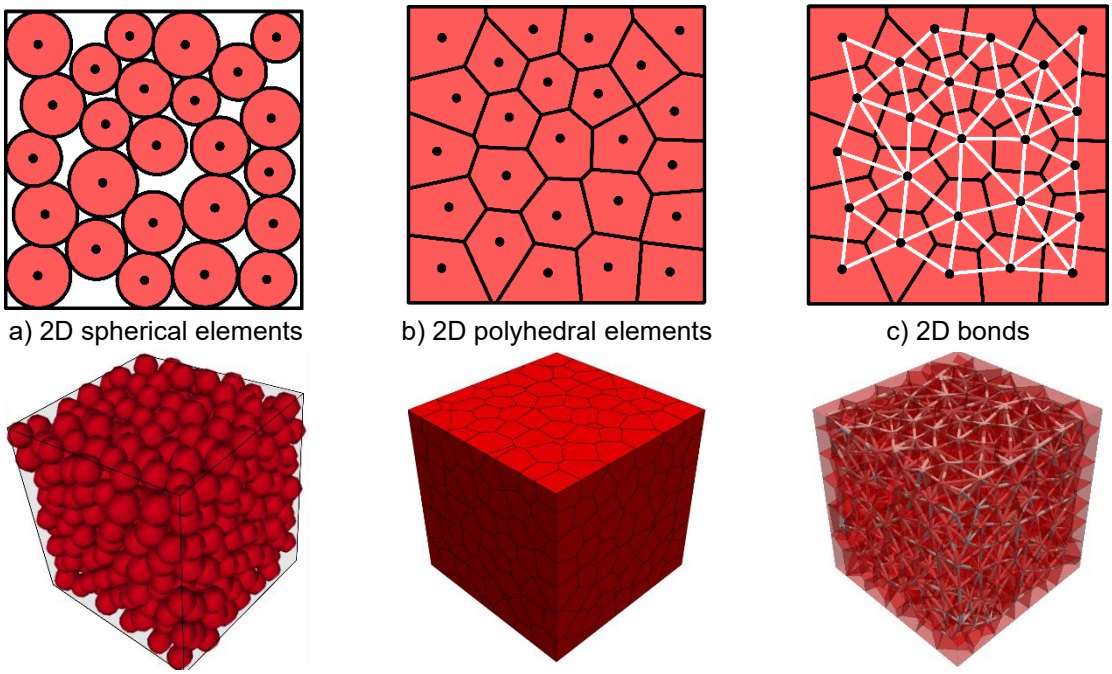

a) 2D spherical elements b) 2D polyhedral elements c) 2D bonds

d) 3D spherical elements e) 3D polyhedral elements f) 3D bonds

Figure II-1: Illustration of iDLSM sample generation (Ranganathan et al., 2025)

II.1.2. Main steps in computing the reaction forces in iDLSM approach

Therefore, iDLSM distinguishes itself from other BPEM-based DEM methods through a key difference in how reaction forces between discrete elements are determined (André et al., 2019; André & Celigueta, 2023). In conventional BPEM techniques, these forces are obtained directly from the relative displacements between bonded elements. By contrast, iDLSM calculates reaction forces using the strains within the bonded elements, while also incorporating effects from their immediate neighboring elements (Ranganathan et al., 2025). A, brief overview of the key steps adopted to compute the reaction forces are explained using the 2D schematic sketch in Figure II-2. Consider a polyhedral DE i in contact with n DEs $j_1, j_2, j_3 \ldots, j_n$ by the contact surface represented by S_{ij_k} (where $k = 1, 2, .., n$). The point O_i and O_{j_k} are the geometric centroids of the polyhedral DEs i and j_k. Within the iDLSM framework, computation of bond ij_k (where $k = 1, 2, .., n$) reaction forces involve seven steps as described below:

1. For each discrete element (i), a continuum displacement field $\vec{d}_k(x, y, z)$[1] is derived by taking into account the displacements of its neighboring elements. In this process, Voigt's

[1] (x, y, z) = local coordinates

License CC BY-NC-ND 4.0

assumption is employed, which approximates the displacement field as linear between the central discrete element i and its n surrounding neighbours (j_1, j_2, ..., j_n). This assumption results in three vectorial unknowns for determining the local displacement field. Since there are typically more equations than unknowns, the iDLSM estimate $\vec{d}_k(x,y,z)$ (André & Celigueta, 2023; Ranganathan et al., 2025) by employing the least squares method;

2. By applying the gradient operator to $\vec{d}_k(x,y,z)$, a Cauchy strain tensor $\bar{\bar{\varepsilon}}_i$ is computed for each discrete element. The Voigt's hypothesis (linear displacement field) results in a constant strain tensor $\bar{\bar{\varepsilon}}_i$. This strain tensor is expressed at the centroid O_i of element (i) (André & Celigueta, 2023; Ranganathan et al., 2025);
3. Each bond ij is assigned a strain tensor $\bar{\bar{\varepsilon}}_{ij}$ derived as the mean of the strain tensors of the two bonded discrete elements i and j using a straightforward formula: $\bar{\bar{\varepsilon}}_{ij} = \frac{1}{2}(\bar{\bar{\varepsilon}}_i + \bar{\bar{\varepsilon}}_j)$ (André & Celigueta, 2023; Ranganathan et al., 2025);
4. The first diagonal strain component (oriented along the ij bond direction) is directly determined from the relative displacements of the i and j discrete elements. Since this measure does not involves averaging as it is direct, one of the three diagonals $\bar{\bar{\varepsilon}}_{ij}$ components are replaced by this strain measurement. Moreover, the relative displacements contribute directly perpendicular to the ij bond direction is incorporated into the off-diagonal (shear) components of $\bar{\bar{\varepsilon}}_{ij}$ (André & Celigueta, 2023; Ranganathan et al., 2025);
5. A Cauchy stress tensor $\bar{\bar{\sigma}}_{ij}$ is computed for each bond from $\bar{\bar{\varepsilon}}_{ij}$ by applying a constitutive stress-strain relationship appropriate for solid continuum materials, specifically employing Hooke's law for isotropic elastic behavior (André & Celigueta, 2023; Ranganathan et al., 2025). Note that more complicated constitutive law can used (Sadd, 2019);
6. Using the direction $\vec{n}_{ij}$ of the ij bond, the stress vector related to the contact surface S_{ij} is computed as: $\vec{\Sigma}_{ij} = \bar{\bar{\sigma}}_{ij} \cdot \vec{n}_{ij}$ (André & Celigueta, 2023; Ranganathan et al., 2025);
7. Given the contact surface area S_{ij} between DEs i and j, the reaction force $\vec{f}_{ij}$ is computed as: $\vec{f}_{ij} = S_{ij} \cdot \vec{\Sigma}_{ij}$ (André & Celigueta, 2023; Ranganathan et al., 2025).

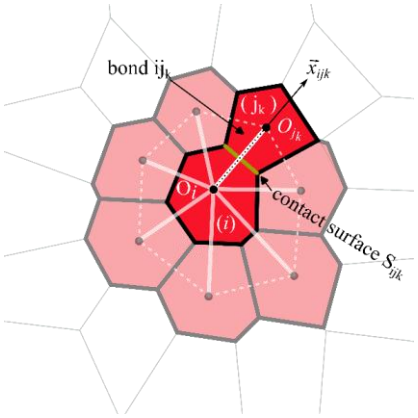

Figure II-2: illustration of basic iDLSM problem in 2D (Ranganathan et al., 2025)

Thanks to these steps, the iDLSM is able to compute a reaction force of each iDLSM bond based on the constitutive stress strain law of the modeled material (André et al., 2019). This feature remains the main interest of this discrete model.

II.1.3. Crack management in iDLSM numerical sample

One of the main strengths of discrete-based methods, such as the DEM, over continuum-based approaches like the FEM is their natural capability to capture discontinuities, including crack formation and propagation (Potyondy & Cundall, 2004). In this work, a straightforward local criterion

License CC BY-NC-ND 4.0

is introduced to simulate brittle fracture (André et al., 2019; André & Celigueta, 2023; Ranganathan et al., 2025). The criterion assumes that cracks initiate exclusively in mode I, an assumption that is particularly suitable for the brittle materials examined in this study. In this model, if the cohesive normal bond stress $\sigma_{xx_{ij}}$, where the local unit axis $\vec{x}_{ij}$ for bond ij is normal to the S_{ij} contact surface (see Figure II-2), reaches the failure strength σ_{max}, the bond is deemed fractured and subsequently excluded from further calculations. The cohesive normal contact stress is simply computed as: $\sigma_{xx_{ij}} = \vec{\Sigma}_{ij} \cdot \vec{x}_{ij}$. When a bond reaches this threshold, the corresponding contact surface S_{ij} is identified as a crack facet (see Figure II-3). After being identified as a crack facet, the surface no longer transmits stresses or forces. In the initial iDLSM model, the crack closure mechanism is not considered, as the bond definitively vanishes when it reaches the crack criterion (Ranganathan et al., 2025). Since the targeted study focuses on thermal contraction, where crack closure remains an important and non-negligible mechanism, this phenomenon is introduced in a revised version of the crack model, as described later in the section II.2.3.

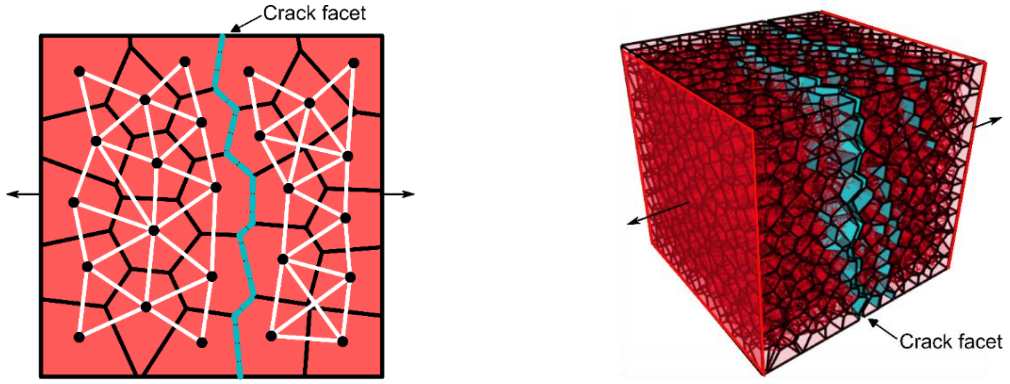

a) 2D view of a tensile test b) 3D view of a tensile test

Figure II-3: Crack-facet representation in iDLSM numerical sample (Ranganathan et al., 2025)

II.2. Enhancements to the original iDLSM model

This section is dedicated to introducing the new enhancement to the iDLSM model that are necessary to predict the microcrack networks and their impact on the macroscopic properties of refractory material. Therefore, this study employs iDLSM based BPEM approach and integrating anisotropic thermal expansion, thermomechanical coupling, and crack closure mechanisms under periodic boundary conditions (Ranganathan et al., 2025).

II.2.1. Periodic boundary condition

Periodic Boundary Conditions (PBC) is a homogenization modelling technique first introduced by Papanicolau and coworkers (Papanicolau et al., 1978) in the 1970s. Periodic homogenization is a numerical technique that enables multiscale analyses, linking the explicitly represented microscale to the upper scale by taking advantage of the periodicity of the microstructure (Drago & Pindera, 2007) in order to represent an infinite medium by replicating the unit cell thanks to periodic conditions. Additionally, researchers have also adopted this technique to enable multiscale modeling, integrating it with a range of numerical approaches, including FEM (Drago & Pindera, 2007), molecular dynamics (Barclay & Zhang, 2021) and DEM (Asadi, 2021). In order to study the influence of the microstructure on macroscopic behaviors such as Young's modulus (Asadi, 2021) or CTE (Ranganathan et al., 2025) of the targeted material, in this work, the PBC technique is applied to represent polycrystalline or multiphase microstructures, facilitating multiscale analyses. Importantly, integrating PBC within the iDLSM framework represents a novel approach that has not been previously reported in the literature. Consequently, the numerical procedures used to incorporate PBC into iDLSM are described in detail in this section.

License CC BY-NC-ND 4.0

II.2.1.1. Understanding Periodic Boundary Conditions in DEM

Periodic Boundary Conditions (PBC) are mathematical and numerical techniques that enable a finite computational domain to be representative of an infinite domain (in space) (Jacques et al., 2014). In order to enhance the visualization for the readers, the concept of PBC is illustrated using a 2D sample with four particles as shown in Figure II-4. In this framework, the finite domain (the highlighted part of Figure II-4) is defined as the central cell containing particles or elements (Asadi, 2021; Ranganathan et al., 2025). This infinite or quasi-infinite domain is created by replicating the central periodic cell around itself, referred to as neighboring or periodic cells, in two directions for 2D and three directions for 3D studies (Barclay & Zhang, 2021; Jacques et al., 2014; Ranganathan et al., 2025). Consequently, the particles or elements within the central periodic cell are known as “master” elements, while those in the neighboring periodic cells are labeled as “slave” elements (Cundall, 1988). The “slave” elements are simply cloned from their “master” elements with equal parameters (shape, density, etc..).

The master elements, located in the central periodic cell, are primarily responsible for physical computations, such as particle interactions (Cundall, 1988). In contrast, the slave elements operate as virtual copies of their corresponding master elements, ensuring seamless motions between them (see Figure II-4). Thus, these slave elements are constrained and dependent on the master elements (Cundall, 1988). Each master element interacts not only with other master elements but also with slave elements located in their periodic neighboring cells (Ranganathan et al., 2025). This model depicts that when a particle exits one side of the volume, it re-enters from the opposite side which is shown in the Figure II-4.

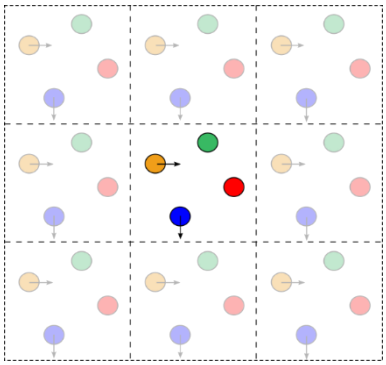

Figure II-4: Central and periodic cells with master and slave elements in a 2D PBC sample.

These principles ensure that action-reaction pairs transmitted across the boundary cancel each other out perfectly.

II.2.1.2. Generation of PBC-iDLSM numerical sample

The procedure for creating a periodic iDLSM domain is illustrated through 2D schematics and 3D visualizations, as shown in Figure II-5. Following a workflow similar to that used for free boundary conditions (see in Figure II-1), the construction of the computational domain begins with packing spherical discrete elements using the Cooker algorithm (André et al., 2015). The main distinction lies in replicating the central unit cell: in 2D, this involves generating eight surrounding periodic cells (Figure II-5a), to enforce periodicity (Ranganathan et al., 2025), while in 3D, 26 periodic cells are created to achieve the same effect. Subsequently, the centroids of the spherical elements (Figure II-5a and b), including those in the replicated cells, serve as seed points (germs) for a Voronoi tessellation (Du et al., 1999), resulting in a polyhedral discrete element domain (Figure II-5c and d). The Voronoi tessellation follows the same strategy described in the previous section. Using germs located in the periodic cells, the periodicity of the polyhedral DEM domain is

License CC BY-NC-ND 4.0

ensured. In this approach, we impose a “dummy” bounding box on the Voronoi tessellation that encompasses both the central unit cell and its periodic replicas (Ranganathan et al., 2025). This yields a parallelepipedal domain with perfectly planar boundary surfaces (see Figure II.1e). To enforce periodic boundary conditions, any cell touching these boundary planes (the “slave” element) is forced to adopt exactly the shape of its corresponding “master” cell in the central unit cell. This trick ensures that the periodic boundary conditions are satisfied even after the Voronoi tessellation. Once again, polyhedral discrete elements are connected using bonds generated through Delaunay tessellations (Figure II-5e and f). Finally, to optimize computational efficiency, elements outside the interaction range of the central unit cell are removed (Figure II-5g and h).

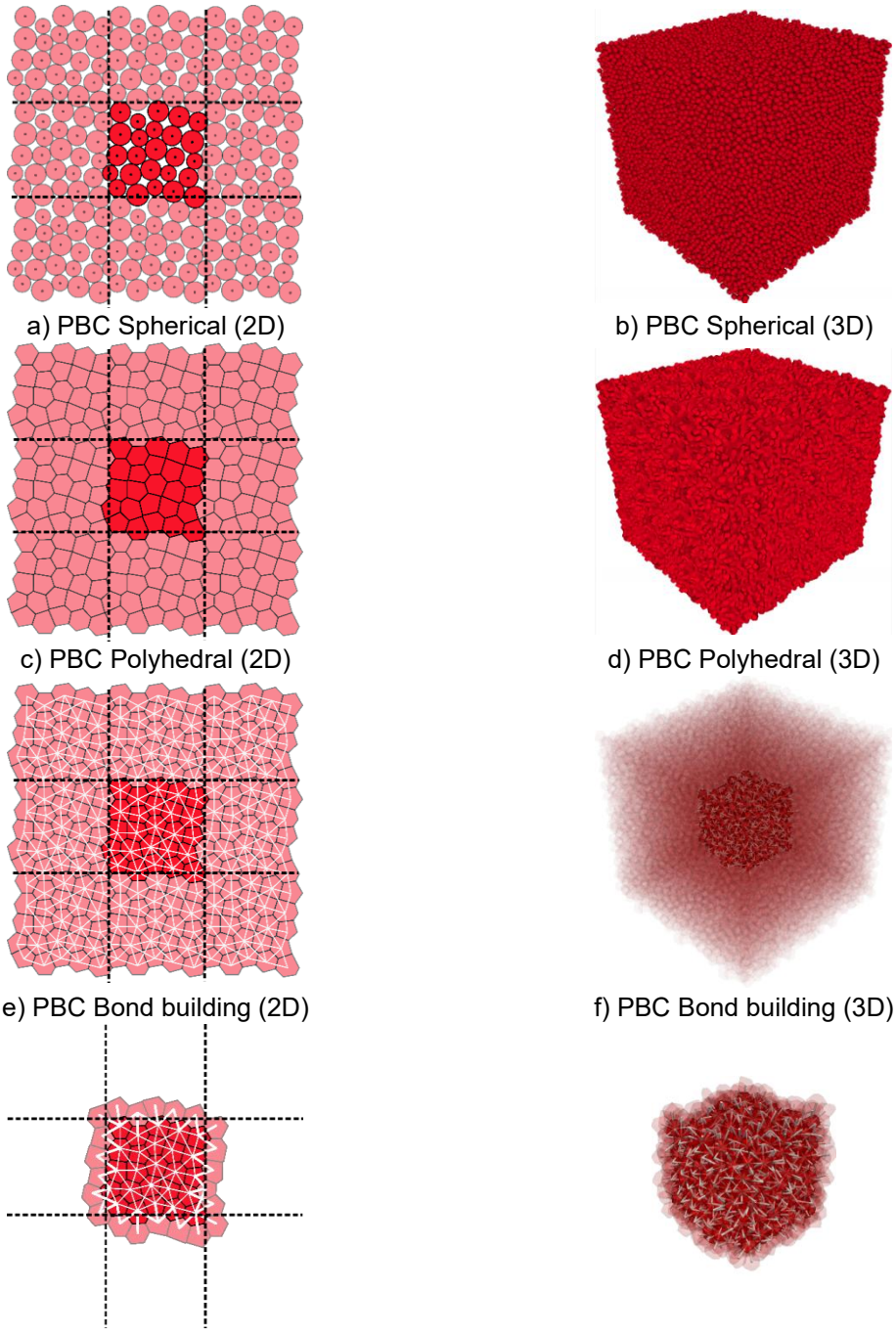

Figure II-5: Procedure to generate PBC-iDLSM box from initial spherical domain to polyhedral bonded domain without ‘‘useless’’ periodic elements (Ranganathan et al., 2025)

License CC BY-NC-ND 4.0

Thanks to this representation, the iDLSM model can be employed to simulate material with complex microstructure which is a feature of the targeted model refractory material (Chapter III).

II.2.1.3. Strategy to impose mechanical loading on PBC numerical sample

In three-dimensional PBC models, external mechanical loads cannot be imposed directly on the sample because there are no physical boundaries present. Within PBC context, the external mechanical loading must be applied indirectly by stretching the central periodic cell as shown in Figure II-6. Stretching is simply applied by adjusting the lengths L_X, L_Y and L_Z of the central periodic cell along the $\vec{X}$, $\vec{Y}$ and $\vec{Z}$ axes[2], respectively (Ranganathan et al., 2025). In order to illustrate this strategy, the uniaxial tensile test (along $\vec{X}$ direction) will be demonstrated in this section for a preliminary understanding. Note that:

- in this loading configuration, the shear extra diagonal components are supposed to be negligible (Ranganathan et al., 2025);
- the term "apparent" is used to denote a (homogenized) measurement of a physical quantity over the entire central unit cell. This differs from local measurements at the scale of individual discrete elements. Apparent quantities are indicated using angle brackets; for instance, an apparent value of a quantity q will be noted between rafters $\langle q \rangle$, (Ranganathan et al., 2025).

Initially, the central periodic box is considered to possess the following dimensions: $L_X \times L_Y \times L_Z$. For the uniaxial loading the applied apparent strain tensor ($\langle \bar{\bar{\boldsymbol{\varepsilon}}} \rangle$) is considered without deviatoric shear components and is expressed as (Ranganathan et al., 2025):

$$\langle \bar{\bar{\boldsymbol{\varepsilon}}} \rangle = \begin{bmatrix} \langle \varepsilon_{XX} \rangle & 0 & 0 \\ 0 & \langle \varepsilon_{YY} \rangle & 0 \\ 0 & 0 & \langle \varepsilon_{ZZ} \rangle \end{bmatrix} \qquad \text{II-3}$$

with:

$$\langle \varepsilon_{XX} \rangle = \frac{\Delta L_X}{L_{X_0}} \qquad \langle \varepsilon_{YY} \rangle = \frac{\Delta L_Y}{L_{Y_0}} \qquad \langle \varepsilon_{ZZ} \rangle = \frac{\Delta L_Z}{L_{Z_0}} \qquad \text{II-4}$$

In this framework, ΔL_X, ΔL_Y and ΔL_Z correspond to the changes in the lengths of the central unit cell during the simulations, whereas L_{X_0}, $L_{Y_0}$and L_{Z_0} indicate the initial lengths of the cell at the beginning of the simulations (Ranganathan et al., 2025).

In the case of the uniaxial tensile loading along the $\vec{X}$ axis, the $\langle \varepsilon_{XX} \rangle$ is directly controlled by the applied boundary condition, whereas the $\langle \varepsilon_{YY} \rangle$ and $\langle \varepsilon_{ZZ} \rangle$ are free parameters which must be determined during computation. To compute the $\langle \varepsilon_{YY} \rangle$ and $\langle \varepsilon_{ZZ} \rangle$ components, a customised "servo-control-loop" process will be used (Asadi, 2021; Ranganathan et al., 2025), which will be described in the present section. In the context of a uniaxial test, the purpose is to calculate the relevant values of $\langle \varepsilon_{YY} \rangle$ and $\langle \varepsilon_{ZZ} \rangle$ that ensure the following apparent stress state:

$$\langle \bar{\bar{\sigma}} \rangle = \begin{bmatrix} \langle \sigma_{XX} \rangle & 0 & 0 \\ 0 & 0 & 0 \\ 0 & 0 & 0 \end{bmatrix} \qquad \text{II-5}$$

[2] In this whole document, the capital letters (X, Y, Z) refer to global coordinates, whereas the lowercase letters (x, y, z) refer to local coordinates

License CC BY-NC-ND 4.0

To target the desired stress state ($\langle\bar{\bar{\sigma}}\rangle$), the resultant apparent stress must be monitored during the simulation. Figure II-6 depicts the monitoring procedure. This process involves measuring the forces along the domain boundaries using the so-called boundary bonds, which are highlighted with bold lines in the Figure II-6 (Ranganathan et al., 2025). Each boundary bond links a discrete element in the central unit cell to a corresponding slave element in one of the periodic cells. In the context of 2D case, the boundary bonds are marked as follow: X^+, X^- , Y^+ and Y^- (and Z^+ and Z^- for 3D) as depicted in the Figure II-6. The apparent stresses are deduced by summing the component of the bond forces ($\vec{F}_{ij_k}$) projected on the normal of a given boundary k (k can be X^+, X^- , Y^+, Y^-, Z^+ and Z^-) divided over the related surface area (S^{X^+}, S^{X^-}, S^{Y^+}, S^{Y^-} , $S^{Z^+}$and S^{Z^-}) of the central unit cell.

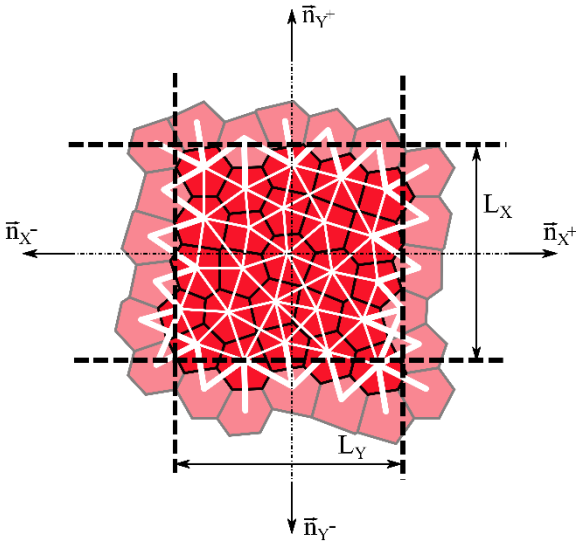

Figure II-6: The 2D central periodic cell together with its associated boundary regions

Therefore, the apparent stresses ($\langle\bar{\bar{\sigma}}\rangle$) is computed based on the stresses acting along X^+, X^-, Y^+, Y^-, Z^+ and Z^- using the following equations (see eq.II-6 - II-12). The apparent shear stresses are not taken into account in this whole study (Ranganathan et al., 2025).

$$\langle\bar{\bar{\sigma}}\rangle = \begin{bmatrix} \langle\sigma_{XX}\rangle & 0 & 0 \\ 0 & \langle\sigma_{YY}\rangle & 0 \\ 0 & 0 & \langle\sigma_{ZZ}\rangle \end{bmatrix} \quad \text{II-6}$$

where:

$$\langle\sigma_{XX}\rangle = \frac{1}{2}\left(\langle\sigma_{XX}^{X^+}\rangle + \langle\sigma_{XX}^{X^-}\rangle\right) \quad \text{II-7}$$

$$\langle\sigma_{YY}\rangle = \frac{1}{2}\left(\langle\sigma_{YY}^{Y^+}\rangle + \langle\sigma_{YY}^{Y^-}\rangle\right) \quad \text{II-8}$$

$$\langle\sigma_{ZZ}\rangle = \frac{1}{2}\left(\langle\sigma_{ZZ}^{Z^+}\rangle + \langle\sigma_{ZZ}^{Z^-}\rangle\right) \quad \text{II-9}$$

License CC BY-NC-ND 4.0

with:

$$\langle \sigma_{XX}^{X^+} \rangle = \frac{\vec{n}_{X^+}}{S^{X^+}} \sum_{j=0}^{X^+} \vec{F}_{ij_{X^+}} \quad \langle \sigma_{XX}^{X^-} \rangle = \frac{\vec{n}_{X^-}}{S^{X^-}} \sum_{j=0}^{X^-} \vec{F}_{ij_{X^-}} \qquad \text{II-10}$$

$$\langle \sigma_{YY}^{Y^+} \rangle = \frac{\vec{n}_{Y^+}}{S^{Y^+}} \sum_{j=0}^{Y^+} \vec{F}_{ij_{Y^+}} \quad \langle \sigma_{YY}^{Y^-} \rangle = \frac{\vec{n}_{Y^-}}{S^{Y^-}} \sum_{j=0}^{Y^-} \vec{F}_{ij_{Y^-}} \qquad \text{II-11}$$

$$\langle \sigma_{ZZ}^{Z^+} \rangle = \frac{\vec{n}_{Z^+}}{S^{Z^+}} \sum_{j=0}^{Z^+} \vec{F}_{ij_{Z^+}} \quad \langle \sigma_{ZZ}^{Z^-} \rangle = \frac{\vec{n}_{Z^-}}{S^{Z^-}} \sum_{j=0}^{Z^+} \vec{F}_{ij_{Z^-}} \qquad \text{II-12}$$

Where the $\vec{n}_{X^+}$, $\vec{n}_{X^-}$, $\vec{n}_{Y^+}$, $\vec{n}_{Y^-}$, $\vec{n}_{Z^+}$ and $\vec{n}_{Z^-}$ are the unit normal vectors perpendicular to S^{X^+}, S^{X^-}, S^{Y^+}, S^{Y^-}, $S^{Z^+}$and S^{Z^-} and $\vec{F}_{ij_{X^+}}$, $\vec{F}_{ij_{X^-}}$, $\vec{F}_{ij_{Y^+}}$, $\vec{F}_{ij_{Y^-}}$, $\vec{F}_{ij_{Z^+}}$ and $\vec{F}_{ij_{Z^-}}$ are the reaction forces of the ij^{th} called boundary bonds (highlighted in bold lines in Figure II-6) (Ranganathan et al., 2025). The rectangular faces of the central parallelepiped unit cell define its boundaries. Their respective areas can be computed as:

$$\begin{aligned} S^{X^+} &= L_Y \times L_Z \\ S^{X^-} &= L_Y \times L_Z \end{aligned} \qquad \text{II-13}$$

$$\begin{aligned} S^{Y^+} &= L_X \times L_Z \\ S^{Y^-} &= L_X \times L_Z \end{aligned} \qquad \text{II-14}$$

$$\begin{aligned} S^{Y^+} &= L_X \times L_Y \\ S^{Y^-} &= L_X \times L_Y \end{aligned} \qquad \text{II-15}$$

Therefore, the resultant apparent stresses are simply computed as the mean of the two opposite stresses as described in the equation (II-7 - II-9) (Ranganathan et al., 2025).

Apparent strains along a specific direction are determined by dividing the change in length by the initial length (see eq.II-4). Shear components can similarly be inferred by tracking the angular changes of the boundary surfaces of the central periodic cell relative to their initial configuration (Ranganathan et al., 2025). This procedure will not be elaborated further here, as apparent shear stresses are considered negligible under the mechanical loading conditions addressed in this study.

Using these expressions, the apparent stresses and strains of the central unit cell can be evaluated throughout the simulation. If the desired stress state, for instance, as given by eq II-6 in the uniaxial test, has not yet been reached, a numerical servo-control loop is employed to steer the simulation toward the specified targeted stress state (Ranganathan et al., 2025). The procedure is to monitor the difference between the current apparent stress state of the central periodic box from the targeted stress state following the next equation.

$$\langle \bar{\bar{\sigma}}_{\boldsymbol{error}} \rangle = \langle \bar{\bar{\sigma}} \rangle - \langle \bar{\bar{\sigma}}_{target} \rangle \qquad \text{II-16}$$

where $\langle \bar{\bar{\sigma}} \rangle$ is the current monitored stress state and $\langle \bar{\bar{\sigma}}_{target} \rangle$ is the targeted stress state.

License CC BY-NC-ND 4.0

Based on the difference ($\langle\bar{\bar{\sigma}}_{error}\rangle$), the simulation adjusts the length of the central unit cell along $\vec{X}$, $\vec{Y}$ and $\vec{Z}$ directions. Note the adjustment of the length can contribute to increase or decrease in the length of the central unit cell. In this study, a Proportional-Integral-Derivative (PID) controller (Ranganathan et al., 2025; Willis, 1999) is employed to gradually adjust the dimensions of the central unit cell so that the desired apparent stress state is reached. To maintain numerical stability, the adjustments are limited to remain within predefined minimum and maximum thresholds. So, the aim of this PID strategy is to minimize the stress error ($\langle\bar{\bar{\sigma}}_{error}\rangle$) by adjusting the stretching of the central periodic cell (Ranganathan et al., 2025).

These incremental stretches, noted δL_X, δL_Y and δL_Z of the central periodic cell must be deduced to minimize the stress error (Ranganathan et al., 2025; Willis, 1999). This adjustment process is governed by the PID controller through the equation below:

$$\overline{\overline{\delta L}} = K_p.\langle\boldsymbol{\sigma_{error}}\rangle + K_i\int\langle\boldsymbol{\sigma_{error}}\rangle.dt + K_d\frac{d\langle\boldsymbol{\sigma_{error}}\rangle}{dt} \quad \text{II-17}$$

Where $\overline{\overline{\delta L}}$ is the stretch matrix defined as:

$$\overline{\overline{\delta L}} = \begin{bmatrix} \delta L_X & 0 & 0 \\ 0 & \delta L_Y & 0 \\ 0 & 0 & \delta L_Z \end{bmatrix} \quad \text{II-18}$$

and where K_p is the proportional gain, K_i the integral gain, $K_d$the derivative gain and t the simulated time (Willis, 1999). Here, the assumption is made that the stretch of the unit central cell along a given direction is directly responsible of the stress variation in the same direction

In this whole study, the maximal acceptable increment or decrement value for δL_X, δL_Y and δL_Z is set to $\pm 1\%$, of the initial lengths L_{X_0}, $L_{Y_0}$and L_{Z_0}. Note that δL_X, δL_Y and δL_Z is related to the length variation between two consecutive time steps. Moreover, in the case of uniaxial stretching along $\vec{X}$ direction, only the incremental elongations δL_Y and δL_Z are guided by this servo-control technique (Ranganathan et al., 2025).

II.2.1.4. Validation of Mechanical loading on PBC-iDLSM numerical sample

To demonstrate and validate the mechanical loading procedure for a PBC numerical sample, a hypothetical elastic material, as specified in Table II-1, is subjected to a quasi-static uniaxial tensile test (Ranganathan et al., 2025). A PBC-iDLSM computational sample containing 20,000 discrete elements within the central unit cell is employed for this purpose. The objective is to assess the accuracy of the calculated apparent mechanical properties, including Young's modulus $\langle E\rangle$ and Poisson's ratio $\langle\nu\rangle$, by comparing them with the input values E and ν provided in the Table II-1. The simulation is carried out under an imposed strain rate of 10^{-7} per iteration, over a total of 10,000 iterations. This validation procedure, involving a verification of "what we put in is what we get out" is common in DEM methods as no clear and robust mathematical demonstration exists (André et al., 2019). Here, the "what we put in" are simply the input mechanical properties of Table II-1 and the "what we get out" are the apparent mechanical properties which must be similar to the input ones (André et al., 2019).

License CC BY-NC-ND 4.0

Table II-1: Hypothetical material properties for elastic tensile test (Ranganathan et al., 2025)			
Young's modulus	E	20	GPa
Poisson's ratio	ν	0.2	-
Tensile strength	σ_{max}	15	MPa
Number of DE	N_{DE}	20k	-

To minimize dynamic effects and expedite convergence toward the static solution, two different damping factors are combined. The first is a numerical damping factor (φ), which is introduced into the velocity Verlet integration scheme (see eq II-1) (André et al., 2019). In this study, a value of $\varphi = 1.3$ is used. The second damping factor is a physical damping factor, denoted as γ, which is introduced into the iDLSM bond. This factor corresponds to a fraction of the critical damping coefficient (Kruggel-Emden et al., 2007). A value of $\gamma = 0.4$ is used in this study.

Figure II-7 presents the outcomes of the quasi-static uniaxial test. As anticipated, the numerical sample maintains the desired apparent stress state $\langle\bar{\bar{\sigma}}\rangle$, as defined in eq.II-5. The corresponding apparent Young's modulus $\langle E\rangle$ is simply deduced by taking the ratio of the measured apparent normal stress $\langle\sigma_{XX}\rangle$ along the loading direction $\vec{X}$ to the imposed strain $\langle\varepsilon_{XX}\rangle$ along the same direction (Ranganathan et al., 2025). It is evident that the calculated apparent Young's modulus $\langle E\rangle$ approaches the input material value E. Likewise, the apparent Poisson's ratios along the $\vec{Y}$ and $\vec{Z}$ directions, $\langle\nu_{YY}\rangle$ and $\langle\nu_{ZZ}\rangle$, are obtained by tracking the apparent strain contractions $\langle\varepsilon_{YY}\rangle$ and $\langle\varepsilon_{ZZ}\rangle$ in their respective directions. Similar to $\langle E\rangle$, these apparent Poisson's ratios converge to the input material Poisson's ratio ν.

In addition, to validate the brittle failure behavior of the hypothetical material, a local tensile strength σ_{max} is also introduced. As expected, the numerical sample exhibits a brittle failure which is shown on Figure II-7 by a sudden decrease of the apparent stress $\langle\sigma_{XX}\rangle$ at 15 MPa which corresponds to the local failure value σ_{max} (Ranganathan et al., 2025). To improve clarity and aid visualization, Figure II-7 shows only the central periodic cell, with cracks highlighted in blue-green.

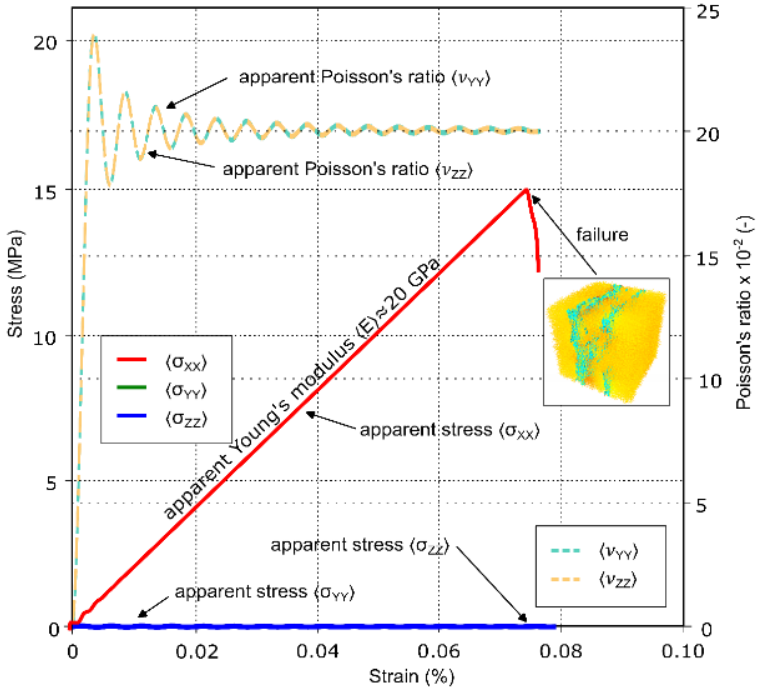

Figure II-7: Stress and Poisson's ratio responses versus strain in a PBC-iDLSM tensile test

License CC BY-NC-ND 4.0

In summary, this study effectively demonstrated a method for applying mechanical loading to a PBC-iDLSM numerical sample, as illustrated through tensile tests on a hypothetical elastic-brittle material (Ranganathan et al., 2025). The results, shown in Figure II-7, exhibit strong qualitative and quantitative agreement with the expected mechanical responses.

II.2.2. Anisotropic thermal expansion

Thermal expansion is described by a coefficient that quantifies the material's dimensional change (expansion or contraction) with temperature. This CTE can be constant or dependent on temperature change. As a preliminary approach, the CTE will be considered constant. As mentioned in the section I.6, the primary focus is to simulate anisotropic thermal expansion of the refractory material (Ranganathan et al., 2025), which is represented by the thermal expansion coefficient tensor defined as follows:

$$\langle \bar{\bar{\alpha}} \rangle = \begin{bmatrix} \alpha_x & 0 & 0 \\ 0 & \alpha_y & 0 \\ 0 & 0 & \alpha_z \end{bmatrix} \quad \text{II-19}$$

Here α_x, α_y and α_z represent the coefficients of thermal expansion along the corresponding spatial directions. Previously, André et al., (2017) proposed a method for simulating isotropic thermal expansion within the DEM framework using cohesive beam bonds. In the present work, a similar approach is adapted to implement anisotropic thermal expansion within the iDLSM framework (André et al., 2017).

II.2.2.1. Formulation of anisotropic thermal expansion for iDLSM approach

To date, the implementation of anisotropic thermal expansion within the DEM framework has not been reported in the literature. Therefore, this capability can be considered a novel contribution, and the numerical methodology is described in detail below. To illustrate the thermal expansion computation, a pair of polyhedral elements is shown in Figure II-8 in two dimensions (Ranganathan et al., 2025). In this figure, points O_i and O_j represent the centroids of two bonded DEs. The model is considered to start at an initial temperature T_0 and in a stress-free state. At this temperature, the bond has relaxed initial lengths of l_x along $\vec{x}$ and l_y along $\vec{y}$.

In this study, thermal expansion is implemented by adjusting the relaxed lengths of the bonds in response to a temperature change $\Delta T = T - T_0$, following an approach analogous to the isotropic case described by André et al., (2017). Consequently, when a temperature change ΔT is applied, the model is expected to expand or contract. Considering discrete element (i) as the reference, discrete element (j) moves by Δl_x along $\vec{x}$ and Δl_y along $\vec{y}$ relative to DE (i). The new relative position of (j)'s centroid becomes O_j'. The displacements Δl_x and Δl_y (and Δl_z for 3D cases) are computed as:

$$\Delta l_x = \Delta T \; l_x \; \alpha_x \quad \text{II-20}$$

$$\Delta l_y = \Delta T \; l_y \; \alpha_y \quad \text{II-21}$$

$$\Delta l_z = \Delta T \; l_z \; \alpha_z \quad \text{II-22}$$

Assuming that discrete element (i) remains fixed, the bond displacements Δl_x and Δl_y (and Δl_z for 3D) are evenly distributed between elements (i) and (j). Additionally, the local bond axis $\vec{x}_{ij}$ is also updated to reflect angular changes arising from the anisotropic character of the thermal expansion (Ranganathan et al., 2025). To reduce computational cost, the geometry and dimensions of the

License CC BY-NC-ND 4.0

polyhedral discrete elements are not modified. Under these conditions, the bond behavior is represented in terms of engineering stresses rather than true stresses, which is justified due to the small magnitude of the thermal strains.

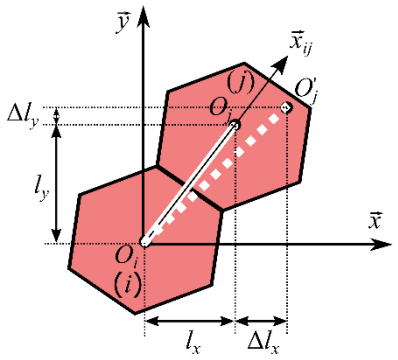

Figure II-8: Schematic representation of anisotropic thermal expansion management in iDLSM framework

It is essential to emphasize that these calculations should begin from the initial stress-free configuration at T_0. As a result, the thermomechanical analysis proceeds in two stages: first, the thermal expansion is determined, and second, the mechanical response is computed while incorporating the previously calculated thermal expansion (Ranganathan et al., 2025). In the current study, a simplified approach is assumed by neglecting thermal conduction and considering a uniform temperature distribution across the sample. So, a separate thermal time step for thermal conduction distinct from the mechanical time step is not needed.

II.2.2.2. Validation of thermal loading on PBC-iDLSM numerical sample

Section II.2.2.1 presented the methodology for computing anisotropic thermal expansion in any DEM-PBM framework, including PBC-iDLSM. In a manner analogous to the approach described in section II.2.1.3 for applying mechanical loading under periodic boundary conditions, thermal loading must also be adapted to PBCs, where free boundaries are absent. As noted previously, thermal conduction is neglected, and the temperature is assumed to remain uniform throughout the numerical sample (Ranganathan et al., 2025). Under these assumptions, the entire sample is considered to be apparently stress-free under a uniform temperature change with iteration. Accordingly, the apparent target stress tensor is defined as:

$$\langle \bar{\bar{\sigma}} \rangle = \begin{bmatrix} 0 & 0 & 0 \\ 0 & 0 & 0 \\ 0 & 0 & 0 \end{bmatrix} \qquad \text{II-23}$$

Similarly, the apparent strains $\langle \varepsilon_{XX} \rangle$, $\langle \varepsilon_{YY} \rangle$ and $\langle \varepsilon_{ZZ} \rangle$ recalculated to verify that the stress-free state is maintained (Ranganathan et al., 2025). The same servo-control loop procedure outlined in section II.2.1.3 is employed to achieve the stress-free configuration defined by eq.II-23.

Once more, to confirm the validity of this method, a preliminary study involving a hypothetical elastic material with anisotropic thermal expansion coefficients is conducted (Ranganathan et al., 2025). The material parameters used in this study are summarized in Table II-2.

License CC BY-NC-ND 4.0

Table II-2: Hypothetical material properties for thermal test (Ranganathan et al., 2025)			
Young's modulus	E	20	GPa
Poisson's ratio	ν	0.2	-
CTE along $\vec{x}$	α_x	-10 × 10^{-6}	K^{-1}
CTE along $\vec{y}$	α_y	10 × 10^{-6}	K^{-1}
CTE along $\vec{z}$	α_z	0 × 10^{-6}	K^{-1}
Number of DE	N_{DE}	20k	-

The thermal loading procedure consists of cooling the sample from 1200 ℃ down to 0 ℃, with 0 ℃ representing the target temperature, at a constant rate of 0.05 ℃ per iteration. Following the cooling phase, the sample is held at the target temperature for a dwell period of 12,000 iterations. The overall simulation comprises 36,000 iterations, encompassing both the cooling and dwell stages (see Figure II-9). To ensure a smooth application of the thermal loading, a hyperbolic tangent function is used at the start and end of the cooling phase (Ranganathan et al., 2025). For this analysis, a PBC-iDLSM numerical sample consisting of 20,000 DEs is used.

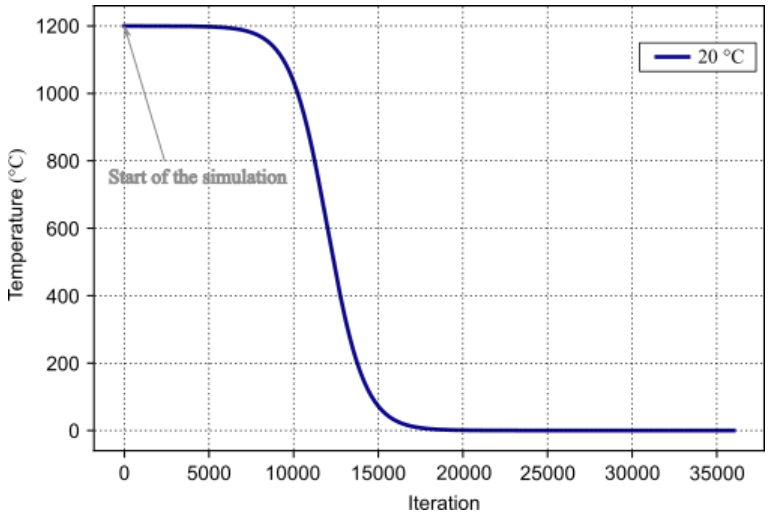

Figure II-9:Iteration versus temperature during cooling simulation (Ranganathan et al., 2025)

The objective of this study is to evaluate the accuracy of the anisotropic thermal expansion implementation. The apparent thermal expansion coefficients $\langle \alpha_X \rangle$, $\langle \alpha_Y \rangle$ and $\langle \alpha_Z \rangle$ are expected to approach the corresponding input coefficients along each spatial direction, as listed in Table II-2 (Ranganathan et al., 2025).

The key results are presented in Figure II-10, showing the evolution of the apparent thermal strain during cooling from 1200 ℃. The thermal strain differs along each spatial direction, reflecting the anisotropic behavior of the numerical sample (Ranganathan et al., 2025). The apparent coefficient of thermal expansion in a given direction can be calculated as the ratio of the corresponding apparent strain $\langle \varepsilon_{XX} \rangle$, $\langle \varepsilon_{YY} \rangle$ and $\langle \varepsilon_{ZZ} \rangle$ to the temperature change ΔT. The reference state for these calculations is the initial stress-free configuration of the sample at 1200 ℃. Accordingly, the apparent thermal expansion coefficients along the $\vec{X}$, $\vec{Y}$ and $\vec{Z}$ directions are determined using the following expressions:

$$\langle \alpha_X \rangle = \frac{\langle \varepsilon_{XX} \rangle}{\Delta T} \qquad \langle \alpha_Y \rangle = \frac{\langle \varepsilon_{YY} \rangle}{\Delta T} \qquad \langle \alpha_Z \rangle = \frac{\langle \varepsilon_{ZZ} \rangle}{\Delta T} \qquad \text{II-24}$$

By evaluating the slopes of the three curves in Figure II-10, the apparent coefficients of thermal expansion are seen to converge toward the input material values, as expected for the numerical

License CC BY-NC-ND 4.0

sample (Ranganathan et al., 2025). These results demonstrate that the proposed model is capable of reproducing the anisotropic thermal expansion behavior of a hypothetical homogeneous material using the PBC-iDLSM framework. From a materials science perspective, this hypothetical homogeneous material can be considered analogous to a monocrystalline material, as it lacks secondary phases or grains with different orientations that could lead to CTE mismatches during thermal contraction under thermal loading (Ranganathan et al., 2025).

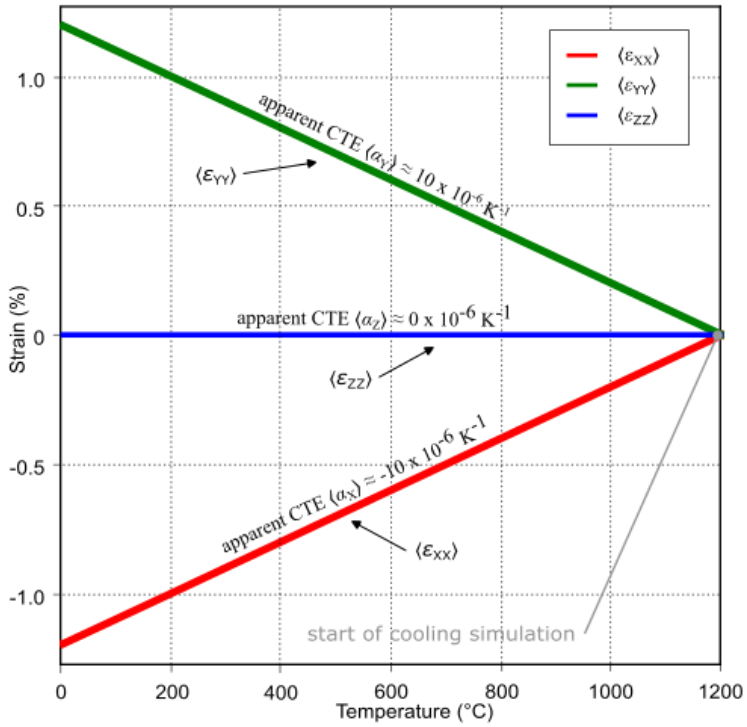

Figure II-10: Evolution of strain versus temperature for a PBC-iDLSM cooling test.(Ranganathan et al., 2025)

In addition, such thermal contraction involves crack closure mechanisms in the refractory materials. So, in order to advance the applications of iDLSM model for refractory applications, integrating the crack closure remains an important and non-negligible mechanism, as the aim of this study is to simulate thermal contraction.

II.2.3. Crack opening and closing management in iDLSM numerical sample

In this study, the crack nucleation and propagation process were already discussed in section II.1.3 for the iDLSM model. Indeed, the crack opening mechanism follows a simplified scheme: once a bond exceeds its tensile strength σ_{max}, it undergoes Mode I crack nucleation. The bond is then deactivated from the calculation, and the resulting crack facet does not transmit any internal forces (Ranganathan et al., 2025).

The crack closure mechanism is introduced to the model to ensure force transmission when cracks begin to close. In this mechanism, normal compressive forces are transmitted across the crack facet, with frictional forces (if considered) contributing to stress transfer. However, in this study, we assume perfect sliding (friction coefficient = 0), so only normal forces are considered during crack closure, with no shear forces transmitted (Ranganathan et al., 2025). As illustrated in Figure II-11, the crack opening and closing scheme is implemented as follows: during the opening mode, the crack surfaces are separated by a small distance $\delta > 0$, and no tensile forces are transmitted. Once the crack surfaces come into contact ($\delta \leq 0$) during the closing mode, the bond regains its

License CC BY-NC-ND 4.0

ability to transfer forces in the normal direction. This mechanism ensures stress and force transmission during crack closure (Ranganathan et al., 2025).



a) Crack opening mode $\varepsilon_{xx} > 0$ b) Crack closing mode $\varepsilon_{xx} \leq 0$

Figure II-11: 3D Illustration of the crack opening and closing (Ranganathan et al., 2025)

To validate the post-crack mechanism and also to demonstrate the importance of the post-crack mechanisms for iDLSM samples, two separate shear test (see Figure II-12) simulations are performed:

1. a “crack-open” study where the cracks had only crack opening mechanism
2. a “crack-reclosure” where the cracks had both the opening and closing mechanisms

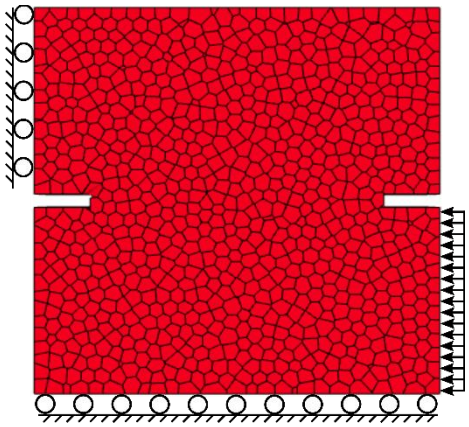

Figure II-12: Numerical sample under shear loading

To enhance the visualization, simple 2D iDLSM numerical sample under free boundary condition submitted to a shear loading is employed (Ranganathan et al., 2025). For these studies, a pre-existing cracked sample is employed, as described in Figure II-12 and a hypothetical elastic material with tensile strength of σ_{max} of 5 MPa is employed. The material parameters used in this study are summarized in Table II-3. The numerical sample is subjected to an imposed displacement rate of 4×10^{-7} per iteration over a total of 50,000 iterations.

Table II-3 : Hypothetical material properties for thermal test

Young’s modulus	E	20	GPa
Poisson’s ratio	ν	0.2	-
Tensile strength	σ_{max}	5	MPa
Number of DE	N_{DE}	2k	-

Figure II-13a and b, depicts the snippets of the final state of the numerical sample under shear test. Despite both methods able to depict crack nucleation and opening as the bonds attain the tensile strength (σ_{max}) of the material, there exist:

- in the case of “crack-open” study, although the numerical sample captures crack opening, it exhibits instability, which arise from the detachment of certain DEs from the domain, as shown in Figure II-13a (Ranganathan et al., 2025);

License CC BY-NC-ND 4.0

- in contrast, in the case of “crack-reclosure” study, this integrated realistic physical mechanism facilitates the stresses and forces transmission by considering the reclosing of cracks. Moreover, this eliminates the presences of instability (Ranganathan et al., 2025). On incorporating the new crack management strategy, numerical sample performs qualitatively better realistic results, as demonstrated in Figure II-13b).

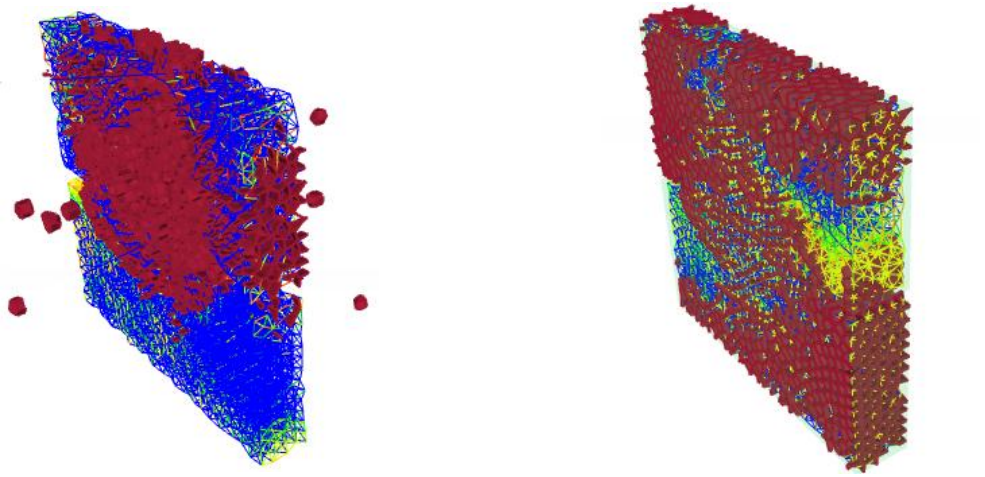

a) “crack open” study b) “crack reclosure” study

Figure II-13: Snippets of numerical sample under shear loading

In conclusion, based on these observations, the crack closure mechanism will be adopted as the default crack mechanism in this whole study.

II.3. Conclusion

In conclusion, this chapter presents the improved Distinct Lattice Spring Model (iDLSM) for modeling brittle elastic media. It highlights the key improvements in representing the interactions between DEs in stress-strain responses and force calculations during discrete element interactions. These improvements aim to achieve continuum-equivalent representations often used in mechanical engineering (similar to those provided by the FEM).

Additionally, this study discusses the advancements needed to enhance the original iDLSM model's applicability for refractory materials. First, the chapter introduces a strategy to incorporate PBC into the iDLSM model, allowing it to mimic the behavior of complex refractory microstructures using infinite cohesive media. The chapter also presents a novel servo-control strategy utilizing a PID controller for load applications for the PBC sample. Indeed, this novel servo-control strategy was validated and demonstrated for uniaxial tensile loading using a hypothetical material. Furthermore, the PBC-iDLSM model has been employed to simulate anisotropic thermal expansion, which is a critical physical phenomenon in a given class of refractory materials that exhibits micro-cracking. Again, the thermal loading using the servo-control technique was valid, using a hypothetical material.

Furthermore, this model also accounts for crack opening and closing mechanisms, which are another essential aspect, enhancing the stability and the applicability of the iDLSM model. Therefore, the developed DEM tool can now simulate multiple crack trajectories under complex mechanical and thermal loading with simple local failure criteria.

As a next step, these numerical strategies are applied to analyze a basic refractory microstructure that exhibits anisotropic behavior, similar to polycrystalline materials. Therefore, Chapter IV is

License CC BY-NC-ND 4.0

dedicated to introducing the numerical methods to (i) generate a polycrystalline numerical sample and (ii) discuss the ability of this sample to describe the anisotropic behavior of polycrystalline materials. Subsequently, these numerical strategies will be utilized to gain insights into a two-constituent composite microstructure described in Chapters V and VI.

License CC BY-NC-ND 4.0

Chapter III. Overview of the reference refractory materials

III.1. Industrial refractory microstructure design - thermomechanical property relationship under thermal expansion effects

This chapter focuses on understanding the thermomechanical properties of both industrial and model refractory materials in relation to their microstructure. Refractories are well known for their high-temperature applications, during which they develop thermal stresses. These stresses induce defects such as microcracking and interfacial decohesion at the microstructural scale, as it cools down from its sintering temperature. Previous studies have shown that several mechanisms contribute to the formation of these defects (during cooling phase), including mismatches in the CTE between phases or grains (M. G. Kakroudi et al., 2009; Mouiya, Martynyuk, et al., 2023; Sridhar et al., 1994; Tvergaard & Hutchinson, 1988). Indeed, the resulting defects are known to influence the thermo-mechanical behaviour and, in some cases, they can improve the thermal shock resistance of refractories. By the way, these defects significantly influence thermal expansion as well as the stress-strain response. Experimental evidence suggests that these defects promote non-linear behaviour that enhances material toughness and increases strain-to-rupture; both of which are desirable for thermal shock applications (Boateng et al., 2025; Grasset-Bourdel et al., 2012; Kakroudi et al., 2008; Mouiya, Tessier-Doyen, et al., 2023). Therefore, specifically understanding the microstructure-property relationship during the cooling phase of the thermal cycle is of high interest, as this is the phase where thermal defects play a key role (Huger et al., 2007; Tessier-Doyen, 2003). Throughout this chapter, several characteristic evolutions of key thermomechanical parameters, such as dilatometry, Young's modulus, and the stress-strain response are highlighted, firstly on some industrial refractory materials (such as cordierite (Boccaccini et al., 2005; Case et al., 1981), polycrystalline alumina (Case et al., 1981) and andalusite (Kakroudi et al., 2008) which are quite complex to analyses) and secondly on some model refractory system (designed on purpose to facilitate the analysis).

Accordingly, this chapter illustrates three industrial refractory material that clearly exhibits such characteristic evolutions and provide more understanding on these aspects by specific experimental studies managed on two model refractory materials (highlighting the roles of microcracking and decohesion in their macroscopic apparent thermomechanical behaviour). Such an approach would help identifying dominant mechanisms among mismatches in the CTE between phases, that leads to these characteristic evolutions. The insights gained will then be used to propose few suitable model materials already investigated experimentally (specific microstructural design promoting characteristic evolutions that are expected) for subsequent investigation of these phenomena using the iDLSM framework.

It is important to highlight some of the material science and ceramic processes technical terms (Biswas & Sarkar, 2020; Boateng et al., 2025; da Luz A et al., 2015; Kingery et al., 1977):

- aggregate: the coarse, typically pre-synthesized refractory particles that form the skeleton of a refractory material;
- matrix: the fine fraction plus binding phase that surrounds/binds the aggregates;
- monocrystal or single crystal: a grain/aggregate exhibiting a single crystallographic domain without internal grain boundaries;
- polycrystal: a grain/aggregate or body composed of many monocrystals separated by grain boundaries;
- castable: a flowable, dry mix of aggregates and fines that, when combined within a liquid (typically water) and cast, hardens at ambient or low temperatures and acquires refractory properties upon drying and firing (thanks to in-situ chemical reactions).

License CC BY-NC-ND 4.0

It is important to note that all experimental results and observations presented in this chapter are drawn from previously published studies (Boccaccini et al., 2005; Chotard et al., 2008; Kakroudi, 2007; Mouiya, 2024) (none of these experimental results come from the present PhD work). This chapter provides a summary of these previous works, including sample preparation (very important step to consider the defects occurrence) and the results obtained using the respective refractory systems. As a final introductory comment, even if it's crucial to understand the full thermal history of a given system (powder preparation, shaping, first heating and sintering, cooling stage of firing, second heating and cooling), a much larger description of the results will be focused on the cooling stages during which multiple microcracks initiation/propagation take place (specific focus of the present PhD).

III.1.1. Cordierite-mullite refractories

This section focuses on understanding the impact of the decohesion/debonding (due to the CTE mismatch) on the thermomechanical properties of the cordierite-mullite. The study done using the Cordierite-Mullite composite is one example, where decohesion occurs between matrix and aggregate (as $\Delta\alpha < 0$) (Boccaccini et al., 2005). Cordierite-Mullite composites (see Figure III-1) are a primary example of industrial refractory materials, widely applied as supports for the rapid sintering of roofing tiles (Huger et al., 2007). The microstructure design aims to balance the thermal shock resistance of cordierite ($2MgO\text{-}Al_2O_3\text{-}5\ SiO2$) with the high-temperature creep resistance of mullite ($3Al_2O_3\text{-}2SiO_2$). That is, cordierite exhibits very low CTE (α = 1.5 to $3\times10^{-6}\,K^{-1}$ in [20 - 1215 ℃] range) and is thus well suited for thermal shock applications, but its creep resistance deteriorates (starting from 1200 ℃). Incorporating mullite, with its high refractoriness, improves its mechanical stability at elevated temperatures (Boccaccini et al., 2005; Huger et al., 2007). Moreover, the mullite rich aggregate exhibits higher CTE (α = 4.5 - $5.3\times10^{-6}\,K^{-1}$ in [20 - 1215 ℃]). These results correspond to the composite in Figure III-1 exhibiting 70wt% cordierite matrix and 30wt% mullite rich aggregate (Chotard et al., 2008). Such composites are well known to depict interface decohesion (see Figure III-1) between the cordierite matrix and mullite aggregate as the CTE mismatch between matrix and aggregate is negative ($\Delta\alpha < 0$).

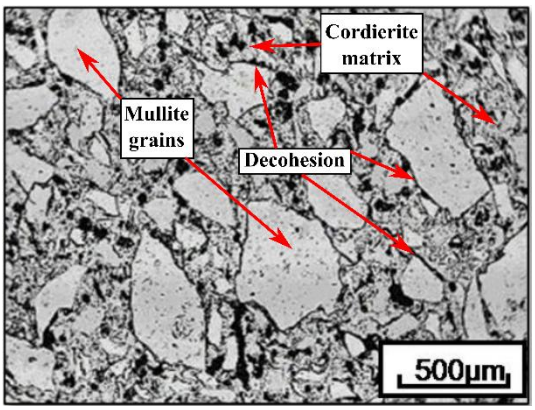

Figure III-1: Cordierite - mullite microstructure with decohesion between matrix and grains (Chotard et al., 2008)

In addition, Figure III-2 depicts the evolution of apparent (also referred as macroscopic) Young's modulus (orange curve) and thermal strain (blue curve) during a full thermal cycle from room temperature up to 1215 ℃ (according to operating condition) (Chotard et al., 2008; Huger et al., 2007). As highlighted by the green curve related to the cumulative hints of acoustic emission (Chotard et al., 2008), this thermal cycle clearly highlights the interface decohesion during the cooling phase. Upon cooling from 1215 ℃, two distinct stages are observed. Up to approximately

License CC BY-NC-ND 4.0

710 ℃, Young's modulus continues to slightly increase, similarly to "standard" ceramics such as pure alumina and suggesting stable bonding. Below 710 ℃, a sudden drop in Young's modulus occurs, followed by a continuous decrease down to room temperature. This reduction indicates the reopening or nucleation of interfacial debonding caused by the negative CTE mismatch ($\Delta\alpha < 0$) between the cordierite matrix and mullite rich aggregates, as supported by the corresponding increase in acoustic emission activity (green curve) (Chotard et al., 2008; Huger et al., 2007).

In the same trend, the blue curve in Figure III-2 depicts the materials thermal strain response during dilatometry test. In the cooling stage, two distinct regimes are again observed. In the initial stage, at high temperature, although the material contracts, the apparent CTE (α) remains high (5.08 × 10^{-6} K^{-1} as indicated by the slope of the curve) in accordance with the well-connected mullite rich aggregate to the cordierite matrix (increasing significantly the CTE value compare to the value of cordierite). Around 710 ℃, a sudden change in slope marks the onset of interfacial decohesion ($\Delta\alpha < 0$), consistent with the increase in acoustic emission activity (green curve). Below this temperature, mullite rich aggregates becomes completely free in their matrix cavities, and their expansion no longer affects the composite's response. At room temperature (see Figure III-2), the final CTE (1.98 × 10^{-6} K^{-1}) logically approaches that of the cordierite matrix alone (1.5-3 × 10^{-6} K^{-1}) (Chotard et al., 2008; Huger et al., 2007).

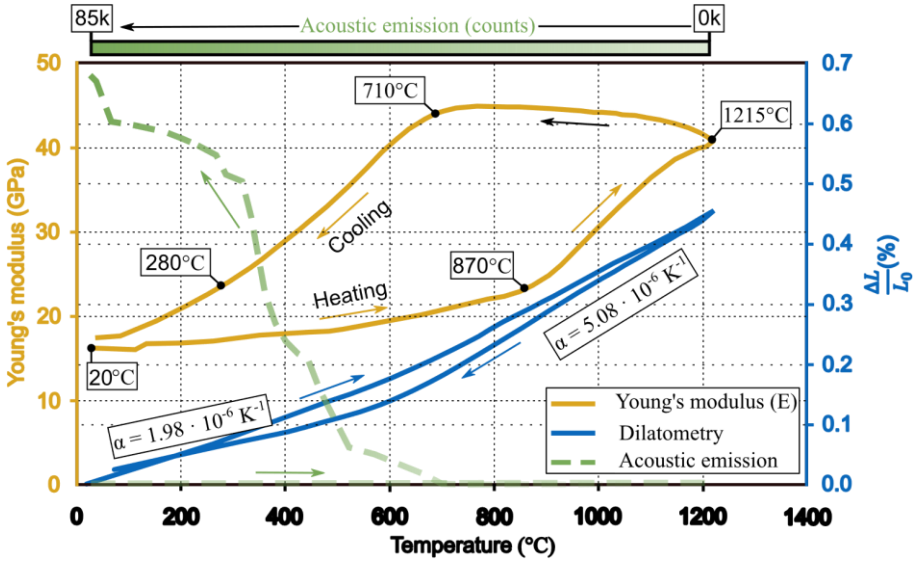

Figure III-2: Young's modulus variation, thermal expansion behavior as well as acoustic emission recording during a thermal cycle up to 1215 ℃ with heating-cooling rate 5 ℃ min^{-1}. Interfacial decohesion which occur during cooling is highlighted by the decrease in Young's modulus, a strong reduction in CTE as well as an important acoustic emission below 710 ℃ (Chotard et al., 2008)

Therefore, the CTE mismatch between aggregate and matrix clearly promote interfacial decohesion within the microstructure during cooling (after sintering), which indirectly affects in a very positive way the composite's thermomechanical response. Notably, the observed decreases in thermal expansion and Young's modulus below 710 ℃ are extremely welcome to enlarge the ability of the material to sustain thermal shock (Chotard et al., 2008; Huger et al., 2007). To further understand these phenomena, it could be of importance to investigate the influence of grain/aggregate size of on the apparent thermomechanical properties and how it contributes to the observed effects (Case et al., 1981; M. G. Kakroudi et al., 2009).

License CC BY-NC-ND 4.0

In fact, the resistance of refractory materials to thermal shock is fundamentally governed by a coherent set of physical properties, whose understanding is essential from the earliest stages of microstructural design. Thermal conductivity (k) and the coefficient of thermal expansion (α) dictate how temperature gradients translate into internal stresses: a low expansion coefficient and an appropriately tuned conductivity help to limit the magnitude of thermal stresses generated during rapid temperature changes (Chotard et al., 2008; Litovsky et al., 1999; Mouiya, Tessier-Doyen, et al., 2023). Young's modulus (E) and the stress-strain behavior ($\sigma = f(\varepsilon)$), particularly the material's ability to exhibit non-linear responses (such as stress relaxation with the introduction of decohesion or microcracks), play a crucial role in redistributing and attenuating these stresses (Chotard et al., 2008; Grasset-Bourdel et al., 2012; Mouiya, Tessier-Doyen, et al., 2023). Thus, the integrated understanding and modelling of these physical properties (well beyond simple experimental characterization) form the foundation of a rational approach to designing innovative, sustainable refractory materials suited to severe thermal environments.

III.1.2. Polycrystalline alumina with large grain

This section addresses the influence of grain size and morphology on the evolution of the apparent thermomechanical properties of refractories. To isolate grain-related effects, single-phase polycrystalline alumina (Al_2O_3), widely used in high temperature applications, is considered in this section. In fact, the rhombohedral crystallographic structure of alumina at small scale leads to a slight anisotropic thermal expansion, with reported coefficients of $\alpha_a = \alpha_b$ = 7.10 to 9.67×10^{-6} K^{-1} and α_c = 8.21 to 10.8×10^{-6} K^{-1} in the [20 - 1500 ℃] range (Case et al., 1981; Fei, 2013). Thus, most of the alumina parts for industrial applications being polycrystalline (consists of millions of grains), their microstructure could develop spontaneous microcracks resulting from thermal stresses generated by the CTE mismatch between adjacent grains during thermal cycles (Case et al., 1981; Yousef et al., 2005). Importantly, these microcracks arise only when the average grain size is above a certain threshold named "Critical size" which has been estimated to be 70 μm (Case et al., 1981). This underscores the intrinsic role of grain anisotropy in initiating microcracks and, consequently, in governing the apparent thermomechanical behavior of the material.

Previous studies have highlighted a correlation between the average grain size of a microstructure and apparent thermomechanical properties, such as Young's modulus (Case et al., 1981). Building on this, Case et al., (1981) conducted a series of experimental investigations to quantify the relationship between average grain size and apparent thermomechanical properties using fracture mechanics-based analysis. In their study, rectangular prism-shaped alumina samples were prepared via dry pressing, followed by sintering at 1650 ℃ for 1 h and subsequent reheating at 1675 ℃ for up to 120 h, during which abnormal grain growth was observed. To enable a comparative analysis, samples were prepared with small grains (average grain size ≈ 12 μm) and large grains (average grain size ≈ 250 - 600 μm), and subjected to thermal treatments to investigate the Young's modulus evolution. For illustration, the Young's modulus results obtained for one representative "small-grain" and "large-grain" samples are shown in Figure III-3a and b.

License CC BY-NC-ND 4.0

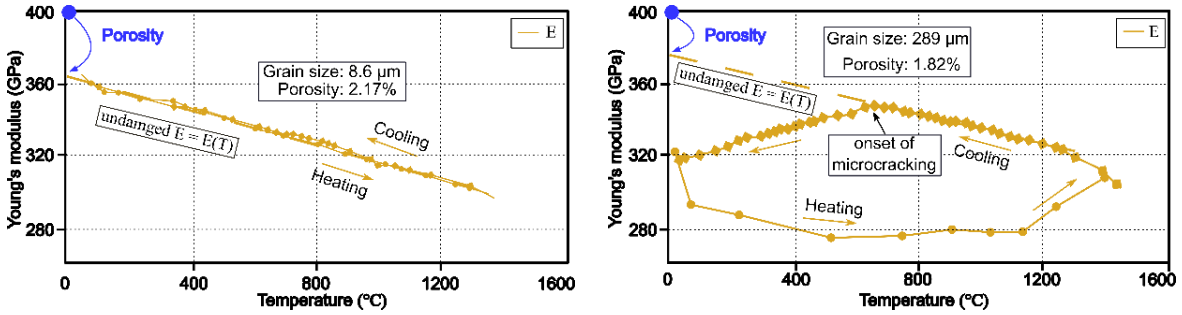

a) "small-grain" (8.6 μm) b) "large-grain" (289 μm)

Figure III-3: Young's modulus evolution versus temperature for different polycrystalline samples (Case et al., 1981)

These results highlight that:

- firstly, it is evident that the evolution of Young's modulus in the "small-grain" sample exhibits no hysteresis, whereas the "large-grain" sample displays significant hysteresis. This behavior suggests that the "small-grain" sample does not develop microcracks, while the "large-grain" sample exhibit microcracking due to CTE mismatch between grains. Furthermore, the presence of hysteresis reflects the reversible opening and closing of these microcracks under thermal cycling (Case et al., 1981);
- secondly, since the "small-grain" sample does not contain microcracks, its cooling behavior follows the undamaged linear behavior line. In contrast, the "large-grain" sample exhibits a sudden drop in Young's modulus at 700°C, deviating from the undamaged linear behavior line, which indicates the temperature at which microcracking initiates (Case et al., 1981);
- dense alumina typically exhibits a Young's modulus of approximately 400 GPa; however, the fabrication process used in this study, aimed at producing a microstructure with a wide range of grain sizes, introduces pores (Case et al., 1981). The presence of these pores contributes to the downward shift of the undamaged linear behavior line for respective samples during cooling, as indicated by blue arrows in Figure III-3.

This observation emphasizes that having average grain size similar to "large grains" plays a dominant role in promoting microcracking and initiating hysteresis behavior, in contrast to "small grains". Moreover, the pronounced sudden drop in the apparent Young's modulus of "large-grain" reflects the loss of material stiffness resulting from microcrack formation (Case et al., 1981).

Globally, this study concluded that alumina samples with average grains depicting a size of approximately 70 μm contribute to microcracking and exhibit hysteresis in Young's modulus (Case et al., 1981). By this, Case et al. provided valuable insights into the influence of grain size on the apparent thermomechanical properties. However, it remains unclear whether the observed effects were solely due to grain size or grain morphology (like the abnormally large grains) that contributed to this hysteresis effect (Case et al., 1981). Additionally, although the impact of microcracking on the evolution of Young's modulus has been established, the influence of porosity remains unclear.

Yousef et al., (2005) conducted a similar study using a microstructure composed exclusively of equiaxed grains (see Figure III-4). For this purpose, alumina samples were doped with magnesia in the preparation step. This approach was employed to suppress abnormal grain growth in alumina and to isolate the influence of grain morphology. Figure III-4 depicts microstructure of the samples prepared using this strategy, where Figure III-4a and b correspond to a sample with average grain size of 16 μm and 99 μm respectively. As noted earlier, fabricating alumina with a wide range of grain sizes can introduce porosity (0.5-3.5%), whose influences should be eliminated to highlight the impact of microcracks on the Young's modulus evolution (Yousef et al., 2005).

License CC BY-NC-ND 4.0

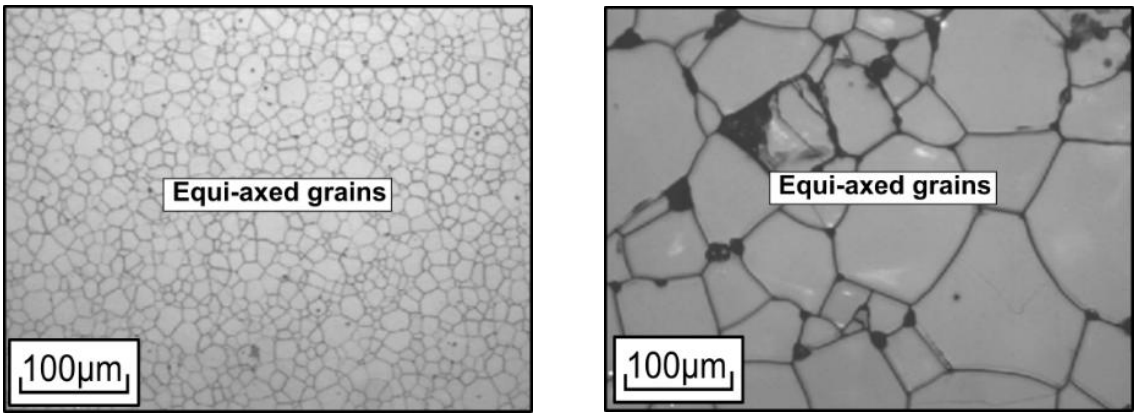

a) average grain size: 16 μm b) average grain size: 99 μm

Figure III-4: Polycrystalline alumina microstructure with equiaxed grains (Yousef et al., 2005)

To isolate the effect of microcracking on the evolution of Young's modulus, the authors (Yousef et al., 2005) proposed a modified representation of Young's modulus versus temperature (see Figure III-5). The modified representation is explained by using the typical evolution of Young's modulus during cooling: the solid line represents large-grained material exhibiting microcracking, while the dashed line corresponds to the extrapolated behavior of an undamaged sample as shown in Figure III-5a. Now, the room-temperature Young's modulus is extrapolated from high-temperature measurements and compared with the actual measured modulus, as illustrated in Figure III-5a. The difference between these (actual and extrapolated) values is called as deviation of Young's modulus (ΔE) and reflects the influences of microcrack only. Therefore, this indicates that the loss ΔE stiffness when cooled by ΔT temperature (difference between the present temperature and maximum temperature of 1500 ℃). This procedure is continued to obtain ΔE for all the temperatures during the cooling stage and plotted as ΔE versus ΔT, as shown in Figure III-5b.

Figure III-5b ΔE versus ΔT, corresponds to four samples with varying average grain sizes. These results highlight that, with increasing grain size, the density of microcracks rises, leading to larger deviations in Young's modulus. Notably, adopting an equiaxed grain morphology also induced microcracking in small-grained configurations (Yousef et al., 2005).

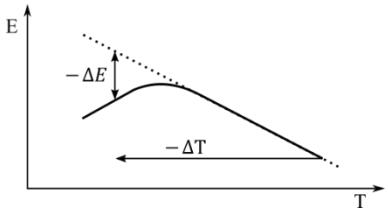

a) modified Youngs modulus representation

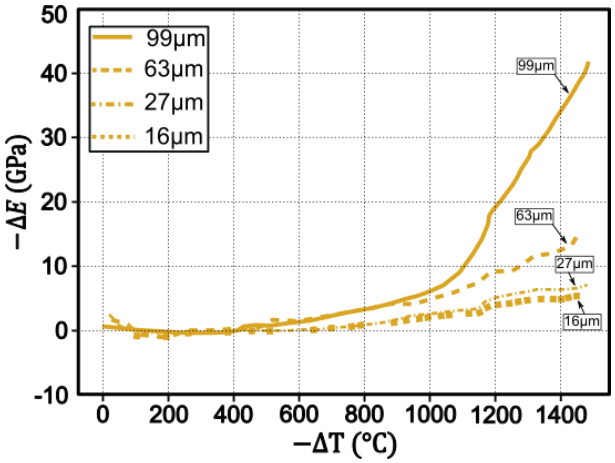

b) ΔE versus ΔT plots

Figure III-5: Illustration of modified Youngs modulus and ΔE versus ΔT plots for different samples (Yousef et al., 2005)

License CC BY-NC-ND 4.0

In conclusion, this study demonstrates that the average grain size plays a decisive role in the initiation of microcracks (due to $\Delta\alpha > 0$) in polycrystalline alumina (Case et al., 1981; Yousef et al., 2005), thereby significantly influencing the evolution of the apparent Young's modulus. This contrast in mechanisms can be interpreted thermodynamically through the framework of Griffith's theory, which governs the conditions for crack initiation and propagation (Evans, 1978; Rice & Pohanka, 1979). In fine-grained system, the potential onset of crack should take place through the many grain boundaries that would spread the local elastic strain energy over numerous small surface (involving a large amount of surface energy). As a result, the critical stress needed locally for such crack growths is high, and microcracks are then energetically not favorable (Rice & Pohanka, 1979). In contrast, for coarse-grained system, the potential onset of crack could take place through few grain boundaries that would spread the local elastic strain energy over few large surfaces (involving a lower amount of surface energy). As a result, the critical stress needed locally for such crack growths is low, and microcracks are then energetically favorable (Rice & Pohanka, 1979).

Consequently, microcracks can form even though the material itself is inherently tough. On understanding the influence of coarse grains on promotion of microcrack density, now, it becomes essential to understand their role when introduced by coarse aggregates (exhibiting monocrystalline) in castable such as alumina based castable (Boateng et al., 2025) or andalusite based castable (M. G. Kakroudi et al., 2009), and to determine how such coarse aggregates exert a significant effect on the overall thermo-mechanical performance of the castable (Kakroudi et al., 2008). In fact, previous experimental studies demonstrate that microcracking strongly governs the thermomechanical response of the refractory materials under thermal shocks. However, it is important to note that the microcracking mechanism observed in polycrystalline alumina differs fundamentally from the interfacial decohesion seen in the cordierite-mullite system. In polycrystalline alumina, microcracks develop as a result of the CTE mismatch between different crystallographic axis of the surrounding grains resulting from an anisotropic atomic structure (Case et al., 1981). Even it is not obvious in the present example, in general such polycrystalline microstructure produces a more pronounce decrease in Young's modulus than the relatively modest stiffness decrease observed in cordierite-mullite system and resulting from a decohesion at the interface between the mullite aggregate and cordierite matrix (Huger et al., 2007). The influence of this microcrack-driven compliance and its impact on thermal shock resistance will be further examined in the following section on an andalusite-based castable.

III.1.3. Andalusite based castable

This section investigates the role of monocrystalline-based aggregates with anisotropic CTE in promoting a dense network of microcracks in refractory castable. Andalusite-based castable serve as a representative case, widely recognized in the steel industry for their excellent thermal shock resistance (Kakroudi, 2007). Numerous studies (Kakroudi, 2007) have highlighted how microstructural features influence the mechanical performance and durability of andalusite refractories under high-temperature service conditions.

Andalusite (Al_2O_3 - SiO_2) is an orthorhombic mineral (a≠b≠c; $\alpha = \beta = \gamma = 90°$) that exhibits strong thermal expansion anisotropy (α_a = 12.9 × 10^{-6} K^{-1}, α_b = 9.6 × 10^{-6} K^{-1} and α_c = 3.1 × 10^{-6} K^{-1}) that has to be compared to the CTE value of the castable matrix (α ≈ 7.6 × 10^{-6} K^{-1}) (Kakroudi, 2007). It is important to note that the result that is presented here is limited to a low temperature range for which the andalusite does not transform into mullite. During thermal cycle up to 1100 ℃, andalusite introduces CTE mismatch between the aggregates and castable matrix, leading to the formation of microcracks and decohesion (Kakroudi et al., 2008). Such effects contribute to the well-known thermal shock behavior of andalusite castable due to crack-induced toughening

License CC BY-NC-ND 4.0

mechanisms (Kakroudi et al., 2009). As a representative example (see Figure III-6a), andalusite - low cement castable (monocrystal andalusite aggregates between 200 μm - 5 mm, see Figure III-6b were subjected to a thermal treatment at 5 ℃/min up to 1100 ℃ with a dwell of 5 h.

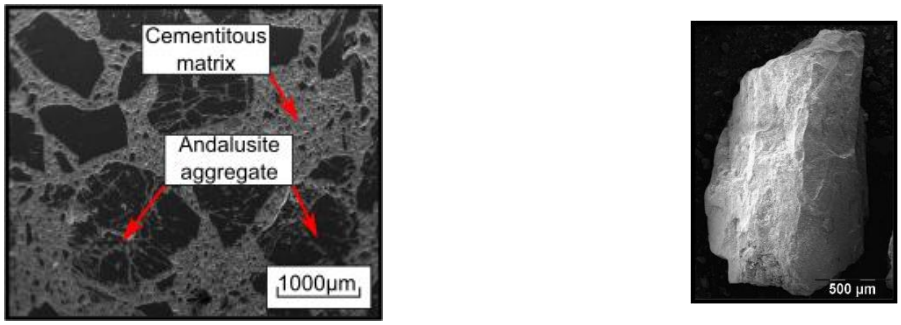

a) composite b) aggregate with single grain

Figure III-6: Andalusite-cementitious microstructure design (Kakroudi, 2007)

Figure III-7, depicts the evolution of castable's thermomechanical properties such as Young's modulus (orange curve in Figure III-7a), Dilatometry (blue curve in Figure III-7a, both as a function of temperature, and room temperature stress-strain response in tension (Figure III-7b) as function of previous temperature exposure. Again, the curves related to first cycle are represented in lighter shade while the curves related to the second cycle is represented by the brighter shade. As the objective of the section is to discuss on the impact of the monocrystalline-based aggregates with anisotropic CTE in promoting dense microcracks, the microstructure evolution at the first cycle is not discussed here. Also, here the focus is mainly given on the cooling stage, so only the second cooling stage will be commented (Huger et al., 2007; Kakroudi, 2007).

Upon cooling from 1100 ℃ (in second cycle), Young's modulus remains stable until ~800 ℃, after which it decreases significantly, reaching values well below the initial state at room temperature. This degradation results from microcracking and aggregate-matrix debonding induced by $\Delta\alpha$ mismatches (both positive and negative), as observed in microstructural examinations (see the microstructure in Figure III-7b) (Kakroudi et al., 2008). Moreover, dilatometry further confirms these mechanisms (blue curve in Figure III-7a). After firing at 1100 ℃, strong aggregate - matrix bonding and closed microcracks yield a higher apparent CTE during early cooling ($8.67 \times 10^{-6}\ K^{-1}$), as indicated in blue curve of Figure III-7a (Huger et al., 2007). It is important to note that this trend is consistent with the CTE value of the matrix ($7.6 \times 10^{-6}\ K^{-1}$) and mean CTE aggregate value ($8.5 \times 10^{-6}\ K^{-1}$, which is the mean of the three crystallographic axes). However, decohesion along the andalusite a-axis (the highest CTE) suppresses the a-axis contribution to the apparent expansion, reducing the final CTE to $5.11 \times 10^{-6}\ K^{-1}$ at room temperature, as indicated in the blue curve of Figure III-7a (Huger et al., 2007).

To further investigate this material, tensile tests were performed at room temperature on the castable in two conditions: (i) cured at 110 ℃ and (ii) fired at 1100 ℃. These tests aimed to highlight the differences in stress-strain response between the two states (Kakroudi et al., 2008). The results obtained from tensile test (see Figure III-7b) depicts that:

- the castable cured at 110 ℃ exhibited a quasi-linear elastic brittle response, indicating that no microcracks were initially present in the microstructure. In contrast, the castable fired at 1100 ℃ displayed a non-linear mechanical response, consistent with the development of a microcrack network during the cooling stage (see microstructure in Figure III-7b (Kakroudi et al., 2008);

License CC BY-NC-ND 4.0

- moreover, on comparing the stress and strain of rupture, it is evident to see the reduction in the stress of rupture, but a significant increase in strain of rupture (from 0.018 % to 0.074 %) (Huger et al., 2007).

This behavior reflects the formation of an extensive microcrack network due to aggregate-matrix CTE mismatch. The microcracks diffuse damage under mechanical loading, thereby enhances the material to sustain thermal shock (Kakroudi, 2007).

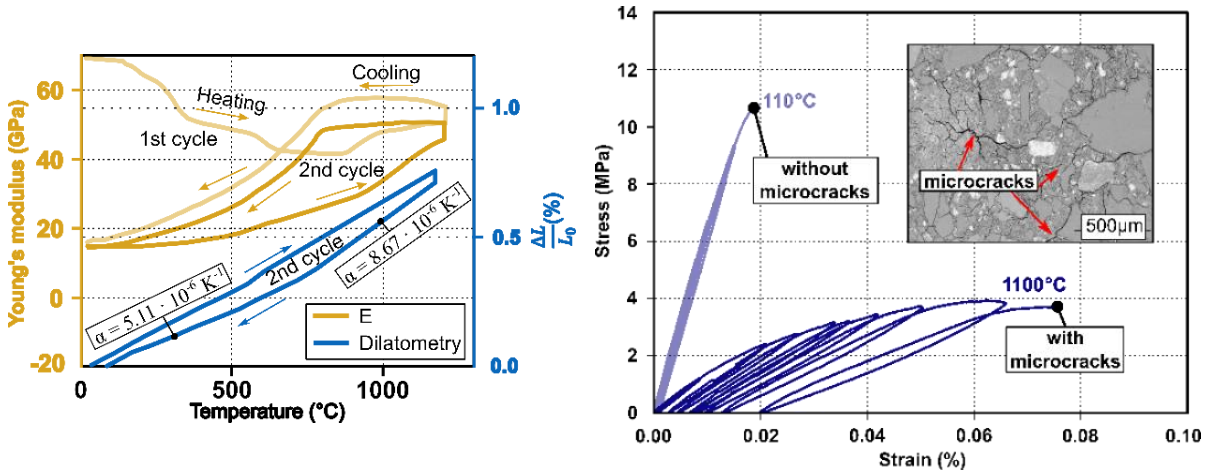

a) Young's modulus and Dilatometry b) Stress-strain

Figure III-7: Thermomechanical properties evolution vs temperature for andalusite-based castable (Huger et al., 2007)

A review of case studies suggests that both decohesion and microcracking have a significant influence on the evolution of the thermomechanical properties of refractory castable (Huger et al., 2007). These mechanisms are reflected in features such as hysteresis in Young's modulus (Chotard et al., 2008; Kakroudi et al., 2008) and dilatometry (Chotard et al., 2008; Kakroudi et al., 2008), sudden slope changes in dilatometry curves, and the introduction of non-linear mechanical responses (Kakroudi et al., 2009). Among these, the influence of microcracking is seen to be more significant than that of interfacial decohesion, highlighting its central role in determining performance.

The characteristics of aggregates exert a decisive influence on the initiation and development of microcracks. Case studies reveal that microcracking (Case et al., 1981; Kakroudi, 2007) or decohesion (Chotard et al., 2008) may arise through two distinct microstructural configurations: (i) due to the CTE mismatch between the aggregate and the surrounding matrix (Chotard et al., 2008; M. G. Kakroudi et al., 2009), or (ii) due to the CTE mismatch between anisotropic grains within the aggregates themselves (Case et al., 1981). In both cases, interactions involve coarser aggregates with larger grain sizes (Case et al., 1981; M. G. Kakroudi et al., 2009), either aggregate-matrix or grain-grain, promote microcrack formation more effectively than finer aggregates. This effect is further intensified when coarse (monocrystal) aggregates (Kakroudi, 2007) or aggregate with fewer coarse grains (Boateng et al., 2025), exhibiting strong anisotropic CTE behaviors, particularly in cases where one crystallographic axis exhibits a very low, nearly zero, or even negative thermal expansion (Boateng et al., 2025; Kakroudi, 2007; Mouiya, 2024). Under such conditions, high thermal stresses are generated during cooling, which drive the development of dense and interconnected microcrack networks. These networks, in turn, exert a pronounced influence on the bulk thermomechanical response of the refractory material (Boateng et al., 2025; Kakroudi et al., 2008; Mouiya et al., 2026).

License CC BY-NC-ND 4.0

Although andalusite-based refractory materials are well known for their ability to withstand thermal shock, and although the microstructural mechanisms responsible for this behaviour are well documented in the scientific literature, their limited refractoriness motivates the search of alternative minerals with improved high-temperature performance. In this context, the use of fused alumina aggregates composed of large, monocrystalline rhombohedral grains appears promising (as reported by (Boateng et al., 2025)), owing to their significant anisotropy in CTE, even though this anisotropy is lower than that of andalusite. Indeed, as demonstrated by Case et al., (1981), the presence of large alumina grains (typically larger than 70 µm) can generate an extensive network of microcracks in polycrystalline alumina, despite the relatively small difference between the CTE values along the a and c crystallographic axes (α_a and α_c). Investigations conducted on castable containing, tabular alumina aggregates and, on the other hand, white fused alumina aggregates have already reported a significant difference in the evolution of Young's modulus as a function of temperature (Boateng et al., 2025). However, despite these recent research efforts, the amount of experimental data currently available remains insufficient to support a robust and meaningful numerical study, which would nevertheless be of great interest in the coming years.

Starting on the investigation of the andalusite based refractory materials (Kakroudi, 2007), the TMC research group in Limoges initiated (in 2008) a lot of experimental investigations on a system based on a similar orthorhombic structure leading to much larger anisotropy in CTE: aluminum titanate (Al_2TiO_5) (Babelot et al., 2011; Doncieux et al., 2017; Mouiya, 2024). Additionally, thanks to some pertinent stabilizers (Mg or Fe) embedded inside (Freudenberg & Mocellin, 1988) (Freudenberg & Mocellin, 1988), the system remains rather stable in a large range of temperature (which facilitate the experimental investigations). For this reason, polycrystalline aluminium titanate has been identified as very suitable model materials to deeply investigate how the microstructure should be designed to tune the different physical characteristics of the material which could enlarge its ability to sustain thermal shocks. Thus, numerous experimental studies (Babelot et al., 2011; Bayer, 1971; Chen & Awaji, 2007; Chen et al., 2021; Doncieux et al., 2017; Mouiya, 2024; Ohin Mensan Daniel et al., 2014; Shan et al., 2022) have been managed using aluminum titanate as model material during the past 15 years, which today offer a large data set for validation of numerical aspect that could be developed today. These previous experimental works on aluminum titanate makes this material a very effective system for isolating and studying the role of coarse anisotropic aggregates in microcrack initiation and propagation driven by CTE mismatch (Mouiya, 2024).

In the context of the present PhD work, two key phenomena are considered: (i) the anisotropy of individual grains in a polycrystalline structure, and (ii) the behavior of composite containing anisotropic monocrystal aggregates. Accordingly, the study is divided into two parts:

1. modelling CTE mismatch between neighboring anisotropic grains in a polycrystalline structure;
2. modelling CTE mismatch between the constituents of a composite system, in which coarse monocrystal aggregates, that exhibit anisotropy CTE, are embedded in a matrix.

By this, both stand-alone aggregate systems and aggregates embedded within a matrix are numerically investigated.

III.2. Aluminum titanate model material

The present section focuses on the key general aspects of aluminum titanate, including its pronounced anisotropic thermal expansion (Bayer, 1971; Mouiya, 2024) and its distinctive macroscopic properties (Mouiya, 2024), as well as on previous studies carried out by the TMC group using AT as a model material. Based on these discussions, the final part of the section identifies the critical features that a virtual model must incorporate in order to investigate refractory model materials, and outlines a strategy for generating a representative polycrystalline model.

License CC BY-NC-ND 4.0

III.2.1. Key general aspects about Aluminum Titanate materials

Aluminum titanate (Al_2TiO_5, AT), also known as tialite, is a synthetic polycrystalline ceramic formed through the stoichiometric solid-state reaction between α-alumina (α-Al_2O_3) and titanium dioxide (TiO_2) at high temperature, typically above 1500 °C (Ohya et al., 2017; Skala et al., 2009; Thomas & Stevens, 1989). AT is widely recognized for its excellent thermal shock resistance which make it particularly suitable for demanding high-temperature applications such as refractory linings in the non-ferrous metal industry (Asbury, 1975), automotive components (e.g., particulate filters) (Backhaus-Ricoult et al., 2010), and certain aerospace applications (Jiang et al., 2012). However, pure aluminum titanate suffers from limited thermodynamic stability at elevated temperatures. In the late 1980s, Freudenberg & Mocellin, (1988) demonstrated that AT decomposes into α-Al_2O_3 and TiO_2 in the temperature range of approximately 850-1280 °C, a behaviour that constitutes a major limitation for its long-term use. To overcome this issue, and building on earlier work by Thomas & Stevens, (1989), and Buscaglia et al., (1994), additive-based stabilization strategies were developed. The introduction of dopants such as MgO, Fe_2O_3, or $SrAl_2SiO_6$ was shown to promote cation substitution within the AT lattice, thereby improving its thermodynamic stability.

The outstanding thermal shock resistance of AT is closely linked to intrinsic properties governed by its microstructure, most notably its exceptionally high thermal expansion anisotropy (Bayer, 1971). At the crystallographic scale, AT exhibits a pronounced contrast between its principal axes: two axes expand significantly with increasing temperature, while the third axis contracts (Bayer, 1971; Mouiya, Tessier-Doyen, et al., 2023). This extreme anisotropy generates substantial internal stresses during cooling after processing, which are relieved through the formation of a diffuse and interconnected network of microcracks throughout the microstructure (Babelot et al., 2011; Doncieux et al., 2017; Mouiya, 2024; Ohin Mensan Daniel et al., 2014). These microcracks play a central role in determining the macroscopic properties of AT, including its reduced effective Young's modulus (Mouiya, Tessier-Doyen, et al., 2023) and its characteristic non-linear, quasi-brittle mechanical behaviour (Mouiya, Martynyuk, et al., 2023). Consequently, understanding the origin of the pronounced CTE anisotropy at the crystallographic level and its influence on macroscopic thermomechanical properties is of particular interest.

III.2.1.1. Huge thermal expansion anisotropy coming from orthorhombic structure

The intrinsic property of AT is due to its orthorhombic crystallographic structure, α-Al_2TiO_5 is well known for its significant thermal expansion anisotropy: α_a= -2.38 × 10^{-6} K^{-1}, α_b = 11.97 × 10^{-6} K^{-1}, α_c = 20.80 × 10^{-6} K^{-1}(Bayer, 1971). AT (Al_2TiO_5) crystallizes in an orthorhombic lattice belonging to the space group *Cmcm* (Skala et al., 2009). Owing to the multiple equivalent lattice descriptions permitted in orthorhombic symmetry, different conventions have appeared in the literature (Angenault, 2001). For the present study, the C-type mode is adopted, where the lattice parameters are ordered as $a < b < c$ (Austin & Schwartz, 1953; Bayer, 1971), as shown in Figure III-8a. Readers are referred to comparative works, such as (Morosin & Lynch, 1972) and (Taylor, 1987), for a detailed discussion of alternative representations (Mouiya, 2024).

Furthermore, AT crystallises in a structure isomorphic to pseudobrookite (Fe_2TiO_5), consisting of distorted oxygen octahedra [MeO_6] that share edges and host two distinct cation sites, indicated as M1 (4c) and M2 (8f) as shown in Figure III-8b (Morosin & Lynch, 1972; Skala et al., 2009). In AT, both Al^{3+} and Ti^{4+} occupy these sites, with preferential distributions of 58.8% Al at M1 and 71.2% Al at M2 (Skala et al., 2009). This unequal occupancy generates substantial distortions, reflected in unusually short O-O distances along the *c*-axis (≈2.5 Å, compared to the typical 2.7-3 Å for undistorted octahedra) (Bayer, 1971; Morosin & Lynch, 1972; Skala et al., 2009). The degree of distortion depends on the ionic radius difference between Ti^{4+} and the substituting cation; when small, as in Fe_2TiO_5, the lattice remains relatively isotropic, but in AT, the 12 pm mismatch between

License CC BY-NC-ND 4.0

Ti^{4+} (0.068 nm) and Al^{3+} (0.050 nm) induces significant octahedral distortion (Bayer, 1971; Mouiya, 2024), directly influencing the lattice parameter *a* (lower CTE) and leading to pronounced structural anisotropy (see Figure III-8c).

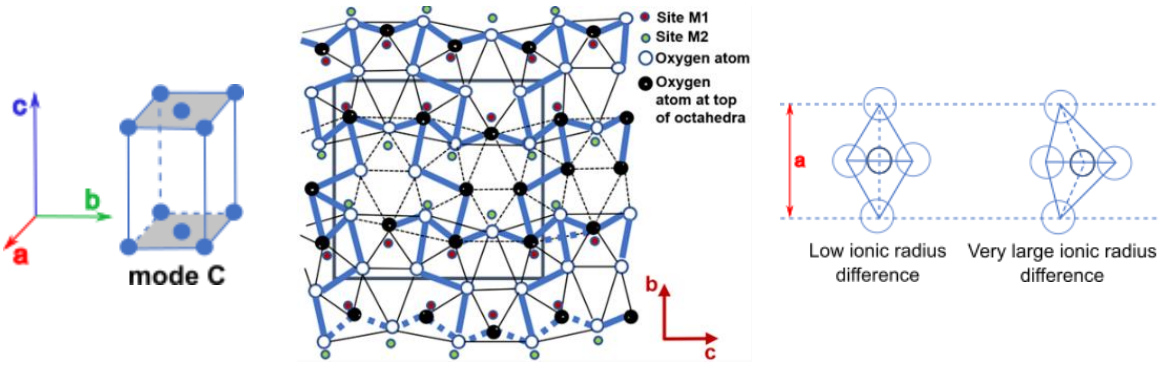

a) orthorhombic lattice (Angenault, 2001)

b) oxygen octahedral distortion (Morosin & Lynch, 1972)

c) axis a - distortion - cation displacement relationship (Bayer, 1971)

Figure III-8: AT's lattice mode and associated octahedral distortions and cation displacements

Figure III-9 illustrates the lattice dilation (α_a= -2.38 × 10^{-6} K^{-1}, α_b = 11.97 × 10^{-6} K^{-1}, α_c = 20.80 × 10^{-6} K^{-1}) of AT (Bayer, 1971), highlighting its anisotropic behaviour arising from the pronounced distortion of [MeO_6] octahedra (Morosin & Lynch, 1972). The expansion is markedly constrained along the *a*-axis due to shortened O-O bonds that limit thermal vibrations, whereas greater dilation occurs along the *b*- and *c*-axes (Bayer, 1971). This anisotropy directly accounts for AT's exceptionally low and direction-dependent CTE, which is the key factor underlying its remarkable thermal shock resistance (Mouiya, 2024).

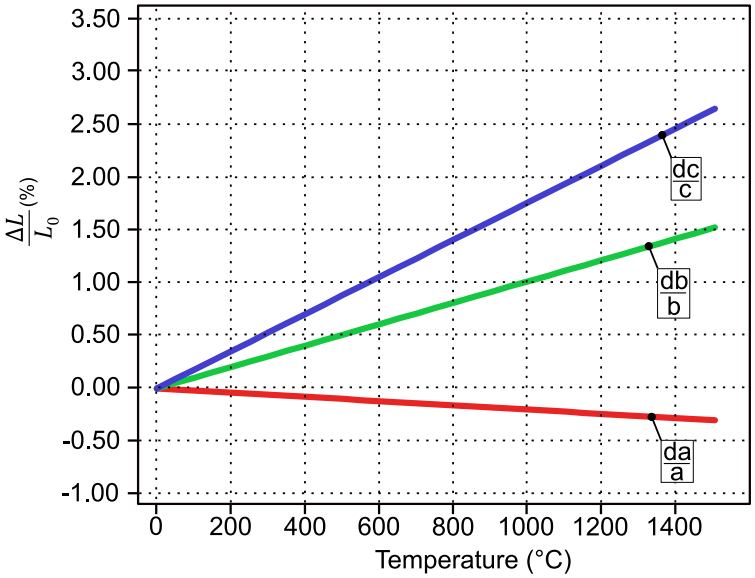

Figure III-9: AT's Lattice dilation (Fei, 2013)

Polycrystalline AT, however, is prone to microcracking under fluctuating temperature conditions (Babelot et al., 2011; Doncieux et al., 2017; Mouiya, 2024). This behaviour, combined with (i) microcrack-dominated, temperature-sensitive nonlinearity, (ii) experimental challenges such as damping, material fragility, and high-temperature apparatus limitations, and (iii) limited practical demand, has so far precluded the determination of the full stiffness tensor for the AT lattice (Chen & Awaji, 2007; Ohya et al., 1988; Violini et al., 2018). Consequently, the literature remains limited

License CC BY-NC-ND 4.0

mainly to scalar measurements of Young's, bulk, or occasionally shear moduli, with no reported values for $\bar{C}_{12}$, $\bar{C}_{13}$, $\bar{C}_{23}$, or $\bar{C}_{44\text{-}66}$ (Chen & Awaji, 2007; Ohya et al., 2017; Violini et al., 2018). It is important to note that once the stiffness tensor of a single grain is known, the scalar Young's modulus of a dense polycrystalline AT sample can be derived using standard homogenization approaches (Mouiya, 2024), such as Voigt (Voigt, 1889), Reuss (Reuss, 1929), or Hill (Hill, 1952, 1963) averaging schemes.

III.2.1.2. Very specific macroscopic property leading to industrial applications

During controlled sintering, abnormal grains develop in AT polycrystalline microstructure (Bae & Baik, 1997). In combination with its anisotropic CTE, this results in the formation of a dense microcrack network due to the CTE mismatch between neighbouring grains during cooling (Babelot et al., 2011; Doncieux et al., 2017; Mouiya, 2024; Ohya et al., 1988). Initially, these microcracks were perceived as defects; however, they were later understood as beneficial features that enhance resistance to thermal shock and cyclic thermal environments (C. Chen et al., 2020). For this reason, AT has been widely employed in demanding applications, such as refractory linings for the nonferrous metals industry (Asbury, 1975), as well as in aerospace and defence components (Jiang et al., 2012).

Research on AT dates back to the 1950s and has evolved through several key stages, primarily focusing on the relationships between microstructure and properties. Early work by Lang et al., (1952) and Buessem et al., (1952) studied AT as a model material and identified hysteresis in dilatometric curves. Later, Ohya et al., (1987) attributed this hysteresis to the opening and closure of microcracks during thermal cycling. Further progress was made by Liu & Perera, (1998), who investigated the evolution of fracture strength and Young's modulus with temperature. They successfully linked these trends to the closure of microcracks and the softening of glassy phases at elevated temperatures (Ohya et al., 1988). Subsequent studies confirmed that the microcracks volume strongly influences the mechanical properties of AT (Babelot et al., 2011) and established a clear link between grain size and microcrack density (Cleveland & Bradt, 1978). By tailoring microstructures through modifications of sintering parameters, researchers have demonstrated how grain size affects strength and crack development (Babelot et al., 2011; Doncieux et al., 2017; Mouiya, 2024). Given AT's inherently low mechanical strength due to its microcracked microstructure, strategies such as grain-boundary strengthening with vitreous phases (e.g., SiO_2) were introduced to enhance both thermal stability and mechanical integrity (Chen et al., 2021).

III.2.2. AT based materials studied by TMC group for understanding microcrack effects

Over the past fifteen years, the TMC group's research on AT has progressed from fundamental microstructural designing toward validation at an industrially relevant scale. Early work focused on Marusu-based compositions to develop simplified "model materials" that reproduce the diffuse damage mechanisms observed in complex industrial refractories (Babelot et al., 2011; Doncieux et al., 2017; Mouiya, 2024; Ohin Mensan Daniel et al., 2014). This approach enabled systematic investigations into how controlled grain coarsening governs microcrack formation and, in turn, affects macroscopic thermomechanical properties. More recently, the research strategy was extended to include Ceramtec® materials in order to address the challenges associated with producing large-scale specimens in an academic environment (Mouiya, 2024). This collaboration provides access to sample volumes suitable for advanced thermomechanical testing, such as tensile and thermal shock experiments, while also enabling a critical comparison between laboratory-designed microstructures and commercially available industrial-grade materials.

III.2.2.1. Marusu based model materials

Babelot et al., (2011), Doncieux et al., (2017), Mouiya, (2024) and Ohin Mensan Daniel et al., (2014) developed three model microstructures (Non-Flexible (NF), Flexible (F), and Very Flexible

License CC BY-NC-ND 4.0

(VF)), with an additional *Ultra Flexible* (UF) grade introduced for further property tuning (see Figure III-10). It was shown that increasing grain size significantly alters AT's mechanical response, producing highly nonlinear behaviour in UF materials characterised by reduced Young's modulus and fracture strength. In recent times, (Mouiya, 2024) conducted a study using the three-model microstructure strategy (NF, F, VF), similar to Figure III-10. Readers are referred to (Mouiya, 2024) for a detailed description of the sintering procedures used to obtain the three model microstructures. These materials were produced by adjusting the sintering thermal cycle, specifically the temperature and dwell time, resulting in distinct microstructural and physical characteristics (Mouiya, Tessier-Doyen, et al., 2023). During sintering, significant grain coarsening occurs, with the initial grain size of approximately 0.3-1.5 µm increasing to varying extents depending on the processing conditions. The NF exhibits a final grain size below 20 µm, along with the highest apparent and relative densities (3.32 g/cm³ and 93.4 %, respectively) and the lowest open porosity (4.5 %). The F shows intermediate grain growth (3-40 µm), a reduced apparent density of 3.21 g/cm³ (90.4 % relative density), and an increased open porosity of 8.3 %. In contrast, the VF is characterized by exaggerated anisotropic grain growth (7–100 µm), accompanied by a counterintuitive decrease in density (3.16 g/cm³, corresponding to 89.1 % relative density) and a further increase in open porosity to 9.1 % (Babelot et al., 2011; Doncieux et al., 2017; Mouiya, 2024; Mouiya, Tessier-Doyen, et al., 2023; Ohin Mensan Daniel et al., 2014).

Consistent with previous studies, the reduction in densification observed in the VF grade, despite the more intensive sintering conditions, is attributed to the formation of an extensive microcrack network associated with abnormal grain growth, with an estimated microcrack volume fraction of approximately 3.9 % for VF compared to 2.7 % for NF (Mouiya, 2024). Furthermore, the larger grains in the VF material are associated with a higher density of microcracks, which in turn enhances the non-linear mechanical response (Mouiya, Tessier-Doyen, et al., 2023), resulting in greater hysteresis and increased strain at rupture, as illustrated in Figure III-10.

Building on these advances, it has become increasingly evident that AT materials constitute a valuable model system for fundamental research. Studies based on the Marusu model material clearly demonstrate how microstructural design governs thermomechanical behaviour under extreme conditions (Babelot et al., 2011; Doncieux et al., 2017; Mouiya, 2024; Ohin Mensan Daniel et al., 2014). In particular, the VF microstructural design highlights the role of abnormally large grains in promoting significant microcracking, which in turn enables the material to exhibit a highly flexible mechanical response (Mouiya, Tessier-Doyen, et al., 2023). This insight is broadly relevant to the field of refractory ceramics, where compositions are deliberately engineered to optimise fracture behaviour and thermal shock resistance in order to avoid catastrophic failure during service (Mouiya, 2024; Ohin Mensan Daniel et al., 2014; Tessier-Doyen, 2003). In this context, simplified AT-VF formulations, containing fewer constituents than conventional industrial refractories, provide an effective platform for isolating the influence of specific microstructural parameters and mechanisms (Mouiya, Tessier-Doyen, et al., 2023).

Despite the valuable insights offered by the Marusu model material into microstructure-thermomechanical property relationships, its in-house preparation is time-consuming. Consequently, producing large-scale specimens, for example, those required for the tensile test and for the ATHORNA device, poses significant practical challenges (Mouiya, 2024). To address these limitations, a collaboration with Ceramtec was established during Mouiya's PhD (Mouiya, 2024) to investigate similar phenomena using Ceramtec materials. Preliminary microstructural analyses revealed that the Ceramtec model material closely resembles the VF Marusu microstructure, making it a promising candidate for extending the research initiated by Mouiya,

License CC BY-NC-ND 4.0

(2024). Accordingly, the following section focuses on the Ceramtec material and its relevance to this study.

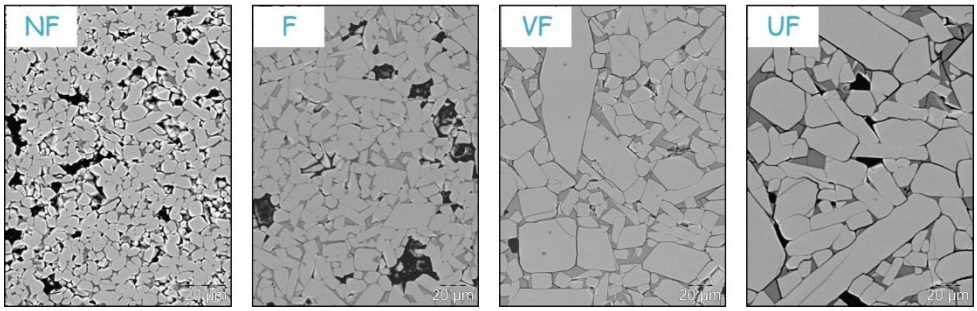

a) Representation of different Marusu AT microstructure (Doncieux et al., 2017; Huger et al., 2011; Mouiya, 2024)

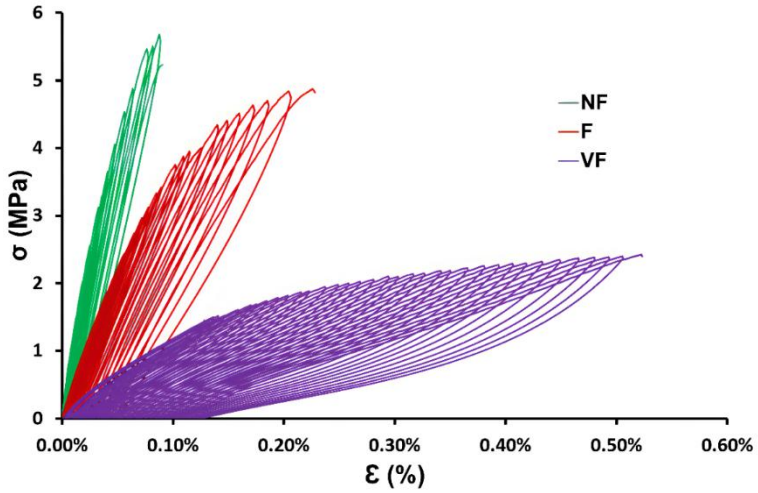

b) Marusu microstructural changes effects on the stress-strain response at room temperature (Mouiya, 2024)

Figure III-10: Microstructures of the different grades of AT and its corresponding stress-strain response under uniaxial tensile cyclic loading

III.2.2.2. Ceramtec model materials

Figure III-11a shows the Ceramtec material, a magnesium-doped AT (Al_2TiO_5) produced by reactive sintering of Al_2O_3 and TiO_5, with minor addition of SiO_2 to stabilize the phase and enhance grain bonding. As already explained above and it is an essential point, this Ceramtec material allows the TMC group to proceed to macroscopic experimental tests, especially tensile tests and ATHORNA thermal shock tests (Mouiya, 2024). It should be nevertheless noted that the chemistry of the system is not exactly comparable to that of Marusu since: i) stabilization is obtained by Mg instead of Fe, ii) a much less quantity of silica is involved (2.89% instead of 13 vol% in Marusu), iii) an incomplete reactive sintering led to some residual Al_2O_3 and TiO_2. In fact, in term of grain size and as well as porosity, this material is still quite comparable to the VF Marusu model material (Mouiya, 2024). Figure III-11b shows SEM images of this AT microstructure, where microcracks, mainly intergranular due to thermal expansion anisotropy, are visible at higher magnification, along with closed pores.

License CC BY-NC-ND 4.0

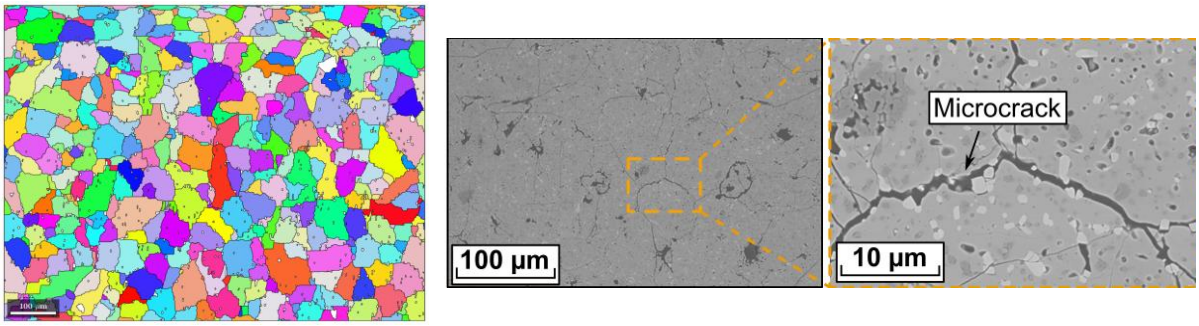

a) EBSD image of AT (courtesy to Mr. Tanguy)

b) SEM image of AT microstructure (Mouiya, 2024)

Figure III-11: Representation of Ceramtec AT's microstructural information's

In conclusion, considering the challenges associated with the in-house preparation of the Marusu material and the strong microstructural and functional resemblance of the Ceramtec material to the VF grade, it is both practical and scientifically relevant to adopt Ceramtec as the model material for the present PhD work (Mouiya, 2024). Accordingly, the following section provides a detailed overview of the macroscopic thermomechanical response of the Ceramtec material.

III.2.2.3. Macroscopic thermomechanical response

This section highlights the impact of the strong anisotropic CTE of AT model material on their thermomechanical properties. As a case study, the results obtained by Mouiya, (2024) are discussed, focusing on the evolution of apparent thermomechanical properties such as Young's modulus and dilatometry response in relation to microstructural changes during cooling. Figure III-12a presents the results for the Ceramtec AT model material (see section III.2.2.2). The orange curve corresponds to Young's modulus, measured using an ultrasound echography technique up to 1400 ℃. The blue curve shows the dilatometry results, while the green dashed line indicates the acoustic emission response (Mouiya, 2024).

The Young's modulus data (see Figure III-12a) clearly reveal a hysteresis loop during the heating-cooling cycle, reflecting the closing and opening of microcracks. The hysteresis is particularly pronounced due to the substantial CTE mismatch between the elongated AT grains. Since the focus here is on the impact of anisotropic CTE during cooling, the heating stage is not discussed in detail (see (Mouiya, 2024) for further information). At the start of cooling at 1400 ℃, the AT sample exhibits 170 GPa and depicts an increasing trend, consistent with the stiffening of the glassy phase. Between 1160 ℃ and 780 ℃, the Young's modulus increases gradually, reflecting an undamaged stage where the AT material behaves like a stable, crack-free ceramic. A critical temperature is observed at ~780 ℃, where a sudden and significant drop in Young's modulus coincides with a spike in acoustic emission counts (green dashed curve Figure III-12a). This marks the onset of microcracking, caused by the substantial anisotropic thermal expansion mismatch between neighbouring grains with random orientations (Mouiya, 2024).

The dilatometry results (blue curve in Figure III-12a) corroborates the above mechanisms. After firing at 1400 ℃, the microcracks are closed and grains are strongly bonded, yielding an apparent CTE of ~10.78 × 10^{-6} K^{-1} during the initial cooling stage. This value closely matches the mean grain CTE (average of three CTE of the monocrystal) of 10.14 × 10^{-6} K^{-1}. As cooling progresses, the apparent CTE gradually decreases to about 8.8 × 10^{-6} K^{-1}, slightly lower than the mean grain CTE. At ~780 ℃, however, a sharp slope change occurs, indicating the triggering of microcracking. After this point, the apparent CTE dramatically shifts to a negative value (−4.73 × 10^{-6} K^{-1}), quite close to that of the AT a-axis CTE (α_a). This behaviour implies that the c-axis expansion (the highest

License CC BY-NC-ND 4.0

CTE direction) no longer contributes significantly to the bulk expansion due to stress relaxation and microcracking. As a result, the final effective CTE of the material at room temperature is strongly reduced (Bayer, 1971; Morosin & Lynch, 1972; Mouiya, 2024; Skala et al., 2009).

In addition, uniaxial tensile tests with loading-unloading cycles were performed under isothermal conditions at different temperatures (see (Mouiya, 2024) for details). Microstructural configurations from both undamaged and damaged regions were considered, corresponding to points-*a* (850 ℃) and-*b* (20 ℃) in the Young's modulus curve (Figure III-12a).

At 850 ℃ (point-*a*), the material shows a brittle, nearly linear elastic response, reaching a strength of ~11.4 MPa without significant hysteresis or residual strain after unloading. In contrast, at 20 ℃ (point-*b*), the response is very nonlinear, with hysteresis and residual strain due to pre-existing microcracks from CTE anisotropy (Figure III-12b). These microcracks expand during loading before localizing into a macrocrack (Mouiya, 2024), producing diffuse damage and a strain increase of ~0.12% at the maximum stress of 8.6 MPa, just before rupture (Mouiya, 2024).

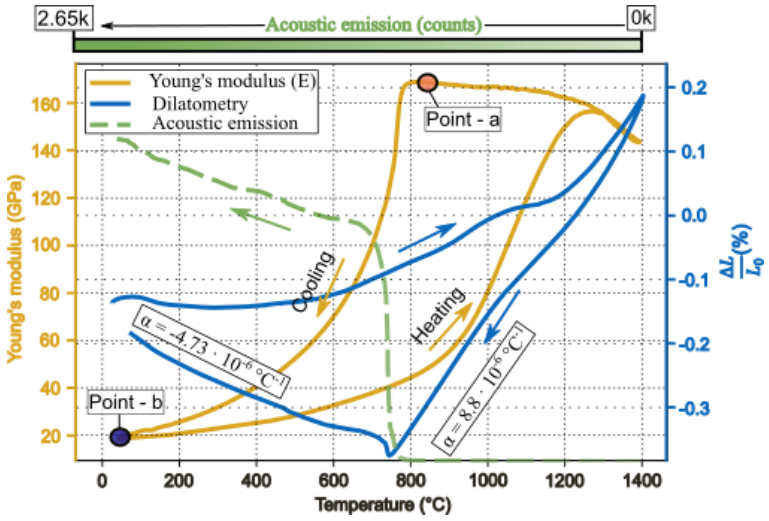

a) Young's modulus and dilatometry

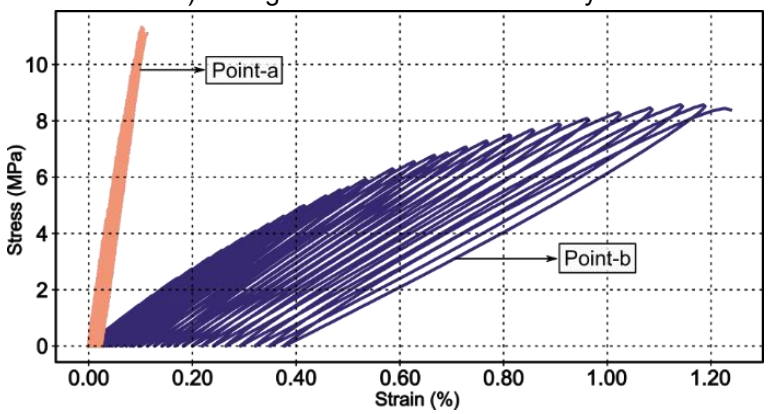

b) stress-strain response

Figure III-12: CERAMTEC microstructural changes effects on the thermomechanical properties versus temperature (Mouiya, 2024)

In summary, the case study highlights that the highly anisotropic CTE of AT single grains, combined with coarser grains in a random local orientation, promotes extensive microcracking during cooling and influences the evolution of apparent thermomechanical properties of the model material (Mouiya, 2024). In addition, these microcracked sample when subjected to mechanical loading,

License CC BY-NC-ND 4.0

exhibits a non-linear response, which is very similar to the previous case study (andalusite based castable (Kakroudi, 2007)).

III.2.3. From real polycrystalline microstructures to virtual ones

This section focuses on digitalizing a polycrystalline microstructure that considers some of the key features of real refractory materials. As discussed in section I.4.4, the application of the iDLSM approach to investigate refractory model materials remains largely unexplored. Overall, limited research has been conducted on modelling materials that exhibit anisotropic CTE and promote microcrack (initiation and propagation) due to anisotropic CTE mismatch, using numerical approaches. To address this gap and isolate the mechanism of microcracking arising from anisotropic CTE mismatch, a virtual polycrystalline model is proposed.

III.2.3.1. Simplified polycrystal design

The AT polycrystalline material consists of multiple grains with orthorhombic crystal structures, each possessing a unique orientation that forms grain boundaries at adjacent interfaces (Mouiya et al., 2024). Sintering generates pores at random locations, both within grains and along boundaries (Mouiya, Tessier-Doyen, et al., 2023). Reproducing the main features of this morphology is essential for realistic microstructure-based modelling.

In the present PhD work, the iDLSM framework (see Chapter II) is employed to simulate polycrystalline models. Accordingly, clustering the DEs into distinct groups enables the generation of a polycrystalline structure. To simplify the model, grains are assumed equiaxed (approximately like Figure III-11a), eliminating the influence of grain shape. Also, the grains are supposed to have random crystallographic orientations. For example, the real microstructure shown in Figure III-13a consists of seven grains. By applying the clustering strategy, a corresponding polycrystalline model with seven equiaxed grains is generated, as illustrated in Figure III-13b.

Now, random crystallographic orientations are assigned to each grain, highlighted by different colors on Figure III-13c. Also, such representations highlight the grain boundaries present in the sample (Mouiya, 2024). This “grain mapping” process allows the assignment of anisotropic properties, such as thermal expansion coefficients and potentially elastic properties, based on the crystallographic orientation. In this model, secondary phases and chemical interactions are neglected, assuming a chemically inert microstructure.

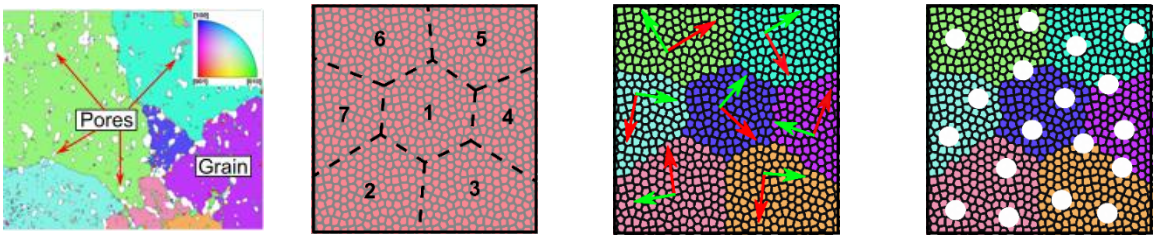

a) EBSD orientation map (Mouiya, 2024) b) DEs clustered as grains c) defining grain boundaries d) embedding pores

Figure III-13: Schematic sketch of strategy to generate simplified polycrystalline model

Porosity, inherent to real AT microstructures, is also incorporated by randomly removing a fraction of DE’s corresponding to the volume fraction of pores observed in the real microstructure. For simplicity, uniform spherical pores are introduced, as shown in Figure III-13d. In this way, the iDLSM framework facilitates the generation of both dense and porous polycrystalline models that faithfully capture the essential features of experimental microstructures.

License CC BY-NC-ND 4.0

Finally, to better replicate the complexity of refractory microstructures, a periodic polycrystalline domain, with or without pores, can be generated using the PBC strategy described in section II.2.1. In this PhD work, the PBC approach is implemented to effectively depict the heterogeneity inherent from a real refractory microstructure, offering a simplified yet representative framework for integrating microstructural variability into the modeling process.

III.2.3.2. Choice of input parameters

The following section outlines the methodology for determining the values of the different thermo-mechanical parameters that are required for performing simulation. Table III-1 list the parameters employed in the study of polycrystalline sample. In this study, due to the lack of stiffness tensor available in the literature, AT grains are assumed to be mechanically isotropic. So, the chosen Young's modulus value of 168 GPa corresponds to the macroscopic experimental value measured at 1200 ℃ (see orange curve in Figure III-12a) (Mouiya, 2024). In addition, as no clear measure of the AT Poisson's ratio at high temperature is available in the literature, the value of 0.28 was chosen from the Materials Project database (Jain et al., 2013). Finally, the three CTE values were obtained from (Bayer, 1971; Doncieux et al., 2017; Fei, 2013), which provide α_a= -2.38 × 10^{-6} K^{-1}, α_b = 11.97 × 10^{-6} K^{-1} and α_c = 20.80 × 10^{-6} K^{-1}. Then, a decreasing ratio of 13% was applied to all these CTE values (see Table III-1) to match the beginning of the experimental dilatometry measurements in Figure III-12a at 1200 ℃. This ratio can be regarded as an implicit means of accounting for the presence of the silica interphase within the microstructure (Mouiya, 2024; Mouiya, Tessier-Doyen, et al., 2023). It is important to note that this decreasing ratio was originally derived from the VF Marusu model (13% accounting to the glassy phase) (Mouiya, 2024).

Table III-1:Input data, assuming to be representative of local properties of each AT grain at initial temperature T_0 = 1200 ℃ (Mouiya, 2024) and used in DEM simulation

Parameters	Type of parameters		Value	Units
Young's modulus	Material	E	168	GPa
Poisson's ratio	Material	ν	0.28	-
CTE along $\vec{a}$	Material	α_a	−1.975 ×10^{-6}	K^{-1}
CTE along $\vec{b}$	Material	α_b	9.9351 ×10^{-6}	K^{-1}
CTE along $\vec{c}$	Material	α_c	17.264 ×10^{-6}	K^{-1}
Number of crystals	Numerical	N	500	-
Number of DE	Numerical	N_{DE}	≈20k	-

For the further simulations of the cooling stage, the temperature range [1200 - 20 ℃] was chosen as AT exhibited significantly negligible viscous behavior below 1200 ℃. So, thermal internal stresses are considered to initiate at this temperature as no viscous flows and creep are present below this temperature (Mouiya, 2024; Ranganathan et al., 2025). Unless otherwise specified, the polycrystalline models in the upcoming chapters use the material properties listed in Table III-1, with parameter variations applied only when explicitly stated.

III.3. Composite model material

Building on the findings of (Kakroudi (2007) on andalusite-based castable, attention was drawn to the potential of using large monocrystalline aggregates exhibiting pronounced anisotropy in their CTE. Andalusite aggregates are able to fully express their crystallographic anisotropy, with thermal expansion along the $\vec{a}$-axis being markedly higher than that of the surrounding cementitious matrix (12.9 × 10^{-6} K^{-1}), while expansion along the $\vec{c}$-axis remains significantly lower (3.1 × 10^{-6} K^{-1}). This directional mismatch creates favourable conditions for stress redistribution during thermal cycling (M. G. Kakroudi et al., 2009).

Inspired by this concept, Mouiya et al., (2026) developed an alumina-aluminum titanate (Al_2O_3/AT) composite architecture through collaborative research (initiated between Saint-Gobain®, Safran®,

License CC BY-NC-ND 4.0

and IRCER) aiming to improve thermal shock resistance via deliberate microstructural design. This approach benefited from the availability of large electrofused aluminum titanate monocrystals originally produced by Saint-Gobain®. Incorporating these highly anisotropic AT inclusions into a fine-grained alumina matrix enabled the creation of a simplified "model material," in which thermal expansion mismatch was intentionally used to generate a controlled population of microcracks during cooling (Mouiya, 2024).

Within this framework, Mouiya and co-workers (Mouiya et al., 2026) systematically investigated the influence of coarse AT monocrystal content on microcrack formation and the resulting evolution of key material properties, including Young's modulus, effective thermal expansion, and stress-strain response. The following sections therefore introduce this composite model system and summarize the principal insights reported in the studies of Mouiya et al., (2026) regarding the role of anisotropic aggregates in enhancing thermal shock tolerance.

III.3.1. Monocrystal AT aggregates

As previously mentioned, here, only monocrystal aggregates will be studied. These AT aggregates are depicted in Figure III-14. Such AT aggregate was sourced from Saint-Gobain® and produced through a carefully controlled electrofusion process (Mouiya et al., 2026). This synthesis method involves melting a precise mixture of precursor oxides in an electric arc furnace, followed by controlled cooling to yield large ingots. These ingots are then subjected to a meticulous grinding and sieving process to obtain relatively large, monocrystals, with a targeted particle size distribution of 150-250 μm (which are coarser aggregates). The resulting aggregates are highly crystalline and exhibit pronounced anisotropy, which is fundamental to their behaviors in composite systems (Mouiya, 2024).

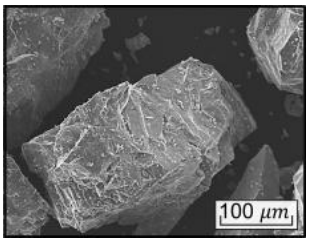

Figure III-14: AT monocrystal (Mouiya et al., 2026)

Chemically, the AT aggregates are not pure Al_2TiO_5 but are intentionally stabilized with dopants to prevent phase transformations as explained in section III.2.1. The grains are primarily composed of aluminum oxide (Al_2O_3, 40.5 wt.%) and titanium oxide (TiO_2, 51 wt.%). To stabilize the material, magnesium oxide (MgO, 4.85 wt.%) and iron oxide (Fe_2O_3, 0.39 wt.%) are incorporated, a common strategy that prevents the apparition of β-Al_2TiO_5 phase during cooling. Minor components include silica (SiO_2, 1.16 wt.%) and zirconium oxide (ZrO_2, 2.1 wt.%). These dopants not only stabilize the crystal structure but also influence the mechanical and thermal properties of the aggregates (Mouiya, 2024).

III.3.2. Alumina-AT composite microstructure

Alumina-AT composites (Figure III-15) were prepared with electrofused AT aggregates (150-250 µm, 0-10 wt.%) embedded (randomly) in a fine-grained alumina matrix (99.8 wt.% Al_2O_3, initial grain size of D_{50} = 0.4 μm, trace MgO). Regarding the sample preparation and sintering processing readers can refer to (Mouiya, 2024). These steps yielded the targeted microstructures with four AT volume fractions (Mouiya et al., 2026).

License CC BY-NC-ND 4.0

Figure III-15a and b present the composite microstructures containing 5 wt% and 10 wt% of AT grains, respectively, which are uniformly dispersed within the alumina matrix. During sintering, controlled microcracking is induced as a consequence of CTE mismatch between the anisotropic AT aggregate and the alumina matrix. The cracks are predominantly radial to the AT aggregates, and it seems they are highly populated in higher volume fraction microstructures in comparison to lower one. The variation in microcrack morphology suggests that the volume fraction of AT plays a critical role in governing the thermomechanical response of the composite, thereby motivating a detailed understanding into the evolution of its thermomechanical properties as a function of temperature (Mouiya, 2024).

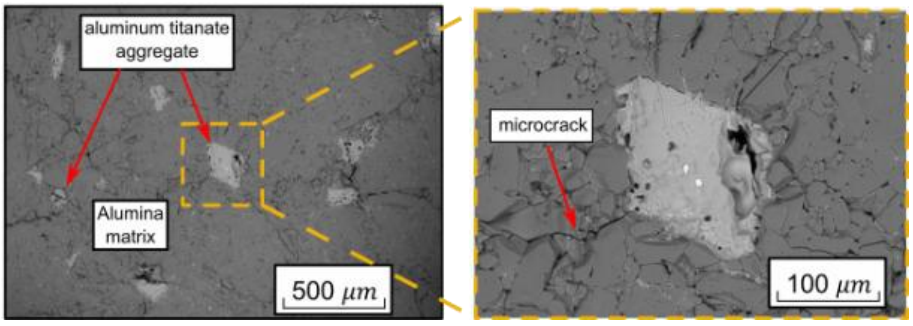

a) 5 wt% of AT

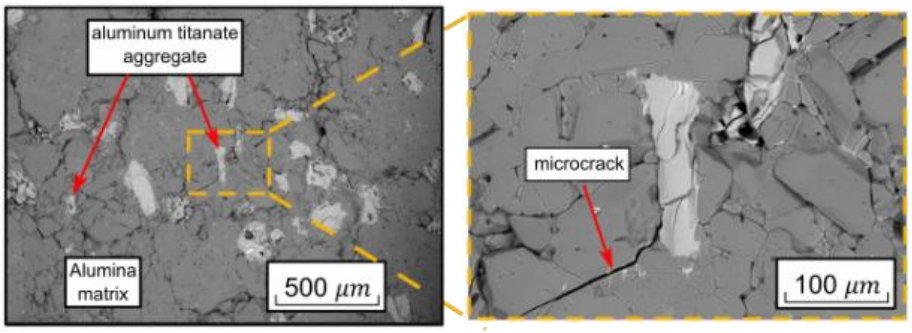

b) 10 wt% of AT

Figure III-15: Composite microstructure design (Mouiya, 2024)

III.3.3. Macroscopic thermomechanical response

This section provides an overview of the four microstructural designs investigated, corresponding to alumina matrices containing 0 wt% (denoted as Al_2O_3/AT-0%), 2.5 wt% (Al_2O_3/AT-2.5%), 5 wt% (Al_2O_3/AT-5%), and 10 wt% (Al_2O_3/AT-10%) aluminum titanate (AT). The corresponding results obtained using high temperature measurements are presented in Figure III-16. Figure III-16a illustrates the role of AT weight percentage in microcrack initiation by acoustic emission technique; Figure III-16b, its effect on the apparent Young's modulus, and Figure III-16c, on the stress-strain behavior (Mouiya et al., 2026).

From Figure III-16a, acoustic emission results clearly show that microcrack density increases with AT content. The 10 wt % composite exhibits the highest microcrack count, as indicated by the "Al_2O_3/AT-10%" curve. As discussed earlier in section III.2.2.3, microcracking strongly influences the apparent thermomechanical behavior. Therefore, understanding how AT volume fraction and the associated microcrack density impact the thermomechanical properties, is essential to interpreting the following results (Mouiya, 2024; Mouiya et al., 2026).

License CC BY-NC-ND 4.0

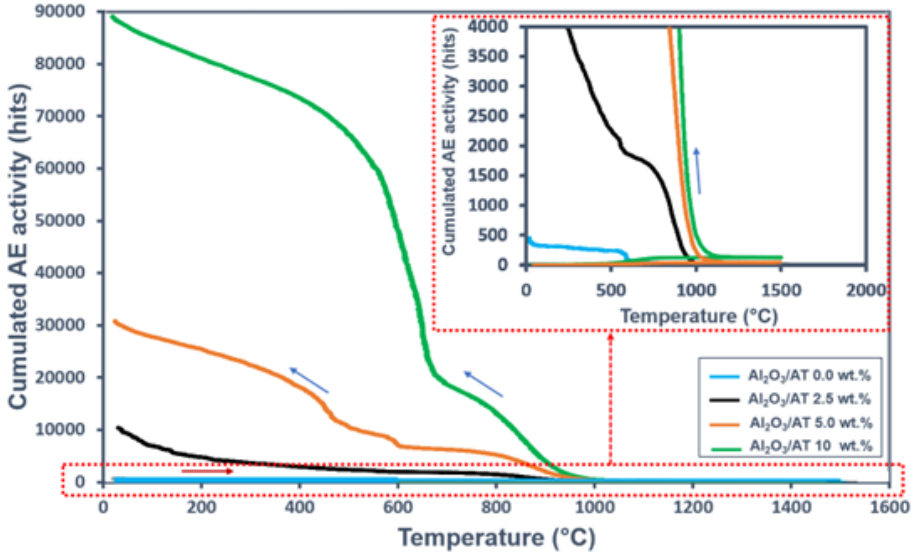

a) acoustic emission

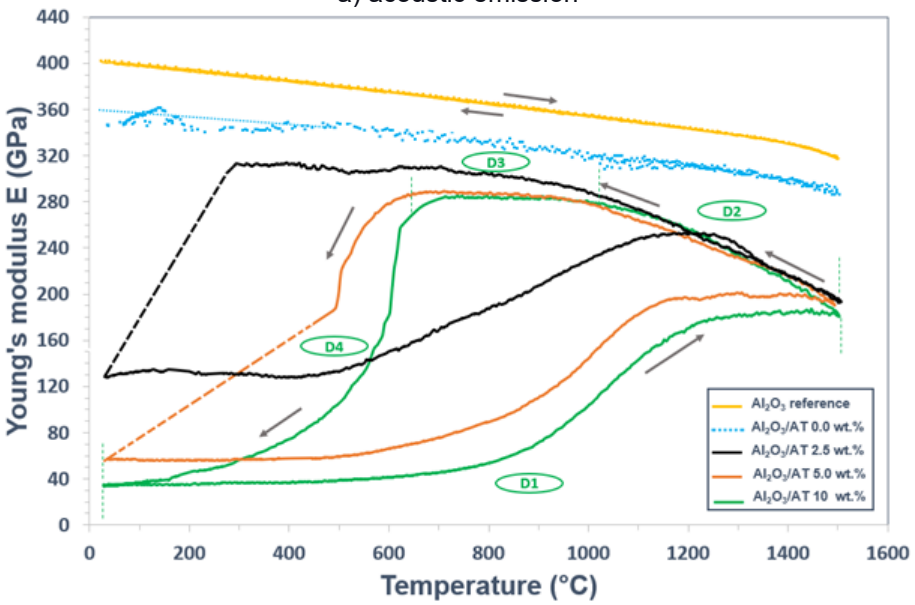

b) Young's modulus

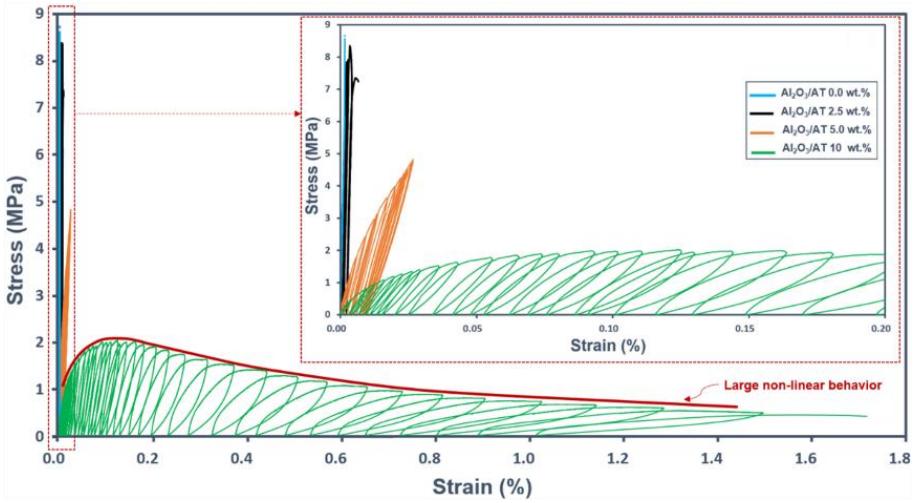

c) stress-strain response at room temperature

Figure III-16: AT volume fraction effects on the composite microstructure-property relationship (Mouiya, 2024)

License CC BY-NC-ND 4.0

This relationship is further illustrated in Figure III-16b, where the incorporation of AT significantly affects the apparent Young's modulus with temperature. Hysteresis becomes more pronounced with higher AT fractions, reflecting the increase in microcrack density during thermal cycle on promoting higher AT wt%. Also, the onset temperature of stiffness drops shifts to higher temperatures as AT content rises, indicating earlier microcrack initiation. Consequently, the Young's modulus decreases more rapidly with increasing AT content, following the order: Al_2O_3/AT-0wt% > Al_2O_3/AT-2.5wt% > Al_2O_3/AT-5wt% > Al_2O_3/AT-10wt% (Mouiya, 2024; Mouiya et al., 2026).

Finally, the mechanical behaviors are revealed through room-temperature tensile tests (Figure III-16c). The 0 and 2.5 wt.% composites show linear elastic behavior up to 6.5 MPa, while higher AT contents increase nonlinearity. The 10 wt.% composite exhibits lower strength but a higher strain to rupture, consistent with its elevated microcrack density. This mechanical response supports the thermal observations, indicating that increased AT content promotes quasi-brittle behavior through microcrack formation and energy dissipation (Mouiya, 2024; Mouiya et al., 2026). Similar trends were reported by (Kakroudi, 2007) for andalusite castable (see section III.1.3), attributed to the anisotropic CTE of andalusite aggregates.

III.3.4. From real composite microstructures to virtual ones

This section focuses on digitalizing a composite microstructure that embodies the key characteristics of real refractory materials. As discussed in section I.4.4, only a limited number of studies have employed numerical approaches to investigate the microstructure-thermomechanical behavior of composite model materials that promote microcrack due to CTE mismatch between the aggregates and the matrix. However, no studies have considered the aggregates as monocrystals exhibiting anisotropic CTE within such composite model material study. To address this research gap and to isolate the mechanism of microcracking induced by anisotropic CTE mismatch between matrix and aggregate, a simplified composite iDLSM model is proposed.

III.3.4.1. Simplified composite design

In the present model, the aggregates are uniformly distributed throughout the composite domain (see Figure III-17a). The inclusion volume fraction, number, and spatial distribution are key parameters in the model. In the reference microstructure (see Figure III-17a), inclusions are randomly distributed throughout the matrix, representing a volume fraction of approximately 11.2 vol% (equivalent to 10 wt%) (Mouiya, 2024). To replicate this configuration while minimizing computational cost, the following simplifications are introduced:

- inclusions are assumed to be spherical;
- overlapping inclusions are not considered;
- the inclusion counts accounts to the target volume fraction;
- inclusions are either randomly or regularly arranged in the PBC domain;
- no pores are considered for simplicity.

Therefore, Figure III-17b and c, illustrates the schematic sketch of a composite virtual model, considering these assumptions. It is worth that, again, periodic boundary conditions are used to enable multi-scale modelling. Clustering approach of aggregate is again employed to segregate the DE's as matrix and inclusion, as depicted in Figure III-17b and c (Nguyen, 2019). Finally, the inclusions are assigned with random local crystallographic orientation similar to section III.2.3.1, which is depicted in Figure III-17d and e. Indeed, such approximations are necessary to highlight the CTE mismatch between matrix and inclusion (Mouiya, 2024). Here the inclusion is considered as a monocrystal that exhibits anisotropic CTE.

License CC BY-NC-ND 4.0

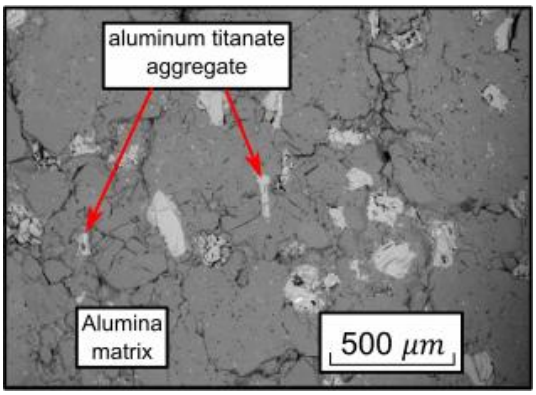

a) real microstructure (Mouiya, 2024)

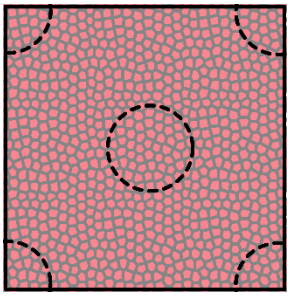

b) virtual microstructure (regular arrangement)

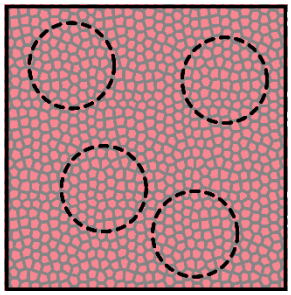

c) clustering for random arrangement

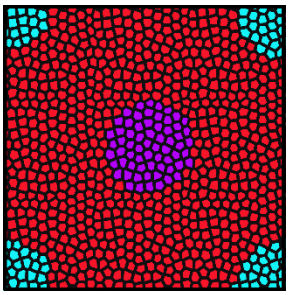

d) regular inclusion with local orientation

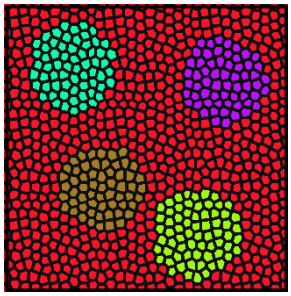

e) random inclusion with local orientation

Figure III-17: Schematic sketch of the strategy to generate composite model

Under PBC, the spatial arrangement of inclusions strongly influences the homogenized behavior of two-constituent microstructures (Firooz et al., 2019; Lemaitre et al., 2016; Mityushev, 2015a, 2015b). In a regular arrangement, the inclusions repeat in an identical pattern throughout the material. This repetition ensures that each sample gives the same overall response, but the response itself depends on direction: the material behaves differently along the lattice axes than along the diagonals, because the geometric pattern favors certain orientations (Firooz et al., 2019). In contrast, a random packing has no preferred direction, each realization of the microstructure is slightly different, producing small variations in the computed results, but when many such random samples are averaged, their overall response becomes uniform in all directions (Firooz et al., 2019; Schneider et al., 2021). Beyond these directional effects, arrangement also governs local interactions: differences in the spacing and clustering of inclusions control where stresses or fluxes concentrate, making effective stiffness highly sensitive to arrangement, especially at high phase contrast (Firooz et al., 2019; Lemaitre et al., 2016; Mityushev, 2015a). Because periodic boundaries effectively wrap the microstructure onto itself, inclusions near the edges can interact with their own periodic images, creating artificial connections unless a minimum separation is maintained (Lemaitre et al., 2016; Schneider et al., 2021). To obtain unbiased and representative results, random representative volume elements (RVEs) must be properly periodized and sampled through multiple realizations (Brisard et al., 2023; Lemaitre et al., 2016; Schneider et al., 2021), while both

License CC BY-NC-ND 4.0

regular and random arrangements must be matched in volume fraction, size distribution, and minimum gap (Brisard et al., 2023; Lemaitre et al., 2016; Schneider et al., 2021). Ultimately, careful control of inclusion arrangement under periodic boundary conditions is essential to ensure that observed differences in effective properties reflect genuine microstructural effects rather than artifacts of geometric repetition, directional bias, or sampling variability (Brisard et al., 2023; Firooz et al., 2019; Lemaitre et al., 2016; Mityushev, 2015a; Schneider et al., 2021).

In practical microstructures, aggregates are generally dispersed within the matrix in a random manner. A first modelling strategy is therefore to reproduce this inherently random spatial distribution of inclusions. However, adopting such a representation requires generating and analyzing multiple microstructural realizations in order to obtain an averaged apparent behavior, since each random configuration introduces statistical fluctuations and potential deviations from perfect isotropy (Asadi, 2021). To reduce this computational burden, one may instead exploit a regular inclusion arrangement combined with periodic boundary conditions (PBC), which, at least geometrically, can provide a single, statistically representative configuration without the need for multiple samples. Care must be taken, however, because even with a regular packing, the presence of randomly oriented crystallographic phases reintroduces stochastic effects that may still influence the effective response. Consequently, a part of this PhD work is to determine which strategy, random versus regular spatial positioning of inclusions under PBC, offers the most reliable and efficient representation of the microstructure within the iDLSM framework.

III.3.4.2. Choice of input parameters

The following section outlines the methodology adopted to determine the thermo-mechanical parameters required for the simulations. Table III-2 lists the parameters employed in the study of the composite sample. The primary objective of this PhD work is to investigate the effect of the anisotropic CTE of the inclusion on microcrack initiation and propagation arising from the CTE mismatch between the matrix and the inclusion.

The Young's modulus of the alumina matrix (E^{Al}) is treated as a temperature dependent property, expressed through a linear trend describing the result experimentally observed for composite material containing Al_2O_3/AT-0% (alumina matrix in Figure III-18a). The Poisson's ratio of alumina (ν^{Al}) has been assumed to be constant in the overall temperature range with a classical value of 0.24 (Tessier-Doyen, 2003). Furthermore, polycrystalline alumina matrix is assumed to exhibit isotropic thermal expansion with a temperature dependent coefficient α^{Al} (dividing by three the volume coefficients a_0, a_1 and a_2 that could be found in (Fei, 2013), see Figure III-18b. This combination of temperature dependent Young's modulus and CTE values ensure a realistic representation of the thermomechanical behavior of alumina matrix.

For the AT aggregate phase, only the Young's modulus (E^{AT}) and CTE's (α_a^{AT}, α_b^{AT} and α_c^{AT}) values differ from those used in section III.2.3.2. In this specific case of the composite, the Young's modulus value has been arbitrarily adjusted to reproduce the experimentally observed result of the composite at high temperature, as shown in Figure III-16b. It is important to note that, although Young's modulus is known to vary as a function of temperature, this behavior is not well documented for AT. Therefore, in this case, Young's modulus was assumed to be constant over the entire temperature range considered. Regarding thermal expansion, the pure AT CTE values have been employed in the model since the structure of the AT aggregates (considered as monocrystals) does not contain any silica, allowing the inherent anisotropy of AT to directly affect the overall thermomechanical behavior. Accordingly, the principal CTE components of AT are thus α_a^{AT}= -2.38 × 10^{-6} K^{-1}, α_b^{AT} = 11.97 × 10^{-6} K^{-1}, α_c^{AT} = 20.80 × 10^{-6} K^{-1}, as reported in Reference (Bayer, 1971; Doncieux et al., 2017; Fei, 2013).

License CC BY-NC-ND 4.0

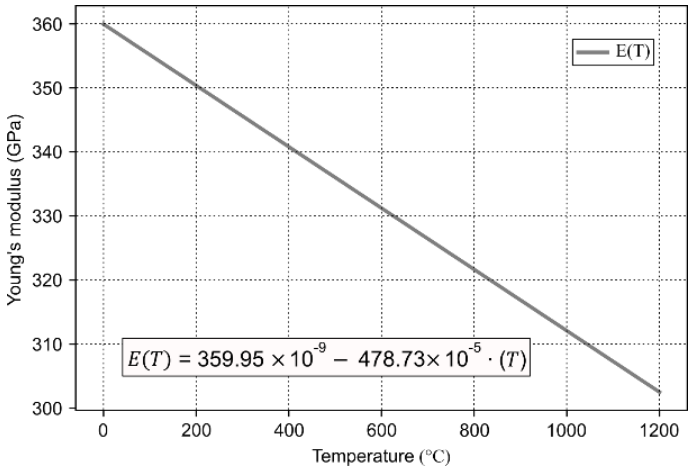

a) Linear trend describing Young's modulus variation versus temperature experimentally observed for composite material containing Al_2O_3/AT-0% (Mouiya et al., 2026; Munro, 2004)

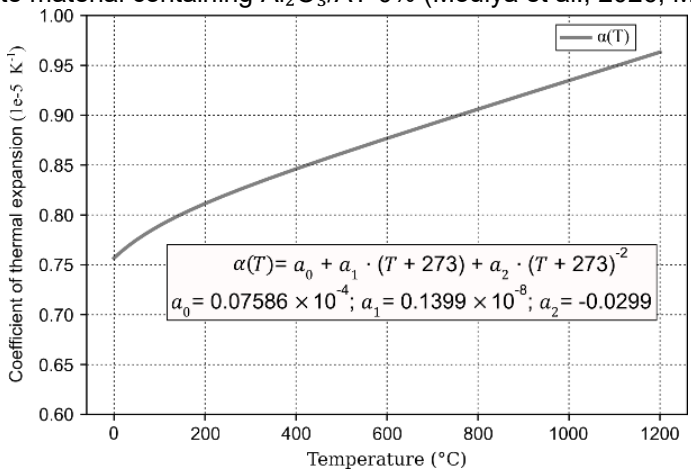

b) Polynomial trend classically used to describe alumina average CTE evolution versus temperature coming from the values of three crystallography axis of a monocrystal (Fei, 2013)

Figure III-18: Analytical equations used to describe thermomechanical property evolution versus temperature for alumina matrix

Table III-2 :Input data, assuming to be representative of local properties of the alumina matrix and of the AT inclusions used in DEM simulation

Alumina matrix	**Symbol**	**Value**	**units**
Young's modulus	E^{Al}	$E(T) = 359.95 \times 10^{-9} - 478.73 \times 10^{-5} \cdot (T)$	GPa
Poisson's ratio	ν^{Al}	0.24	
Isotropic CTE	α^{Al}	$\alpha(T) = a_0 + a_1 \cdot (T + 273) + a_2 \cdot (T + 273)^{-2}$ $a_0 = 0.07586 \times 10^{-4}$; $a_1 = 0.1399 \times 10^{-8}$; $a_2 = -0.0299$	K^{-1}
AT inclusion	**Symbol**	**Value**	**units**
Young's modulus	E^{AT}	120	GPa
Poisson's ratio	ν^{AT}	0.28	
CTE along $\vec{a}$	α_a^{AT}	-2.38×10^{-6}	K^{-1}
CTE along $\vec{b}$	α_b^{AT}	11.97×10^{-6}	K^{-1}
CTE along $\vec{c}$	α_c^{AT}	20.80×10^{-6}	K^{-1}
Numerical properties	**Symbol**	**Value**	**units**
Number of inclusions	N	5	
Number of DE	N_{DE}	20k	

License CC BY-NC-ND 4.0

Again, the temperature range of [1200 − 20 ℃] was selected for thermal loading for the same reason explained in section III.2.3.2. Unless stated otherwise, all subsequent composite models use the material properties in Table III-2, with variations applied only when specified.

III.4. Expected Outputs and Workflow using Different Model Microstructure

During cooling, both the AT and composite model materials are prone to microcracking due to the CTE mismatch between neighbouring grains and two phases (Mouiya, 2024). For example, Figure III-11b shows an SEM image of a sintered AT microstructure with microcrack branching, along grain boundaries and into grains. However, no existing technique can dynamically monitor crack trajectories (in a microstructure) during cooling. So, a question arises about the location of microcrack nucleation and the directions of their propagation.

The modelling technique enables in-situ monitoring of microcracks. Section II.2.3 details the crack management procedure in the iDLSM framework. The crack is considered to appear when a bond between two DE's reaches the material's strength. For an illustration purpose the crack management is explained using the polycrystalline model material. In such a case, a microcrack is initiated and a post-processing geometrical technique is applied to determine whether this microcrack exists as a single isolated one or as a part of a cluster of "touching" microcracks identifying by a unique label and color (Figure III-19a). This technique will be helpful to understand, as cooling progresses, if the microcracks are interconnected into networks, occasionally merging into a larger crack system (see an illustration in Figure III-19b). This allows iDLSM to accurately track the evolving microcrack/crack trajectories within the numerical sample (Ranganathan et al., 2025, 2026).



a) cracks at random location b) merging of cracks

Figure III-19: Crack extension identification mechanisms in iDLSM framework

Furthermore, as shown in Figure III-12, the evolving microstructure significantly affects the apparent behaviour. Following the approach outlined in section II.2, iDLSM quantifies thermal strain, Young's modulus, and stress-strain response as functions of temperature during the thermomechanical simulations. The thermomechanical framework adapted in the present PhD is illustrated in Figure III-20. The framework follows four main stages (Ranganathan et al., 2025):

1. Generation of the polycrystalline sample (with or without pores);
2. Assigning material properties to the model.
3. Running cooling simulation:
   (i) the sample is cooled from 1200 ℃ to 1100 ℃…20 ℃ (Ranganathan et al., 2025, 2026);
   (ii) microcrack trajectories and stress evolution are continuously monitored;
   (iii) as an outcome, the dilatometric response of the numerical samples are extracted;
4. Running tensile test simulation:
   (i) the microcracked sample is subjected to uniaxial tensile monotonic and cyclic loading;
   (ii) as an outcome of monotonic loading, the Young's modulus and stress-strain response is evaluated as functions of the cooling temperatures. In addition, the irreversible strains exhibited by the sample are captured under cyclic loading.

License CC BY-NC-ND 4.0

This stepwise framework enables detailed understanding of the microstructure-property relationships that control the thermomechanical performance of the model refractory material.

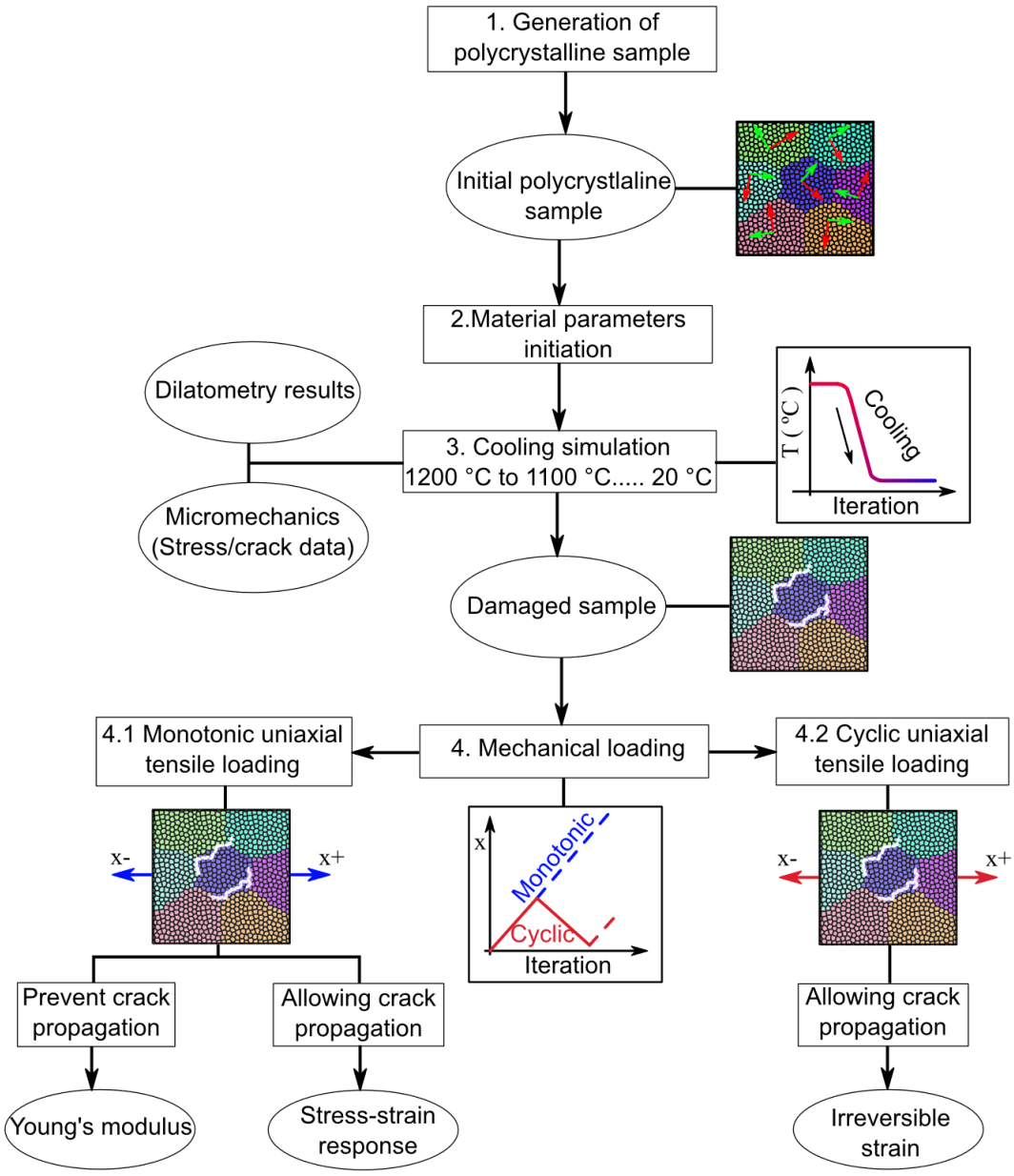

Figure III-20: Thermomechanical analysis framework

With this in mind, Figure III-21 provides an overview of the workflow considered in this PhD study. The figure highlights the introduced two-model microstructure design, where AT and Al_2O_3/AT are used as the model material systems.

License CC BY-NC-ND 4.0

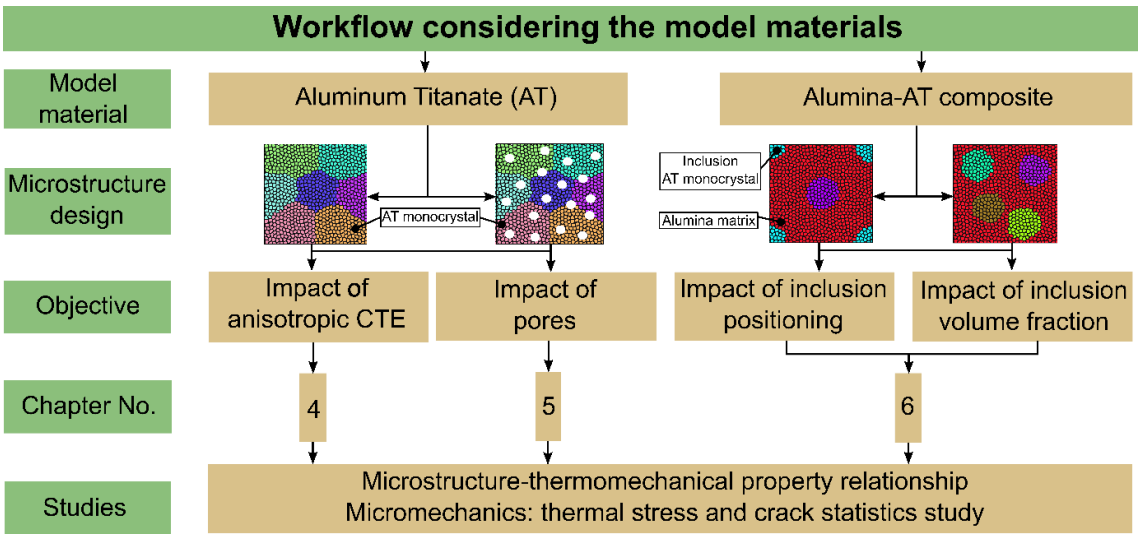

Figure III-21: Overview of the workflow considering different model material and microstructure

License CC BY-NC-ND 4.0

Chapter IV. iDLSM modelling of microcracking induced by anisotropic thermal expansion: polycrystalline case study

IV.1. Introduction

Having explored microstructure-property relationships in refractories through four industrial case studies (see Chapter III), it is now important to highlight the interest and also to validate the applicability of the iDLSM framework for investigating refractory microstructures.

The previous case studies reveal that aggregate characteristics have a strong influence on microcrack initiation and propagation that play a major role on thermal shock resistance. Microcracking or decohesion typically arises from CTE mismatches between grains within aggregates (Mouiya, Tessier-Doyen, et al., 2023) or between the aggregate and matrix (M. G. Kakroudi et al., 2009). This effect intensifies when coarse grains exhibit pronounced anisotropic CTE behavior, particularly when one crystallographic axis shows near-zero or negative expansion, as in andalusite (Kakroudi et al., 2008; Mouiya et al., 2026), leading to high thermal stresses during cooling and the formation of dense, interconnected microcrack networks that affect the bulk thermomechanical response.

As discussed previously, few prior works (approx. 5) have numerically examined the influence of anisotropic CTE with cracks (Fertig & Nickerson, 2016; Geraci & Aliabadi, 2018; Ortiz & Suresh, 1993; Sridhar et al., 1994; Zhang et al., 2020). Building on the work of Case et al., (1981) and Yousef et al., (2005), the use of a polycrystalline material enables isolation of anisotropic CTE effects and the introduces grain-grain interactions that promote microcracking. However, alumina is unsuitable as its anisotropic CTE and resulting microcrack density are less pronounced than those of andalusite (Kakroudi, 2007). At the same time, as explained in section III.1.3, while andalusite-based refractories exhibit excellent thermal shock resistance, their limited refractoriness motivates the exploration of alternative aggregates.

Aluminum titanate (AT) is a suitable model material (Babelot et al., 2011; Doncieux et al., 2017; Huger et al., 2011; Mouiya, 2024; Ohin Mensan Daniel et al., 2014), combining superior physical properties with CTE anisotropy comparable to andalusite (Kakroudi, 2007). Its orthorhombic crystal structure induces intrinsic anisotropic thermal expansion, and abnormal grain growth during sintering can promotes CTE mismatches that initiate microcracking. Consequently, microcracked AT exhibits a very strong non-linear macroscopic mechanical response, which experimental evidence links to material toughening, higher fracture toughness, and enhanced thermal shock resistance (Mouiya, Martynyuk, et al., 2023). Therefore, in order to deepen the understanding of the anisotropy CTE's impact on microcrack initiation, a simplified polycrystalline AT material is employed as a model material.

In fact, despite considering the simplified microstructure (such as AT) as model materials, they could exhibit complex thermomechanical behavior that can mimic some aspects of industrial refractories (Huger et al., 2007). Hence, it is crucial to understand better the strong relationships between such simplified microstructures and the macroscopic thermomechanical behavior of these model materials in order to enhance the understanding of real industrial materials. Numerical modelling, like DEM, can help to have a better view of such complex phenomena as it facilitates multiscale analysis including microcracking phenomena, which is crucial feature to investigate refractory materials (André et al., 2017; Asadi, 2021; Nguyen, 2019). In this way, preliminary goals of this PhD were to push the possibility of the DEM tool to:

License CC BY-NC-ND 4.0

- model a polycrystalline numerical domain integrating the grains with its local crystallographic orientations;
- deal with anisotropic CTE (which is a quite new feature for DEM);
- implement full 3D periodic boundaries for enhancing multiscale analyses;
- monitor and capture the initiation, propagation, coalescences and branching of microcracks due to thermal cycle.

The objectives of the studies are to:

- understand the impact of the anisotropic CTE of materials on the promotion of microcracks
- finally, insight on the microstructure-thermomechanical properties relationship (versus temperature) using the captured micromechanics and its corresponding apparent thermomechanical response.

Hence, to achieve such local to apparent (micro to macro) multi-scale simulations in DEM, a dedicated numerical approach will be proposed in this chapter. In such a perspective, the iDLSM DEM contact model was chosen as it is capable of representing a domain equivalent to continuum medium and simulate multiple crack initiations and propagations without fastidious calibration processes (André et al., 2019; André & Celigueta, 2023). This advanced model was introduced in detail in Chapter II. In addition, enhancements were introduced to account for anisotropy in thermal expansion, crack closure mechanisms and thermomechanical coupling within the framework of periodic boundary conditions. This study will insight on the influences of the microstructural changes (microcracks initiation and propagation) on the thermomechanical properties such as Young's modulus, dilatometry, stress-strain response, etc.

So, this proposed numerical approach aims to simulate the thermomechanical properties of polycrystalline AT material by using periodic homogenization technique (see section II.2.1). The advantage of using periodic homogenization approach is to allow working on a pseudo-infinite domain with a limited number of Discrete Element (DE)s by replicating a representative volume cell (see section II.2.1). Thus, this approach enables such cross-scale transition from the unit periodic cell, representative of the microstructure to the "infinite domain", which is representative of the macroscale. Here, the thermomechanical properties such as dilatometry and Young's modulus will be investigated as a first study in order to validate such a novel approach with DEM. After this validation step, then, this approach will be exploited to monitor the thermal stress distributions inside the microstructure. Also, a deep study of the microcrack network (with respect to the local crystallographic axes) is proposed. Lastly, the apparent stress-strain response is investigated in order to evaluate the material's performance under thermal shock conditions.

IV.2. Virtual DEM lab development for polycrystalline AT model material

The purpose of the present study is to simulate how AT polycrystalline material undergoes anisotropic thermal expansion during cooling stage (after sintering process). In reality, AT polycrystalline material have characteristic features such as grains, grain boundaries and local crystallographic orientations for each grain at the microstructural scale (Mouiya, 2024). Therefore, this section is dedicated to introducing the strategy for generating a polycrystalline numerical sample. In addition, here, the procedure for the thermomechanical simulations and the monitoring of thermomechanical property evolution (Young's modulus and potential anisotropy) of the model material (Ranganathan et al., 2025) are presented.

IV.2.1. Polycrystalline microstructure digitalization strategy

In this section, the strategy for constructing the whole periodic domain, including grains and their local orientations, will be described. Figure IV-1 provides schematic illustrations of the proposed

License CC BY-NC-ND 4.0

strategy. The first step consists of generating a PBC-iDLSM domain (see Figure IV-1a) containing N_{DE} polyhedral discrete elements, following the procedure outlined in section II.2.1.2. In this work, a polycrystalline material is represented as a collection of N_{GR} grains, each with its own geometry, crystallographic orientation, and contact with neighboring grains. The grains are assumed to have randomly distributed crystallographic orientations. To define the grain boundaries, a Voronoi tessellation is applied (Du et al., 1999), where each Voronoi cell corresponds to a single grain, as illustrated in Figure IV-1b. The resulting domain is referred to as the "grain mask." This grain mask is then superimposed onto the original PBC-iDLSM sample. It is important that the grain mask itself maintains periodicity to preserve the consistency of the polycrystalline structure.

In the final step (see Figure IV-1c), the grain mask is applied to the PBC-iDLSM sample, generating the PBC-Periodic Grain Boundary (PBC-PGB) domain. Through this masking approach, each DE centroid in the PBC-iDLSM sample is assigned to a specific grain boundary. The resulting PGB-iDLSM sample consists of N_{GR} grains, each represented by a cluster of N_{GR}^{DE} DEs and identified by unique colors. Each grain is then assigned a randomly oriented crystallographic axis, and the grain shapes are assumed to be approximately equiaxed (Ranganathan et al., 2025).

Two scenarios can occur regarding the bonds between discrete elements:

1. When both bonded DEs belong to the same grain, the bond is assigned to that particular grain (Ranganathan et al., 2025);
2. When the bonded DEs belong to different grains, the bond is randomly assigned to one of the two grains. This assignment is consistently applied to all corresponding periodic bonds to maintain the integrity of the PBC (Ranganathan et al., 2025).

This approach is similarly extended to the three-dimensional case, resulting in a 3D PGB-iDLSM model, as illustrated in Figure IV-1d.

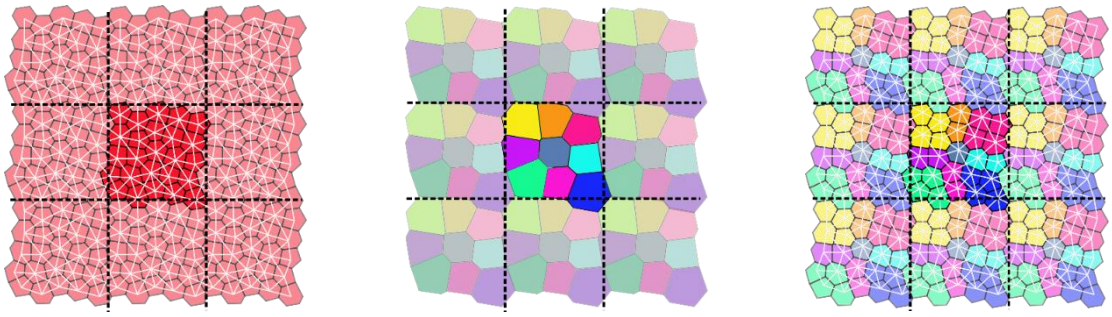

a) 2D PBC sample b) 2D grain mask c) 2D results

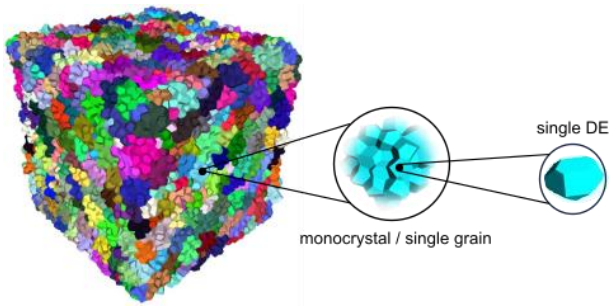

d) 3D results

Figure IV-1: Illustration of polycrystalline domain generation

License CC BY-NC-ND 4.0

IV.2.1.1. Validation of anisotropic thermal expansion

The previous section outlined the procedure for generating the PGB-iDLSM model. In this section, the thermal anisotropy of each individual grain is incorporated according to its randomly assigned crystallographic orientation. The central unit cell is defined as 100 × 100 × 100 μm^3 (see Figure IV-1d) to represent the bulk cohesive material. While the general approach for modeling anisotropic thermal expansion using iDLSM was presented in section II.2.2.1, the key distinction here is that the thermal expansion behavior is assigned based on the local crystallographic orientation of each grain (Ranganathan et al., 2025). To verify the anisotropic thermal expansion of the sample, a similar approach which was proposed in Section II.2.2.2 is employed. Therefore, a polycrystalline sample is cool down from 1200 ℃ to 0 ℃. This sample is assigned with material parameters summarized in Table III-1, associated with the high-temperature behavior of AT material (see section III.2.3.2). The readers can refer to section III.2.3.2 to get more explanation on the methodology for determining the values of the different thermo-mechanical parameters and about the chosen temperature range.

The apparent thermal expansion coefficients are tracked throughout the cooling simulations (Ranganathan et al., 2025). Because the sample contains multiple grains with randomly assigned crystallographic orientations, the overall apparent thermal expansion coefficient of the sample is expected to converge toward the average of the local coefficients of the individual grains (Ranganathan et al., 2025). The mean thermomechanical response of the polycrystalline numerical sample is illustrated in Figure IV-2. The average apparent coefficient of thermal expansion is computed by taking the mean of the apparent CTE values along the three spatial directions (see Eq.IV-1):

$$\langle \alpha_{mean} \rangle = \frac{\langle \alpha_X \rangle + \langle \alpha_Y \rangle + \langle \alpha_Z \rangle}{3} \qquad \text{IV-1}$$

Note, an apparent quantity q will be noted between rafters $\langle q \rangle$. As shown on Figure IV.2, as expected, the apparent mean coefficient of thermal expansion $\langle \alpha_{mean} \rangle$, converges rapidly toward a value of 8.415 × 10^{-6} K^{-1}, just after the brutal vertical gap (this gap is a numerical artefact due to dynamic effects which is often present at the beginning of DEM simulations) (Ranganathan et al., 2025). This value is very close to the mean value (8.41 × 10^{-6} K^{-1}) of the material's CTE (see Table III-1), given by:

$$\alpha_{mean} = \frac{\alpha_a + \alpha_b + \alpha_c}{3} \qquad \text{IV-2}$$

License CC BY-NC-ND 4.0

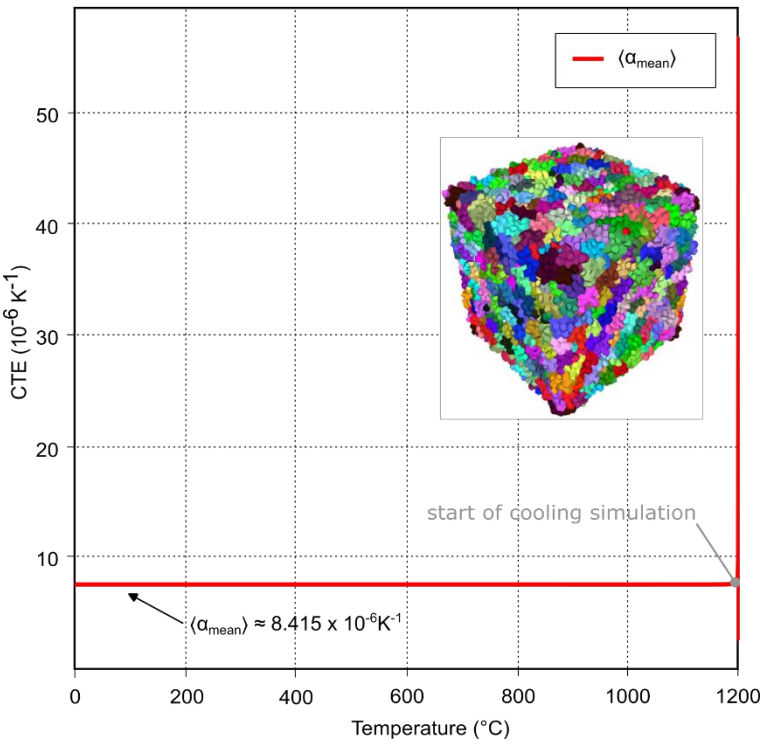

Figure IV-2: Evolution of mean CTE versus temperature for a PBC-PGB-iDLSM cooling test

Therefore, these results justify that the PGB-iDLSM model exhibit the correct behavior (anisotropic thermal expansion of the AT material), as expected with almost negligible error (0.05%) (Ranganathan et al., 2025). As a next step, as the polycrystalline sample is generated using randomization strategy, an additional validation of this randomisation strategy on the deduced macroscopic CTE of the sample (a statistical study) is required to depict the reliability of the PGB-iDLSM model.

IV.2.1.2. Verification of sample randomization's impact on the macroscopic CTE

The previous section shows that the polycrystalline numerical model exhibits a correct behaviour regarding thermal expansion for one given sample. In addition, this section proposes to conduct a similar study on many different samples. This statistical study is required in order to study the influence of the randomization strategy, which is a natural process involved in sample generation (Ranganathan et al., 2025). Specifically, the statistical validation aims to confirm that the selected number of grains per central periodic cell and the number of discrete elements per grain are adequate to produce accurate apparent CTE responses. Here, the statistical study is conducted using 9 different polycrystalline numerical samples containing approximately similar number of DEs and grains. All nine numerical samples were simulated using identical material parameters. The results for each sample, including the apparent mean coefficient of thermal expansion, are summarized in Table IV-1 , Overall, the average of the apparent CTE values across all samples was **8.410** $\times$ 10^{-6} , with a corresponding standard deviation of **0.03** $\times$ 10^{-6} respectively (Ranganathan et al., 2025).

License CC BY-NC-ND 4.0

Table IV-1: Apparent mean CTE values obtained from nine samples, all using identical material parameters

Sample	Mean CTE $\langle\alpha_{mean}\rangle$	Sample	Mean CTE $\langle\alpha_{mean}\rangle$	Sample	Mean CTE $\langle\alpha_{mean}\rangle$
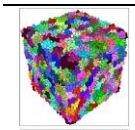	8.415×10^{-6}	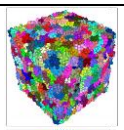	8.416×10^{-6}	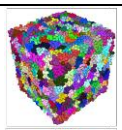	8.411×10^{-6}
	8.412×10^{-6}		8.406×10^{-6}		8.414×10^{-6}
	8.406×10^{-6}	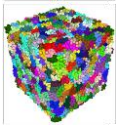	8.407×10^{-6}	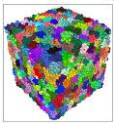	8.416×10^{-6}

The results of this statistical analysis indicate that the average apparent coefficient of thermal expansion across all nine numerical samples closely matches the mean local CTE value of 8.41×10^{-6} K^{-1}, with a deviation of less than 0.02%. Furthermore, the standard deviation of the apparent mean CTE is extremely low, around 0.036%, demonstrating that the results from the entire sample set are highly consistent. These findings confirm the reliability and reproducibility of the simulations when using 500 grains per central periodic cell and 40 DEs per grain (Ranganathan et al., 2025).

IV.2.1.3. Internal thermal stresses study

Beyond the analysis of apparent thermal expansion, the internal stress distribution can also be evaluated. For demonstration, the stress profile of Sample 1 (see Table IV-1) is monitored throughout the thermal treatment. Figure IV-3 presents the internal stress state of the numerical sample at two representative temperatures. During cooling, thermal stresses develop due to mismatches in the coefficients of thermal expansion at grain boundaries and at junctions where grains interact (Ranganathan et al., 2025). The stresses displayed in Figure IV-3 range from −375 MPa and +375 MPa, with tensile stresses considered positive and compressive stresses negative. In Figure IV-3a and b, the color-coded stresses represent the cohesive normal contact stress $\sigma_{xx_{ij}}$ of each bond, which is linked to the failure criterion described in section II.1.3. As expected, at the initial temperature of 1200 ℃ (see Figure IV-3a), the sample is stress-free. However, by 300 ℃ corresponding to a temperature change of ΔT = −900 ℃, the stress distribution becomes heterogeneous, and some bonds reach stress levels approaching or exceeding the material's failure threshold. This indicates the necessity of incorporating a crack management strategy to study fracture mechanisms during the cooling of the polycrystalline sample.

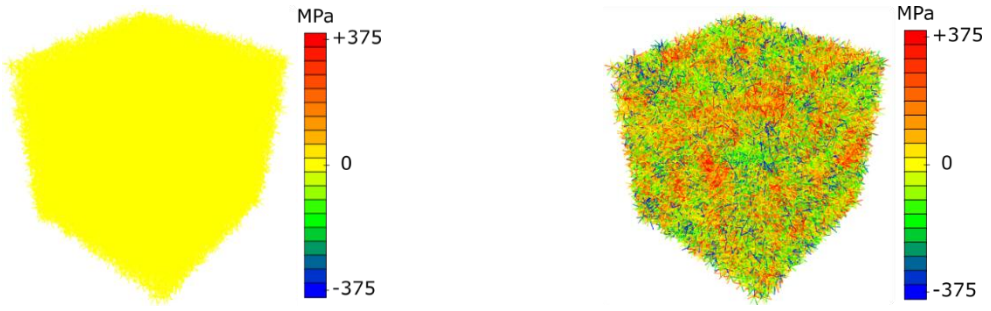

a) stress state at 1200 ℃ b) stress state at 300 ℃

Figure IV-3: Stress state snippets of polycrystalline numerical sample at two temperatures

License CC BY-NC-ND 4.0

IV.2.1.4. Crack management with closing mechanism

A failure strength is introduced to trigger crack nucleation when the local failure criteria, as defined in section II.1.3, are met. As explained in the section II.1.3, the failure strength is supposed to occur in mode I and the related threshold is symbolized by σ_{max}. To demonstrate the importance of the post-crack mechanisms for the refractory applications. Again, two separate studies, “crack-open” and “crack-reclosure,” similar to section II.2.3 under cooling simulation, are conducted using sample 1. To summaries, a “crack-open” study considers only crack opening mechanism while a “crack-reclosure” study considers both the opening and closing mechanisms (Ranganathan et al., 2025).

In both the studies, the tensile strength value σ_{max} of 375 MPa was selected. To align with experimental data, this value was selected so that the Young’s modulus of the AT material at room temperature is close to 20 GPa (see Figure IV-7). Thus, the material properties for this study are those listed in Table III-1, with the added value of σ_{max} = 375 MPa. The results of these models captured at 20 °C are shown in Figure IV-4, where crack facets are highlighted in blue (Ranganathan et al., 2025).

From the Figure IV-4a and b, despite both methods are able to depict crack initiation and opening due to CTE mismatch, there exist differences in the captured complex microcrack network. The differences are:

- in the case of “crack-open” study, although the model can capture crack opening, the numerical sample exhibits instabilities due to missing physical mechanisms. These instabilities occur when certain discrete elements detach from the domain, as illustrated in Figure IV-4a. Detached elements may cross the boundaries of the central periodic unit cell, violate the periodic boundary conditions and introduce numerical artifacts and instability into the simulation (Ranganathan et al., 2025).
- in contrast, in the case of “crack-reclosure” study, this integrated realistic physical mechanism facilitates the stress and force transmissions by considering the reclosing of cracks. Moreover, this eliminates the presences of “flying elements” which violates the periodicity of the domain. Therefore, the sample 1 performs better with this new crack management strategy as demonstrated in Figure IV-4b (Ranganathan et al., 2025).

In conclusion, based on these observations, the crack closure mechanism will be adopted as the default crack mechanism in the next numerical studies.



a) “crack-open” study b) “crack-reclosure” study

Figure IV-4: Snippets of the AT numerical samples at 20 °C

IV.2.2. Evaluation of apparent CTE and Young’s modulus

The objective of the current DEM model is to qualitatively track the evolution of the apparent coefficient of thermal expansion and Young’s modulus of the bulk sample during the cooling process. Thermomechanical simulations are conducted using DEM numerical sample 1 (see Table IV-1). As previously described, each grain within the numerical sample is assigned a random crystallographic orientation, and the grains are visualized in different colors in Figure IV-1d. Each grain is formed by approximately 40 discrete elements. The input data correspond to the local

License CC BY-NC-ND 4.0

properties of each AT grain at 1200 ℃ (Ranganathan et al., 2025) are summarized in Table III-1 combined with a tensile strength value σ_{max} of 375 MPa. For getting more details on the choice of the material properties and temperature range, readers can refer to section III.2.3.2.

The thermomechanical simulations presented in this section are carried out in two sequential steps (Ranganathan et al., 2025):

1. cooling simulation: this step represents the post-sintering cooling of the material. During this phase, cracks are allowed to form and propagate naturally within the sample.
2. pure mechanical tensile test, performed on the cooled sample obtained from the previous step, this test does not permit further crack growth. The primary objective of this stage is to determine the apparent Young's modulus of the multi-cracked numerical sample.

Additionally, the progression of the coefficient of thermal expansion is monitored during the cooling stage (Ranganathan et al., 2025). Initially, the numerical samples are considered to be at 1200 ℃ and are assigned the input properties listed in Table III-1. At this high temperature, the samples are assumed to be in a relaxed, stress-free state, with temperature uniform throughout the domain. For the cooling simulations, the samples are gradually subjected to thermal loading from 1200 ℃ to 20 ℃. As discussed in section III.2.3.2, thermal stresses are assumed to begin developing as the temperature decreases. The cooling procedure is carried out in increments of 100 ℃, with a mechanical simulation performed after each thermal step.

Throughout the cooling process, the apparent thermal strain components $\langle\varepsilon_{XX}\rangle$, $\langle\varepsilon_{YY}\rangle$ and $\langle\varepsilon_{ZZ}\rangle$ of the numerical sample are continuously tracked. These directional strains are subsequently combined through averaging to compute the apparent mean coefficient of thermal expansion, $\langle\alpha_{mean}\rangle$, using the following expression:

$$\langle\varepsilon_{mean}\rangle = \frac{\langle\varepsilon_{XX}\rangle + \langle\varepsilon_{YY}\rangle + \langle\varepsilon_{ZZ}\rangle}{3} \qquad \text{IV-3}$$

In order to measure the mean apparent CTE $\langle\alpha_{mean}\rangle$ by this process, the numerical dilatometry results for aluminum titanate (apparent thermal strain vs. temperature) are obtained, as shown in Figure IV-5 and compared to the experimental measurements (Mouiya, 2024). Figure IV-5 shows that the current numerical model can produce quantitative results for the AT material. Specifically, the model replicates the trend of contraction (decrease in thermal strain), which is consistent with the experimental results. On the other hand, around 700 ℃, the change in slope (in both the curves) indicates a sudden increase in microcrack formation in the numerical sample (Ranganathan et al., 2025).

This can also be observed in Figure IV-6, which draws the evolution of microcracks for different temperatures. Here, each isolated non-connected crack is depicted by a different color. As explained earlier, in the iDLSM model, cracks are represented by a crack facet. During the cooling stage, microcrack initiation happens at random locations due to the CTE mismatch. For example, when two crack facets share a common edge, they are considered as the same crack and they are highlighted by a single color (Ranganathan et al., 2025). During the cooling stage, these microcrack small networks propagate and they tend to merge to form a single complex microcrack network (see Figure IV-6d, e and f). Indeed, the final color of the complex crack network is assigned by identifying the dynamic microcrack network (among the already existing cracks) that propagates fast and contributes to merging mechanisms (see Figure IV-6d, e and f).

License CC BY-NC-ND 4.0

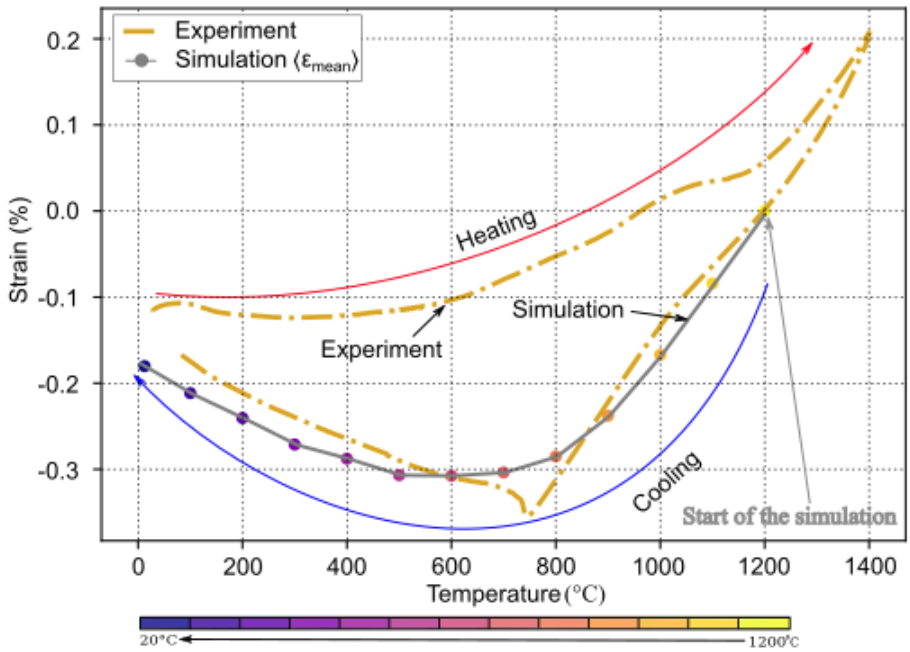

Figure IV-5: Experimental and numerical dilatometry results of AT

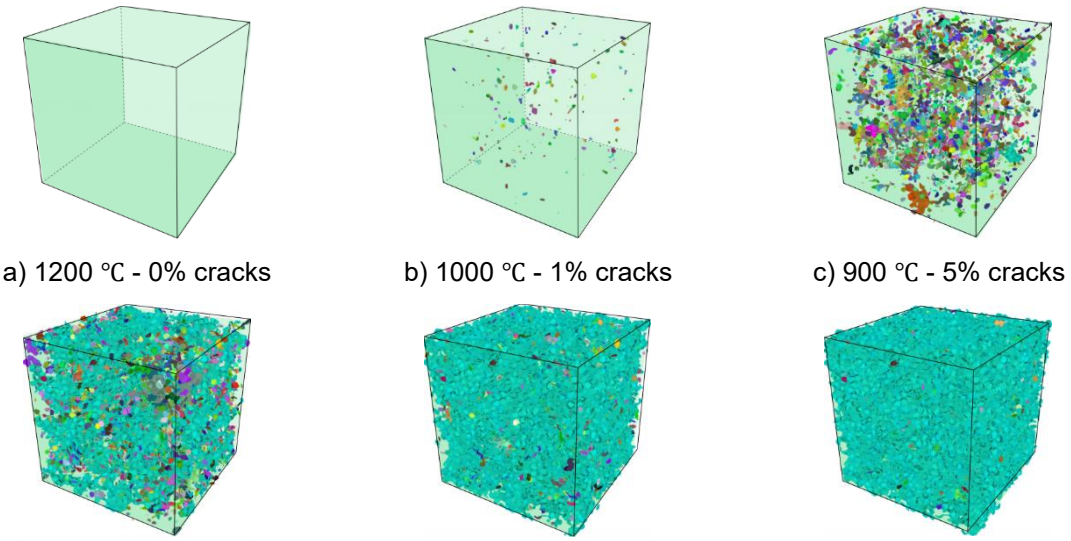

a) 1200 ℃ - 0% cracks b) 1000 ℃ - 1% cracks c) 900 ℃ - 5% cracks

d) 750 ℃ - 21% cracks e) 600 ℃ - 32% cracks f) 400 ℃ - 46% cracks

Figure IV-6: Evolution of microcrack network

It is important to emphasize that the intrinsic material properties of individual grains, defined at the microstructural scale, are assumed to be temperature-independent throughout the simulation. Consequently, any variation in the apparent coefficient of thermal expansion of the numerical sample arises exclusively from the development and evolution of microcracks.

After each cooling step from 1200 ℃ to 1100 ℃, 1000 ℃, … successively down to 20 ℃, the resulting microcracked numerical samples are subjected to a quasi-static uniaxial tensile test. During these mechanical tests, further crack growth is suppressed so that the effective Young's modulus of the damaged samples can be accurately evaluated. In this work, the apparent Young's modulus $\langle E \rangle$ is computed as the ratio between the apparent normal stress $\langle \sigma_{XX} \rangle$ and the imposed apparent strain $\langle \varepsilon_{XX} \rangle$ (Ranganathan et al., 2025). Owing to the presence of numerous randomly

License CC BY-NC-ND 4.0

oriented grains within the microstructure, the apparent Young's modulus is assumed to be isotropic with respect to the loading direction.

The variation of $\langle E \rangle$ as a function of temperature is presented in in Figure IV-7. As shown (see Figure IV-7), the apparent Young's modulus progressively decreases as the temperature is reduced from 1200 ℃, reflecting the formation and development of a microcrack network within the numerical sample (see Figure IV-6). Furthermore, the computed evolution is in good agreement with the qualitative trends reported in experimental observations. It should be noted that the local tensile strength, σ_{max} = 375 MPa, was specifically selected to reproduce the experimentally measured Young's modulus at room temperature.

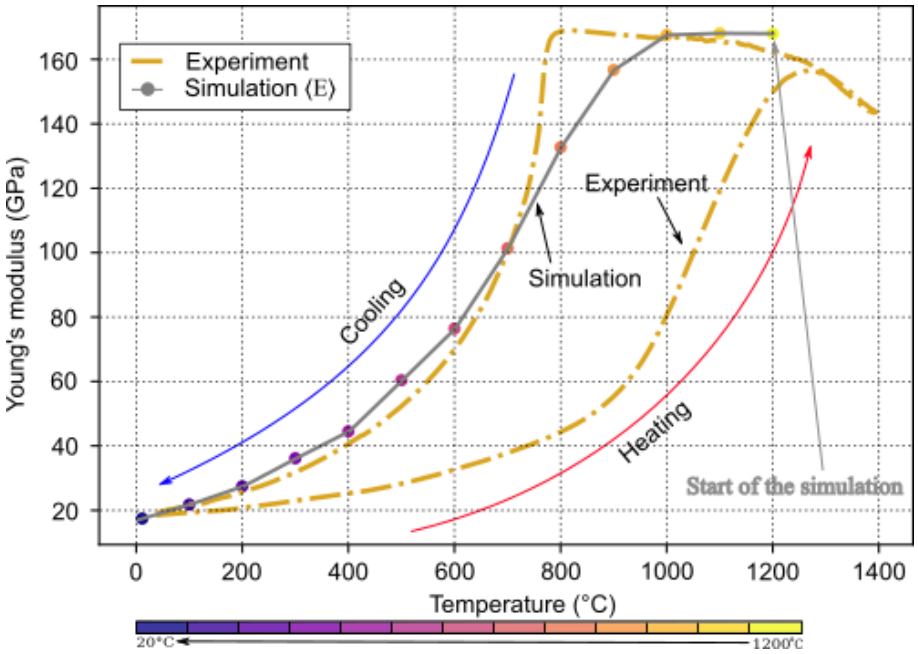

Figure IV-7: Experimental and numerical results of AT's Young's modulus vs temperature

IV.2.3. Convergence study

Convergence studies are essential in the DEM framework to verify the reliability and robustness of the simulation results (André et al., 2012; André & Celigueta, 2023). In this study, a convergence analysis was conducted to ensure that the results are independent of the discretization level and to determine the minimum number of DEs needed to achieve reproducible outcomes, as discussed in section IV.2.2 (André & Celigueta, 2023). The evolution of the apparent Young's modulus (see Figure IV-7) was chosen as the key parameter to assess model convergence.

Three levels of discretization were examined, producing numerical samples with different DE counts per periodic unit cell: approximately 10k, 20k, and 30k DEs. Each sample consists of 500 grains, with each grain assigned a random crystallographic orientation and represented by a distinct color for visualization, as mentioned in previous section IV.2.1. Consequently, each grain comprises roughly 20, 40, and 60 DEs in the 10k, 20k, and 30k DE samples, respectively, reflecting progressively finer discretization (see Table IV-2).

Since the initial packing of the DEs is random, four independent polycrystalline samples were generated for each DE count to capture variability due to the stochastic arrangement. In total, this study examines 12 numerical samples (3 discretization levels × 4 random realizations). Each sample is assigned the local material properties of aluminum titanate grains at 1200℃ as listed in Table III-1.

License CC BY-NC-ND 4.0

Table IV-2: Numerical samples with different polycrystalline structure for convergence study			
Numerical sample	10k elements	20k elements	30k elements
Polycrystalline structure 1	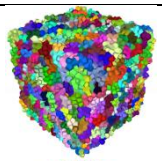	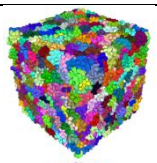	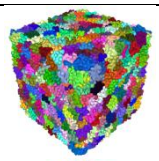
Polycrystalline structure 2			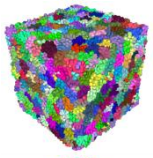
Polycrystalline structure 3			
Polycrystalline structure 4			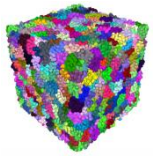

For the convergence analysis, thermomechanical simulations (as described in section IV.2.2) were carried out to determine the apparent Young's modulus for each numerical sample. The average results for samples with 10k, 20k, and 30k DEs are presented in Figure IV-8. Firstly, it is evident that, regardless of discretization level, the computed Young's modulus values show good agreement with experimental data. Furthermore, the three curves do not exhibit any systematic trends or significant deviations, as highlighted in the zoomed-in sections of Figure IV-8 at various temperatures. These observations indicate that the model has achieved sufficient convergence and the results can be considered reliable. For subsequent analyses, the 20k DE sample was selected to balance computational efficiency with accuracy.

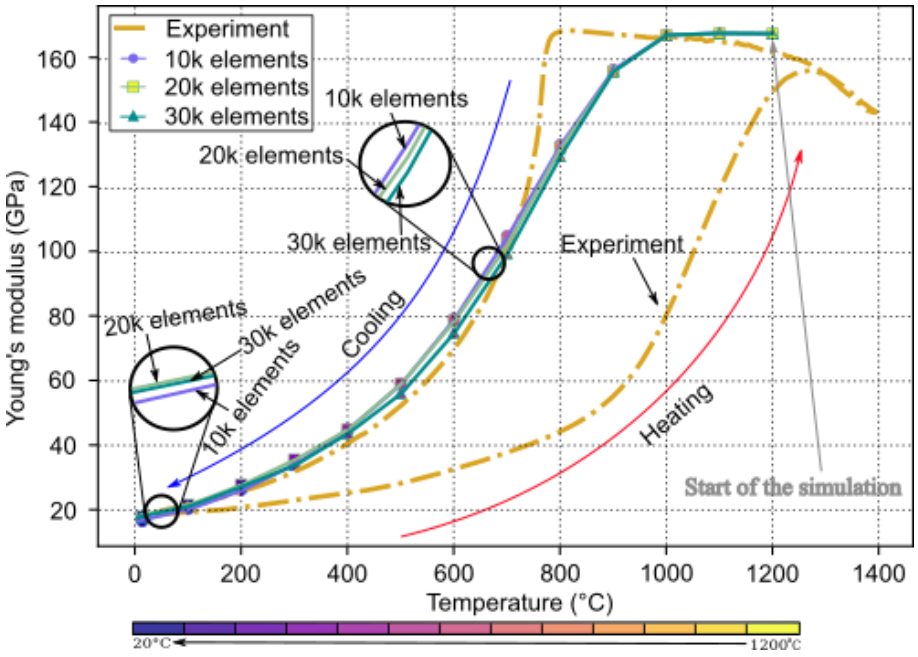

Figure IV-8: Apparent Young's modulus of aluminum titanate as a function of temperature for numerical samples with 10k, 20k, and 30k discrete elements

License CC BY-NC-ND 4.0

IV.3. Numerical modelling of thermomechanical damage in a model material

The aim of the present study is to exploit the proposed model, to further advance the understanding of the micromechanical behavior of aluminum titanate, the proposed polycrystalline DEM model can be employed to (Ranganathan et al., 2026):

- evaluate how stress is distributed throughout the sample with respect to the local crystallographic orientations;
- track the initiation and extension of cracks under combined thermal and mechanical loading across different temperatures;
- examine crack surfaces to distinguish between isolated cracks and interconnected crack networks;
- differentiate between intragranular cracks (within individual grains) and intergranular cracks (along grain boundaries) based on their spatial locations;
- monitor the development of irreversible strains associated with crack propagation during tensile testing.

Firstly, this study is crucial for understanding the sustainability of microstructures in response to thermal shocks. In high-temperature applications, materials experience heterogeneous internal thermal compressive and tensile stresses at the microstructural level (Mouiya, 2024; Nosewicz et al., 2020; Razavi et al., 2024). When these stresses reach the materials' tensile strength, they promote microcracks (initiation and propagation). The evolution of these microcracks significantly affects properties such as the CTE and Young's modulus (see section III.1). Therefore, monitoring internal thermal stresses is essential for gaining insights into the material's microstructure sustainability under such conditions.

Secondly, as indicated in Figure IV-6, cracks typically initiate as small, isolated, non-connected entities and propagate to form a complex network during the cooling process. Observing the crack trajectory can provide valuable information about the material, such as how the local dominant CTE influences crack orientation, where microcracking initiates (specifically identifying the dominance of intergranular versus intragranular cracks during cooling), and whether the cracks exist as isolated entities or as part of a complex network at the microstructural level (Razavi et al., 2024).

For this purpose, a polycrystalline numerical sample (Ranganathan et al., 2026) is employed in this section to demonstrate the strategy for monitoring thermal stresses and crack statistics for the AT model material. It is important to clarify key material science definitions related to crack types to facilitate the understanding of the observations presented in the following sections (Callister Jr & Rethwisch, 2020):

- **Intergranular cracking** refers to cracks that propagate along the grain boundaries, i.e., between adjacent grains.
- **Intragranular cracking** refers to cracks that form and propagate within the interior of a single grain.
- **Transgranular cracking** refers to cracks that traverse from one grain to another, cutting through the grains rather than following their boundaries.

IV.3.1. Thermal stress study

In a preliminary investigation aimed at exploring the development of thermal stresses and their interaction with microcracks, two separate scenarios were considered (Ranganathan et al., 2026):

- a “no-crack” scenario, in which crack initiation and propagation were suppressed;
- a “crack” scenario, in which cracks were allowed to form and grow.

Firstly, such a study is quite necessary to understand the microstructures sustainability towards thermal shocks. As already known that the samples exhibit thermal stresses, therefore, monitoring it, would reveal the weak regions at the microstructural scale (Nosewicz et al., 2020). Performing

License CC BY-NC-ND 4.0

this study, by separating it into “no-crack” and “crack”, allows to monitor the distribution patterns of stresses in the microstructural scale on the presences and absence of microcracks (Ranganathan et al., 2026). Moreover, these studies highlight the amount of internal stresses released due to the microcracking phenomenon and the amount of stress range that the sample exhibits with and without microcracks. Furthermore, this study helps understanding the predominant local orientation in exhibiting thermal stresses and relationships between the different local orientations.

Again, a cooling simulation was performed using the numerical sample, where the sample is cooled from $1200\ ℃$ to $20\ ℃$, using a uniform cooling rate. At the start of the cooling simulation, the similar assumptions of section IV.2.2 were considered for the numerical sample. As explained before the numerical samples exhibits significant thermal stresses (due to CTE mismatch between grains), during the cooling process. As shown in section IV.2.1.3, the thermal stresses within the numerical sample can be visualized in three dimensions; however, representing these stresses in the presence of microcracks is challenging in 3D. To facilitate understanding, several simulations were conducted using a 2D polycrystalline sample with free boundary conditions for illustrative purposes. Figure IV-9 presents this 2D sample as a qualitative, pedagogical representation to help readers visualize the stress distribution. In both 2D and 3D depictions, internal thermal stresses are color-coded as described in section IV.2.1.3 (blue for compressive stresses and red for tensile stresses), and the magnitude of the normal longitudinal stresses is indicated by the bond thickness (Ranganathan et al., 2026).

For the “no-crack” scenario, the numerical sample with internal thermal stresses is shown in Figure IV-9b, with its corresponding 3D view presented in Figure IV-10b. In contrast, in the “crack” scenario, microcracks develop once the local tensile stress exceeds the material’s strength ($\sigma_{max} = 375\ MPa$) is reached. The initiation of these cracks is determined using a local stress criterion for Mode-I failure, as described in section II.1.3 (Ranganathan et al., 2026). In the figures, microcracks are highlighted in black (Figure IV-9c), with the 3D representation shown in Figure IV-10c.

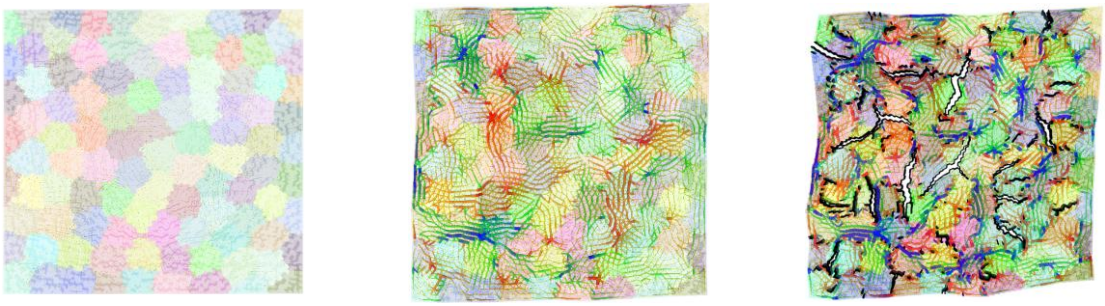

a) stress-free state at 1200 ℃ b) stress state representation in “no-crack” study c) stress state representation in “crack” study

Figure IV-9: Microstructural changes in a 2D numerical sample in two case studies

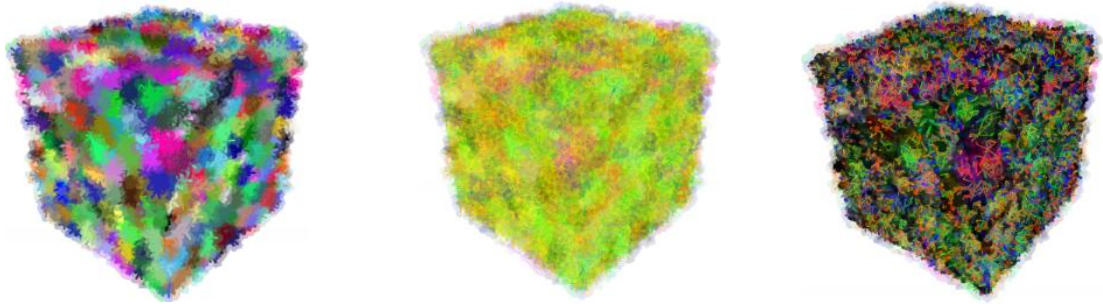

a) stress-free state at 1200 ℃ b) stress state representation in “no-crack” study c) stress state representation in “crack” study

Figure IV-10: Microstructural changes in the 3D numerical sample in two case studies

License CC BY-NC-ND 4.0

Thermal stresses were measured and recorded in both the “no-crack” and “crack” scenarios at intervals of $100\ ℃$, and are presented as 3D distribution plots (see Figure IV-11 and Figure IV-12). Therefore, in both cases, the local thermal stresses are represented along the grain orientations ($\vec{a}$, $\vec{b}$, $\vec{c}$). As mentioned in section III.2, the crystallographic convention for AT used here follows the approach of Mouiya, (2024). Specifically, the Figure IV-11 corresponds to the “no-crack” study, while Figure IV-12 corresponds to the “crack” study. In these 3D plots, the x-axis denotes temperature (℃), the y-axis shows the thermal stress range (MPa), and the z-axis indicates bond frequency (Ranganathan et al., 2026).

These figures (Figure IV-11 and Figure IV-12) provide insights into the local mechanical behaviour of the numerical samples and illustrate how thermal stress distributions evolve with temperature. Key observations common to both studies (Ranganathan et al., 2026) include:

- stress distribution enlarged during the cooling process, with the “no-crack” case exhibiting a larger enlargement compared to the “crack” case;
- the distributions shift along the thermal stress axis as cooling progresses, reflecting the overall rise in thermal stress; however, this shift is absent in the “no-crack” scenario;
- In the “crack” scenario, both the enlargement and shift of the stress distributions are reduced, due to the initiation and propagation of cracks.

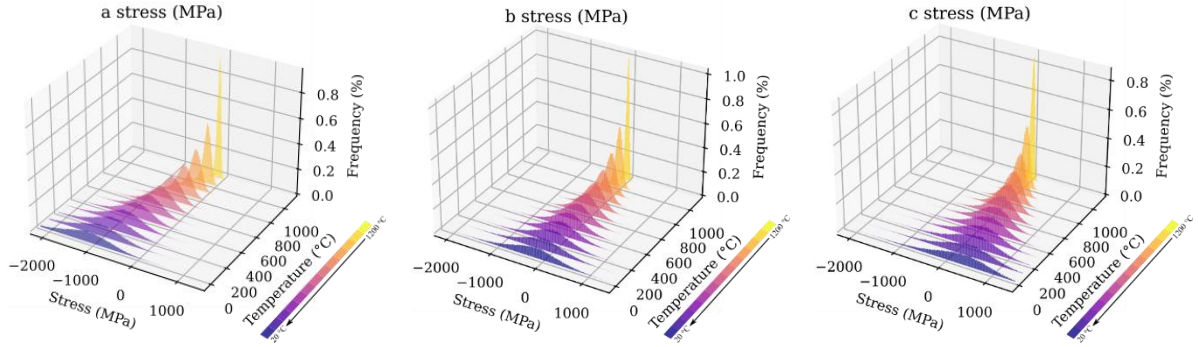

a) thermal stress distribution along $\vec{a}$ b) thermal stress distribution along $\vec{b}$ c) thermal stress distribution along $\vec{c}$

Figure IV-11: Thermal stress distribution versus temperature for the “no-crack” study

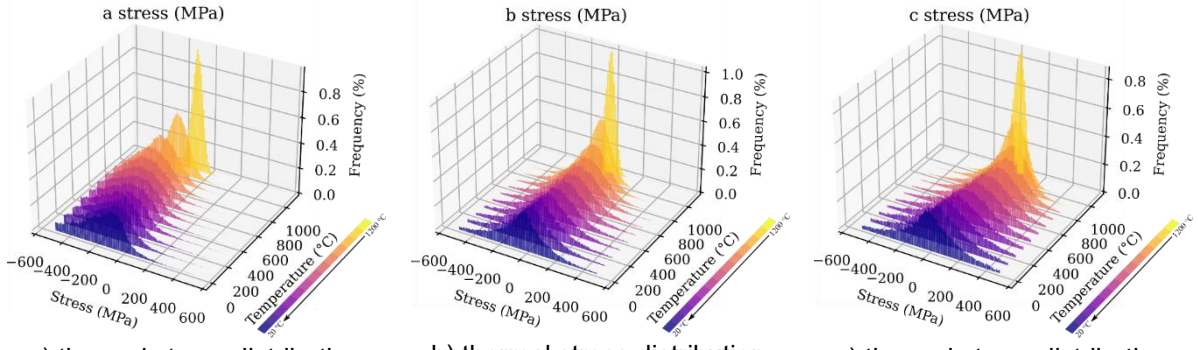

a) thermal stress distribution along $\vec{a}$ b) thermal stress distribution along $\vec{b}$ c) thermal stress distribution along $\vec{c}$

Figure IV-12: Thermal stress distribution versus temperature for the “crack” study

Consequently, the stress distributions can be characterized using their mean and standard deviation, as they closely resemble Gaussian distributions. The Figure IV-13a illustrates the evolution of the mean thermal stress for the “no-crack” scenario, whereas Figure IV-13b shows the corresponding results for the “crack” scenario. On the other hand, the Figure IV-14 describes the standard deviation in both the studies.

License CC BY-NC-ND 4.0

From the Figure IV-13a and b several similarities and differences between the two studies can be observed. Likewise, the Figure IV-14a and b also exhibit certain commonalities and distinctions (Ranganathan et al., 2026). Therefore, the key similarities identified in both studies are as follows:

- The mechanical responses varied along the different orientations ($\vec{a}$, $\vec{b}$, $\vec{c}$) (see Figure IV-13a and b). Specifically, the orientation $\vec{a}$ exhibited a predominantly compressive behavior, orientation $\vec{c}$ showed a tensile response and orientation $\vec{b}$ depicted an average response of $\vec{a}$ and $\vec{c}$. This indicates the existence of relationships between the orientations ($\vec{a}$, $\vec{b}$, $\vec{c}$) in relation to the thermal stresses;
- additionally, the standard deviation of the thermal stresses (see Figure IV-14a and b) increased throughout the cooling process. Notably, the “no-crack” scenario showed a higher standard deviation compared to the “crack” case, reflecting greater variability in stress distribution when cracks were absent.

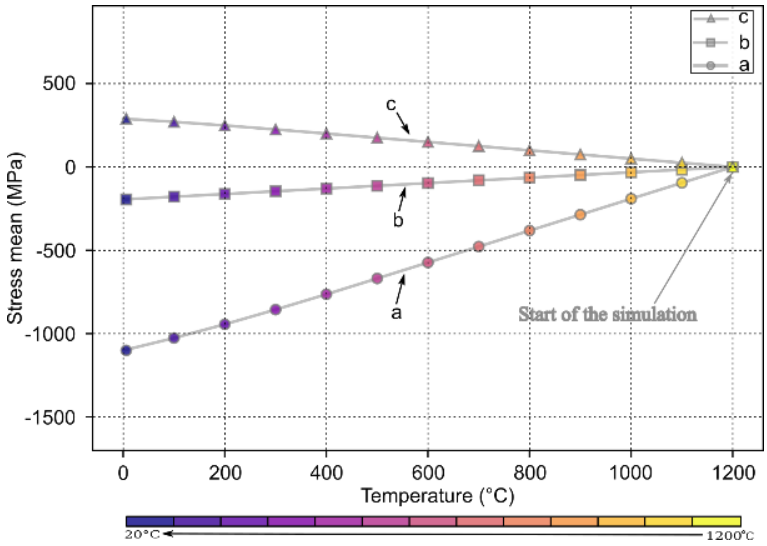

a) “no-crack” study

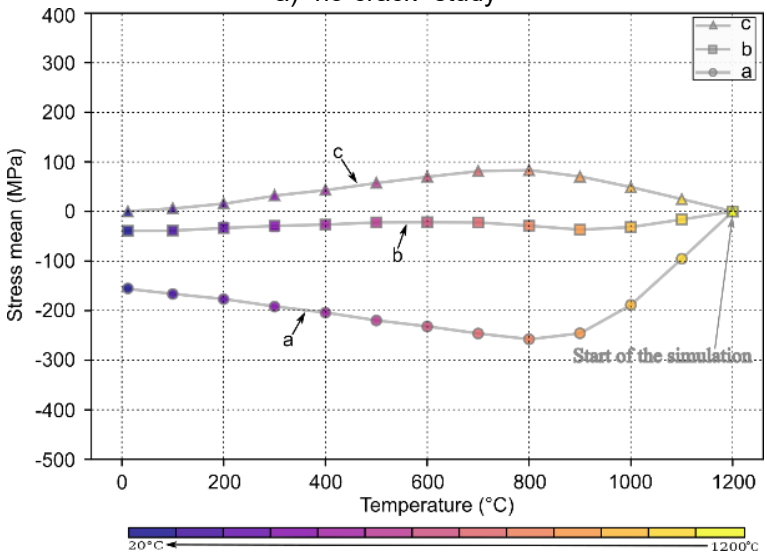

b) “crack” study

Figure IV-13: Temperature-dependent evolution of the mean thermal stress

The differences between the two studies can be summarized as follows:

- in the “no-crack” scenario, the mean thermal stresses (see Figure IV-13a) increase steadily (or monotonically) along all orientations ($\vec{a}$, $\vec{b}$, $\vec{c}$). In contrast, in the “crack” scenario, the stresses (Figure IV-13b) rise up to approximately $700\,℃$, followed by a sudden drop,

License CC BY-NC-ND 4.0

indicating the onset of microcracking within the temperature range [700 - 20 °C] (Bruno et al., 2010; Mouiya, Tessier-Doyen, et al., 2023; Ranganathan et al., 2025);

- the mean thermal stresses (see Figure IV-13a) in the “no-crack” study exceed the material’s tensile strength (375 MPa) in the temperature range [700 - 20 °C], whereas in the “crack” study, the stresses (Figure IV-13b) remain below the tensile strength throughout cooling;
- regarding variability, the standard deviation in the “no-crack” case (see Figure IV-14a) shows a stable phase between [1200 - 800 °C], whereas the “crack” scenario (see Figure IV-14b) exhibits only a pseudo-stable phase. Between [800 - 400 °C] the “no-crack” case shows a rapid increase in standard deviation along $\vec{a}$ but with smaller increases along the other two orientations. In contrast, in the case of “crack” study, in the temperature range [800 - 400 °C] all three orientations display a pronounced rise in standard deviation. Finally in both studies, in both cases, the standard deviation stabilizes during the final cooling stage from [400 - 20°C].

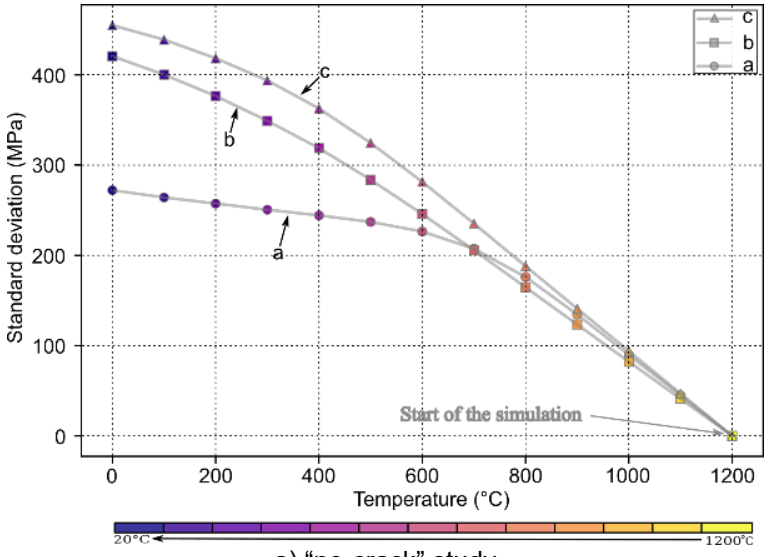

a) “no-crack” study

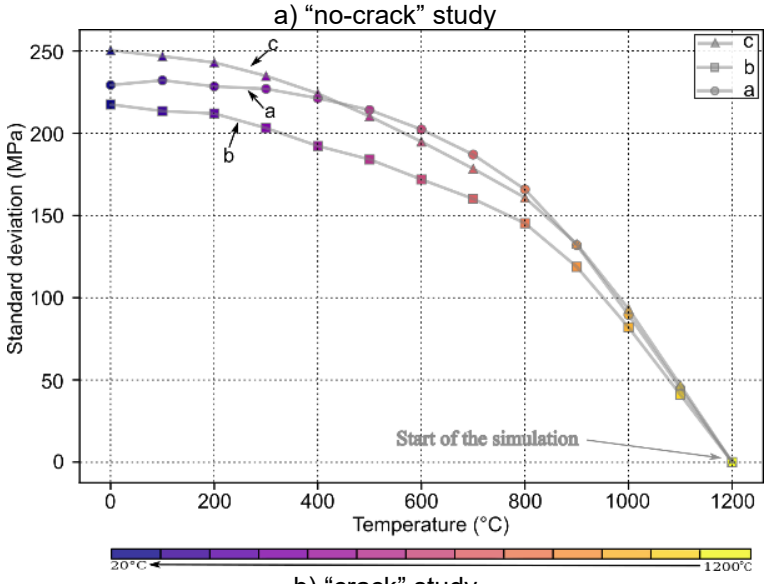

b) “crack” study

Figure IV-14: Temperature-dependent evolution of thermal stress standard deviation

The differences in thermal stress evolution between the two studies reflect the amount of the stresses relieved through microcracking. Moreover, the Figure IV-13b shows that the mean stress is decrease once crack initiates, indicating the presences of skewed distribution (see Figure IV-12). This skewed distribution means that the sample relaxes the internal tensile stresses as a

License CC BY-NC-ND 4.0

consequence of microcracking and on the other hand, the compressive stresses are preserved in the sample as the distribution exhibits a negatively skewed value. Additionally, the figure highlights that the $\vec{c}$ orientation, which experiences tensile stress, corresponds to the highest CTE of the material (α_c = 17.26×10^{-6} K^{-1}), whereas the $\vec{a}$ orientation, under compression, has the lowest CTE (α_a = −1.97×10^{-6} K^{-1}). This indicates that microcracking is strongly influenced by the orientation with the highest CTE, and suggests that most microcracks form perpendicular to the $\vec{c}$ orientation, consistent with Mode-I fracture behavior (Ranganathan et al., 2026). Similar findings were reported by Bruno et al., (2010) who employed the semi-empirical Integrity Factor (IF) model, validated through EBSD and Neutron Diffraction (ND) measurements on the High-Pressure Preferred Orientation (HIPPO) instrument. These results underscore the importance of understanding the relationship between grain orientation $(\vec{a}, \vec{b}, \vec{c})$ and microcrack development. Consequently, the "crack" study is used for further analysis of microcrack statistics in the following sections.

IV.3.2. Analyses of the micro-crack network

This section focuses on the analysis of microcrack statistics in the "crack" study, with the goal of understanding how microcracks develop, their preferred orientations, spatial distribution, and the mechanisms behind the formation of complex crack networks (Ranganathan et al., 2026). Figure IV-15, depicts the evolution of microcracks and material damage as a function of temperature. In this context, a microcrack is defined as a bond that has reached the tensile strength threshold ($\sigma_{max} = 375\ MPa$). As described earlier, a broken bond is deactivated but can regain its load-carrying ability under compression, simulating the crack closure effect. The microcrack count is therefore expressed in relative terms, calculated as the ratio of broken bonds to the total number of bonds in the numerical sample. In parallel, the apparent damage parameter is tracked, defined as the ratio of the current Young's modulus (E_i) to the initial modulus (E_0) of the sample.

Figure IV-15 reveals a sharp rise in the number of microcracks around 700 ℃, consistent with the trend observed in the mean thermal stress evolution shown in Figure IV-13b. This indicates that the numerical sample develops a dense microcrack network over the temperature range of [700 - 20 ℃]. Indeed at 20 ℃, the sample contains approximately 90.8k microcracks, corresponding to 60% of all bonds and an overall damage factor of 88%. Analyzing these microcrack statistics in detail provides further insight into the structure and progression of the existing crack networks.

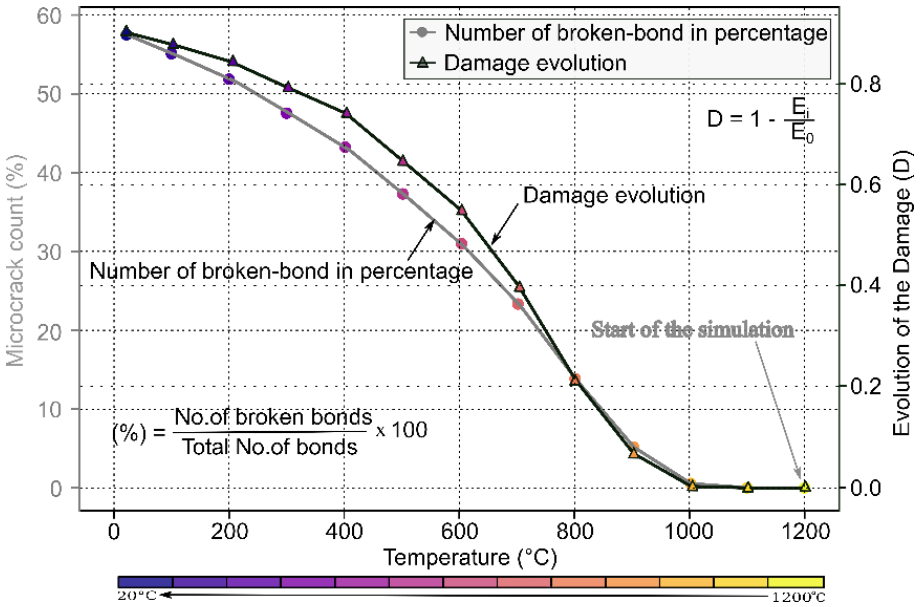

Figure IV-15: Recording of crack count and damage states versus temperature

License CC BY-NC-ND 4.0

IV.3.2.1. Preferential crack orientation

To analyse the orientation of microcracks, the unit normal vectors ($\vec{n}$) of the crack facets were tracked and recorded throughout the cooling simulation. Figure IV-16a illustrates a bonded DE pair subjected to tension. When the bond reaches the tensile strength ($\sigma_{max} = 375\ MPa$), a microcrack forms, represented by a crack facet, as shown in Figure IV-16b. Each of these crack facets is associated with two normal vectors, which describe its spatial orientation $\vec{n}_1$ and $\vec{n}_2$ and their relationship is: $\vec{n}_1$ = - $\vec{n}_2$ (Ranganathan et al., 2026).



a) bonded DE under tension b) crack-facet with the broken bond

Figure IV-16: Bonded polyhedral DE pair under mode-I failure

These normal vectors are represented in relative to the local grain orientation ($\vec{a}$, $\vec{b}$, $\vec{c}$), as illustrated in Figure IV-17. Therefore, the $\vec{n}_i$ ($i = 1, 2$ as a crack-facet will have two faces) vectors are projected to the planes ab, bc and ca, that are formed by combination of $\vec{a}$, $\vec{b}$, $\vec{c}$ axes. The projection of $\vec{n}_i$ vectors to these planes gives $\vec{n}_i^{ab}$, $\vec{n}_i^{bc}$ and $\vec{n}_i^{ca}$, where $(i = 1, 2)$, as illustrated in the Figure IV-17. This procedure is applied to all crack facets. For each crystallographic plane (ab, bc and ca), the projected $\vec{n}_i$ are analysed as a function of their angular orientations α_{ab}, α_{bc} and α_{ca}. The resulting angular distributions are then displayed using polar histograms, as shown in Figure IV-18a, c and e. Note that, in Figure IV-18a, "$\vec{a}$" is the horizontal axis aligned along 0° while the "$\vec{b}$" is the vertical axis aligned along 90°. An identical interpretation applies to Figure IV-18c and e. The polar histograms account for both normal vectors, $\vec{n}_1$ and $\vec{n}_2$ which leads to symmetric distributions, as indicated by the dotted lines in Figure IV-18a, c and e. These histograms correspond to 1000 ℃ (Ranganathan et al., 2026).

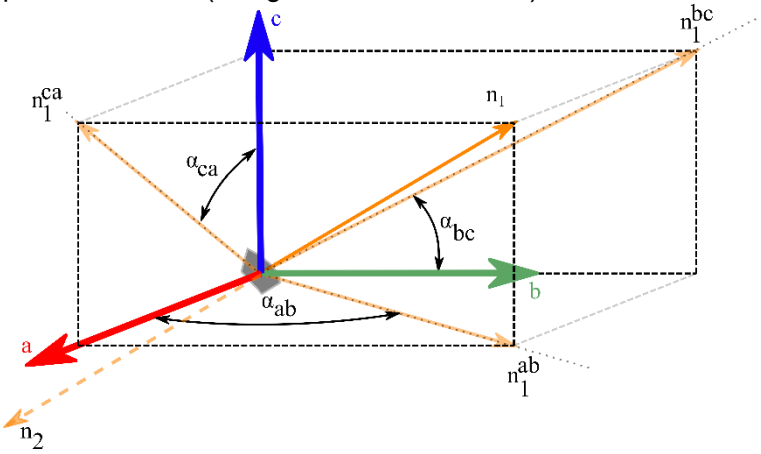

Figure IV-17: Representation of the $\vec{n}$ in relation to the local grain orientation

The microcrack orientations observed at 1000 °C (see Figure IV-18a, c and e) reveal the following trends:

- in the ab-plane, the normal vectors exhibit a widely dispersed angular distribution, whereas in the bc- and ca-planes, the majority of normal vectors are preferentially aligned with the $\vec{c}$ orientation. It should be noted that the $\vec{c}$ axis corresponds to angles of 90° and 270° in bc-plane and along 0° or 180° in ca -plane;

License CC BY-NC-ND 4.0

- the highest concentrations of normal vectors occur at 90° and 270° in ab -plane and bc-plane and 0° or 180° in ca-plane. Among the three planes, the ca-plane exhibits the greatest frequency of normal vectors;
- these observations indicate that, at 1000 °C , most microcracks are oriented perpendicular to the $\vec{c}$ orientation.

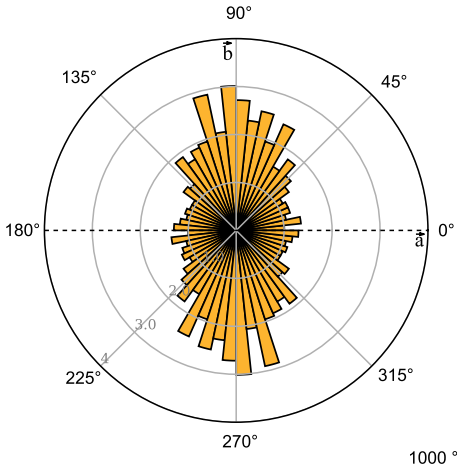

a) polar representation of α_{ab} (ab-plane)

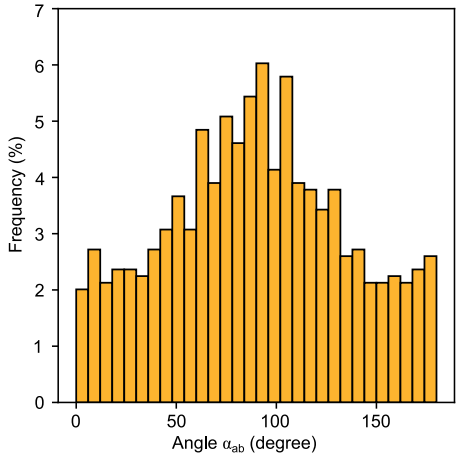

b) linear representation of α_{ab} (ab-plane)

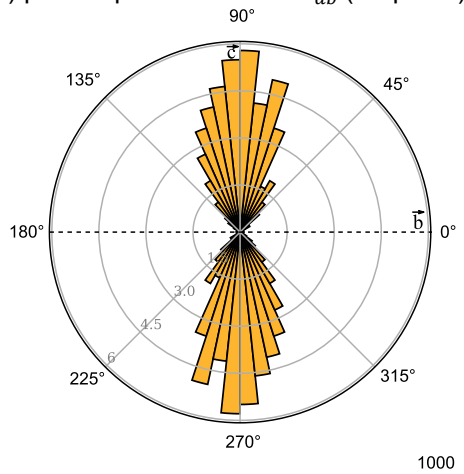

c) polar representation of α_{bc} (bc-plane)

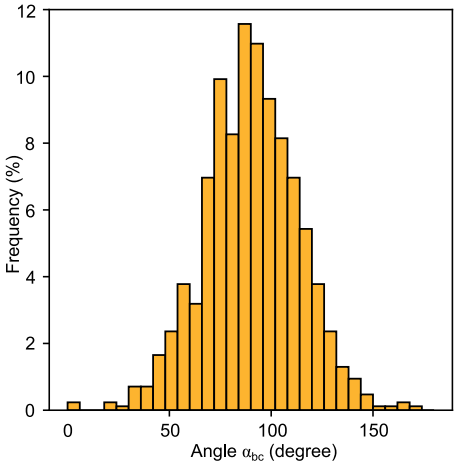

d) linear representation of α_{bc} (bc-plane)

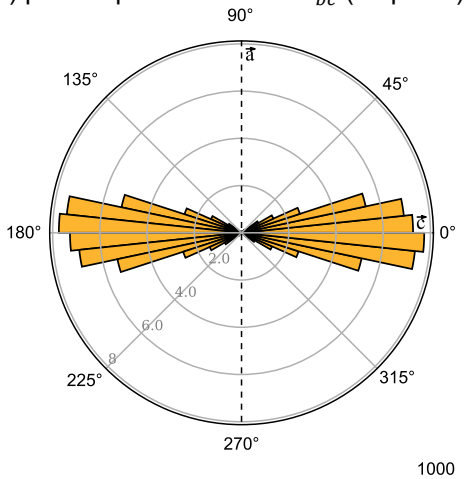

e) polar representation of α_{ca} (ca-plane)

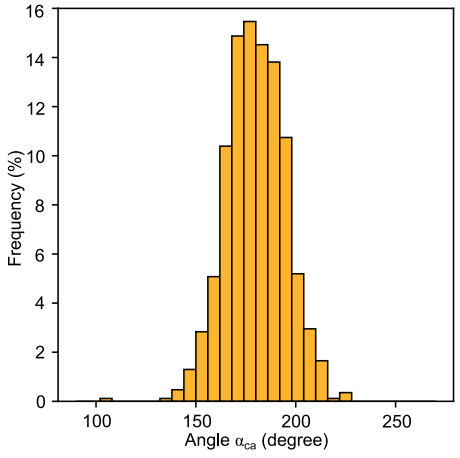

f) linear representation of α_{ca} (ca-plane)

Figure IV-18: Orientation angle distributions of microcrack "$\vec{n}$ " in different local grain planes 1000 °C

License CC BY-NC-ND 4.0

To facilitate visualization of how microcrack normal vector orientations evolve with temperature, a linearization approach was adopted. Owing to the inherent symmetry of the orientation distributions, only data from one side of the symmetry axis were retained in the linear representation, thereby avoiding redundant calculations. This approach is illustrated in Figure IV-18b, d, and f. For instance, in the ab-plane, which exhibits symmetry about the 0°-180° axis, only orientations within this range were mapped onto the linear scale (see Figure IV-18b). Similarly, for the bc and ca-plane, the orientation data were linearized using symmetry ranges of 0°-180° and 90°-270°, respectively, as shown in Figure IV-18d and f. The resulting linearized datasets, recorded at 100℃, intervals, were subsequently assembled into three-dimensional representations (see Figure IV-19a, b and c). In these plots, temperature (°C) is shown along the x-axis, the orientation range of the normal vectors (degrees) along the y-axis, and the corresponding frequency along the z-axis (Ranganathan et al., 2026).

The observed widening of the normal vector orientation range indicates that microcrack propagation becomes increasingly dispersed at lower temperatures. This behaviour reflects the development of complex and tortuous crack paths within the numerical samples during the final stages of cooling.

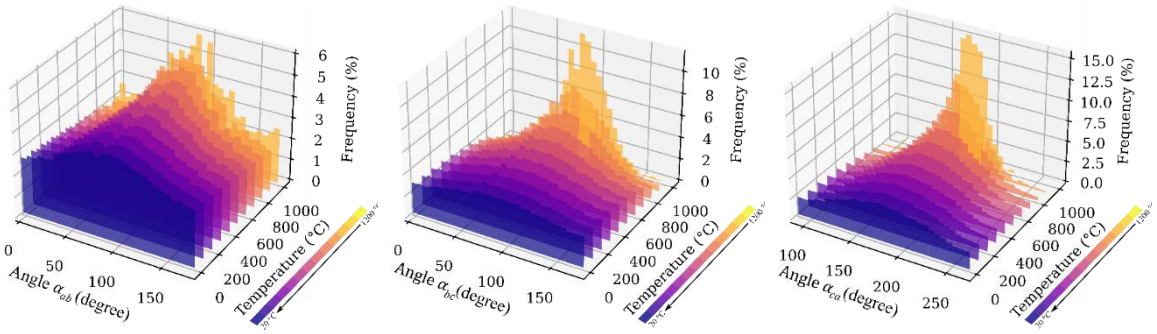

a) linear representation of α_{ab} in ab plane

b) linear representation of α_{bc} in bc plane

c) linear representation of α_{ca} in ca plane

Figure IV-19: Orientation angle distributions of microcrack "$\vec{n}$ " in different planes of local grain's orientation versus temperature

Since the orientation distributions closely resemble Gaussian profiles, their evolution can be quantitatively described using the mean and standard deviation as functions of temperature. In this case, only the standard deviation is presented in Figure IV-20, as the mean orientation remains essentially constant throughout the cooling process.

Figure IV-20, reveals the following trends:

- at high temperatures, the standard deviation associated with the "ca-plane distribution plot" and "bc-plane distribution plot" curves are relatively low, whereas higher values are observed for the "ab-plane's distribution plot" curve. This suggests that the normal vectors are confined to a narrow angular range in the "ca" and "bc" planes, while exhibiting a more dispersed distribution in the "ab" planes.
- all three standard deviation curves show an overall increase with decreasing temperature, indicating a progressive broadening of the normal vector orientation range;
- the standard deviation trends for the "ca-plane distribution plot" and "bc-plane distribution plot" are similar, whereas the "ab-plane distribution plot" follows a distinct evolution;
- among the three planes, "ca-plane distribution plot" consistently exhibits the lowest standard deviation across the temperature range, implying a more uniform orientation of the normal vectors. Consequently, the microcracks are predominantly and consistently aligned perpendicular to the ca-plane.

License CC BY-NC-ND 4.0

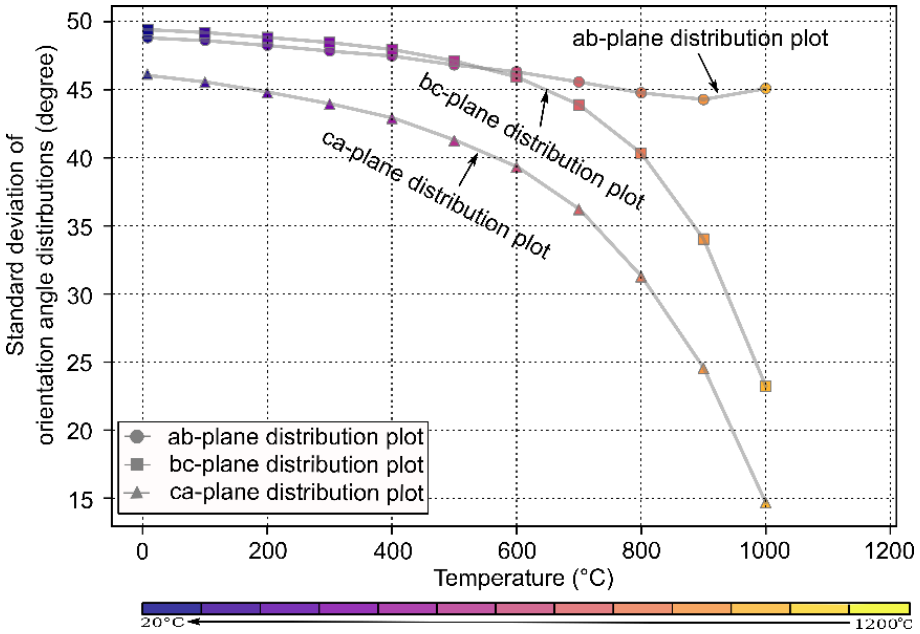

Figure IV-20: Standard deviation of the microcracks $\vec{n}$ distribution angle versus temperature

While, Figure IV-20 provides insight into the degree of microcrack orientation dispersion, it does not identify the dominant crack orientations. To determine the preferential planes and directions of microcracking, it is therefore necessary to quantify the distribution of normal vectors across different crystallographic planes and orientations. Vector and plane projection techniques are employed to identify the closest crystallographic direction associated with each microcrack normal vector $\vec{n}$.

The preferential orientation of each normal vector is determined by projecting $\vec{n}$, onto the unit vectors of the local grain axes ($\vec{a}$, $\vec{b}$, $\vec{c}$). The axis corresponding to the largest projection magnitude is considered the closest direction to the normal vector, and the associated orientation is assigned to the corresponding crack facet. The resulting orientation statistics are presented as a function of temperature in Figure IV-21, where the normal vector count is expressed as the ratio of vectors aligned with a given preferential axis to the total number of bonds in the numerical sample.

Figure IV-21 shows that the majority of microcrack normal vectors are aligned with the $\vec{c}$ orientation (that corresponds to highest CTE value), followed by $\vec{b}$ and $\vec{a}$ orientation. This indicates that most microcracks are oriented perpendicular to the $\vec{c}$ orientation. Moreover, the corresponding crack-facet are mainly in the ab plane which is perpendicular to the $\vec{c}$ orientation. Consequently, the associated crack facets are predominantly located within the ab-plane, which is orthogonal to the $\vec{c}$ orientation. Therefore, these results confirm that the highest CTE (α_c = 17.26×10$^{-6}K^{-1}$) plays a dominant role in microcrack initiation and propagation, consistent with the stress evolution trends observed in Figure IV-13b. Comparable conclusions were reported by Bruno et al., (2010) using the Integrity Factor (IF) model, which was validated through experimental EBSD measurements (Bruno et al., 2010). Their results demonstrated that microcracks preferentially initiate perpendicular to the crystallographic direction associated with the highest CTE, which represents the weakest mechanical link in AT materials (Ranganathan et al., 2026).

License CC BY-NC-ND 4.0

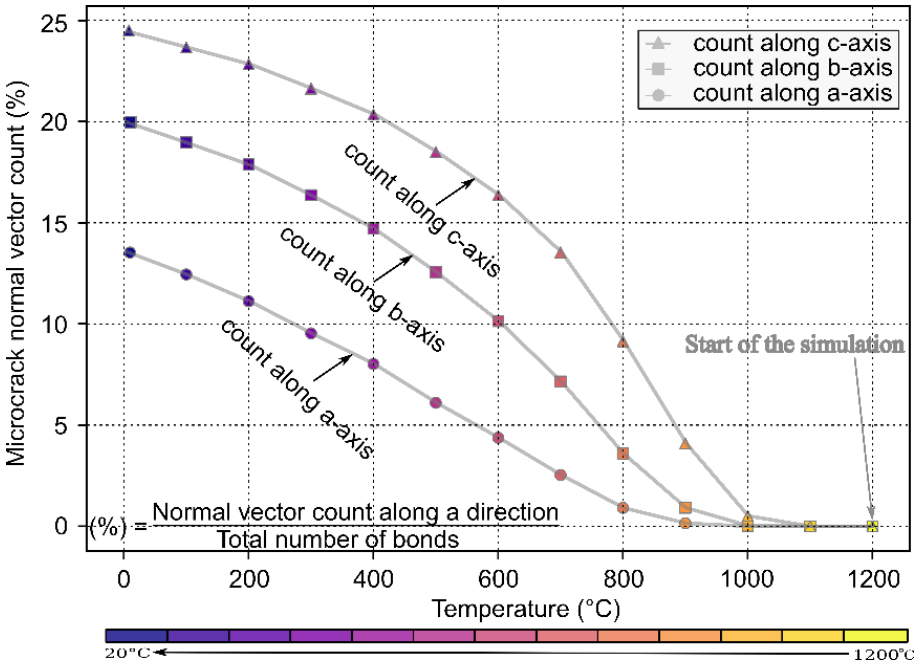

Figure IV-21: Microcrack $\vec{n}$ count in relation to the local crystallographic axes versus temperature

IV.3.2.2. Monitoring on the nature of cracks: Interface vs Bulk

This section is dedicated to locating the microcracks within the numerical sample. Mapping these locations helps reveal the dominant microcracking mechanisms and their dependence on temperature within the microstructure. For clarity and visualization, a 2D polycrystalline sample with free boundary conditions, as shown in Figure IV-22, s used for illustrative purposes. Regarding the bonds, as explained in section IV.2.1, two possible situations may arise, as illustrated in Figure IV-22a:

- the bonded DEs belonging to the same grain (Bulk bonds);
- the bonded DEs connecting two different grains (Interface bonds).



a) bonds b) cracks

Figure IV-22: Schematic representation of bulk and interface cracks along with their corresponding bonds in a 2D polycrystalline sample

Two distinct bond types are used to categorize the microcracks as either bulk cracks or interface cracks, as illustrated in Figure IV-22b. In this figure, microcracks are shown as black crack facets. This approach allows a clear distinction between cracks occurring within the bulk or those located

License CC BY-NC-ND 4.0

along the interface. It is important to highlight here that the term "**bulk crack**" refers to intragranular cracks and the term "**interface crack**" refers to intergranular cracks. In addition, few **clustered "bulk cracks"** could be referred as transgranular cracks (see section IV.3 for the definition) (Ranganathan et al., 2026).

Figure IV-23a and Figure IV-23b shows the evolution of bulk and interface cracks as the temperature decreases. Note, the Figure IV-23a presents the absolute number of microcracks, while the Figure IV-23b shows the relative contributions, with the sum of bulk and interface cracks normalized to 100%. Initially, the numerical sample contains 87,509 bulk bonds and 68,843 interface bonds.

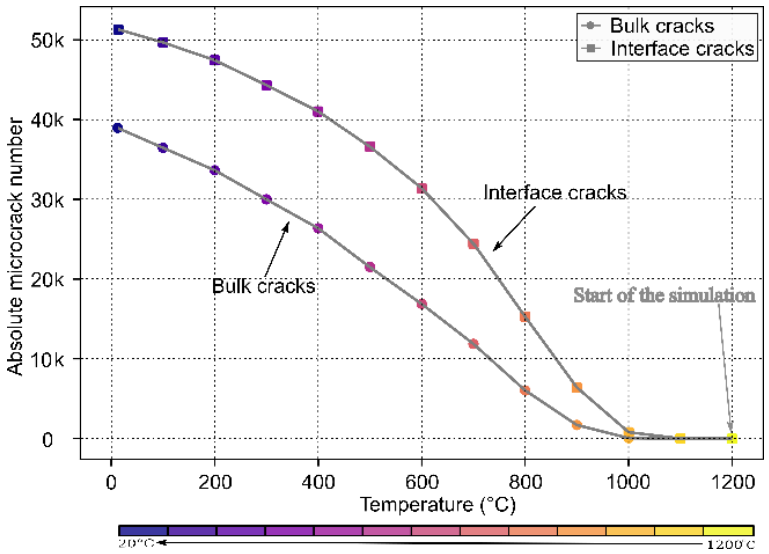

a) absolute evolution

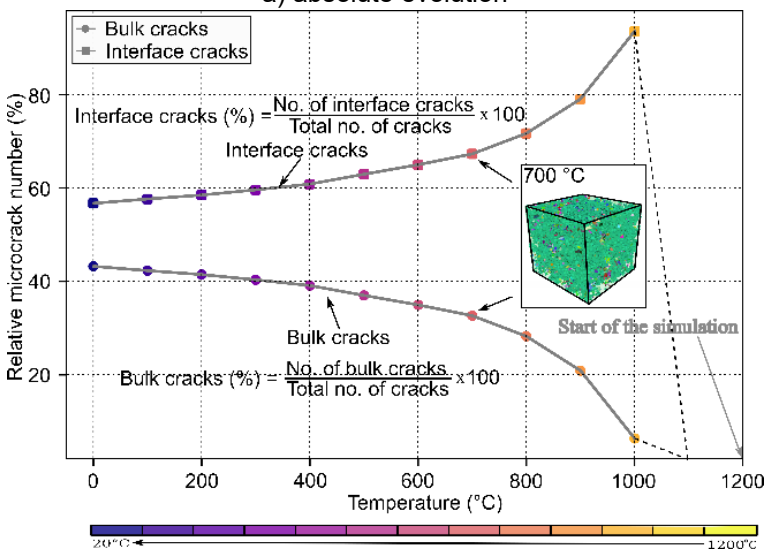

b) relative evolution

Figure IV-23: Evolution of the interface and bulk cracks versus temperature

From Figure IV-23a, several observations can be made:

- interface cracks dominate, indicating that thermal stresses arising from CTE mismatch are primarily concentrated at grain boundaries, consistent with experimental findings (Babelot et al., 2011; Huger et al., 2011; Mouiya, Tessier-Doyen, et al., 2023);
- both bulk and interface cracks exhibit a pseudo-stable stage between [1200 - 800℃] followed by rapid propagation from [800 - 400℃] and finally stabilize between [400 - 20℃] range;

License CC BY-NC-ND 4.0

- the rapid propagation phase is more pronounced for interface cracks compared to bulk cracks.

From Figure IV-23b, highlights that:

- at high temperatures, the interface cracks are dominant;
- as the temperature decreases, interface cracking diminishes while bulk cracking becomes more significant.

These trends suggest that microcracks initially form at grain interfaces (intergranular) and subsequently propagate into the grain interiors (intragranular). This observation aligns with experimental SEM studies (Babelot et al., 2011; Huger et al., 2011; Mouiya, Tessier-Doyen, et al., 2023). Therefore, the pattern observed in Figure IV-23b, also raises the question of whether microcracks exist as isolated instances or as part of larger, interconnected crack networks. To investigate this, a follow-up analysis focusing on the surface area of microcracks was performed to distinguish between isolated cracks and connected crack networks.

IV.3.2.3. Monitoring of the crack surface area

This section focuses on distinguishing isolated cracks from crack clusters, which are formed by interconnected crack facets. To achieve this, the surfaces of crack clusters are monitored during the cooling simulation. Tracking this information helps to better understand microcrack propagation and the formation of interconnected crack networks. The results are displayed in a 2D bar plot in Figure IV-24. To maintain scale-independence, the crack surface is normalized by the volume of the periodic unit cell, giving the crack surface per unit cell volume. In the plot, the x-axis represents individual crack cluster labels, while the y-axis indicates the total surface area of each crack cluster, calculated as the sum of the surfaces of the connected crack facets. Each bar represents either an isolated crack or a crack cluster formed by connected facets. Two cracks are considered connected if they share an edge, as illustrated in Figure IV-22b. In the Figure IV-24 different colors are used to differentiate the crack clusters.

Key observations from Figure IV-24 include:

- the first microcracks appear at 1000 ℃ (Figure IV-24a), initially forming small, isolated crack networks. This is reflected in the smooth decreasing trend in the crack density distribution;
- at 900 ℃ (simulation snippet in Figure IV-24b), new microcracks form while existing isolated cracks propagate in multiple directions, leading to the development of extended crack networks through clustering;
- notably, around 700 ℃ (Figure IV-24c), multiple crack networks merge into a single, complex crack network, which corresponds to the sharp decline in crack density. Few isolated microcracks remain;
- at 600 ℃, several remaining isolated cracks have merged with the primary network, reducing the number of distinct crack clusters. This indicates that crack propagation remains relatively stable during cooling, which can be observed by comparing Figure IV-24c and d;
- A similar merging and clustering mechanism continue in the temperature range [600 - 20 ℃] (Figure IV-24 (d-f))

Ultimately, the numerical sample is populated with 42 $\left(\frac{m^2}{m^3}\right)$ crack surface per unit cell volume at the end of cooling process. As highlighted in the Figure IV-24f only one single complex “zig-zag” crack network is present with few numbers of isolated cracks. In addition, such zig-zag complex crack networks were observed in the SEM analysis done by (Mouiya, 2024).

License CC BY-NC-ND 4.0

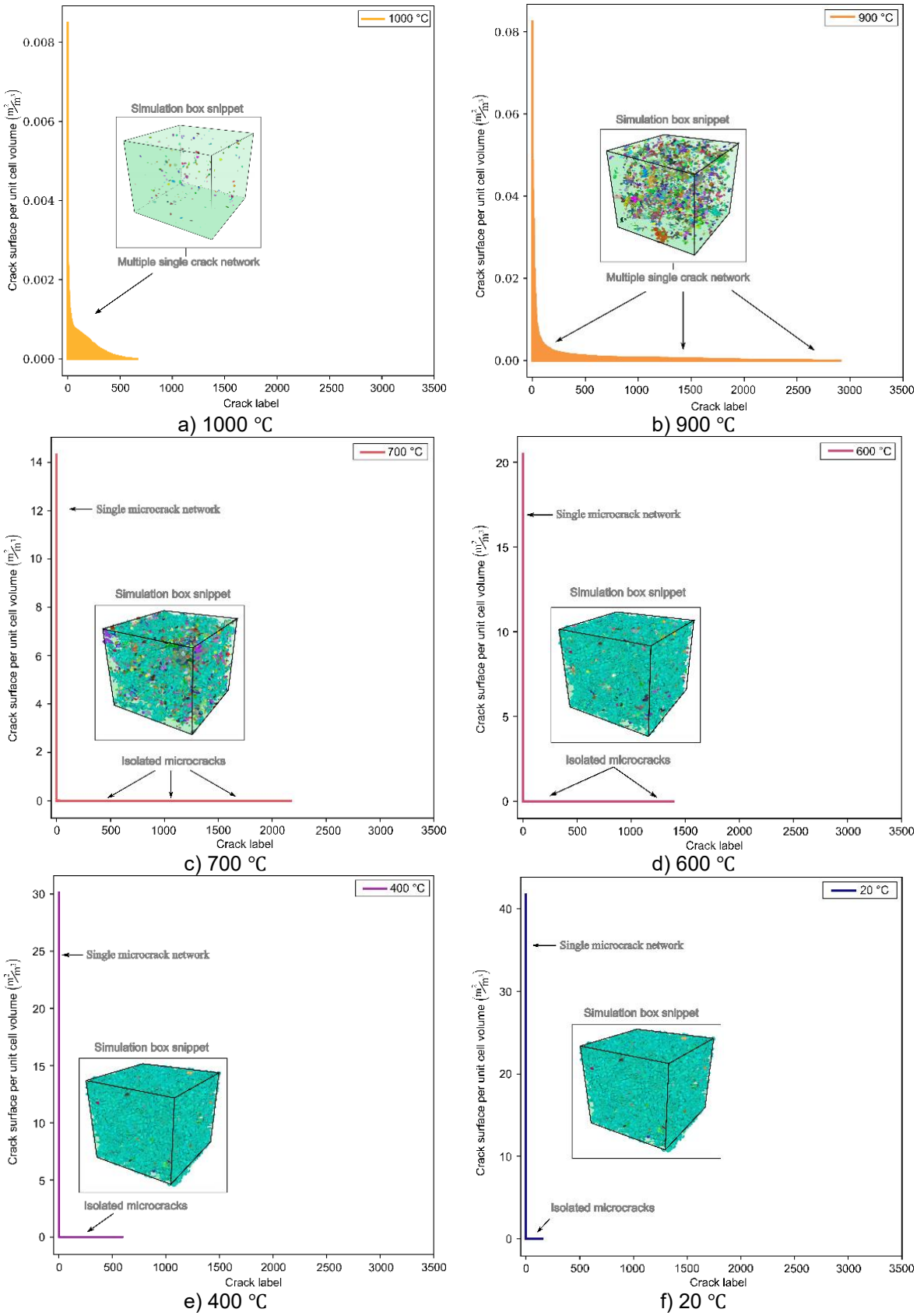

Figure IV-24: Monitoring of crack surface distribution at different temperature

IV.3.3. Apparent stress-strain response of microcracked numerical sample

This section focuses on analyzing the apparent stress–strain responses of the microcracked numerical samples. Following the cooling process, the samples are subjected to uniaxial tensile

License CC BY-NC-ND 4.0

loading. Unlike the preliminary study, pre-existing microcracks are now allowed to propagate, enabling a more realistic simulation of mechanical tensile behavior. Figure IV-25 presents the evolution of the apparent stress-strain curves for the damaged numerical samples at various temperatures. Apparent stress and strain were calculated following the methodology described in section II.2.1.4. From the Figure IV-25, several observations can be made:

- notably at high temperature [1200 - 1100 ℃], the samples display a typical brittle response;
- In the intermediate range [1000 - 800 ℃], the post-peak region increasingly exhibits non-linear behavior, particularly as the temperature moves further from 1200 ℃;
- at the lower temperature range of [700 - 20 ℃], non-linear behavior is observed in both the pre-peak and post-peak regions, reflecting the presence of a dense network of microcracks below 700 ℃;
- the peak stress decreases as the temperature are reduced;
- strain peak shows a decreasing trend from [1200 - 700 ℃], followed by an increase in strain-peak in the temperature range [700 - 20 ℃].

These trends indicate a progressive change in mechanical behavior as the temperature decreases. The response transitions from linear brittle behavior at high temperatures to quasi-brittle non-linear behavior at lower temperatures. At room temperature, the numerical sample exhibits pronounced non-linear behavior, a feature associated with enhanced thermal shock resistance, as reported in previous studies (Huger et al., 2011; Kakroudi et al., 2009; Mouiya, Martynyuk, et al., 2023). This transition in mechanical response, driven by microstructural evolution and microcrack initiation, has also been observed experimentally (Mouiya, 2024). The following sections aim to elucidate the mechanisms underlying this pronounced change in mechanical behavior.

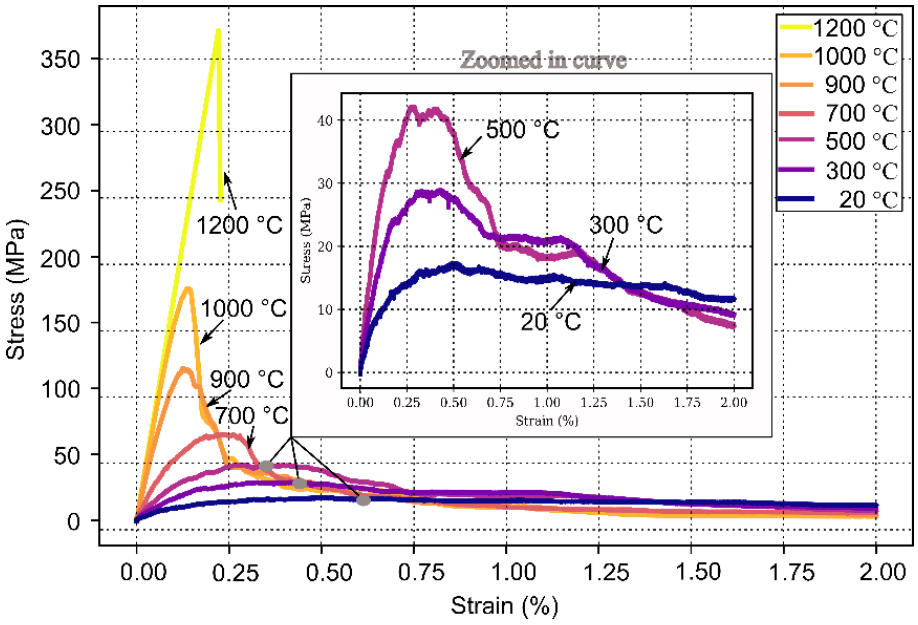

Figure IV-25: Evolution of apparent stress-strain versus the temperature

IV.3.4. Factors promoting non-linear stress-strain response

In this section the factors triggering non-linear stress-strain response are investigated. For this purpose, the initiation and propagation of the microcracks are recorded. In addition, the numerical samples are subjected to cyclic tensile loading to monitor the irreversible strains exhibited by the numerical sample.

IV.3.4.1. Internal thermal stress effects on the apparent stress-strain response

This section focuses on analysing the evolution of pre-existing microcracks formed during the cooling process and their influence on the apparent stress-strain response during uniaxial tensile

License CC BY-NC-ND 4.0

testing. To distinguish this from the earlier concept of a “crack network,” the term “microcrack” here specifically refers to individual broken bonds. Figure IV-26, Figure IV-27 and Figure IV-28 illustrate how microcrack propagation correlates with the apparent stress-strain behaviour at different temperatures. In these figures, a twin-axis format is used: the horizontal axis represents the apparent strain, the primary vertical axis corresponds to apparent stress, and the secondary vertical axis shows the relative number of microcracks. The microcrack count is calculated as the ratio of broken bonds (including those formed during cooling) to the total number of bonds in the numerical sample.

At temperatures ranging from [1200 to 1100 ℃], Figure IV-26a and b indicates that:

- no pre-existing microcracks are present before applying the uniaxial tensile load;
- crack initiation and propagation occur abruptly, as indicated by the rapid increase in the microcrack count, reflecting unstable crack growth and a characteristic brittle response at these temperatures;
- even in the absence of pre-existing microcracks at 1200 and 1100 ℃, the peak stress (stress of rupture) decreases with temperature, suggesting the influence of internal tensile stresses at 1100 ℃ (as illustrated in section IV.3.1) that reduce the sample’s strength.

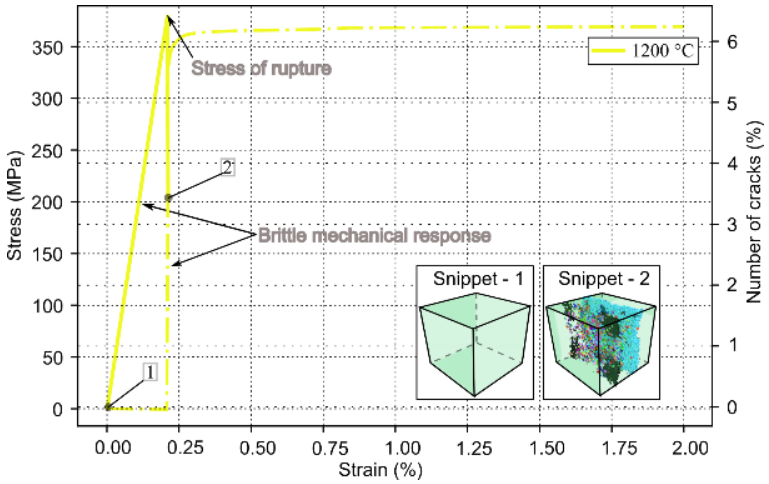

a) 1200 ℃

b) 1100 ℃

Figure IV-26: Thermal effects impact on the stress-strain behaviour in [1200-1100 ℃] range

At the intermediate range of [1000 to 800 ℃], Figure IV-27a and b indicates that:

- up to the peak stress (stress of rupture), crack propagation occurs in a relatively stable manner; however, the material still exhibits a brittle response. This indicates that the

License CC BY-NC-ND 4.0

existing thermal stresses and microcracks are not sufficient to induce a fully non-linear behaviour;

- beyond the stress peak, a slight non-linear response emerges, suggesting that crack propagation continues in a controlled manner and reflecting the presence of diffuse damage mechanisms at the microstructural level (Mouiya, 2024);
- the stress peak itself continues to decrease, highlighting the influence of internal thermal stresses as noted in previous observations.

These results imply that achieving stable crack propagation requires the numerical sample to possess a sufficient amount of complex microcrack networks along with significant internal thermal stresses.

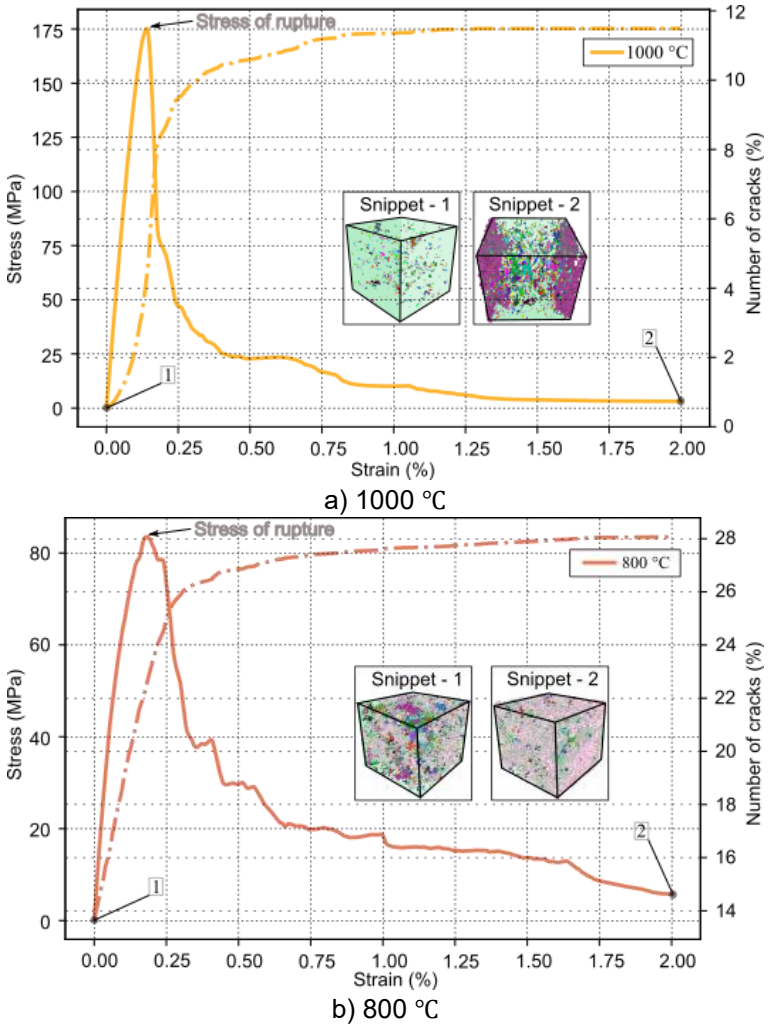

Figure IV-27: Thermal effects impact on the stress-strain behaviour in [1000-800 °C] range

At a temperature range of [700 to 20 °C], Figure IV-28a and b indicates that:

- the full non-linear behaviour is observed across this temperature range, encompassing both the pre-peak and post-peak regions of the stress-strain response;
- the extent of nonlinearity depends on the magnitude of pre-existing internal thermal stresses and the microcracks;
- during the initial loading phase, up to the stress peak, pre-existing microcracks propagate in a stable manner, suggesting the presence of crack-resisting mechanisms driven by internal compressive thermal stresses. This behaviour reflects diffuse damage mechanisms at the microstructural scale, as discussed in reference (Mouiya, 2024);
- Beyond the stress peak, stable crack growth continues, accompanied by an increase in the rupture strain, consistent with observations reported in (Mouiya, 2024).

License CC BY-NC-ND 4.0

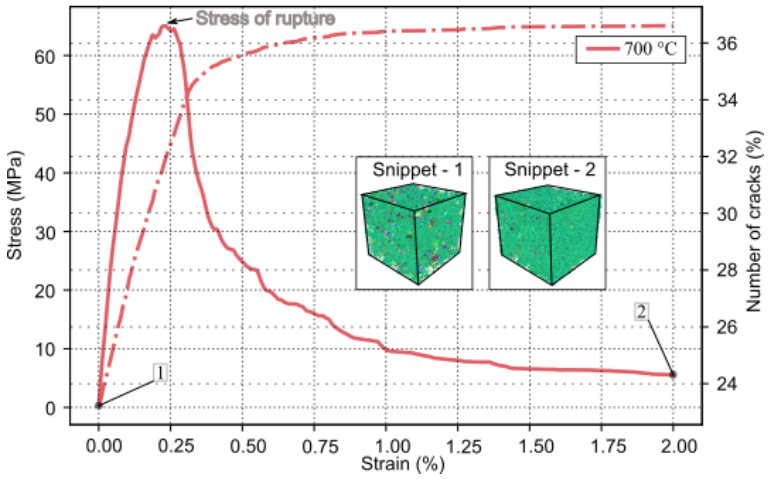

a) 700 °C

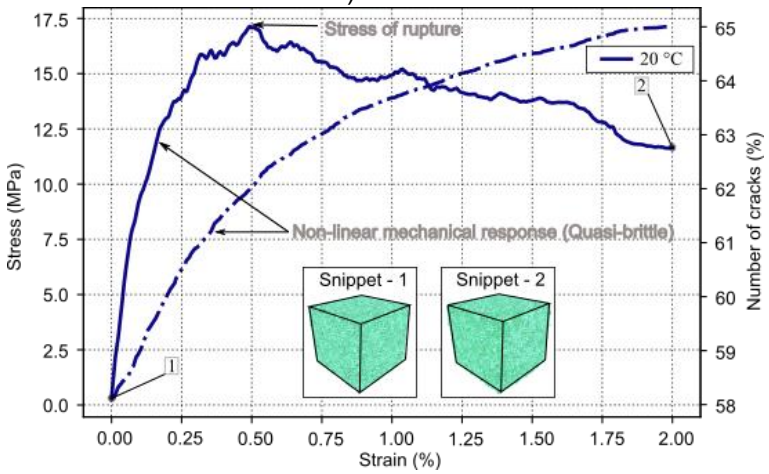

b) 20 °C

Figure IV-28: Thermal effects impact on the stress-strain behaviour in [700-20 °C] range

Therefore, understanding the interplay between pre-existing thermal stresses (estimated from the thermal stress distribution plots in section IV.3.1) and the presence of microcracks is essential for explaining changes in the mechanical behaviour of the material. To quantify the number of pre-existing microcracks required to influence the numerical sample's response, Figure IV-29 presents the total crack count before and after the mechanical loading phase.

In the Figure IV-29, microcrack evolution is plotted as a function of temperature, represented by three distinct curves corresponding to different stages of tensile testing. The "Start of simulation" curve indicates the number of microcracks formed during the cooling process. The "End of simulation" curve shows the total microcrack count after the tensile test, when the sample exhibits negligible stiffness. The "Difference" curve represents the increase in microcracks induced by the mechanical loading, calculated as the difference between the "End of simulation" and "Start of simulation" curves.

From the Figure IV-29, it appears that:

- the "Start of simulation" curve consistently shows fewer microcracks than the "End of simulation" curve;
- in the temperature range [1200 to 800 °C], the pre-existing microcracks count ranges from 0% to 15%, with mechanical loading causing an additional 6% to 15% increase in microcrack count;
- in the temperature range [800 to 20 °C], the pre-existing microcracks count increases from 15% to 58%, while mechanical loading contributes an additional 6% to 15% increase;

License CC BY-NC-ND 4.0

- The declining trend of the “Difference” curve in the 800 to 20 ℃, suggests the activation of crack resistance mechanisms around 700 ℃.

Therefore, these results indicate the presence of two different stages for the “Difference” curve. The 700 ℃ temperature mark seems to be the transition point from the stage-1 (1200 to 700 ℃) to stage-2 (700 to 20 ℃). Now, on correlating the observation seen in Figure IV-25 and Figure IV-29, it is observed that the transition from brittle to quasi-brittle non-linear response is also at the 700 ℃ temperature mark. In correspondence, (Mouiya, 2024) observed the transition of brittle to non-linear mechanical response approximately around 700 ℃ by experimental study. Indeed, further investigations are needed to make sure if the correlated conclusions is not just a coincident rather an important conclusion to relate the transition of mechanical response with the observed crack statistics.

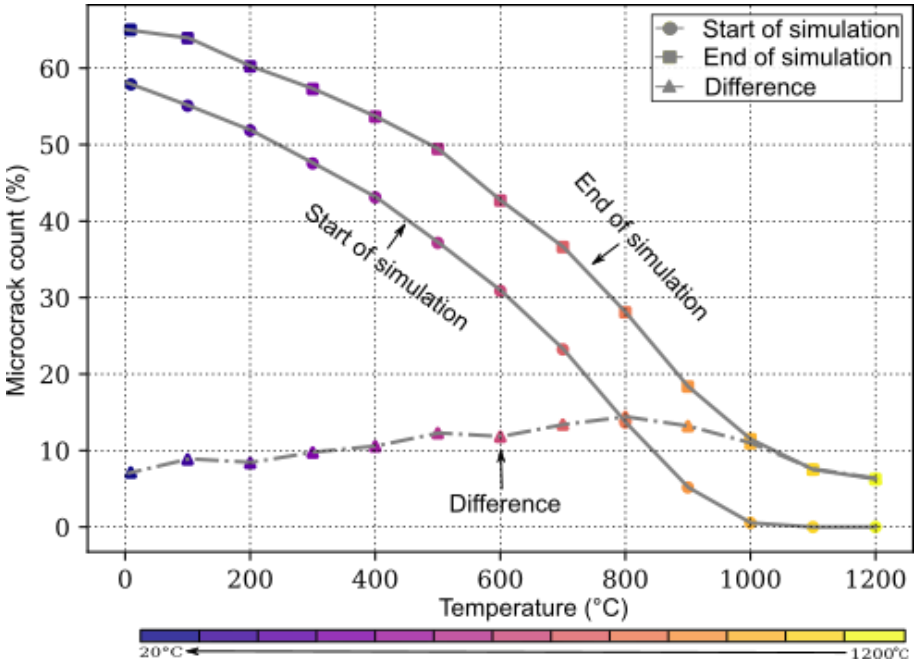

Figure IV-29: Progression of microcracks in the model material as a function of temperature

IV.3.4.2. Irreversible strain effects on the apparent stress-strain response

This section focuses on tracking and recording irreversible strains within the numerical sample. To highlight these permanent deformations, a cyclic uniaxial tensile test is conducted. Because periodic boundary conditions are employed, the cyclic loading follows the stretching strategy described in section II.2.1.3 with the key modification being the presences of an unloading phase.

In the present study, the loading and unloading sequence is performed as illustrated in Figure IV-30. Specifically, the Figure IV-30a and Figure IV-30b correspond to cyclic tests applied to samples cooled from 1200 ℃ to 1000 ℃ and 1200 ℃ to 500 ℃. During the loading phase, the numerical sample is stretched at a constant rate (r) per iteration. The unloading phase is applied at the same rate until the apparent stress ($\langle\sigma_{XX}\rangle$), along the loading direction reaches the targeted value. The number of iteration (N) required to reach the stretch peak (ΔL_X^{peak}) is determined simply by:

$$\Delta L_X^{peak} = r \times N \qquad \text{IV-4}$$

This stretch is applied as a linear function. Once it reaches the peak value (ΔL_X^{peak}), the unloading phase commences, during which the sample is relaxed at the same rate (r). Throughout this phase, the apparent stress ($\langle\sigma_{XX}\rangle$) is monitored to ensure that the targeted zero-stress state which marks

License CC BY-NC-ND 4.0

the beginning of a reloading phase at the same rate (r). Figure IV-30a and Figure IV-30b illustrates two different cycles at different temperature. For the following cycles, the target stretch amplitude is increased by 20% relative to the initial peak, as illustrated in Figure IV-30a and Figure IV-30b. This loading-unloading sequence is repeated throughout the simulation. The cyclic procedure is applied to the numerical sample that has already been damaged during the cooling process.

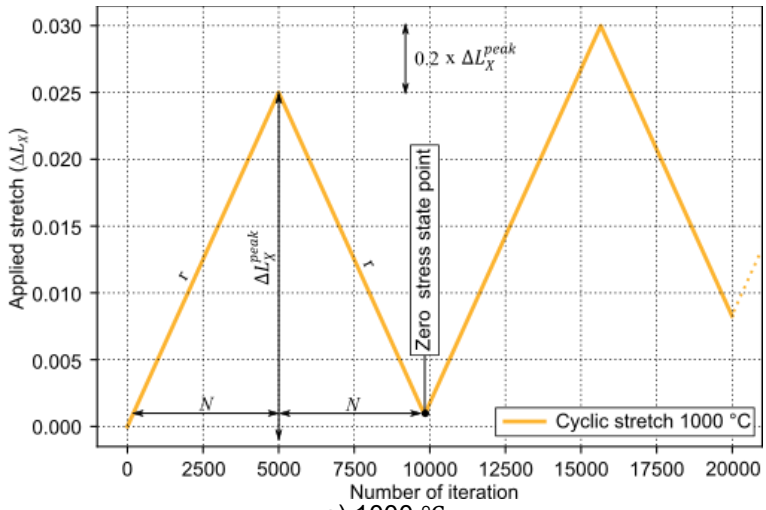

a) 1000 ℃

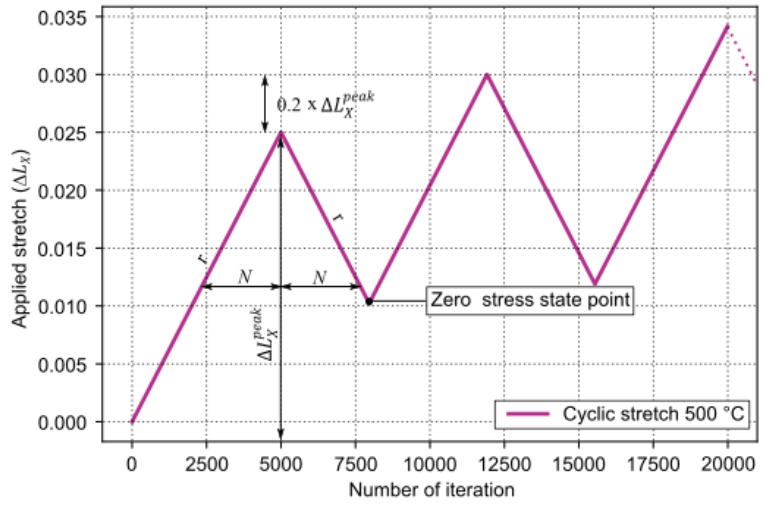

b) at 500 ℃

Figure IV-30: Evolution of the applied cyclic stretch over successive iterations

As in the previous section, pre-existing microcracks are allowed to propagate during the simulation. Figure IV-31a and Figure IV-31b presents the stress-strain responses of samples cooled from 1200 ℃ to 1000 ℃ and to 500 ℃, respectively. Consistent with earlier observations (see Figure IV-25), the numerical samples exhibit a non-linear mechanical response. However, this previous approach did not provide information regarding the development of irreversible strains.

Figure IV-31a and b illustrates that:

- the stress-strain response demonstrates the presences of irreversible strains;
- the unloading phases exhibit linear responses;
- the global rigidity of the numerical samples is reduced indicated by the decrease of slope during the successive unloading phases.

License CC BY-NC-ND 4.0

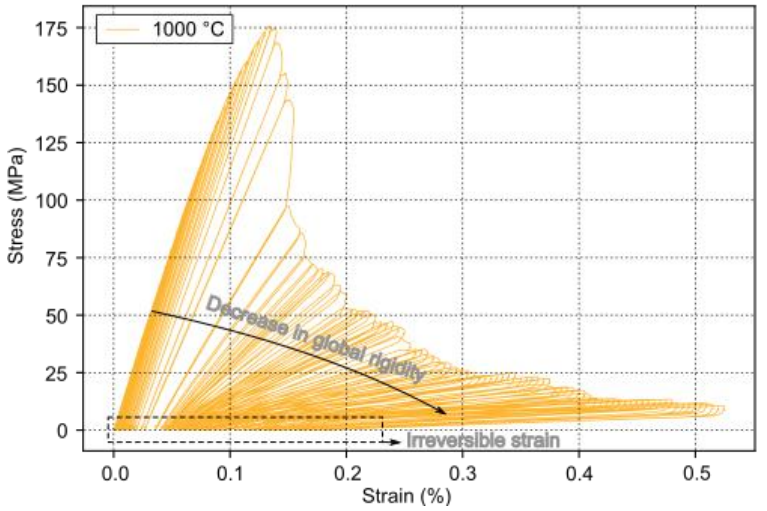

a) at 1000 ℃

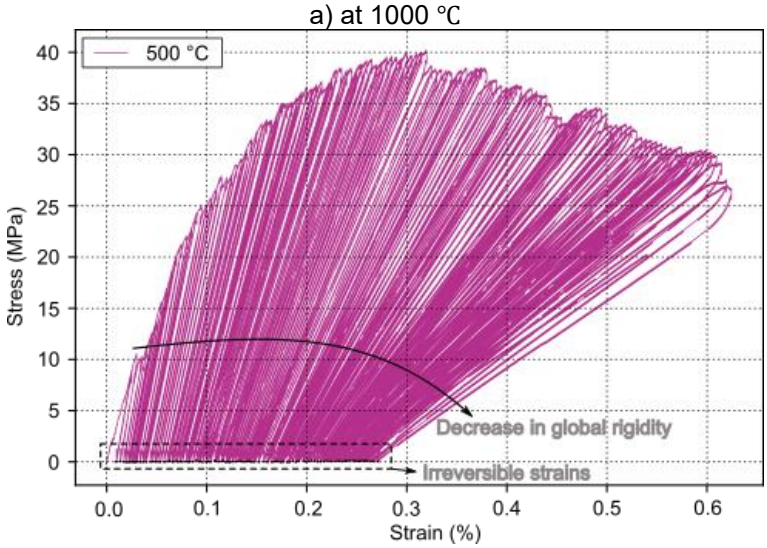

b) 500 ℃

Figure IV-31: Monitoring irreversible strain development under uniaxial cyclic loading

This type of mechanical response is characteristic of quasi-brittle materials (Mouiya, 2024), which exhibit progressive damage due to microcrack extension. Furthermore, the irreversible strains observed, though not explicitly modeled as plasticity in the present framework, result from the accumulation of thermal stresses during cooling. These stresses are partially relieved through microcrack propagation, leading to irreversible, “pseudo-plastic” strains that manifest in the apparent response of the numerical samples

Thus, this study highlights that the observed non-linear behavior and irreversible strains are driven by the formation of complex microcrack networks and the development of internal thermal stresses. These microstructural mechanisms play a key role in enhancing the material’s sustainability under thermal shock. This study highlights the role of accumulated internal stress within the microstructure in driving irreversible strain. Moreover, this internal stress exacerbates the nonlinear stress-strain response through a stress-redistribution mechanism as microcracks propagate.

IV.3.5. Numerical vs experimental: microcracked sample response under cyclic loading

In this section the cyclic mechanical response of the microcracked sample (at 20 ℃) was monitored at the room temperature. In order to validate the DEM tool, the simulations results are compared to the experimental results as shown in the Figure IV-32 (Mouiya, 2024). These figures show the mechanical response of AT numerical (see Figure IV-32a) and the experimental

License CC BY-NC-ND 4.0

(see Figure IV-32b) samples under uniaxial cyclic tensile loading. This figure illustrates just the early stages of the tensile test with a few loading cycles. In the case of the numerical sample, the cyclic uniaxial loading was performed by the strategy described in section IV.3.4.2.

Despite using simplified input material properties and simplified microstructure, the simulation results in terms of capturing irreversible strain how strong qualitative agreement and close quantitative correspondence with the experimentally measured stress-strain responses, as shown in Figure IV-32a and b. Indeed, the numerical and experimental values, in terms of stress peak and irreversible strains (with a very slight discrepancies as highlighted in Figure IV-32), fall within the same order of magnitude, which is particularly noteworthy given the simplifying assumptions inherent in the numerical model.

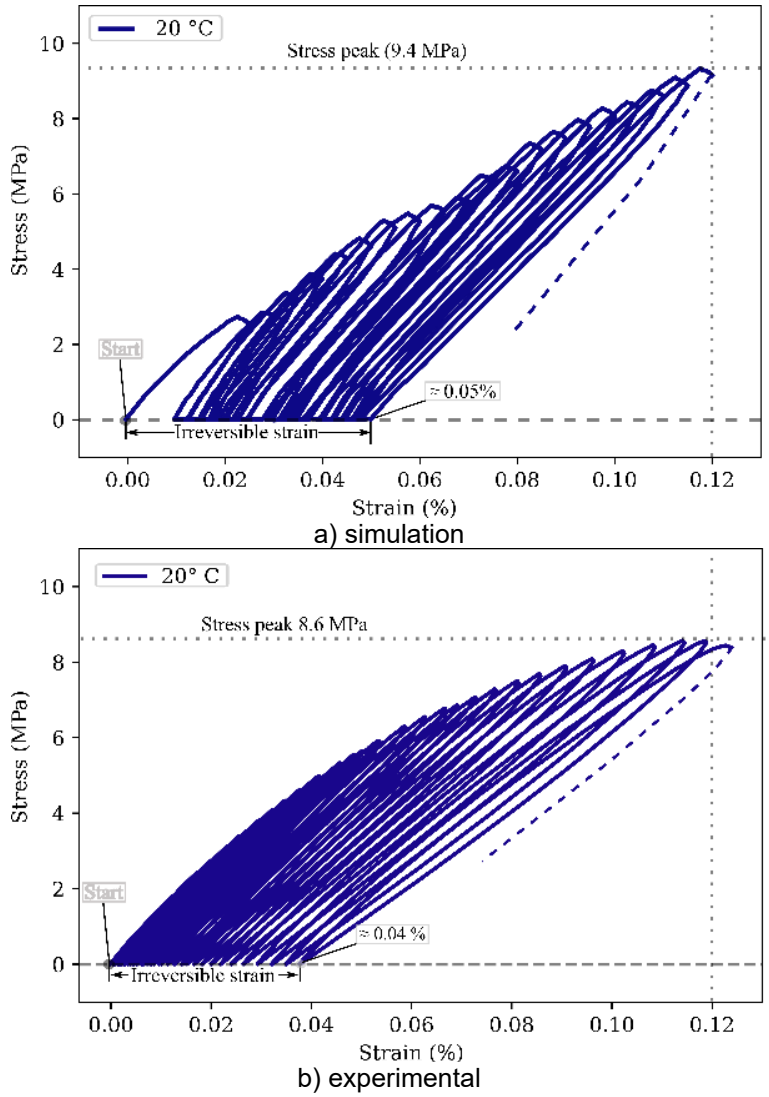

Figure IV-32: Cyclic uniaxial stress-strain response of AT under cyclic loading at 20 °C

Consequently, these findings demonstrate that the model successfully reproduces the key mechanisms responsible for the temperature-dependent emergence of non-linear material behavior. In addition, this tool facilitates the understanding of the micromechanics (internal thermal stress, microcracking etc) occurring at the microstructural scale during CTE mismatch and their impact on the microstructure-thermomechanical property relationship.

License CC BY-NC-ND 4.0

IV.4. Conclusion

In summary, the proposed DEM framework successfully reproduces anisotropic thermal expansion and fracture mechanisms in polycrystalline materials driven by grain-scale mismatches in thermal expansion. By explicitly accounting for crack initiation and propagation, the model provides valuable insight into the link between microstructural features and the resulting macroscopic thermomechanical response of refractory materials. AT was selected as a benchmark material to assess and validate the capabilities of the numerical approach. The simulations demonstrate that the developed DEM model is able to capture the emergence and interaction of complex microcrack networks during cooling, a phenomenon that remains challenging to represent accurately using conventional continuum-based methods such as the FEM.

Firstly, the novel DEM tool is employed to monitor the impact of microstructural evolutions (due to the promotion of microcracks) on the apparent thermomechanical properties, such as Dilatometry and Young's modulus (Ranganathan et al., 2025). Indeed, these results depicted both the quantitative and qualitative aspects of the experimental results. Next, the polycrystalline numerical sample is used to investigate the microstructural evolution during cooling simulations. First, the DEM framework enabled the tracking of thermal stress development throughout the cooling stage. In addition, the numerical approach successfully reproduced several key mechanisms observed in AT materials, including stress relaxation associated with crack initiation, the effect of grain-dependent crystallographic orientations on thermal stress distribution, and the emergence of pseudo-plastic behavior.

Additionally, the model enables the observation of microcrack initiation and propagates as the temperature decreases during cooling. Statistical analyses of the resulting cracks were conducted to investigate preferred crack orientations, determine their initiation mechanisms and propagation paths, and assess whether cracks remain isolated or evolve into interconnected networks at the microstructural scale. These analyses reveal a strong correlation between the crystallographic orientation of AT grains and their tendency to generate microcracks. The simulations show that, at elevated temperatures, microcracking begins as small, spatially localized crack network with well-defined preferred orientations. As cooling progresses, these networks progressively extend and coalesce, ultimately forming an extensive and highly interconnected complex crack network characterized by a wider and more dispersed range of orientations (Ranganathan et al., 2025).

In addition, the DEM framework was used to evaluate the apparent stress-strain behavior of the material under monotonic mechanical loading at different cooling temperatures. The resulting responses demonstrate that the model successfully captures the progressive transition of the material behavior from a brittle regime to a non-linear, quasi-brittle response. Furthermore, the simulations reveal the role of internally generated thermal stresses in governing both the rupture strength and the tendency for crack initiation and propagation during monotonic loading. Finally, the DEM approach proves capable of tracking irreversible deformation mechanisms, often referred to as pseudo-plasticity, arising from crack evolution under cyclic mechanical loading (Ranganathan et al., 2025).

Therefore, the DEM tool can be used to analyses more complex systems such as embedding pores into the sample to investigate the impact of pores and pores-microcrack interactions on the materials responses.

License CC BY-NC-ND 4.0

Chapter V. iDLSM modelling of microcracking induced by anisotropic thermal expansion: porous polycrystalline case study

V.1. Introduction

Having explored the effects of anisotropic CTE on multiple crack initiation and propagation in a dense (polycrystalline) material in the previous chapter, it is now essential to examine the role of pores which is often present in refractory microstructures (Z. Chen et al., 2020; Hou et al., 2022; Nemaleu et al., 2023; Tessier-Doyen, 2003; L. Yang et al., 2022). This investigation will focus on how pores influence the thermomechanical behaviors of numerical samples closer to industrial refractories (Bruno et al., 2010; Bruno & Kachanov, 2016; Honda et al., 2009; Nishikawa et al., 2001; Roy, 2025; Smith et al., 2013).

The presence of pores is common in refractory microstructures. The introduction of pores into the refractory microstructure helps the material to improve its insulating properties and reduce its density (lightweight) (Z. Chen et al., 2020; Hou et al., 2022; Nemaleu et al., 2023; Studart et al., 2006). Usually, a pore in refractories is void formed from the interstices between grains of aggregate or between matrix and an aggregate, that is either completely or partially surrounded by solid grains (Callister Jr & Rethwisch, 2020). Unlike microcracks, which are commonly modeled as penny-shaped, planar flaws with very small thickness-to-radius aspect ratios ($\zeta = c/a \ll 1$), pores in brittle ceramics and rocks are often treated as quasi-spherical or moderately aspherical voids with aspect ratios close to unity and therefore are not usually considered planar cracks, pores in brittle ceramics are often treated as quasi-spherical or moderately aspherical voids with aspect ratios close to unity and therefore are not usually considered planar cracks (Yuan et al., 2021). In the literature, pores are typically quantified by volume fraction, either as total porosity or open porosity (% or cm^3/cm^3) (Chaudhuri & Sircar, 1981; Roy, 2025; Tessier-Doyen, 2003). It is noted that this volume fraction is less than 1% in dense materials, while it can be from 1% or more in porous materials (Tessier-Doyen, 2003). Additionally, key parameters such as pore size (for understanding size distribution statistics), shape (to analyze shape distribution and the effects of orientation), and spatial statistics (including density and connectivity, which impact pore spacing and openness) are closely linked to processing methods, microstructural design, and the resultant properties of the materials (Andersson, 1996; Callister Jr & Rethwisch, 2020; Chaudhuri & Sircar, 1981; Nishikawa et al., 2001; Roy, 2025).

The specific mechanisms involved in processing refractory ceramics contribute to the formation of porosity (Callister Jr & Rethwisch, 2020; Chaudhuri & Sircar, 1981). These mechanisms include the burnout of organic binders and fugitive additives, thermal decomposition of carbonates or hydrates, or the entrapment of air during mixing (Kazemi, 2019; Sarkar, 2020; Zhang et al., 2018). Gases released during these reactions can create closed pores, while incomplete sintering and grain boundary grooving can preserve micro- and mesopores (Callister Jr & Rethwisch, 2020; Terzić & Pavlović, 2009; Tessier-Doyen, 2003). Additionally, the pyrolysis of carbonaceous binders results in interconnected coke porosity, which can affect oxidation resistance and thermal shock behavior (Zhang et al., 2018).

At room temperature, the impact of pores on material properties can be classified into different categories. Firstly, the presence of pores tends to degrade the "bulk" properties that are directly related to the load-bearing or heat-conducting solid phase (Hirata et al., 2017; Nishikawa et al., 2001; Pandey et al., 2014; Smith et al., 2013). These properties include density (Chaudhuri & Sircar, 1981), Young's modulus (Callister Jr & Rethwisch, 2020), shear modulus (Phani & Sanyal, 2008), bulk modulus (Phani & Sanyal, 2008), fracture strength (Ashizuka et al., 2002; Nishikawa et

License CC BY-NC-ND 4.0

al., 2001), and thermal conductivity (Smith et al., 2013), among others. In contrast, properties such as the CTE and melting temperature are primarily not affected and remain stable or change little unless the pore volume exceeds certain thresholds (greater than 20-30% by volume) (Hirata et al., 2017; Roy, 2025). As a result, they are often regarded as effectively constant, for standard low-porous refractory materials.

Finally, from the literature, it can be understood that properties such as Poisson's ratio (which is dependent on higher-order microstructural information) (Tessier-Doyen, 2003), fracture toughness (which depends on pore size/shape and crack-bridging effects) (Yang et al., 2002), and thermal shock resistance (which is dependent on several pore-sensitive variables) (Coble & Kingery, 1955; Roy, 2025) are highly microstructure-dependent. Experimentally, it has been observed that introducing porosity in refractory material significantly acts as crack arresters or deflectors (Lee & Moore, 1998) at the microstructural scale and is believed to contribute in improving the thermal shock resistance (Coble & Kingery, 1955; Luo et al., 2020; Yang et al., 2002; Zhang et al., 2018). Although extensive research has examined the effect of porosity on various macroscopic properties of ceramic materials (as discussed above), limited information is available in the literature regarding the micromechanics of porous microstructures and the role of pores in the thermal-shock sustainability of refractory materials (Bruno et al., 2010; Bruno & Kachanov, 2016).

Therefore, this Chapter aims to simulate and perform a comparative study between a dense and a porous microstructure with the DEM approach proposed in Chapter II and Chapter IV. To conduct this study, multiple pores, representing a specified volume fraction (%) and distributed at random locations, are modeled. Here, the primary objective of the study is to investigate the impact of pores on the microstructure and its apparent thermo-mechanical properties, considering multiple crack initiation and growth, similar to Chapter IV. As mentioned in Chapter II, the BPEM-based DEM approach is employed to model the fracture mechanisms under the sintering process of refractory materials. Again, the iDLSM model is being used (see Chapter II).

For this purpose, a simplified porous AT polycrystalline numerical sample as a model material is employed for this study. A simplified porous polycrystalline model (achieved by embedding pores into the simplified model proposed in Chapter IV) is employed in this chapter. Later, this model is employed to perform a thermomechanical simulation and to gain insight into the impact of pores on the thermomechanical properties (such as apparent CTE and Young's modulus) and micromechanics (such as internal thermal residual stresses and crack statistics similar to Chapter IV) at the microstructural scale of the model material. In addition, the apparent response of the porous domain under monotonic and cyclic tensile loading is monitored. Therefore, to gain insight into the role of pores, the results obtained using the dense polycrystalline model material in Chapter IV are used as a reference result to enable a comparative study for a porous and non-porous systems.

V.2. Porous polycrystalline model

The aim of this study is to better understand the difference in behavior of the dense and porous polycrystalline materials during the post-processing cooling step after the sintering processes. Therefore, this section introduces the strategy for embedding pores into the targeted AT polycrystalline microstructure. In addition, this section is dedicated to monitoring the evolution of the thermomechanical properties (Young’s modulus and CTE (Ranganathan et al., 2025)) of the porous model material and perform a comparative study with the dense AT microstructure described in Chapter IV.

License CC BY-NC-ND 4.0

V.2.1. Porous polycrystalline microstructure digitalization strategy

The strategy for generating a polycrystalline sample (Ranganathan et al., 2025) with N_{GR} grains, each with its own geometry, crystallographic orientations and touching grains, was already described in section IV.2.1. In this section, the strategy of embedding pores into the numerical polycrystalline microstructure will be described. In the present study the pores are assumed to have spherical geometry. Moreover, the pores are considered to be non-connected and randomly located into the microstructure. The model is simplified by considering only isolated spherical pores, thereby reducing complexity while retaining essential features of porosity.

As it is challenging to visualize the pores embedded in the 3D sample, the strategy is illustrated using a 2D sketches as shown in Figure V-2. As a first step, a polycrystalline sample (PBC-PGB) with N_{GR} grains (see Figure V-2a) are generated using the strategy described in section IV.2.1.

Now, to embed pores into the sample of interest, firstly a pores-Representative Volume Synthetic Image (pores-RVSI) is generated. The advantage of using 2D or 3D synthetic images is to enable future usage of experimental images acquired with SEM, FIB-SEM or 3D tomograph techniques (Longchamp et al., 2024). The strategy to generate pores-RVSI is described below:

- N_{pores} spheres are packed inside a cubic domain (see Figure V-1a), in a random manner. Note, the radius of the spheres could be kept constant or could be randomly distributed with respect to a defined statistical distribution function. Each sphere represents a pore. The packing of the spheres is done using an algorithm that is implemented using the Python language. This algorithm generates spheres and arranges them in random positions across the 3D space without undergoing overlapping. A mathematical criterion is being employed to preserve non-overlapping arrangement and a function named “random-spheres” from the “porespy” (an inbuilt python library (Gostick et al., 2019)), is being used to assign the coordinate (spheres centroids) for the arrangement of spheres. Moreover, the targeted number of spheres or targeted volume fractions of the sphere is being used as the controlling parameter and to stop the algorithm from arranging spheres in the 3D space. The Napari python library (napari Work, 2019) is used for visualizing the obtained (3D) synthetic image as shown in Figure V-1d;
- now, in order to define the pores-RVSI, a cubical transitory sub-domain (internal box in Figure V-1a) is being employed. Here, the dimensions of the pores-RVSI are similar to the dimensions of the central unit cell (the term defined in section IV.2.1) of the PBC-PBG sample;
- now, this transitory sub-domain acts as a boundary to perform a selection process of spheres. In this selection process, the spheres that touch or belong into the volume of the sub-domain are treated as “set-1“ (highlighted in black) and the other spheres as “set-2” (highlighted in red in Figure V-1a). Finally, the red spheres, belonging to “set–2” are deleted (see Figure V-1b), while the spheres belong to the “set-1” are preserved;
- lastly, this pores-RVSI is treated as the central unit cell (the highlighted central region in Figure V-1b) to generate PBC-Pores Mask Synthesized Image (PMSI) (see Figure V-1c) by replicating the central unit cell. This process ensures periodicity of the PBC-PGB sample.

License CC BY-NC-ND 4.0

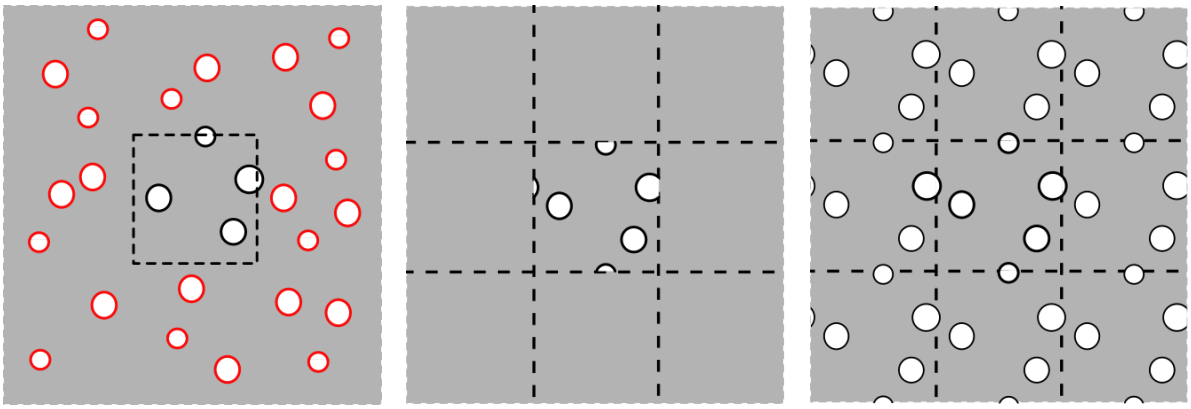

a) 2D main domain b) 2D pores Unit Central Cell (UCC) c) 2D replicating UCC

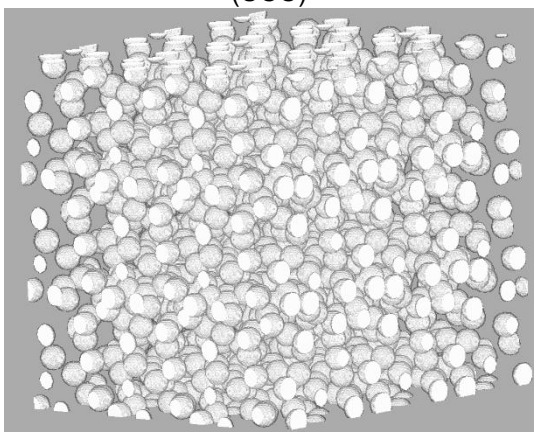

d) 3D result

Figure V-1: Illustration of the strategy to generate the PBC-PMI sample

As an outcome, the PBC-PMSI respects the dimension of the PBC-PGB sample. Now, this PBC-PMSI is applied as a mask to the PBC-PGB sample. Finally (see Figure V-2c), applying such a masking strategy facilitates the generation of porous polycrystalline domain. In other words, the masking strategy identifies all the DEs centroids that belongs into the pore's regions and eliminates them from the model.

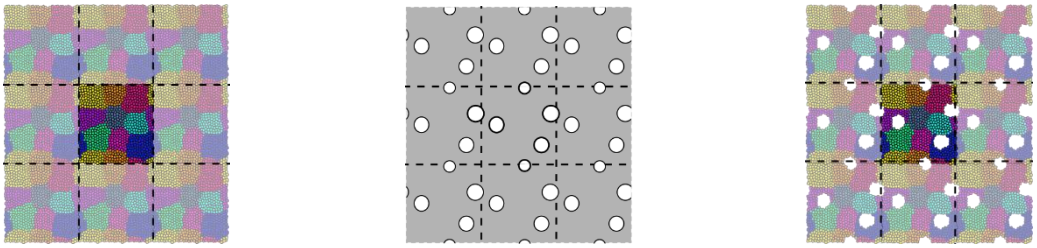

a) 2D polycrystalline sample b) 2D pores mask c) 2D results

d) 3D results

Figure V-2: Illustration of porous polycrystalline domain generation

License CC BY-NC-ND 4.0

This strategy facilitates embedding the pores into the polycrystalline sample using synthetic image. Moreover, this principle can be employed to embed pores into any PBC sample of interest by using it with synthetic or, as a perspective for further studies, real image acquired by different microscopy techniques such as SEM, FIB-SEM or 3D-tomograph (Longchamp et al., 2024).

V.2.2. Anisotropic thermal expansion of porous polycrystalline elastic domain

The porous polycrystalline domain is subjected to a cooling thermal treatment (similar to section IV.2.1.1) to verify the impact of pores on the apparent anisotropic thermal expansion (Hirata et al., 2016, 2017; Roy, 2025). Again, the porous polycrystalline numerical sample considers the thermal anisotropy of each grain with randomly assigned local crystallographic orientation (Ranganathan et al., 2025), as explained in section IV.2.1. In this study, the crack initiations and propagations are prevented as the impact of pores solely on the CTE is the target of this study (and not cracks). In addition, as the pores are embedded in random manner, an additional statistical validation is needed (with the similar principle to section IV.2.1.2).

To ensure this key point, porous polycrystalline samples with three different Volume Fraction (VF) of pores are generated. The chosen VF values are: 4.2% (also referred as “Pores-4.2%”), 8.4% (also referred as “Pores-8.4%”) and 12.6% (also referred as “Pores-12.6%”). The generated polycrystalline samples consist of 500 crystals, as mentioned in section IV.2.1.1. It should be emphasized that the selected pore VF was arbitrary and not based on any targeted microstructural parameter.

Indeed, a spherical pore of equal radii ($10\mu m$) are embedded into the numerical sample (having grains of size 15.6 μm approximately) at random location. Therefore, the embedded pores might either be inside a grain or at the junctions of two or more grains. As embedding of pores involves random processes, three polycrystalline samples are built for each targeted VF of pores. Therefore, this study employs a total of 3 numerical samples per targeted VF which gives a total of 9 numerical samples. Note, again, 2D samples with same pores VF are employed for pedagogical and illustration purpose.

All the 9 numerical samples are imposed with a cooling thermal load from 1200 ℃ to 0 ℃ (Ranganathan et al., 2025). Again, the apparent CTE is monitored during the cooling simulations. When cracks are absent, the collective response of the polycrystalline assembly causes the apparent thermal expansion coefficient to converge toward the mean of the local grain thermal expansion values, equal to (8.41×10^{-6} K^{-1}) (Ranganathan et al., 2025). For example, the Figure V-3 shows the obtained results employing the 12.6% VF sample. In this figure, as expected, the apparent mean CTE converges toward a value very closer to 8.41×10^{-6} K^{-1}.

License CC BY-NC-ND 4.0

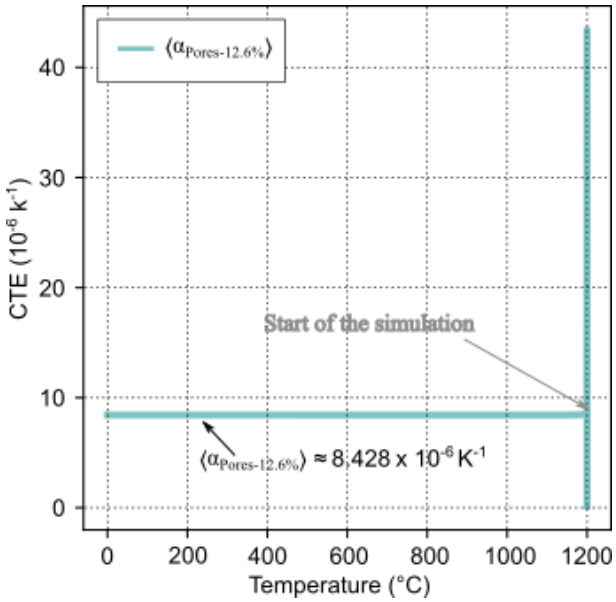

Figure V-3: Evolution of mean CTE vs temperature during cooling of porous polycrystalline domain

The final results for all 9 samples are summarized in Table V-1, where the apparent CTE $\langle\alpha\rangle$ for each sample is listed.

Table V-1: Apparent mean CTE values for 9 different samples

Volume fraction of Pores (%)	Apparent CTE $\langle\alpha\rangle$ (K^{-1})	Mean CTE value for the three samples with similar volume fraction (K^{-1})
4.2%	8.400×10^{-6} 8.451×10^{-6} 8.410×10^{-6}	8.420×10^{-6}
8.4%	8.421×10^{-6} 8.450×10^{-6} 8.424×10^{-6}	8.431×10^{-6}
12.6%	8.421×10^{-6} 8.431×10^{-6} 8.428×10^{-6}	8.426×10^{-6}

Firstly, from the results shown in Table V-1, as expected, the apparent mean CTE $\langle\alpha_{mean}\rangle$, converges toward a value very closer to 8.41×10^{-6} K^{-1}, which is the mean apparent value of the material's CTE (Ranganathan et al., 2025). This indicates that the removal of the bonds and elements, consequent to pores creation process, does not impact significantly the apparent CTE of the numerical sample.

From the literatures, it is understood that, as the CTE is a parameter that is dependent on the crystal lattice status, it depicts no-change when the pores VF is less than 30% (Hirata et al., 2016, 2017; Roy, 2025). Therefore, from the material science perspective, the CTE is unaffected with the pore's presences. This confirms that the results are reliable, despite embedding different VF% of pores in the numerical sample.

License CC BY-NC-ND 4.0

V.2.3. Mechanical response of porous polycrystalline domain

In this section, the mechanical response of the porous polycrystalline domain is monitored under quasi-static tensile test employing the same strategy as described in section II.2.1.3. The objectives are to understand the impact of the pores on the Young's modulus and the stress-strain response (Munro, 2004; Nishikawa et al., 2001). To ensure this key point, the 9 polycrystalline samples introduced in section V.2.2 are subjected to quasi-static tensile test. Therefore, again, the 4.2%, 8.4% and 12.6% samples are employed. The numerical samples are assigned with the same input properties as summarized in Table III-1.

Again, the apparent Young's modulus $\langle E \rangle$ is deduced by taking the ratio of the measured apparent normal stress $\langle \sigma_{XX} \rangle$ along the loading direction $\vec{X}$ to the imposed strain $\langle \varepsilon_{XX} \rangle$ along the same direction (Ranganathan et al., 2025). From the results (see Figure V-4) the estimated apparent Young's modulus $\langle E \rangle$ suggests that (initial slope of the stress-strain curve) value is not equal to the input material's Young's modulus E, but lower than E. Indeed, Figure V-4 depicts that, the deduced $\langle E \rangle$ decreases as the VF% of pores increases in the numerical sample, which is as expected from the material science perspective (Callister Jr & Rethwisch, 2020; Phani & Sanyal, 2008; Tessier-Doyen, 2003).

In addition, deducing the effective Young's modulus using Hashin-shtrikman approach (Hashin & Shtrikman, 1963) will act as a supportive argument. For this purpose, the effective Young's modulus of 12.6% numerical sample is deduced. This approach is chosen as it is most suitable for ideal spherical inclusions (Hashin & Shtrikman, 1963). Therefore, the effective value is computed using the equations (V-1 - V-3). Indeed, the effective Young's modulus is computed by considering zero stiffness for pores. Considering the assumption, the deduced effective Young's modulus is 130.15 GPa, which is closer to the value of 127 GPa obtained numerically. Indeed, the analytically deduced effective values for 4.2% is 154 GPa and 8.4% is 141 GPa. Again, it still preserves the same adequation with numerical results. This depicts that the iDLSM approach deduces quantitatively a convincing result.

$$\langle K^{-} \rangle = K_m + \frac{V_p}{\left(\left(\frac{1}{K_p - K_m}\right) + \left(\frac{3V_m}{3K_m + 4G_m}\right)\right)} \quad \text{V-1}$$

$$\langle G^{-} \rangle = K_m + \frac{V_p}{\left(\left(\frac{1}{G_p - G_m}\right) + \left(\frac{3V_m}{3K_m + 4G_m}\right)\right)} \quad \text{V-2}$$

$$\langle E^{-} \rangle = \frac{9K^{-} \cdot G^{-}}{3K^{-} + G^{-}} \quad \text{V-3}$$

To study the brittle failure of the porous numerical sample, a local tensile strength is also introduced. As expected, the porous numerical sample exhibited a brittle failure (see Figure V-4) and depicted a failure before the local tensile strength (σ_{max} = 375 MPa). The apparent tensile strength of respective porous sample is highlighted by the stress-peak mark in the Figure V-4. This indicates that, on increasing the VF% of pores will strongly reduce the apparent tensile strength of the model material, which is an expected behavior from the material sciences perspective (Ashizuka et al., 2002; Pandey et al., 2014; Savchenko et al., 2014). As explained earlier for Youngs modulus, the same reason holds for the drop in tensile strength versus increase in pores VF%.

License CC BY-NC-ND 4.0

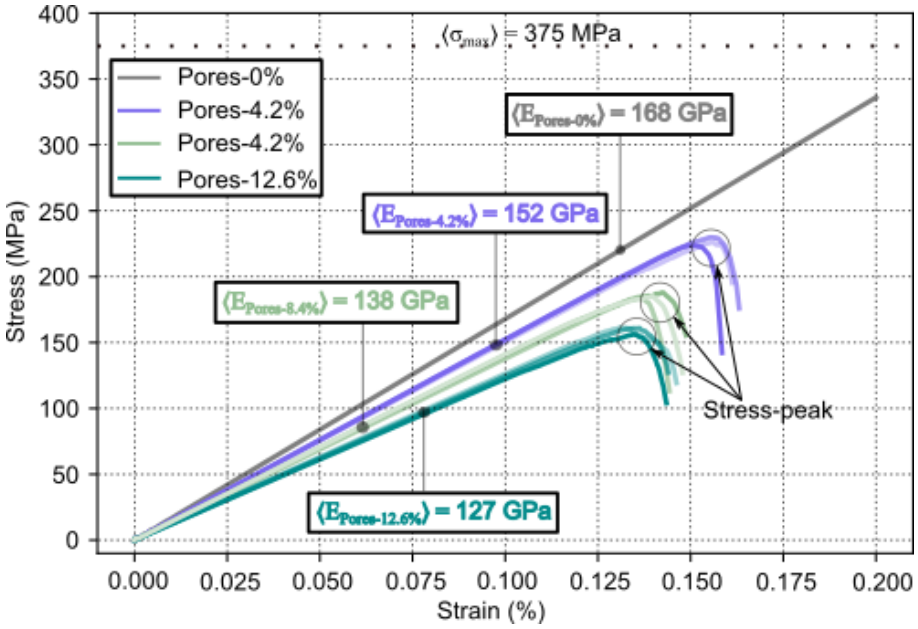

Figure V-4: Evolution of stresses versus strain for a dense and porous sample

Thanks to this study, it confirms that the porous polycrystalline domain exhibit results as expected from mechanical and material science point of view. Indeed, for the future studies, the “Pores-12.6%” sample will be employed to insight the role and impact of pores on the microstructure-thermomechanical properties relationship. From here on, the “Pores-12.6%” will be referred as porous.

V.3. Apparent behavior of porous polycrystalline aluminum titanate

This section focuses on deepening understanding on the impact of the pores on the thermomechanical properties of AT model materials during post-sintering process. Here, a comparative study is performed by considering a dense and a porous microstructure in order to illustrate the differences in the thermomechanical behavior (CTE and Young’s modulus evolutions). Here, the results obtained in section IV.2.2, are employed as the reference to perform this comparative study.

V.3.1. Dilatometry

The numerical approach proposed in section IV.2.2 is employed again, to perform thermomechanical simulation using the 3D porous sample. Again, as a first step, the porous sample is submitted to a cooling simulation employing the assumptions mentioned in the previous chapter (see section IV.2.2). The numerical sample is assigned with the input data (see Table III-1) and are assumed to be in relaxed state at 1200 ℃ (Ranganathan et al., 2025). Indeed, porous samples are cooled from 1200 ℃ to 20 ℃. The cooling simulations are conducted for every 100 ℃ of cooling.

The evolution of the apparent strain versus temperature for both dense and porous materials are shown in the Figure V-5. These results show that the porous sample exhibits a trend similar to the dense versus temperature. Similar to section IV.2.2, the samples exhibit a contraction trend between 1200 ℃ and 700 ℃ (see Figure V-5). In addition, microcracking begins with a sudden slope change around 700 ℃, occurring within the [700 - 20 ℃] range (Ranganathan et al., 2025).

Despite having the same trend, the samples exhibit different expansion rates after the microcrack onset mark (approximately at 700 ℃), which is indicated by the different slopes for the dense and porous curves in Figure V-5. In fact, the difference between the dense and porous curves can be explained by slightly lesser volume of microcracks in the porous sample. This variation in amount

License CC BY-NC-ND 4.0

of microcrack may have various reasons such as (Bruno & Kachanov, 2016; Coble & Kingery, 1955; Pandey et al., 2014; Roy, 2025; Shyam et al., 2015):

- due to the reduction in stiffness with the presences of pores;
- due to the differences in the exhibited stress-fields with and without pores-presences;
- due to the existence of pores and crack interactions,
- due to much-scattered crack distribution with the presences of pores.

Therefore, further micromechanical investigations are needed to better understand the reason behind the reduction of microcrack volume fraction in the temperature range [700 ℃ - 20 ℃].

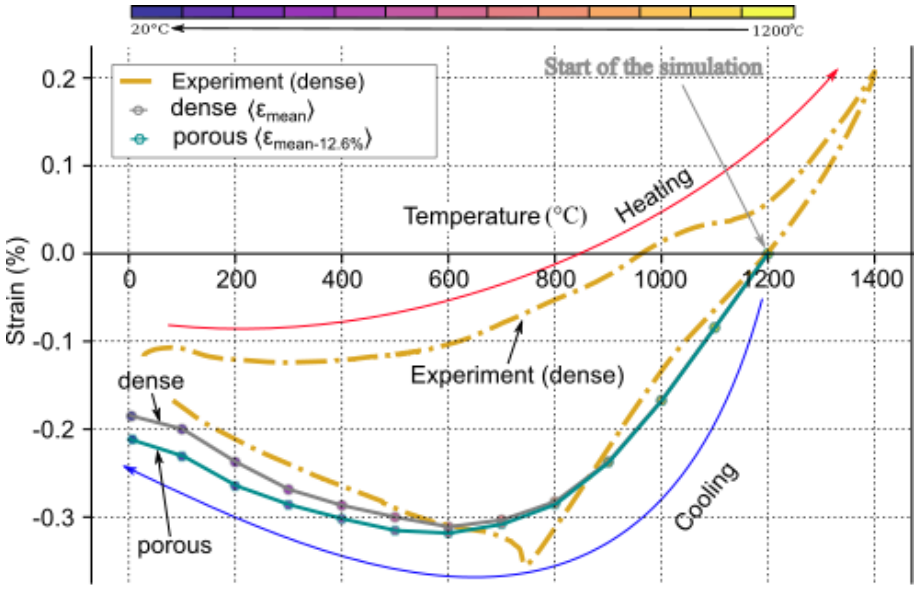

Figure V-5: Evolution of thermal strain versus temperature for dense and porous AT

V.3.2. Young's modulus

Again, after each cooling simulation from 1200 ℃ to 20 ℃, the numerical samples undergo quasi-static tensile test (similar to section IV.2.2). During this test, crack extensions are prevented to deduce the apparent Young's modulus ($\langle E_{12.6\%} \rangle$) (Ranganathan et al., 2025). Its evolution is depicted in Figure V-6, including the dense sample for a comparative study. Figure V-6 illustrates that both the samples depict the same trend with a drop as the temperature decreases from 1200 ℃. These drops indicate a strong increase of microcracks.

However, Figure V-6 depicts the key differences in the behavior of porous from the dense sample. Firstly, despite assigning the same input properties to the samples, as expected, the porous depicted a lower Young's modulus in comparison to the dense (Callister Jr & Rethwisch, 2020). As explained in section V.2.3, the porous sample is less stiff than the dense one which is also observed in the section V.2.3. Secondly, despite having a huge difference in the Young's modulus in the high temperature range [1200 - 700 ℃], the difference between the curves decreases in the low temperature range [700 - 20 ℃]. In order to understand this trend, a relative Young's modulus representation such as ratio deduced from porous by dense Young's modulus can be plotted (Hirata et al., 2017; Tessier-Doyen, 2003).

License CC BY-NC-ND 4.0

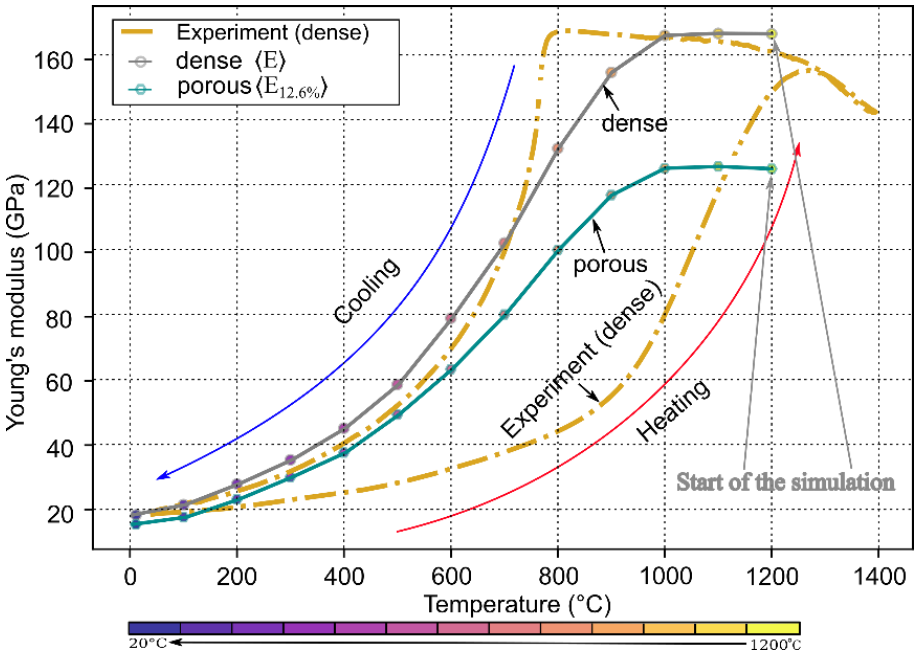

Figure V-6: Evolution of Youngs modulus results of dense and porous aluminum titanate material

Figure V-7 shows the evolution of the relative Young's modulus with temperature, derived from the data in Figure V-6, and expressed as the percentage ratio of the porous by dense Young's modulus. This study accounts to understand by what factor will the elastic stiffness degrades with the combined effects of porosity and any thermally-induced damage versus temperature.

From Figure V-7, it is evident that the porous sample exhibits lower stiffness compared to the dense, primarily due to the presence of (non-rigid) void volume inside the porous sample. Additionally, the porous demonstrates distinct trends at different stages: before the onset of microcracks, after the onset of microcracks, and once a complex microcrack network is established. Specifically:

- in the temperature range of [1200 - 1000 ℃], the porous sample maintains approximately 75% of the stiffness of the dense sample;
- after the onset of microcracks (below 1000 ℃), the porous sample shows an increase in relative stiffness, peaking around 500 ℃ (10% improvement);
- below 500 ℃, the stiffness of the porous sample exhibits almost negligible change (less than 5%), indicating stabilization in the material response.

Therefore, these observations indicate a slight difference in the behavior of the dense and porous samples. However, investigating the underlying micromechanics, such as stress distribution and microcrack evolution, both before and after the onset of microcracking, particularly in porous materials, could provide valuable insights. Such an understanding may help clarify the subtle differences in mechanical behavior between the porous and dense samples.

License CC BY-NC-ND 4.0

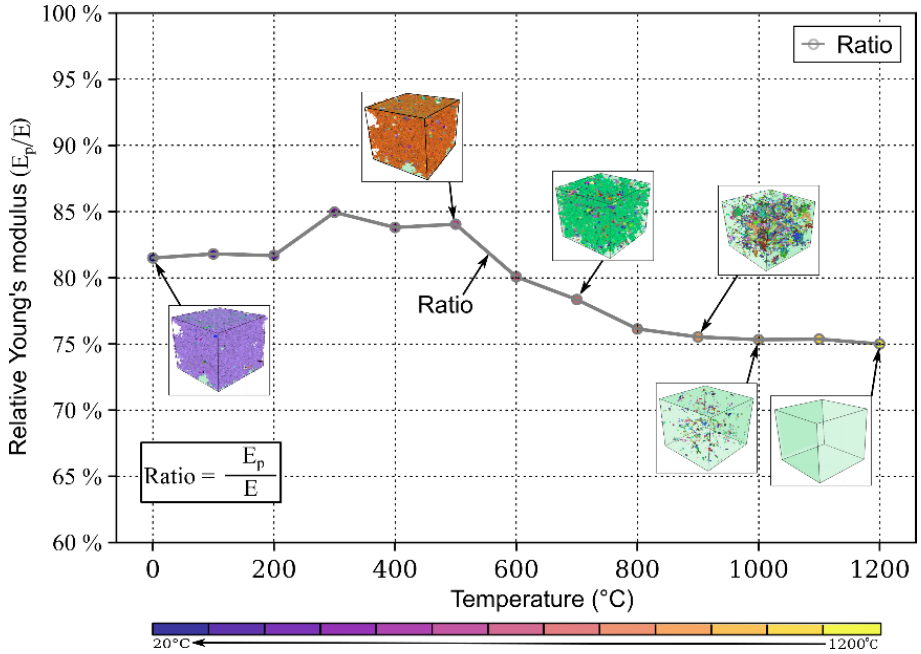

Figure V-7: Relative representation of Youngs modulus versus temperature

V.4. Micromechanical investigations

From the section V.3, it was obvious to see the presences of few discrepancies in the thermomechanical behaviors of the porous sample from the dense one versus temperature. To extend the understanding on the role and impact of pores, this section focuses on monitoring the micromechanics such as stresses or strains and microcracks during cooling simulations (similar to (Ranganathan et al., 2025)).

V.4.1.1. Thermal stress study

In this section, the thermal stress distribution of the porous sample is monitored (similar to the section IV.3.1). As described earlier, the monitored data are recorded and represented in a 3D distribution plots as a function of temperature (see section IV.3.1). Moreover, the monitored local thermal stresses are expressed along the local grain orientation ($\vec{a}$, $\vec{b}$, $\vec{c}$) as explained in section IV.3.1. Again, in an aim to better understand these distribution plots and as they resemble a Gaussian distribution, the data are directly represented by the mean and standard deviation parameters, as shown in Figure V-8. Lastly, the results of porous are compared to the dense reference sample (Ranganathan et al., 2026).

Firstly, from the Figure V-8a it appears that, porous sample exhibits anisotropic thermal stresses along the different crystallographic orientations ($\vec{a}$, $\vec{b}$, $\vec{c}$). Moreover, both the samples depict the similar trend in evolution of the mean thermal stress versus temperature, in different orientations ($\vec{a}$, $\vec{b}$, $\vec{c}$) as shown in Figure V-8a.

Despite both the samples depicts similar trend (see Figure V-8a) versus temperature, the porous exhibits lower mean thermal stresses than the dense, especially along the orientation $\vec{c}$. This is indicated by the captured values and the slope of the curve “c-porous” in Figure V-8a. Indeed, orientation $\vec{c}$ is the key parameter that influences CTE mismatch because it is related to the highest CTE (α_c = 17.26 × 10^{-6} K^{-1}) (Bruno et al., 2010). Therefore, Figure V-8a indicates that the localized tensile stresses contributed by the α_c in porous is lower in comparison to the dense at the intermediate temperature range [1000 - 300 ℃]. Moreover, this confirms that the presences of pores influence the stress-fields at the microstructural scale. In addition, in some way, pores lowering the

License CC BY-NC-ND 4.0

impact of orientation $\vec{c}$ in contributing to CTE mismatch as discussed in section IV.3.1. Therefore, this raises a question on whether the pores act as stress concentrators or is this an indication of presences of other mechanisms at the microstructural scale.

Moreover, both the sample depict similar standard deviation of stress versus temperature (see Figure V-8b), which indicates the existence of very similar distribution in the thermal stresses.

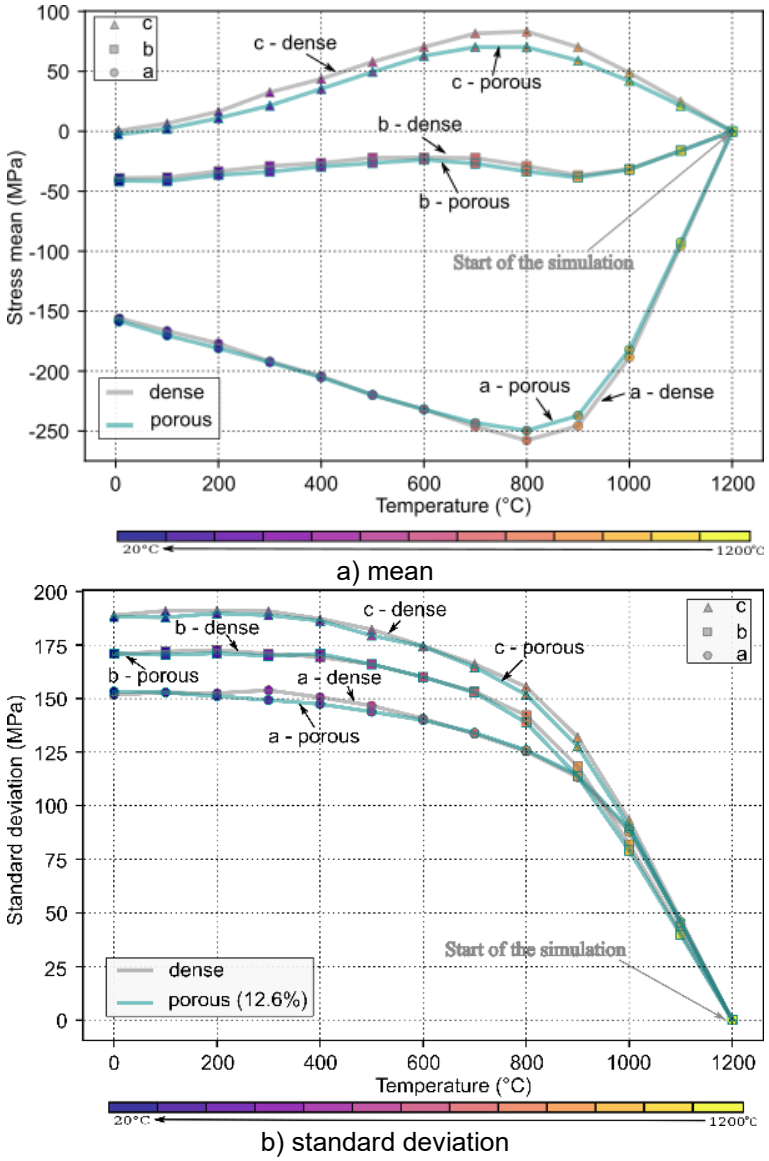

Figure V-8: Mean and standard deviation of the thermal stress distribution versus temperature

V.4.1.2. Analyses of the micro-crack network

This section investigates the microcrack statistics in porous sample. The aim of this section is to assess whether pores play a significant role in the evolution of microcracking, or if microcrack development occurs independently of porosity. With this in mind, it is necessary to monitor the preferential orientation, their spatial positions, and the mechanisms governing the emergence of complex crack patterns (Chaudhuri & Sircar, 1981; Nishikawa et al., 2001; Roy, 2025). For this purpose, the results obtained for the dense numerical sample is used as a reference here. Figure V-9, illustrates the microcrack evolution as a function of temperature for porous sample (12.6% of porosity) in comparison to the dense samples. As previously explained, a microcrack is defined as a bond that has reached the tensile strength ($\sigma_{max} = 375\ MPa$). The microcrack count

License CC BY-NC-ND 4.0

is expressed in relative terms, calculated as the ratio of the number of broken bonds to the total number of bonds within the numerical sample (Ranganathan et al., 2026).

Figure V-9 shows that both samples depict a similar trend in crack evolution, showing a strong increase in microcracks in the range [1200 - 700 ℃] followed by a slowdown stage below 700 ℃. This observation is in line with the previous observations concerning mean thermal stresses, Young's modulus and dilatometric evolutions. However, a slight difference is observed in the recoding of the microcracks for the dense and porous samples. At 20 ℃, a total of 90.8k microcracks were identified in the dense sample, representing 58% of the total bonds (accounting a damage factor of 88%). In contrast, the porous sample had 73.14k which corresponds to 55% of total bonds (accounting a damage of 86%). So, it appears that porous sample exhibit a little lesser number of microcracks than the dense sample. Therefore, extending the study with microcrack data might reveal further insights on influences of pores and its role on the microcracks.

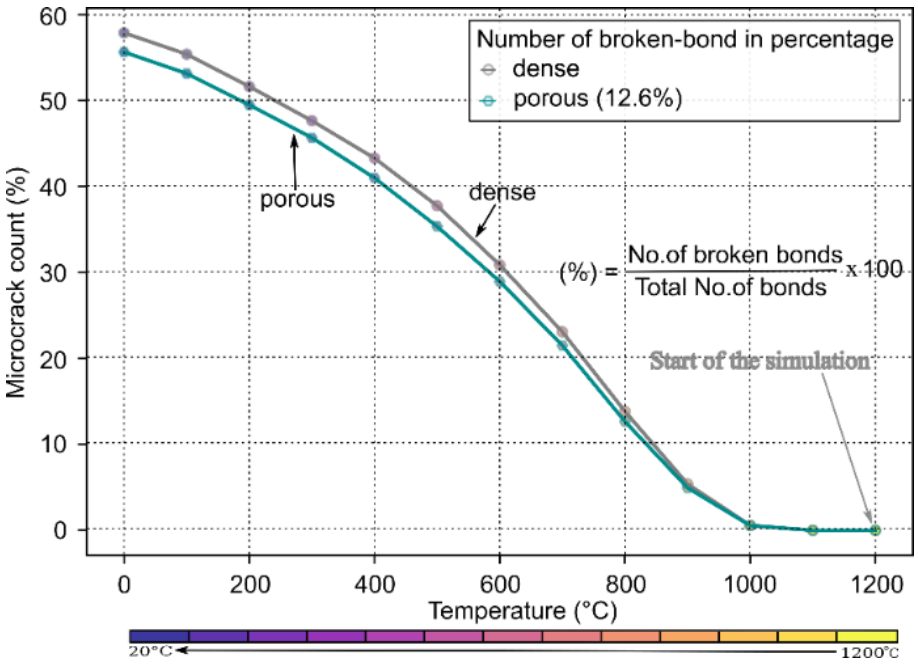

Figure V-9: Relative microcrack number as a function of temperature

V.4.1.2.1. Monitoring on the location of cracks: Interface vs Bulk

The present section focuses on identifying the differences in the location of microcracking between the porous and dense. Indeed, this study examines the primary microcracking mechanisms as they evolve with temperature, in relation to their positions within the microstructure. Again, the similar strategy from section IV.3.2.2 was employed to record the statistics of the interface and bulk cracks during the cooling simulation. It is important to recall that the term interface describes the crack initiated between two grains (refers intergranular crack) and the term bulk describes the crack initiated inside a grain (refers intragranular cracks). In addition, few clustered "bulk cracks" could be referred as transgranular cracks (see section IV.3 for the definition) (Ranganathan et al., 2026).

Figure V-10a and b show the absolute progression of bulk and interface cracks with increasing temperature. In contrast, the Figure V-11a and b present the relative evolution, where the combined contributions of bulk and interface cracks are normalized to 100%. Note, the porous samples have initially 73.8k bulk bonds and 58k interface bonds, which is lesser than the bond counts in dense, as mentioned in section IV.3.2.2.

The Figure V-10a and b depicts the similar insights to the section IV.3.2.2. The interface (or intergranular) cracks are dominant at high temperatures. This observation confirms that

License CC BY-NC-ND 4.0

interfacial regions are the primary sites where thermal stresses, due to CTE mismatch, begin to form (or intergranular region) (Ranganathan et al., 2026). In addition, despite the introduction of pores in the sample, both the interface and bulk absolute cracks have qualitatively an evolution similar to dense sample. However, the key difference lies with the recording of absolute crack count versus temperature. It is explicit to see that the number of cracks is lower in porous than in the dense (see Figure V-10).

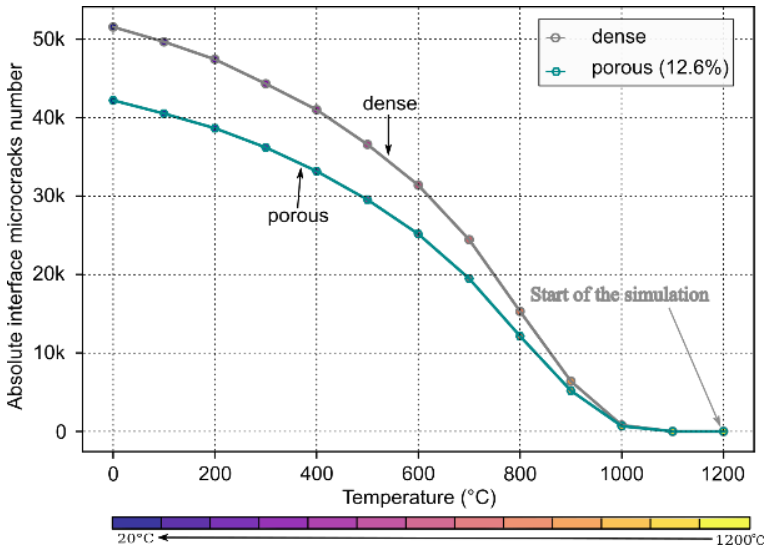

a) interface crack (absolute)

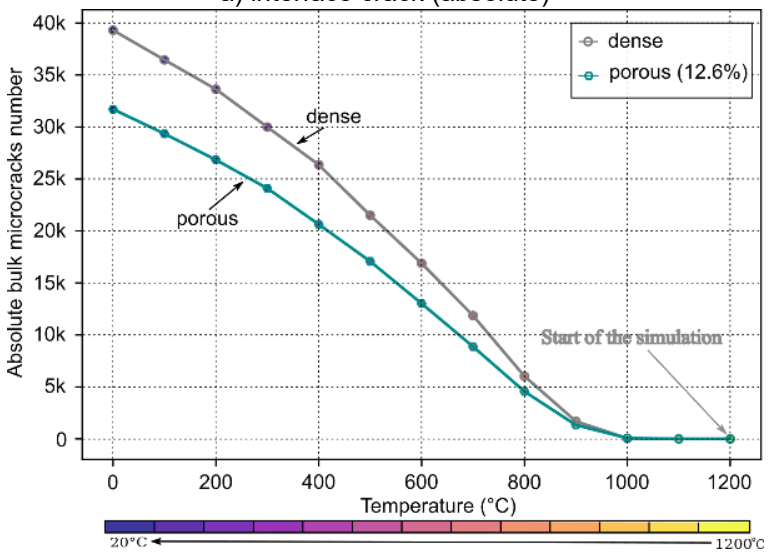

b) bulk crack (absolute)

Figure V-10: Absolute evolution of interface and bulk crack versus temperature

The next question arises on the influences of pores on the crack locations. For this purpose, the crack data are expressed in relative format, which is the percentage of number of interface or bulk cracks by the total number of cracks. (see Figure V-11). Both samples exhibit similar trends as described in section IV.3.2.2. At high temperatures, interface cracks are predominant, but their proportion decreases as the temperature increases, while bulk cracking shows the opposite behavior. And these results depict that there are no significant influences of pores on the microcracking location and their relative evolution toward temperature.

License CC BY-NC-ND 4.0

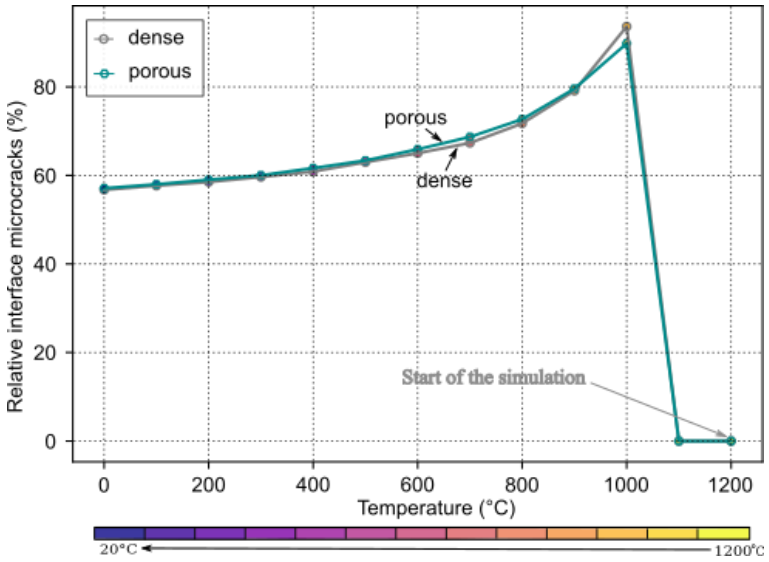

a) interface (relative)

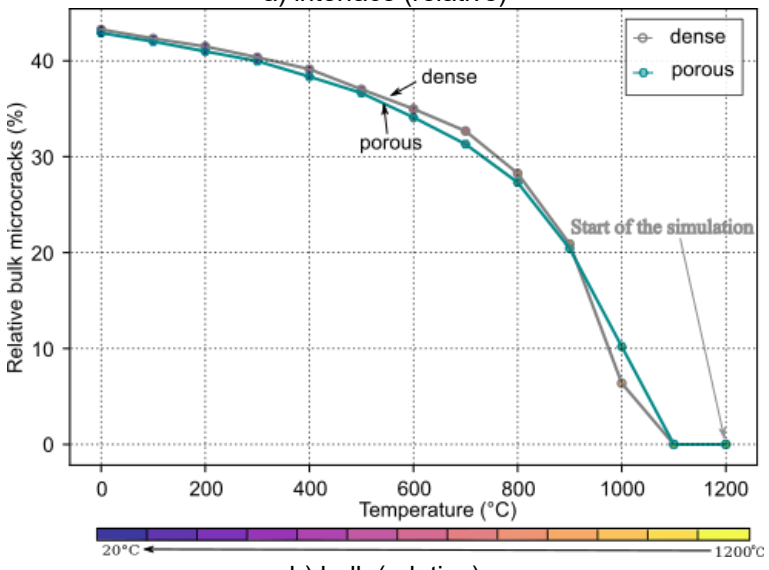

b) bulk (relative)

Figure V-11: Relative evolution of interface and bulk crack versus temperature

From this study, it is understood that the (spherical) pores have no significant influences on the crack locations (Roy, 2025). However, it is important to check if the pores influence the preferential orientation of the microcracks (Bruno et al., 2010).

V.4.1.2.2. Preferential crack orientation

To investigate the effect of pores on microcrack orientations, the unit normal vectors ($\vec{n}$) of crack facets in the porous samples (see Figure IV-16b) were tracked and recorded during the cooling simulation, following the same methodology described in section IV.3.2.1. As explained before, once the tensile strength is reached ($\sigma_{max} = 375\ MPa$), the microcracking is visualized by the appearance of the crack-facet as shown in Figure IV-16b. These normal vectors are expressed in relation to the local crystal's orientation ($\vec{a}$, $\vec{b}$, $\vec{c}$), as illustrated in Figure IV-17 (Ranganathan et al., 2026). Therefore, the normal vectors are projected to the planes ab, bc and ca, that are formed by combination of $\vec{a}$, $\vec{b}$, $\vec{c}$ axes. Similar to section IV.3.2.1, the linear distribution data, collected every 100 ℃, are presented using the mean and standard deviation as functions of temperature, due to their similarity to Gaussian distribution (Ranganathan et al., 2026). Here, only the standard deviation is plotted in Figure V-12, since the mean values remain essentially constant with temperature

License CC BY-NC-ND 4.0

In order to highlight the role of pores, the obtained results of the porous sample are compared with the dense sample. Despite the presences of pores, the porous samples depicted a very slight discrepancy in the orientation of normal vector statistics in different crystallographic planes verses temperature as shown in Figure V-12. These discrepancies are observed only in the recorded values of the normal vector statistics in the "ab" planes for the porous sample at high temperatures. As an outcome, these results depict that still the $\vec{n}$ vectors in ca-plane has the lowest standard deviation and are uniformly oriented. Therefore, the microcracks are still uniformly oriented perpendicular to the ca-plane (Ranganathan et al., 2026).

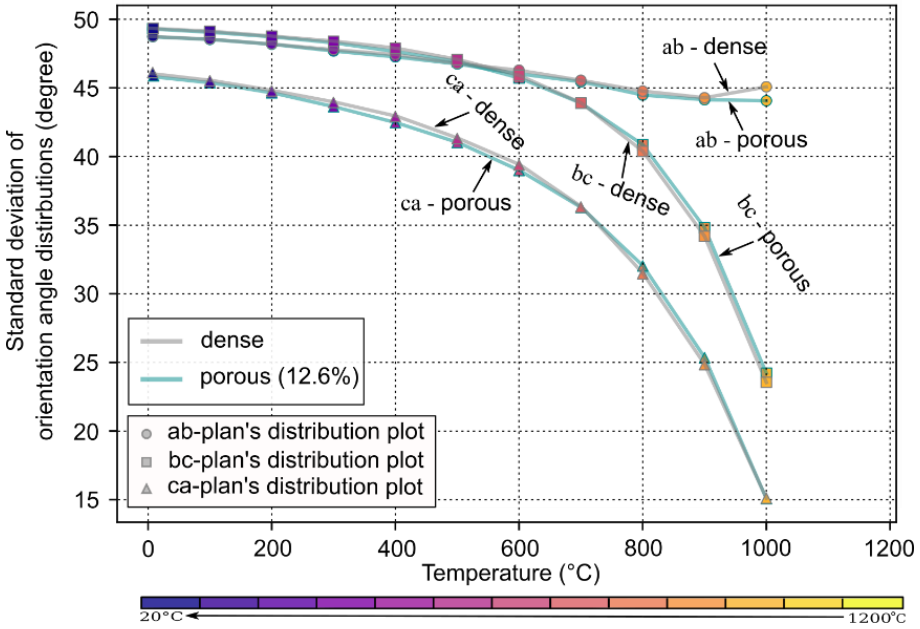

Figure V-12: Crack $\vec{n}$ angles distribution's standard deviation vs temperature

This study indicates that the presence of (spherical) pores does not have a significant impact on preferential crack orientations (Chaudhuri & Sircar, 1981; Roy, 2025). However, the analysis is limited to uniform, spherical pores of equal size and the study should be extended for different pores morphology and size (Andersson, 1996; Nishikawa et al., 2001; Roy, 2025). Consequently, since no preferential orientation exists in the porous architecture, the influence of pores on crack orientation is considered negligible. In conclusion, the dense sample exhibits a higher microcrack count than the porous sample, while the orientation and nature of cracking remain similar. Consequently, the total crack surface is larger in the dense sample, which is why detailed surface area monitoring is not included in this chapter, as the focus is on highlighting the key comparative differences.

V.5. Mechanical study

This section focuses on examining the apparent stress-strain behavior of the numerical samples (Pandey et al., 2014; Shyam et al., 2015). Following the cooling process, the samples are subjected to both monotonic and cyclic uniaxial tensile loading (Ranganathan et al., 2026). Unlike the analysis presented in section V.3, these studies allow pre-existing microcracks to propagate during loading.

V.5.1. Monotonic uniaxial tensile loading

This section investigates the apparent stress-strain response of porous samples under monotonic uniaxial tensile loading conditions. Again, to highlight the impact of pores on the materials mechanical response, the obtained results of porous are compared with the dense sample (see Figure V-13). Indeed, as explained in section V.2.3, the pores definitely contributed to the reduction

License CC BY-NC-ND 4.0

in apparent stress peaks and initial stiffness but it is interesting to see the mechanical response of the porous under thermomechanical coupled condition.

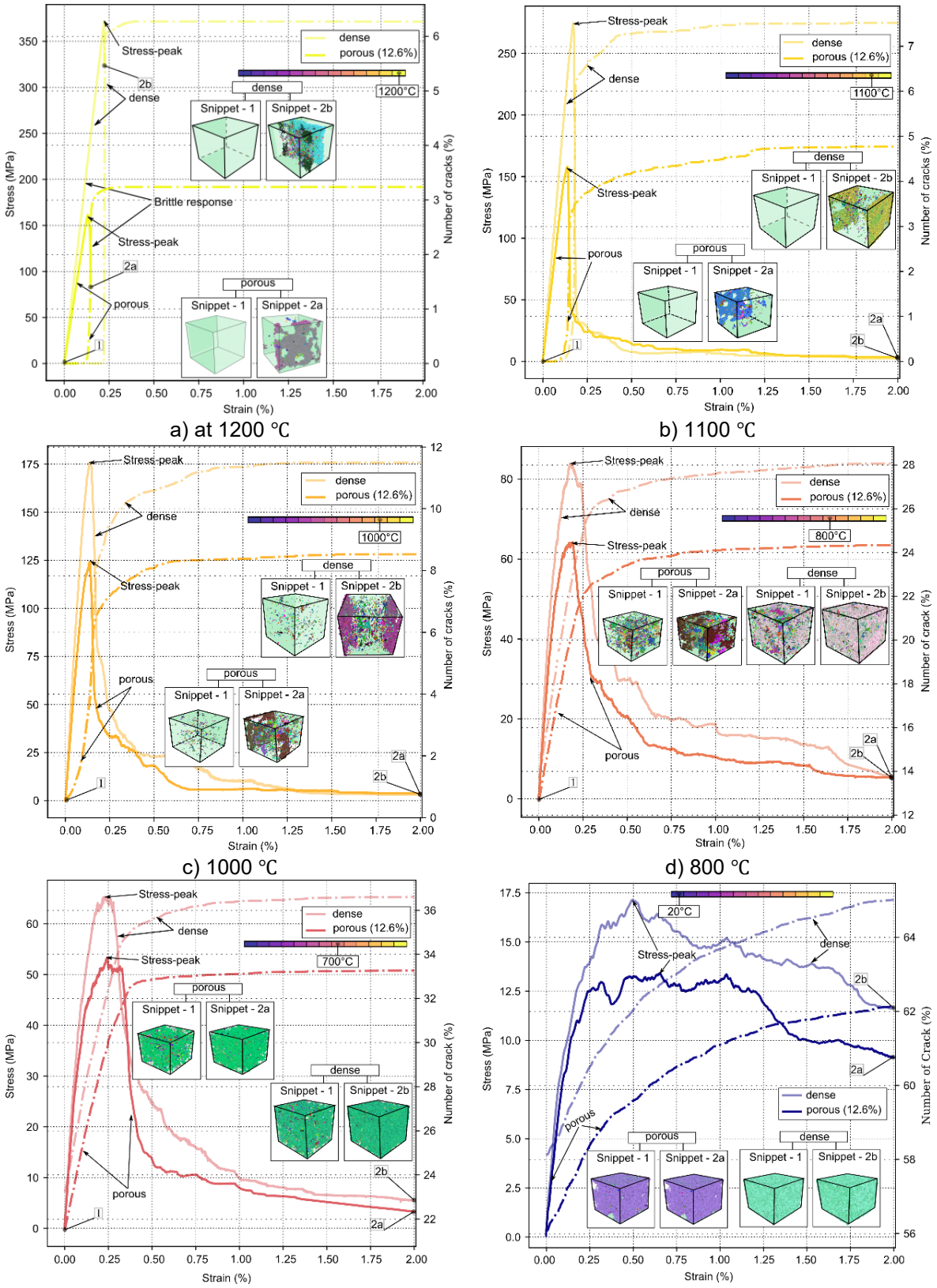

a) at 1200 °C

b) 1100 °C

c) 1000 °C

d) 800 °C

e) 700 °C

f) 20 °C

Figure V-13: Thermal effects influence on apparent stress-strain in [1200-20 °C] range

License CC BY-NC-ND 4.0

Notably, both the samples exhibit similar trend of mechanical response versus temperature as shown in Figure V-13. As expected, the porous sample depict lower stress peak than the dense sample (Ashizuka et al., 2002; Pandey et al., 2014; Savchenko et al., 2014). In addition, from the results it appears that the porous sample depicted significant lower ultimate strength - both in stress and strain peaks, in comparison to the dense. Moreover, the porous depicts higher degree of non-linearity, as shown in the Figure V-13 (c-f).

Thanks to this study, the results show that porous samples exhibit greater flexibility than dense samples. Therefore, it is of interest to capture the apparent stress-strain response of the porous numerical sample under cyclic loading, in order to assess potential differences in the amount of irreversible strain between the dense and porous samples.

V.5.2. Cyclic uniaxial tensile loading

The present section focuses on monitoring irreversible strain and on assessing whether pores contribute to its development. After the cooling process, the porous samples are subjected to cyclic uniaxial tensile loading, using the strategy described in section IV.3.4.2. The apparent stress-strain responses versus temperature are shown in Figure V-14. It is interesting to extend the study to highlight the other difference in the recorded irreversible strains and global rigidity of both the samples.

At the high temperature range [1200 - 1100 ℃], the Figure V-14a and b indicates that:

- no pre-existing microcracks (see the snippets in Figure V-14a and b were present before uniaxial tensile loading;
- the porous sample, despite not having any pre-existing microcracks and internal thermal stresses at 1200 ℃, demonstrated irreversible strains after the peak stress, as shown in Figure V-14a. These irreversible strains developed post the initiation and propagation of cracks during the tensile test. In addition, from the simulation's snippets (snippet-2a in Figure V-14), it appears that the crack trajectories include the broken bonds from the pore's boundaries. This indicates pores seems to act as stress concentrators. In contrast, the dense sample does not have such mechanisms and does not depict irreversible strains at 1200 ℃. In the literatures, usually such irreversible response, is correlated with the presences of complex crack network that involves mechanisms like frictional sliding of cracks, partial/incomplete crack closure of the complex crack etc (Gao et al., 2013). However, further investigations are needed to confirm this behaviour;
- at 1100 ℃, still the porous depicts the irreversible strain while the dense does not depict such a response, even with the presence of internal thermal stresses. Again, the trend in crack trajectory highlights the same reason to the one at 1200 ℃;
- in addition, pores and crack interactions occurs due to localized internal tensile stresses exhibited during cyclic tensile loading, rather than from the tensile stresses at pore boundaries during cooling;
- despite having different microstructural situations, the unloading phases exhibit linear responses;
- the porous depicts reduction in global rigidity, indicated by the decrease of slope during the successive unloading phases, while it is not visible for dense.

Therefore, these results suggests that additional mechanisms (as pores acting as stress concentrators) are present in porous samples promoting the relaxation of internal stresses (in the case of 1100 ℃) and the development of irreversible strains at high temperatures.

At the intermediate temperature [1000 - 800 ℃] (Figure V-14c and d), it appears that:

- the porous and dense samples have the pre-existing (isolated and extended) microcrack networks and internal thermal stresses;
- both samples show irreversible strains. Specifically, porous sample exhibits irreversible strain due to additional mechanism along with microcracking, while the dense sample

License CC BY-NC-ND 4.0

shows irreversible strain only from microcracking. Interestingly, the total irreversible strain in the porous sample is slightly lower than that in dense, at 1000 ℃. However, both samples display the same level of irreversible strain as the temperature approaches 800 ℃;
- the global rigidity of both the samples reduces as indicated by the decrease of slope during the successive unloading phases. The porous seems having lower global rigidity than the dense.

Therefore, these results suggest that, as the temperature decreases, the tensile stresses originated during cooling is dominant and higher in exhibiting (complex) microcrack network than by the tensile stresses originated during mechanical loading (Pandey et al., 2014; Shyam et al., 2015).

Lastly, at the final temperature range of [700 - 20 ℃] (see Figure V-14e and f), it appears that:
- at the microstructural scale, both the samples have a dense complex microcrack network, as shown in the simulation;
- the captured irreversible strains are almost the same for both the samples. This indicates that the tensile stresses originated during cooling is dominant. In addition, pores no longer act as stress concentrators.

These results highlight that the porous always depicts lower stiffness than the dense versus temperature. In fact, the porous microstructures exhibit localised tensile stresses in two ways (Pandey et al., 2014; Shyam et al., 2015). That is, the localized tensile stresses:
- originate during cooling due to CTE mismatch similarly to dense material
- originate during mechanical loading especially around the pore boundaries.

At high temperatures the cracks are mainly initiated during the tensile test, where the pores act as stress concentrators. In contrast, as the temperature decreases, the number of cracks due to CTE mismatch increases. As an outcome, the role of pores acting as stress concentrators is supressed at the room temperature. Therefore, these results highlight that the pores exhibit better degree of non-linear mechanical response which is one of the expected parameters for thermal shock application. However, there is no significant observation on its ability to depict better strain of rupture for enhancing fracture energy dissipation that is a key parameter to sustain thermal shock.

V.6. Conclusion

In this chapter, a masking strategy (using synthetic images) to embed pores with the iDLSM approach is proposed. As a demonstration, “spherical” pores were incorporated into a polycrystalline sample, and a comparative study was performed between porous and dense polycrystalline models (building on the results from Chapter IV). The DEM tool revealed the promotion of fracture behaviors (such as crack initiation and propagation) driven by the CTE mismatch between grains, in both porous and dense domains.

By incorporating crack evolution with and without the presence of (spherical) pores, the model enhanced our understanding of how microstructural features influence the macroscopic thermomechanical properties, specifically, apparent thermal strain and Young’s modulus, of the AT model material. The results were quantitative and aligned well with experimental trends (Figure V-5 and Figure V-6) in both the cases. Importantly, the results depicted a meaningful insight such as:
- no change in the thermal strain was observed in the elastic stage (before the onset of microcracking);
- the porous domain depicted a lower Young’s modulus than the dense one in the elastic stage.

However, the key differences in the results (porous and dense sample) emerged after microcrack initiation, particularly in the evolution of apparent thermal strain (Figure V-5) and Young’s modulus (Figure V-6). To address these differences the micromechanical study was performed.

License CC BY-NC-ND 4.0

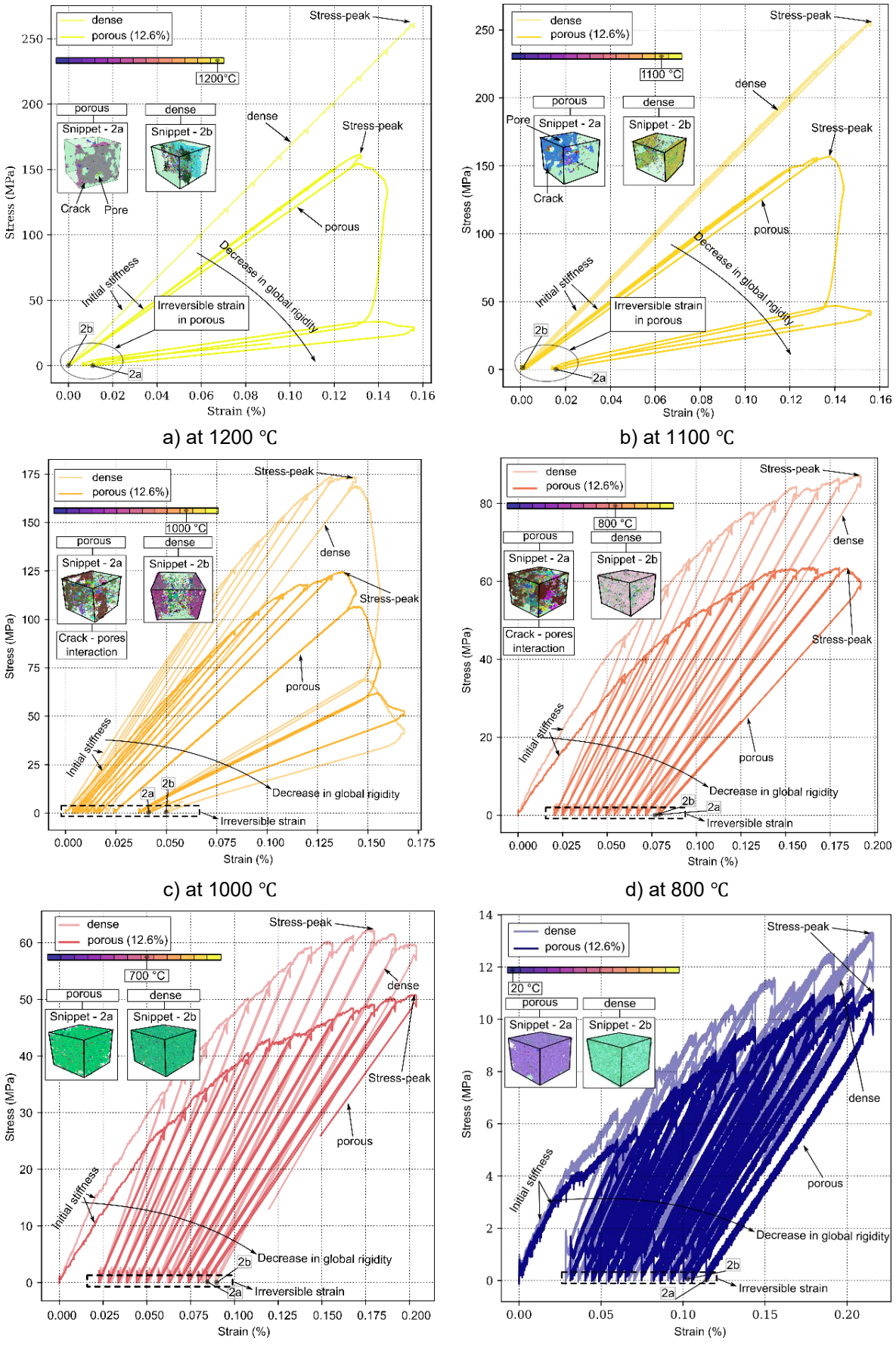

Figure V-14: Irreversible strains captured during uniaxial cyclic loading in [1200-20℃] range

License CC BY-NC-ND 4.0

The sample with spherical pores was employed to investigate microstructural evolution during cooling. Thermal stress study using the DEM tool, compared with dense samples, revealed slight differences in the influence of local orientation on stress distribution, suggesting that (spherical) pores do not affect significantly the microstructural stress field. The model also captured microcrack initiation and propagation with cooling, showing that porous samples (spherical pores) exhibited slightly lower microcracks than dense ones. Insights into preferential crack orientation, origins, and trajectories (see section V.4.1.2) indicated largely similar fracture mechanisms in both cases, with only minor variations due to (spherical) porosity. However, Literatures (Nishikawa et al., 2001; Roy, 2025) indicate that pore geometry, including size, shape, and distribution, significantly influences microstructural stress fields, thereby directing microcrack initiation and propagation. In particular, elongated pores act as “stress directors,” steering fractures along high-stress curvatures (Andersson, 1996). Therefore, further investigations are necessary considering non-spherical pores to make sure the pores don’t play significant role at the microstructural scale.

In addition, the DEM tool was employed to monitor the apparent stress-strain response under monotonic and cyclic loading as a function of cooling temperature. The results revealed that the porous sample exhibited a higher degree of nonlinearity and a lower peak stress compared to the dense sample. However, in terms of peak strain, it was not clear whether the porous sample could sustain larger strains than the dense sample, despite its stronger nonlinear response. The model also tracked irreversible strains (pseudo-plasticity) during cyclic loading. Notably, the porous samples exhibited irreversible strain at elevated temperatures (at 1200 ℃), whereas no such behavior was observed in the dense samples at high temperatures. This effect is attributed to possible additional mechanisms associated with the presence of pores under cyclic loading. However, as this interpretation remains tentative, further investigations are required to confirm and clarify these observations.

In contrast, once microcracking began, both samples showed irreversible strain, with the magnitude of irreversible strain in the porous sample approaching to that of the dense sample as the cooling temperature neared 20 ℃. This trend suggests that two distinct mechanisms operate at the microstructural scale of the porous sample (see section V.5.2). Furthermore, the dominance of these mechanisms shifts with temperature, leading to the observed differences in behavior at high versus low temperatures. Overall, the porous samples appear more flexible and less rigid compared to the dense sample.

Overall, this work highlights the role and impact of pores as a microstructural feature on macroscopic mechanical responses, showing that the presence of pores introduces additional flexibility to the material. As a next step, the DEM tool should be extended to model composite materials, such as systems where coarser aluminum titanate inclusions are embedded within an alumina matrix. Such developments would provide deeper insights into the influence of coarser inclusions (with anisotropic CTE) on the long-term sustainability of the composite. These findings will also support the industry in optimizing microstructural design for refractory applications.

Although pores naturally form during the sintering of refractory materials and contribute to reducing material weight (Callister Jr & Rethwisch, 2020; Z. Chen et al., 2020; Hou et al., 2022; Zhang et al., 2018). Industrial refractories are typically designed with minimal porosity to limit corrosion, as penetrating slags can accelerate degradation (Z. Chen et al., 2020; Fu et al., 2019; Kazemi, 2019). Therefore, microstructural design must be carefully optimized to balance performance and sustainability.

In the present study, the analysis is restricted to uniform, spherical, and unconnected pores, about 35-40 vol% with a 10 μm size, which are larger and simpler than those found in actual industrial materials (Fu et al., 2019; Hou et al., 2022; Nemaleu et al., 2023). To enhance realism, the model

License CC BY-NC-ND 4.0

should be extended to incorporate overlapping or connected pores (>40 vol%) with random sizes, shapes, and morphologies, including fine pores (<1 μm) typical of refractories. While such refinement is feasible, it is computationally expensive, as embedding fine pores may require highly refine numerical discretization, which increases significantly the number of discrete elements.

License CC BY-NC-ND 4.0

Chapter VI. iDLSM modelling of microcracking induced by anisotropic thermal expansion: composite case study

VI.1. Introduction

After discussing the porous microstructure and its impact on the apparent thermomechanical behavior in the previous chapter, it is interesting to explore how coarser aggregates (an essential component of refractories) affect apparent thermomechanical behavior of the composite (da Luz A et al., 2015; Kakroudi, 2007; Mouiya, 2024). Refractory aggregates are coarse ceramic grains that are preformed and typically range in size from micrometers up to centimeters (Boateng et al., 2025; Braulio et al., 2008; da Luz A et al., 2015). These aggregates are sized according to a specific particle-size distribution and are embedded into bricks or castable to create a load-bearing framework (da Luz A et al., 2015). In fact, they contribute thermal, mechanical, and chemical stability during use at high-temperature. Moreover, they also help control crack paths and heat flux under high-temperature applications. The finer particles, along with a binder, make up the matrix that fills the spaces around the aggregates, which together are termed as composite material (da Luz A et al., 2015; Kingery et al., 1977).

As mentioned in Chapter I and Chapter III, among the different composites, the majority are composed of two or more constituents that experience different thermal expansion during the post-sintering process (da Luz A et al., 2015; Huger et al., 2011; Peruzzi, 2000). Depending on the difference in thermal expansion coefficient, distinct microstructural crack configurations can be observed during cooling as explained in section III.1.

Numerous studies (Boccaccini et al., 2005; Chotard et al., 2008; Grasset-Bourdel, 2011; Kakroudi, 2007; Khlifi, 2019; Mouiya, 2024; Tessier-Doyen, 2003) were performed to investigate the impact of the microcracks on the apparent Young's modulus (using ultrasonic echography technique in long bar mode test) of the composite materials. As explained earlier in Chapter III, from these studies, the authors have noticed the impact of microcracks on the Young's modulus versus temperature following hysteresis loops (probably coming from the closing and reopening of microcracks) and have also observed a significative drop in Young's modulus after the onset of these microcracks (Boateng et al., 2025; Joliff et al., 2007; M. G. Kakroudi et al., 2009; Mouiya et al., 2026; Tessier-Doyen et al., 2006). Moreover, the significant Young’s modulus drop strongly depends on the microstructural configurations that are achieved due to CTE mismatch. For example, as discussed in section III.1, the drop in Young's modulus was significant in the case of andalusite-based castable (with single grain andalusite) in comparison to other castable, as the andalusites depict high anisotropy in CTE in comparison to other aggregates illustrated in this section.

The performance of composites for high-temperature applications depends on several interrelated factors. These include the mineralogy, which determines the stable high-temperature phases and aggregate-matrix bonding (Boateng et al., 2025; Sarkar, 2020), and the thermomechanical properties such as the CTE (Grasset-Bourdel et al., 2012) and thermal conductivity (Smith et al., 2013). Additionally, the morphological framework, encompassing parameters like particle size (Liu et al., 2016), shape (Mouiya et al., 2024), aggregate volume fraction (Grasset-Bourdel et al., 2012), and porosity content (Ashizuka et al., 2002), governs the type and size of critical flaws (Merlani et al., 2001). Because so many variables influence performance of industrial refractories, establishing a clear microstructure-property relationship is challenging and requires extensive experimental investigation.

License CC BY-NC-ND 4.0

To improve the understanding of industrial refractories and their behavior under thermal treatment, a simplified composite material, discussed in section III.3.4.1, comprising two components (a matrix and an aggregate) is used as a model system. As highlighted in section III.3.4.1, parameters such as the arrangement, shape, size, and volume fraction of the aggregates play a key role in the design of the composite model (da Luz A et al., 2015). In this chapter, a highly simplified composite model material will be investigated.

As observed from the case studies (see section III.1), coarse monocrystalline aggregates exhibiting anisotropic CTE are particularly advantageous, as their anisotropy promotes the formation of a high density of microcracks (Kakroudi, 2007; Mouiya et al., 2026). Therefore, the main objective of this study is to investigate how coarse, anisotropic aggregates composed of monocrystalline grains influence microcracking when embedded within a ceramic matrix. For this purpose, monocrystalline aluminum titanate aggregates embedded in an alumina matrix are employed as the reference material in this chapter (Mouiya et al., 2026). Further details on the selection of the coarse monocrystalline aggregate and the model material are provided in section III.3.

In this chapter, simulations and analyses are performed to explore the relationships between microstructure and apparent thermomechanical properties using the simplified composite model material, considering two different aggregate arrangements. The iDLSM framework, incorporating thermomechanical coupling, crack closure, anisotropic thermal expansion, and periodic boundary conditions, is again employed (see Chapter II and Chapter IV). To conduct this study, multiple aggregates (also referred to as inclusions) representing a specified volume fraction are digitalized. The primary objective is to examine the effects of aggregate positioning strategy, anisotropy and volume fraction on the resulting microstructure and apparent thermomechanical behaviour, taking into account multiple crack initiation and growth phenomena, similar to the analyses presented in Chapter IV.

VI.2. Microstructure digitalization strategy

The experimental microstructure of the alumina-aluminum titanate composite material is shown in Figure III-15. This microstructure highlights key features such as the matrix, aggregates, grain boundaries, and the local crystallographic orientations of individual aggregate grains at the microscale. Since this study focuses on monocrystalline aggregates, this section introduces the strategy used to construct a numerical composite sample consisting of only two constituents. Furthermore, it presents the methods employed to arrange inclusions within the matrix, both randomly and regularly, as described in section III.3.4.1. These two positioning strategies are designed to evaluate whether the iDLSM framework can deal with different positioning strategy on the computed apparent thermomechanical properties.

From here on, the material sciences terms will be replaced as follows:

i. "aggregate" will be referred as "inclusion";
ii. "grain-boundary" will be referred as "interface".

VI.2.1. A first strategy: random positioning of inclusion

In this section, the strategy for constructing the whole periodic domain, including matrix, randomly positioned inclusions with their local orientations, will be described. The strategy is illustrated in the Figure VI-1 sketches.

To begin with, the initial step (see Figure VI-1a) generates the PBC-iDLSM domain using polyhedral DEs, following the same procedure outlined in section II.2.1.2. With the PBC-iDLSM domain in hand, the packing of inclusion process is initiated to generate randomly positioned and non-interpenetrating spherical inclusions with a uniform radius distribution. The packing process begins

License CC BY-NC-ND 4.0

with the input parameters listed in the Table VI-1. It uses an iterative trial-and-error process for randomly positioning the inclusion without overlapping. The average radius (R_{avg}) and the radius dispersion percentage (R_{disp}) are used to randomly pick a sphere radius (R_{sp}) value during the iterative process.

Table VI-1: List of input parameters for the "Generate Inclusion" algorithm

Description	Parameters	Value	Units
Average inclusion radius	R_{avg}	User-defined	μm
Dispersion radius	R_{disp}	10%	-
Targeted volume fraction	P_{VF}	11.2%	-
Incremental radius	ΔR	1%· R_{sp}	μm

In the first step, N_{inc}"imaginary" spheres with radius R_{sp} are positioned at random locations within the central periodic cell (100 × 100 × 100 μm^3) of the PBC-iDLSM domain, as illustrated by the blue spheres with solid lines in Figure VI-1b. Their positions are defined within the accepted 3D space, and these inclusions are subsequently replicated across all other periodic cells of the PBC-iDLSM domain.

Next, the volume fraction of the spheres within the central unit cell, highlighted central cell in Figure VI-1b, is computed. This is achieved by determining whether the centroid of each DE lies inside the region of the imaginary spheres. It should be noted that the inclusion volume fraction is calculated based on bonds fraction rather than element fraction (Nguyen, 2019). In order to compute this volume fraction, which is an important targeted parameter, the bonds are counted as matrix, inclusion and interface as follows:

- if both bonded DEs belong to the inclusion set, the bond is classified as an inclusion bond (bonds between two blue DEs in Figure VI-2);
- if both bonded DEs belong to the matrix set, the bond is classified as a matrix bond (bonds between two red DEs in Figure VI-2);
- If one DE belongs to the matrix set and the other to the inclusion set, the bond is assigned to the interface set (white bonds in Figure VI-2).

The computed volume fraction (C_{VF}) determines whether the packing process should continue, since it proceeds recursively.

If the target volume fraction is not reached ($C_{VF} < P_{VF}$), the radii of the imaginary spheres are increased incrementally (R_{sp} = R_{sp} + ΔR), as illustrated by the dashed circles in Figure VI-1, until the desired inclusion volume fraction is achieved ($C_{VF} \approx P_{VF}$). In this study, the interface bonds are assumed to have the same material properties as the matrix. Following this procedure, the final composite sample, shown in Figure VI-1c, is obtained.

License CC BY-NC-ND 4.0

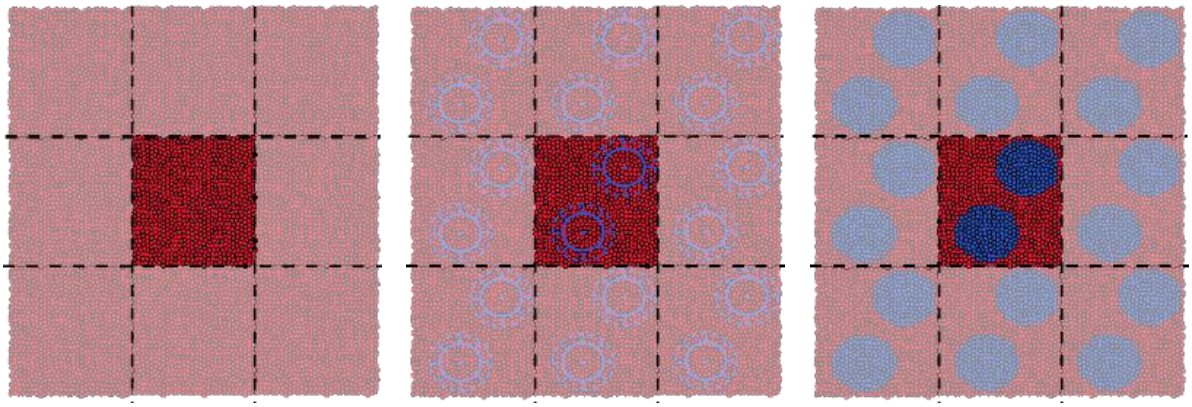

a) 2D PBC sample b) 2D imaginary inclusion c) 2D results

Figure VI-1: Illustration of generating 2D composite domain with randomly positioned inclusion

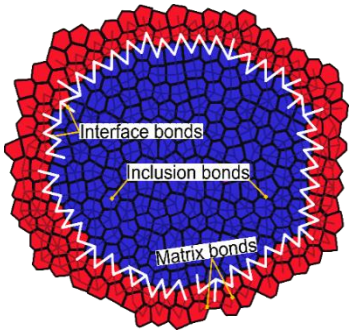

Figure VI-2: Illustration of matrix, interface and inclusion bonds in a 2D sample snippet

Each inclusion in Figure VI-1c is treated as a single grain and assigned a unique label, such as "inclusion-1", "inclusion-2"…" inclusion-N_{inc}". Additionally, each inclusion has a local orientation that is assigned randomly. The varying local orientations of each inclusion are illustrated in Figure VI-3 by using different colors.

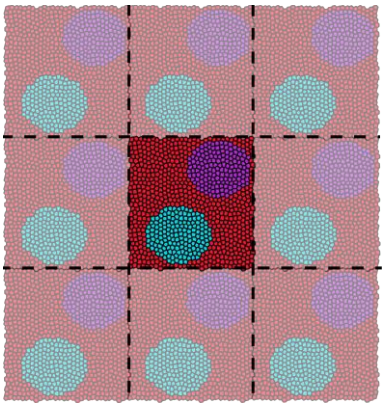

Figure VI-3: Illustration of the 2D composite sample with local orientations assigned to the inclusions

The Figure VI-4 illustrates a 3D numerical sample (with 20k DEs) generated using the strategy described earlier. This 3D sample contains five inclusions (that accounts to 11.2% volume fraction), each approximately 42 μm of diameter (in the 100 × 100 × 100 μm^3 central unit cell). As shown in this Figure, these inclusions respect the periodicity of the unit central cell. Notably, the orange inclusion is situated at a corner, meaning that all the orange DE clusters along the edges of the box are part of the same inclusion (see Figure VI-4b).

License CC BY-NC-ND 4.0

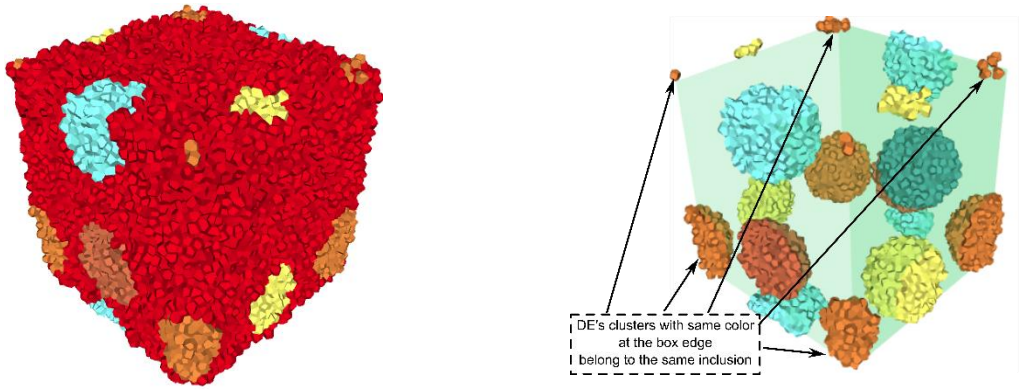

a) sample view b) inclusion view

Figure VI-4: Unit central cell of the 3D composite sample

The strategy for generating composite samples differs from that used for porous polycrystalline samples discussed in the previous chapters (Chapter V). In the porous case, a representative volume synthetic image was employed as a mask to embed pores, with no need of bond classification since pores does not have material properties (see section V.2.1). By contrast, composite sample generation requires bond classification to assign different material properties to distinct phases.

VI.2.2. A second strategy: regular positioning of inclusion

A composite model with regularly positioned inclusions is a common approach for investigating composite materials in a periodic context. The response is generally independent of the periodic unit cell size, leading to consistent results (Grasset-Bourdel, 2011). Regular packing further improves convergence and model robustness by reducing variance (as explained in section III.3.4.1). Consequently, employing regular inclusion arrangements offers notable numerical efficiency, as supported by various studies (Asadi, 2021; Firooz et al., 2019; Schneider et al., 2021), and provides an attractive strategy for implementation within the iDLSM framework. Therefore, the regular positioning strategy in a periodic context and a comparative study (regular versus random positioning) will be performed, in the next section, to check whether the positioning of the inclusion hold any dependency in the context of iDLSM framework.

In this section, the strategy for constructing the whole periodic domain, including matrix, inclusion positioned regularly and with their local orientations, will be described. The strategy is illustrated in the schematic sketches in Figure VI-5. Again, the initial step (see Figure VI-5) entails generating the PBC-iDLSM domain using polyhedral DEs, following the same procedure outlined in section II.2.1.2.

With the PBC-iDLSM domain, again the arranging of inclusion process is initiated to generate regularly positioned inclusions of uniform radius. This positioning process is similar to the one described in section VI.2.1. The key differences lie in the first step of the iteration process by introducing N_{inc} imaginary inclusion with a specified radius R_{sp}, as shown with blue spheres with solid lines in Figure VI-5b. However, it is important to highlight here that, all parameters in Table VI-2 are employed excluding the Dispersion radius (R_{disp}), as the strategy implicitly specifies radius R_{sp}. Their locations are specifically at the face centers and at the corners of the central periodic cell, in the 2D case (see Figure VI-5c). In 3D, the inclusions are positioned at centroid, face centers and corners of the box (see Figure VI-7).

License CC BY-NC-ND 4.0

In addition, the other steps involved in the positioning process remains the same as the section VI.2.1, in an aim to achieve the targeted volume fraction, as illustrated in Figure VI-5c. By this process, as shown in Figure VI-6, the composite sample with inclusions regularly positioned and assigned with random local orientation, is obtained.

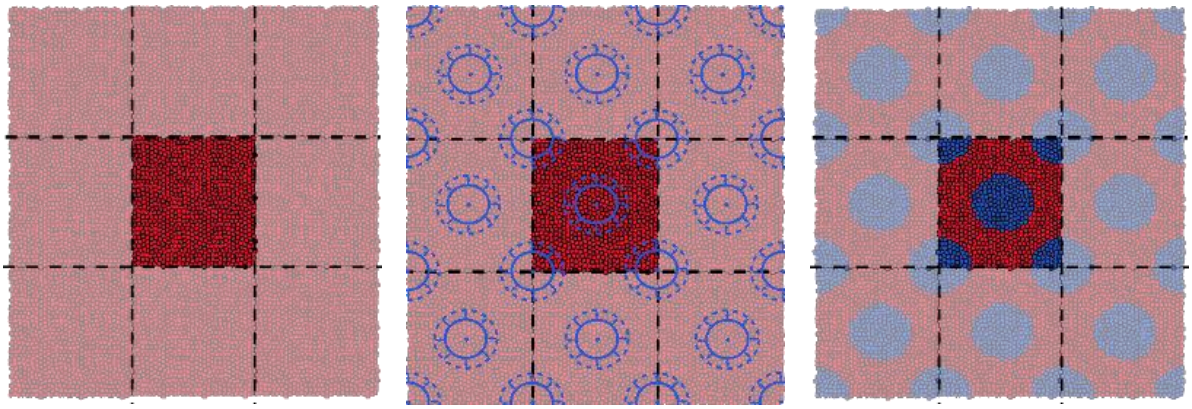

a) 2D PBC sample b) 2D imaginary spheres c) 2D results

Figure VI-5: Illustration of generating 2D composite domain with regular positioned inclusion

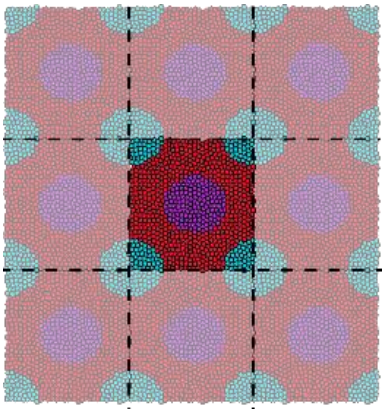

Figure VI-6: Illustration of the 2D composite sample with local orientations assigned to the inclusions

The Figure VI-7 illustrates the 3D numerical sample (with 20k DEs) generated using the strategy described earlier. This 3D sample contains five inclusions (that accounts to 11.2% volume fraction), each approximately 42 μm of diameter (in the 100 × 100 × 100 μm^3 central unit cell). Notably, the brown inclusion is situated at a corner, meaning that all the brown DE clusters along the edges of the box are part of the same inclusion (see Figure VI-7b).

License CC BY-NC-ND 4.0

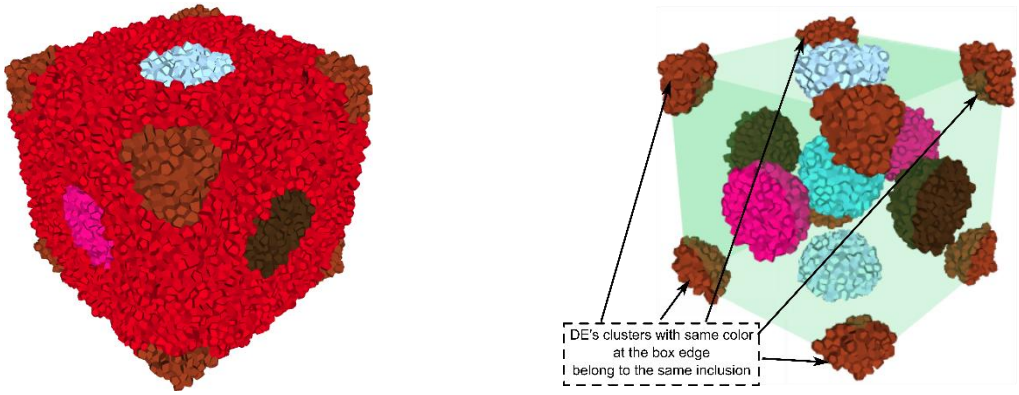

a) sample view b) inclusion view

Figure VI-7: Illustrates the 3D composite sample with regularly positioned inclusions

Using these strategies, composite samples with both random and regular inclusion arrangements can be generated. These samples are then employed to investigate the influence of inclusion positioning numerical strategy on the microstructure-property relationships of the composite.

VI.3. Validation of the numerical sample

In order to validate the composite sample, two studies are being planned. The first study aims to investigate how the positioning of inclusions, whether placed randomly or regularly within the matrix, affects the apparent Young's modulus of the composite sample. The second study will examine the effect of the volume fraction of inclusion on the apparent Young's modulus of the composite (Mouiya et al., 2026). Numerical results obtained in both studies will be compared with experimental results. Henceforth, as introduced in section III.3.3, the experimental results of alumina-aluminum titanate composite material will be used here.

VI.3.1. Impact of inclusion positioning methods on apparent Young's modulus

This section focuses on investigating how the positioning of inclusions within the matrix affects the apparent Young's modulus. It is important to highlight that the "Random" samples, which involve embedding inclusions randomly, require additional samples to take into account the variability of the random process and to enable statistical study (Garrard & Abedi, 2020; Nguyen, 2019). To address this, five "Random" samples and one "Regular" sample are utilized in this study, as shown in Table VI-2. In both cases, only five inclusions are considered, which accounts to a volume fraction 11.2% where each inclusion size is 42 μm approximately, in the 100 × 100 × 100 μm^3 central unit cell. Now, all six samples are subjected to thermomechanical simulations in order to evaluate their apparent Young's moduli.

Table VI-2: List of "Random" samples employed for the statistical study

Sample label	"Regular"	"Random1"	"Random2"	"Random3"	"Random4"	"Random5"
Inclusion view	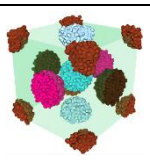	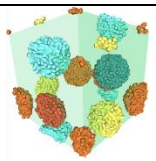	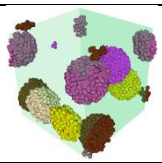	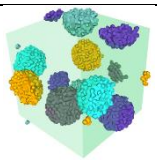	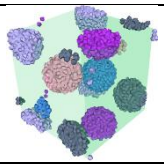	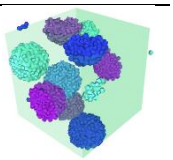

In this study, a thermomechanical simulation is conducted using the method described in the section IV.2.2. Each sample is subjected to a cooling thermal load from 1200 ℃ to 20 ℃.

The material properties used in the simulations are summarised in Table III-2 and detailed in section III.3.4.2. However, it is important to summaries few key assumptions. It is considered that

License CC BY-NC-ND 4.0

the alumina matrix has a temperature-dependent Young's modulus (Figure III-18a), which is derived from the "Al_2O_3/AT-0 wt%" microstructure response in Figure III-16b. In contrast, the inclusion AT Young's modulus is fixed at 120 GPa at 1200 ℃ to match the experimentally observed composite stiffness (Figure III-16b) (as explained in section III.3.4.2). Poisson's ratios of 0.244 for alumina and 0.28 for AT are adopted. It is considered that Alumina exhibits an isotropic, temperature-dependent CTE (Figure III-18b), whereas AT shows anisotropic expansion with α_a= -2.38 × 10^{-6} K^{-1}, α_b = 11.97 × 10^{-6} K^{-1} and α_c = 20.80 × 10^{-6} K^{-1}. For more information on the resources of the individual data, readers are referred to section III.3.4.2.

The matrix and inclusion tensile strengths are ($\sigma_{max}^{mat} = 235\,MPa$) and ($\sigma_{max}^{inc} = 1000\,MPa$), respectively; the matrix strength is calibrated to match the apparent Young's modulus at room temperature (similar to the strategy applied in section IV.2.2 for polycrystalline model), while the inclusion is assumed to have a very high tensile strength as its monocrystalline and its defect free.

Again, during the cooling process, the samples exhibit significant thermal stresses due to CTE mismatch between matrix and inclusion, which can lead to the formation of microcracks once the tensile strength of the material is reached.

To calculate the Young's modulus, the microcracked numerical samples are then subjected to quasi-static tensile test following each cooling simulation, starting from 1200 ℃ and continuing to 1100 ℃, 1000 ℃, and so on, down to 20 ℃. During these tests, crack propagation is prevented. The resulting apparent Young's modulus $\langle E \rangle$, defined as the ratio of the apparent normal stress $\langle \sigma_{XX} \rangle$ to the imposed apparent strain $\langle \varepsilon_{XX} \rangle$ is presented for all six samples (Ranganathan et al., 2025), alongside the experimental results in Figure VI-8.

Firstly, the results in Figure VI-8 depicts that:

- the apparent Young's modulus of the six numerical sample increases within the temperature range of 1200-1000 ℃. Since no microcracks are present and the alumina matrix follows an analytically defined temperature-dependent modulus (which depicts an increasing trend), the model exhibits an increasing trend between 1200 ℃ and 1000 ℃. In contrast, the reduction in Young's modulus from 1000 ℃ to 20 ℃ reflects the initiation and propagation of microcrack networks within the numerical sample.
- all six samples show quantitative results that are consistent with the trends observed in the experimental data (Mouiya et al., 2026), even though there are discrepancies in the obtained $\langle E \rangle$ values at different temperature after the onset of microcracks due to their random structure (Garrard & Abedi, 2020; Nguyen, 2019). Lastly, all the samples hold a stiffness of 40GPa at the room temperature, which aligns well with the experimental results (Mouiya et al., 2026);
- The results indicate that all five "Random" samples yield quantitative results. Furthermore, the data do not have any obvious order or pattern in the evolution of the apparent Young's modulus.

All six samples are not able to depict the sudden slope change similar to the experimental data at 600 ℃. This observation raises the question of whether the exact local orientations of the inclusions are required or whether lack of additional physics in the microscale prevents the model from capturing the sudden drop in Young's modulus. These questions highlight the need for further investigation to obtain more results.

License CC BY-NC-ND 4.0

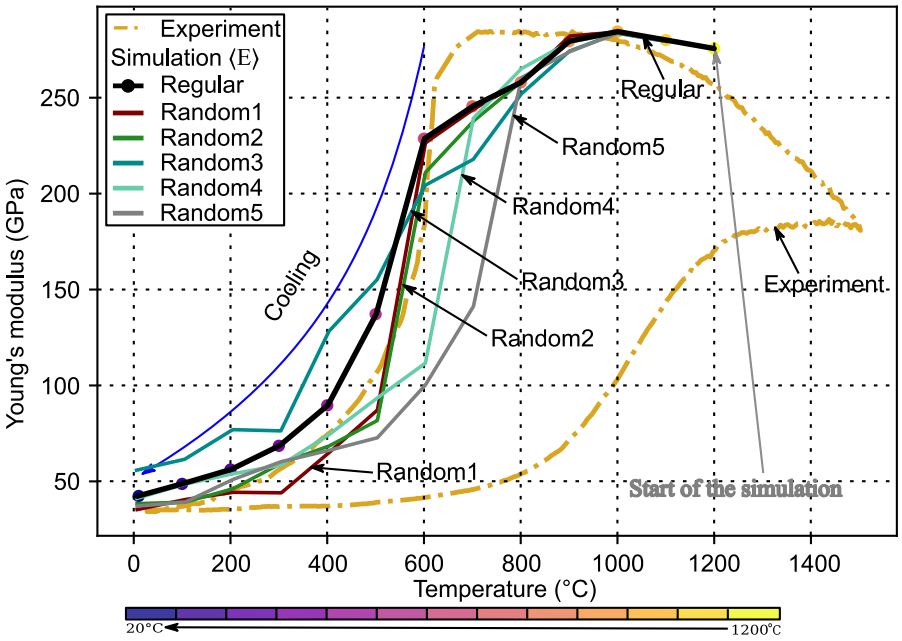

Figure VI-8: Experimental and numerical results of alumina - aluminum titanate composite Young's modulus evolution versus temperature

Also, the results indicate that the arrangement of inclusions, whether regular or random, does not affect significantly the trend in the apparent Young's modulus. Therefore, upcoming studies will focus on using the "Regular" sample for this purpose as it mimics an "average trend" of the five randomized samples. Additionally, this arrangement simplifies the packing process and is computationally most efficient to construct, and is easier to visualize and post-treat.

VI.3.2. Impact of volume fraction on apparent Young's modulus

This section focuses on investigating the impact of the volume fraction of inclusions on the apparent Young's modulus (Grasset-Bourdel et al., 2012; Mouiya et al., 2026). As mentioned before, here only the regular sample will be considered. For this study, "Regular" samples consisting of 20k DEs were constructed with volume fractions of 5.6% and 11.2% (see Figure VI-9). An inclusion size of 34 μm was used for the 5.6% volume fraction, while a size of 42 μm was used for the 11.2% volume fraction sample. It is important to note that the inclusions shown in Figure VI-9a and b are assigned random local orientations, which are visually represented by different colors in these figures. In this section, the results for "Regular-5.6%" are compared with experimental data, while the results for "Regular-11.2%" have already been validated in the previous section.

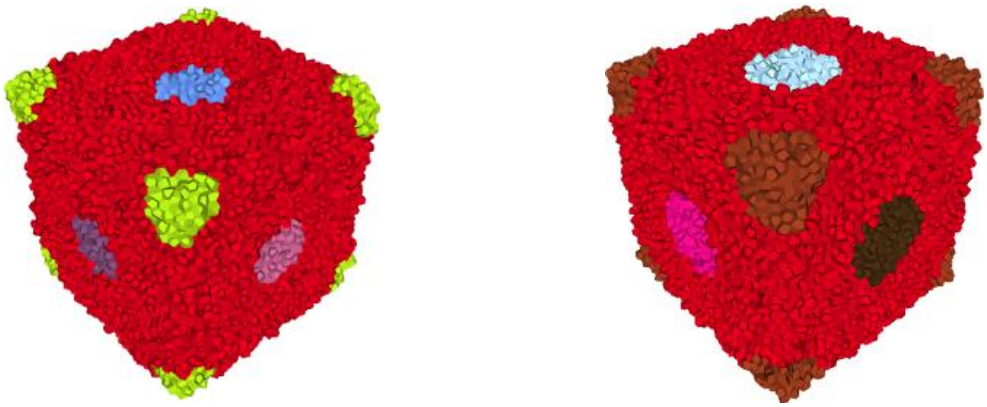

a) "Regular-5.6%" b) "Regular-11.2%"

Figure VI-9: illustration "Regular" samples with 5.6% and 11.2% inclusion volume fractions

License CC BY-NC-ND 4.0

Figure VI-10 shows the results obtained from the thermomechanical simulation. The "Regular-5.6%" exhibits results that qualitatively align with the trend of the experimental curve (Mouiya et al., 2026). Even if the numerical result is not quantitatively very close to the experimental curves, it is worth to mention that, in this case, the numerical sample exhibits a very sudden drop which is in line with the experimental trend (Mouiya et al., 2026). Although numerical results are available in the temperature range [500 - 20 ℃], validation of this range is not possible due to the lack of experimental data, which stems from the challenges encountered during experiments.

Regarding the impact of the inclusion volume fraction on the evolution of Young's modulus, Figure VI-10 shows that the numerical results follow a trend similar to the experimental results (Mouiya et al., 2026). The similarities are:

- the "Regular-5.6%" sample exhibits a higher apparent Young's modulus, indicating greater stiffness compared to the "Regular-11.2%" sample versus temperatures, as shown by the respective curves. This difference can be attributed to the higher matrix volume fraction in the "Regular-5.6%" sample, since the matrix itself possesses greater stiffness;
- the "Regular-5.6%" sample exhibits a reduction in stiffness at a lower temperature compared to the "Regular-11.2%" sample. Specifically, the "Regular-5.6%" begins to decrease at a temperature of 600 °C, while the "Regular-11.2%" starts to decrease at 1000 °C. As explained in section VI.3.1, the reduction in Young's modulus is attributed to the microcrack initiation and propagation. This indicates that increasing the volume fraction conducts to early start of microcracking during the cooling process.

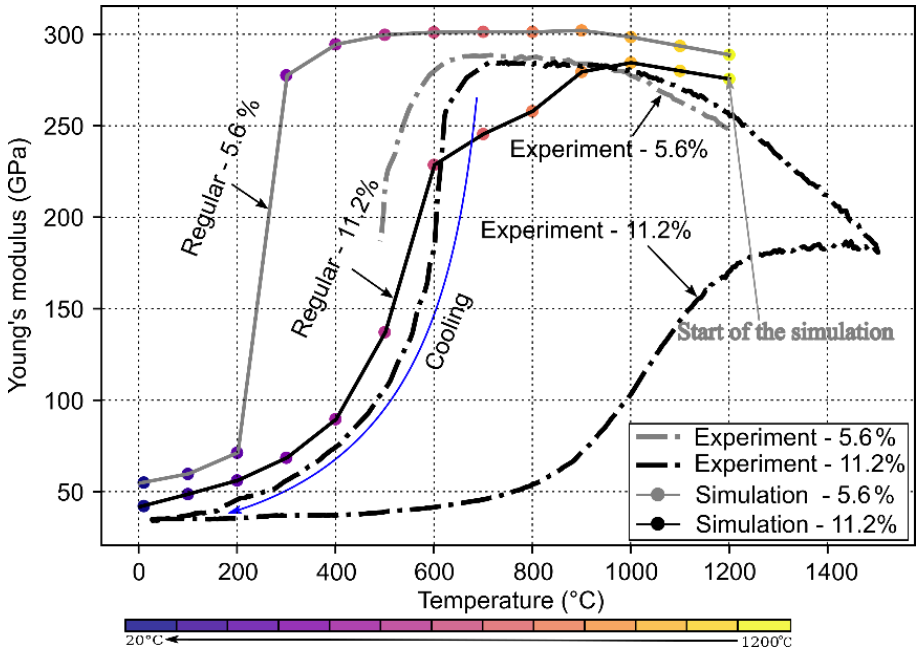

Figure VI-10: Volume fraction effects on Young's modulus vs temperature (experiment from Mouiya et al., 2026vs. simulation)

However, for the "Regular-5.6%" sample, further investigation including experimental work is necessary. Consequently, the comparative study intended to identify the micromechanical differences linked to the modification of the volume fraction will not be further addressed. However, the micromechanics of the "Regular-11.2%" sample will be examined as reference sample to better understand the different mechanics initiated by the inclusion. In the next studies, the "Regular-11.2%" sample will be employed and simply be referred as reference sample.

License CC BY-NC-ND 4.0

VI.4. Micromechanics study

The section, aims to expand the understanding in the micromechanics of alumina-aluminum titanate composite material. For this purpose, the numerical sample will be investigated to:

- study the stress distribution across the sample in the presences of the inclusions;
- monitor distribution of crack initiation and propagation;
- monitor crack surfaces to identify isolated and merged cracks;
- segregate between the intergranular cracks and intragranular cracks.

These studies are useful for understanding the evolution of microstructures in response to thermal loadings. It is already known that samples subjected to temperature change exhibit thermal internal stresses due to the CTE mismatch between the matrix and the inclusions (Grasset-Bourdel et al., 2012; M. G. Kakroudi et al., 2009; Mouiya et al., 2026). As shown in the previous section, in the Young's modulus evolution study, this CTE mismatch can lead to the initiation and propagation of microcracks which significantly drops the stiffness of the material. Therefore, monitoring the distribution of thermal stress will help identify the microcracking mechanism and provide insights into the dominant CTE orientation along the crystallographic axes (similar to Ranganathan et al., 2026) that primarily triggers the mismatch between the matrix and the inclusions.

Also, tracking the trajectories of microcracks will help determine if there are any preferential orientations for the cracks and pinpoint their locations (similar to Ranganathan et al., 2026). This includes identifying dominant cracking mechanisms, such as intergranular or intragranular cracking. Also, a question arises if the microcracks exist as isolated instances or as a complex crack network within the sample's microstructure.

VI.4.1. Thermal stress study

Again, the cooling simulation is performed, where the sample is cooled from $1200\,℃$ to $20\,℃$ at constant cooling rate. At the beginning, the sample is at $1200\,℃$. At this temperature, the sample does not exhibit internal stresses as shown in Figure VI-11a and there is no pre-existing crack in the sample as shown in Figure VI-12a. It is important to recall here that, the internal thermal stresses are represented using a color code, where the yellow color denotes zero stress state, the red color denotes tension (positive values) and blue denotes compression (negative values). These stresses correspond to the magnitude of the stress vector along the direction of the bond (normal stresses) (similar to Ranganathan et al., 2026). In this study, stresses ranging from -235 MPa to +235 MPa are monitored, the positive value corresponding to the tensile strength of the matrix.

Once the sample cools down from $1200\,℃$, it begins to exhibit internal stresses (both compressive and tensile) due to the CTE mismatch between the matrix and the inclusion, as shown in Figure VI-11b. The stresses present in the sample (see Figure VI-11b) are below the tensile strength of the material, so the sample does not show any microcracks, as illustrated in Figure VI-12b. Also, it appears that the most of the inclusions seem to be mainly in tension (red color) while the interfaces are mainly in compression (blue color) and the matrix seems to have a zero-stress (yellow color).

On further continuing to cool, the sample exhibits increased stress levels that reach the local tensile strength of the material (235 MPa), promoting microcracks. Figure VI-11c and Figure VI-12c illustrates the state of the sample, after microcracking, where the:

- sample exhibits compressive stresses primarily, with significantly lower number of bonds in tension, see Figure VI-11c;
- cracks seem to initiate and propagate preferentially along the inclusion-matrix interfaces.

License CC BY-NC-ND 4.0

From the last observation it is evident to see that the sample preserves the compressive thermal stresses after microcracking, depicted by the blue color bonds in Figure VI-11c.

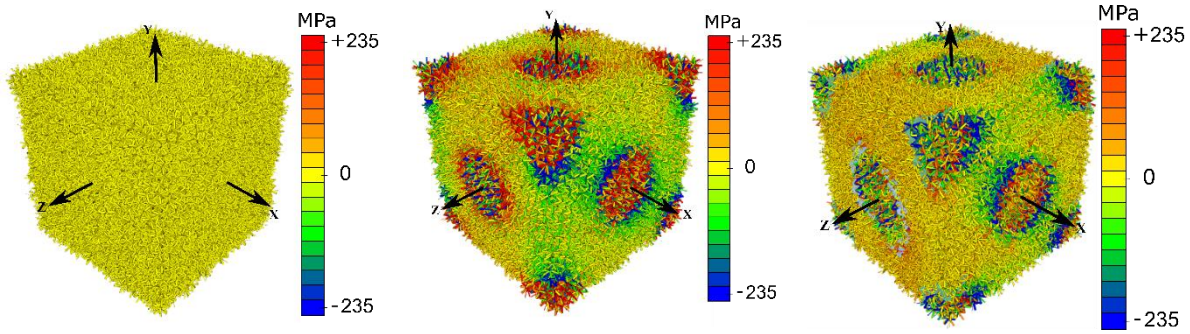

a) initial state (1200 ℃) b) pre-microcrack state (1000 ℃) c) post-microcrack state (700 ℃)

Figure VI-11: Stress states of the sample during cooling

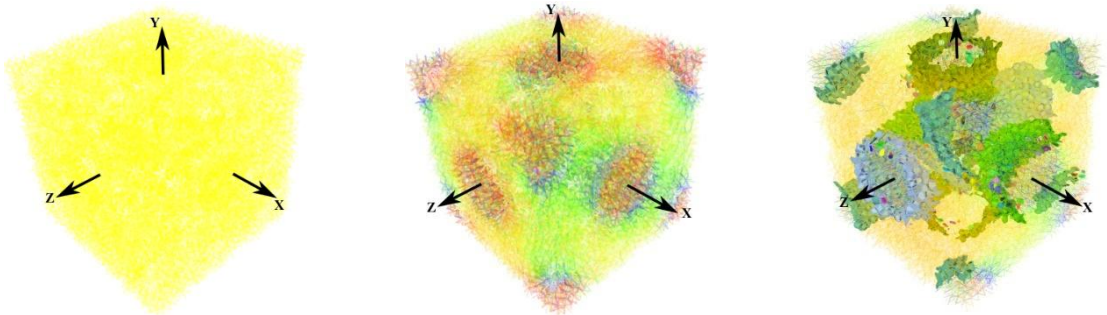

a) initial state (1200 ℃) b) pre-microcrack state (1000 ℃) c) post-microcrack state (700 ℃)

Figure VI-12: Micro-crack visualization in relation to the sample's stress state during cooling

In addition to these qualitative observations, thermal stresses are then monitored and recorded at each 100 ℃ of cooling, and the results are represented in 3D distribution plots (see Figure VI-13) (similar to Ranganathan et al., 2026). It is important to note that local orientations are defined only for the inclusions which exhibits anisotropic CTE while no local orientation is considered for matrix as it exhibits isotropic CTE. In this context, the local stresses of "matrix bonds" are expressed according to the local grain orientations ($\vec{a}$, $\vec{b}$, $\vec{c}$) of its nearby inclusions. In the following 3D histogram plots, the x-axis represents temperature (℃), the y-axis represents the thermal stress range (between -600 and 600 MPa), and the z-axis represents bond frequency.

The different panel of Figure VI-13 represents:

- from a) to c), the local mechanical response of the matrix,
- from d) to f), the local mechanical response of the interface, and
- from g) to i), the local mechanical response of the inclusion.

From these figures, it appears that:

- during the cooling process, the stress distributions broaden prior to the onset of microcracking. This enlargement is particularly evident in the interface and the inclusions;
- the stress distributions also exhibit a progressive shift of the distribution plots during cooling. This effect is most pronounced in the inclusion and the interface, whereas the matrix does not display a significant shift;

License CC BY-NC-ND 4.0

- following the onset of microcracking, the distribution plots depict reduction in both the shift and enlargement in the matrix stress distributions.

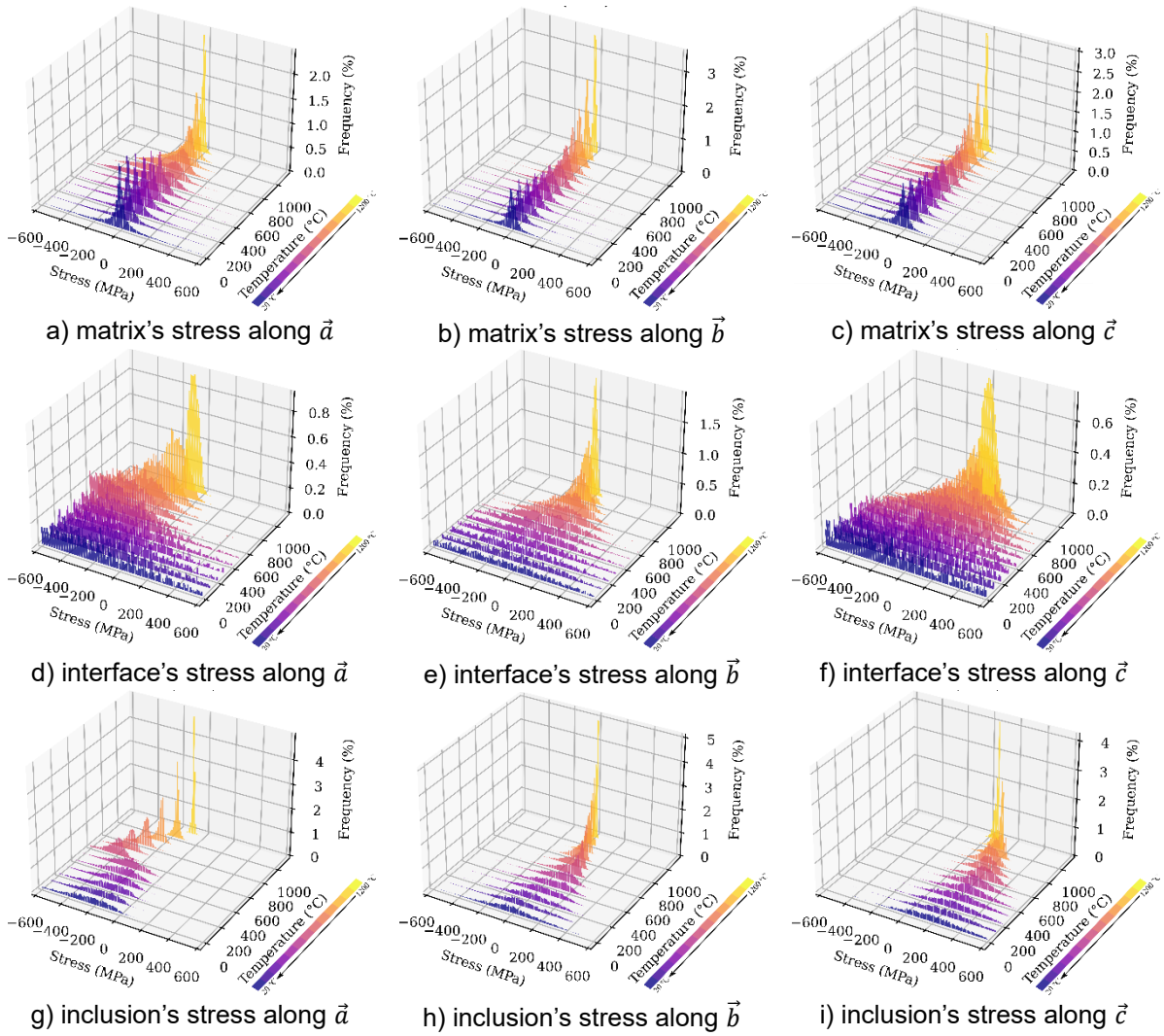

a) matrix's stress along $\vec{a}$ b) matrix's stress along $\vec{b}$ c) matrix's stress along $\vec{c}$

d) interface's stress along $\vec{a}$ e) interface's stress along $\vec{b}$ f) interface's stress along $\vec{c}$

g) inclusion's stress along $\vec{a}$ h) inclusion's stress along $\vec{b}$ i) inclusion's stress along $\vec{c}$

Figure VI-13: Thermal stress distribution versus temperature for the "crack" study

Therefore, the stress distributions of the matrix, interface, and inclusions can be quantitatively represented by their mean and standard deviation parameters, as they can be approximated by a Gaussian distribution (similar to (Ranganathan et al., 2026)). Figure VI-14 presents the evolution of the mean thermal stresses and their corresponding standard deviations in the matrix, inclusions, and interface, respectively.

From the Figure VI-14, it is understood that: during cooling, the matrix (Figure VI-14a) and interface (Figure VI-14c) mainly experience compressive stresses, whereas the inclusion (see Figure VI-14e) exhibits strong anisotropy. Between 1200 and 600 ℃, the mean thermal stresses increase steadily across all phases, indicating the promotion of both tensile and compressive stresses. Around 600 ℃, a sharp stress drop marks the onset of microcrack formation, most pronounced along $\vec{a}$ in the interface. Below this temperature, orientation-dependent stress release suggests a coordinated microcracking process driven by anisotropic thermal stress evolution. The mean stress drops in the matrix and interface corresponds to the release of compressive stresses while in the inclusion it involves both compressive and tensile components, reflecting complex stress redistribution. With decreasing temperature, the stress range broadens and the interface exhibits the largest variation, showing the highest standard deviation among all regions.

License CC BY-NC-ND 4.0

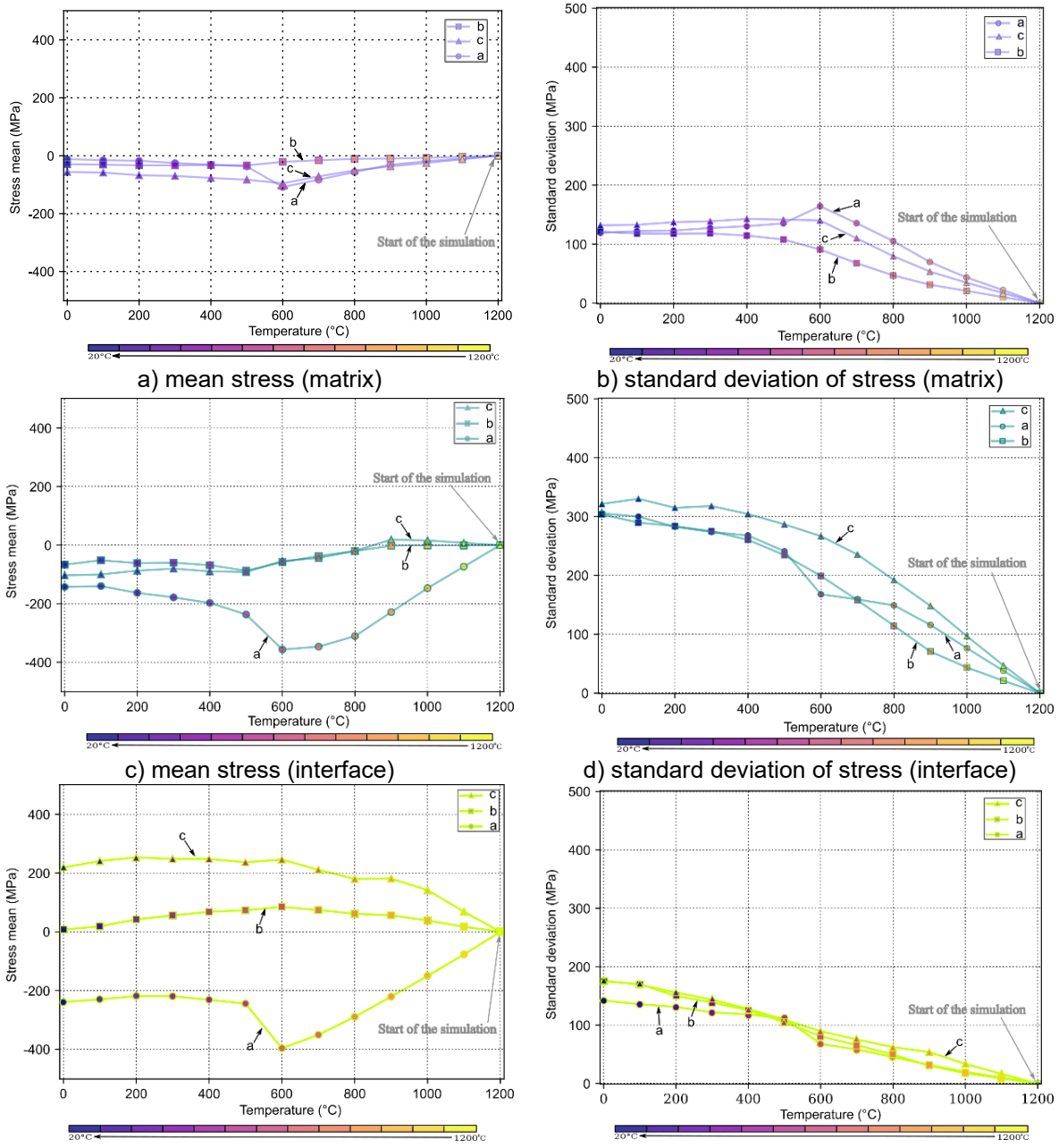

a) mean stress (matrix)

b) standard deviation of stress (matrix)

c) mean stress (interface)

d) standard deviation of stress (interface)

e) mean stress (inclusion)

f) standard deviation of stress (inclusion)

Figure VI-14: Stress distribution's mean and standard deviation evolution versus temperature

As mentioned earlier, differences in the CTE play a crucial role in generating stresses during cooling. These results suggest that:

- it was observed that compressive stresses are dominant in the sample;
- as the drop in mean stress were mostly observed in the curves that denote mean compressive stresses, it was obvious to see high amount of internal tensile stresses released are corresponding to the stress induced due to CTE mismatch along $\Delta\alpha_a$, during microcracking;
- most pronounced sudden drop in mean thermal stress values in the matrix, interface, and inclusion occurs along the $\vec{a}$ orientation, compared to the other two orientations. This indicates that, the difference in CTE ($\Delta\alpha$) along $\vec{a}$ is the highest and positive, and this elevated CTE appears to be the dominant factor contributing to microcracking.

License CC BY-NC-ND 4.0

Consequently, it can be inferred that most microcracks are likely to initiate perpendicular to the $\vec{a}$ orientation.

This observation indicates that a relationship may exist between local orientations ($\vec{a}$, $\vec{b}$, $\vec{c}$) and microcrack. To explore this further, microcrack statistics are analysed in the following sections to provide deeper insights into the reference model material Razavi et al., 2024.

VI.4.2. Analyses of the micro-crack network

This section investigates the microcrack statistics. The objective is to understand microcrack evolution, their preferred orientations and spatial arrangement, and the mechanisms driving the development of intricate crack networks (Ranganathan et al., 2026).

Figure VI-15, presents the temperature-dependent evolution of microcracking and damage. Accordingly, microcrack activity is quantified using a relative measure, defined as the proportion of broken bonds with respect to the total number of bonds in the numerical sample (Ranganathan et al., 2026). In addition, the is defined as the ratio between the current Young's modulus (E_i) value on the initial Youngs modulus (E_0) of a numerical sample (Öchsner, 2016).

From Figure VI-15, it is understood that:

- in [1200 - 1000 ℃] range, both the microcrack count and damage factor remain nearly constant, indicating a stable microstructure with no observable crack formation;
- in [1000 - 600 ℃] range, a gradual increase in both parameters suggests the onset of microcrack initiation and the beginning of microstructural degradation;
- in [600 - 400 ℃] range, a sudden rise in microcrack count and a sharp increase in the damage factor occur, marking the development of a dense microcrack network;
- in [400 - 20 ℃] range, the crack growth rate progressively decreases, indicating a saturation in microcracking and stabilization of the microstructure at lower temperatures.

Indeed at 20 ℃, the numerical sample had 43.8k (38.6k in the matrix, 4.9k in the interface and 309 in the inclusion) microcracks which corresponds to 28% of total bonds and a damage factor of 85%. Therefore, by extending the analysis to microcrack data, additional information can be gained regarding the present crack networks.

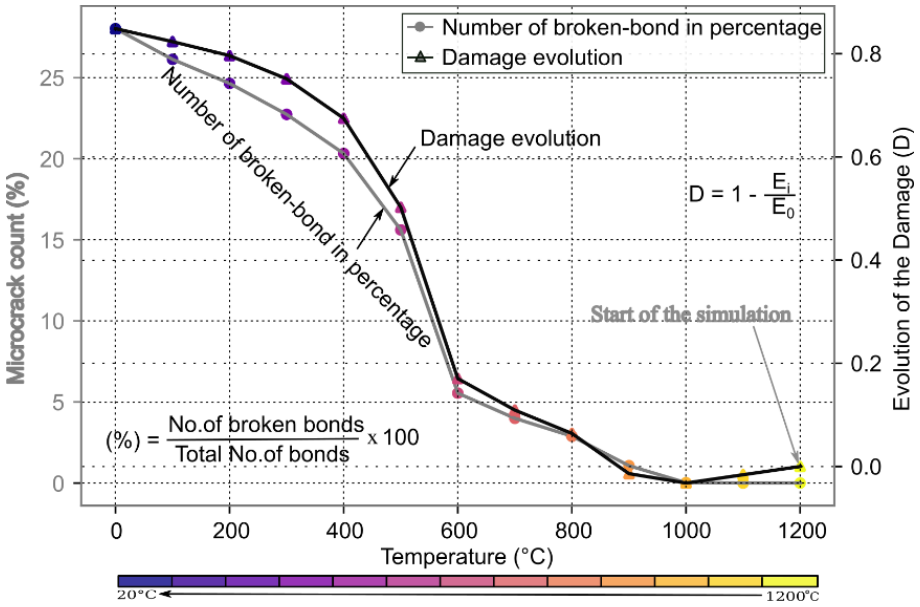

Figure VI-15: Recording of crack count and damage states of numerical sample vs temperature

License CC BY-NC-ND 4.0

VI.4.2.1. Preferential crack orientation

To assess the influence of inclusions on microcrack orientation, the unit normal vectors ($\vec{n}$) of the crack facets (see Figure IV-16b) were tracked and recorded throughout the cooling simulation, following the methodology described in section IV.3.2.1.

Again, it is important to recall that in the present sample, only inclusions have local orientation. Therefore, in this study, the cracks unit normal vectors are expressed in relation to the nearest inclusions local orientation ($\vec{a}$, $\vec{b}$, $\vec{c}$). For this purpose, the strategy of projecting normal vectors on to the local crystallography plane (ab, bc and ca) is being employed (see section IV.3.2.1), as illustrated in Figure IV-17. As an outcome of this representation is the polar histogram plot, as illustrated in Figure IV-18. Later a linearisation strategy proposed in section IV.3.2.1 is adapted here, considering the axes of symmetry in each plane ab, bc and ca, where only half the data are considered for the analysis (Ranganathan et al., 2026). For the present study, the axes of symmetry in each plane are: ab: 90-270°, bc: 0-180° and ca: 0-180°. Finally, the linear distribution data, collected every 100 ℃, are arranged into the 3D plots as shown in Figure VI-16. It is important to highlight that readers can refer to section IV.3.2.1 to get more details on how this polar histogram plots are obtained.

In the Figure VI-16, the x-axis represents temperature (℃), the y-axis indicates the $\vec{n}$ Vector orientation intervals (in degrees), and the z-axis denotes the frequency of occurrence. Figure VI-16(a-c) correspond to the cracks $\vec{n}$ distribution in the sample.

From these figures (see Figure VI-16), it is evident that the cracks $\vec{n}$ are primarily oriented between 90-270° in ab, 0-180° in bc and 0-180° in ca plane versus temperatures. Furthermore, an enlargement of the $\vec{n}$ orientation range is observed, suggesting that the microcracks have propagated in a scattered orientation. This behavior indicates the presence of a complex crack trajectory in the samples, particularly at low temperatures.

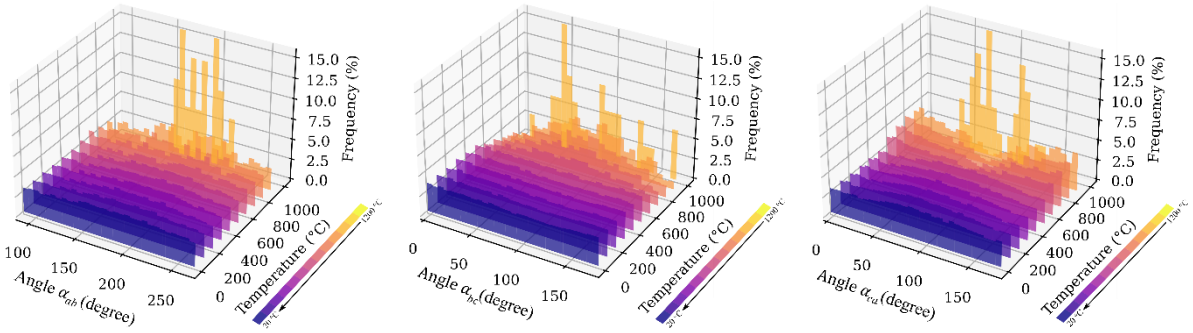

a) α_{ab} in ab plane (global) b) α_{bc} in bc plane (global) c) α_{ca} in ca plane (global)

Figure VI-16: 3D linear microcracks $\vec{n}$ orientation vs temperature

Now, using the strategy mentioned in section IV.3.2.1, the $\vec{n}$ are analysed in different planes and directional orientations are monitored and expressed in the inclusion's local crystallographic axes, as shown in Figure VI-17. It is important to highlight here that the presented microcrack $\vec{n}$ vectors distribution in Figure VI-16, is segregated as microcracks in matrix, interface and inclusion regions. Indeed, expressing the closest axes for each set would improve the investigations. Therefore, Figure VI-17a corresponds to the matrix, Figure VI-17b to the interface and Figure VI-17c to the inclusions.

The results show the matrix and interface follow similar trend. In the [1200-600 ℃] range, cracks in the matrix are mainly perpendicular to the $\vec{c}$ orientation and at the interface they appear in both the

License CC BY-NC-ND 4.0

ab and bc planes, with a slight preference along the $\vec{c}$ orientation. In the [600-20 °C] range, cracks in both the matrix and interface are primarily aligned along the a-axis, forming facets in the bc-plane.

In addition, by computing the CTE mismatch ($\Delta\alpha$) between the matrix and inclusion (Tessier-Doyen et al., 2006), it is found that $\Delta\alpha_a$ is positive, while $\Delta\alpha_b$ and $\Delta\alpha_c$ are negative during cooling. This suggests that, in the case of interface, $\vec{n}$ oriented along the $\vec{a}$ direction correspond to microcracking, whereas those aligned along the $\vec{b}$ and $\vec{c}$ directions correspond to decohesion. Consequently, it can be inferred that decohesion (the combined effect along the $\vec{b}$ and $\vec{c}$ directions) is more pronounced than microcracking at the interface versus temperature range.

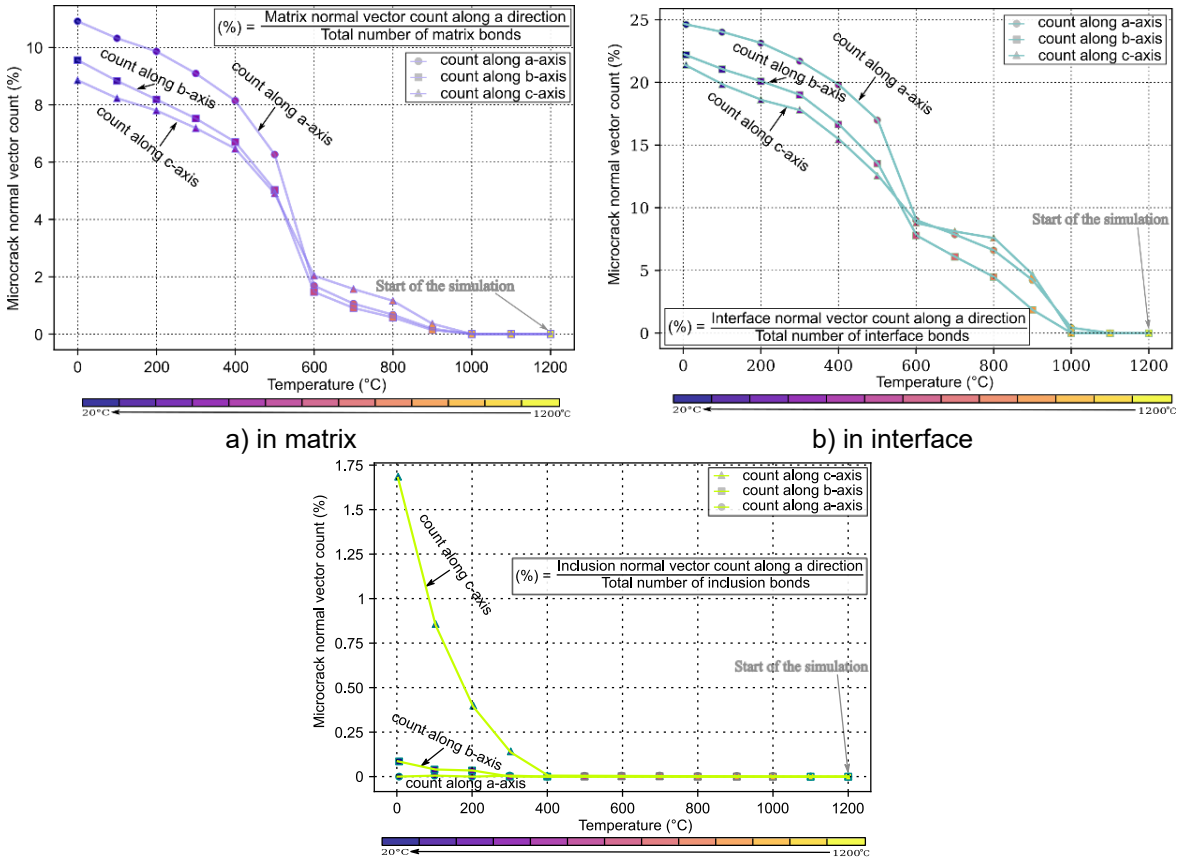

a) in matrix

b) in interface

c) in inclusion

Figure VI-17: Crack $\vec{n}$ count in relation to inclusion's local crystallographic axes vs temperature

These results helped deduce the dominant cracking mechanisms versus temperature at the interface, where it appears that decohesion was approximately twice the amount of microcracking. Finally, some cracks occur below 400 °C in the inclusion mainly perpendicular to the c-axis, which indicates the involvement of the highest CTE of AT (α_c) to initiate microcracks.

VI.4.2.2. Monitoring on the location of cracks: Interface vs Bulk

The present section focuses on identifying the location of the microcracks. Indeed, this data help understanding the crack trajectories in the microstructure. Figure VI-18 depicts the evolution of cracks in matrix, interface and inclusion regions versus temperature. Note, the Figure VI-18a, corresponds to microcracks absolute values, while the Figure VI-18b corresponds to relative values (sum of the cracks in matrix, interface and inclusion accounts to 100%). The numerical sample initially have approximately 131k matrix, 17k inclusion and 7k interface bonds.

License CC BY-NC-ND 4.0

From the Figure VI-18a, it appears that the cracks in matrix are highly dominant and the matrix crack propagation rate is more aggressive. From Figure VI-18b, it appears that, at high temperatures, interface cracks are dominant (accounting for nearly 100% of the cracks). As the temperature decreases, their proportion progressively declines, while bulk cracking in the matrix region shows an increasing trend. Therefore, this indicates that the microcracking happens at interface and extents as a bulk crack in the matrix, which is aligned with the results observed in section VI.4.2.1. Among these, the amount of crack in inclusion remains negligible.

These results along with the insights done in section VI.4.2.1 suggests that, a highly interconnected microcracks network exists within the matrix. In addition, these results are in line with the SEM observations done by Mouiya et al., 2026 in an experimental study. The next section will conduct a study to monitor the surface area of microcracks, providing insight regarding this topic.

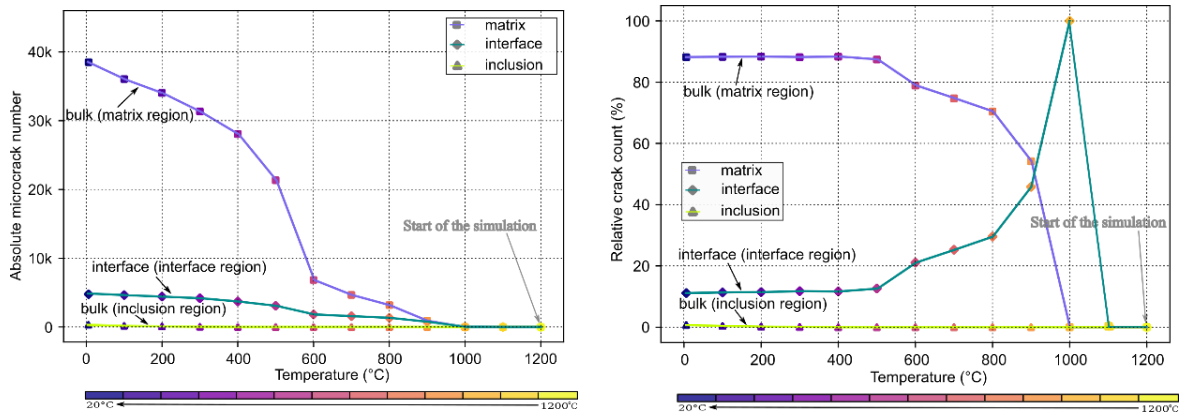

a) absolute evolution b) relative evolution

Figure VI-18: Evolution of cracks in matrix, at interface and in inclusion versus temperature

VI.4.2.3. Monitoring of the crack surface area

This part of the study examines how to discriminate between individual cracks and groups of interconnected crack facets, employing the strategy introduced in section IV.3.2.3, related to monitoring of surface of crack clusters, is performed during cooling simulation. The outputs are represented in a 2D bar plot, as illustrated in Figure VI-19. Here, crack surface per unit cell volume is monitored. Again, the x-axis denotes crack cluster label and the y-axis denotes their corresponding surface in the following Figure VI-19 each crack cluster are identified by different colors.

From Figure VI-19, it appears that:

- the first occurrence of microcracking was observed at 1000 ℃, as shown in Figure VI-19a;
- between [900 - 700 ℃], the simulation snippets in Figure VI-19b and c illustrate that new microcracks were initiated while existing isolated cracks propagate in multiple directions;
- notably, around 600 ℃, two complex crack networks were present, as depicted in the crack density distribution plots in Figure VI-19d;
- between [600 - 500 ℃], the two single complex crack networks merged to form a single complex crack network;
- between [500-20 ℃], a number of previously isolated microcracks appear to have coalesced with the main crack network, as can be seen by comparing Figure VI-19e and f.

Ultimately, the numerical sample is populated with 20 $\left(\frac{m^2}{m^3}\right)$ crack surface per unit cell volume at the end of cooling process. Figure VI-19f) shows that, following cooling, one dominant interconnected

License CC BY-NC-ND 4.0

crack network persists, along with a limited number of isolated cracks. Comparable complex networks were also identified in the SEM work of Mouiya et al., 2026.

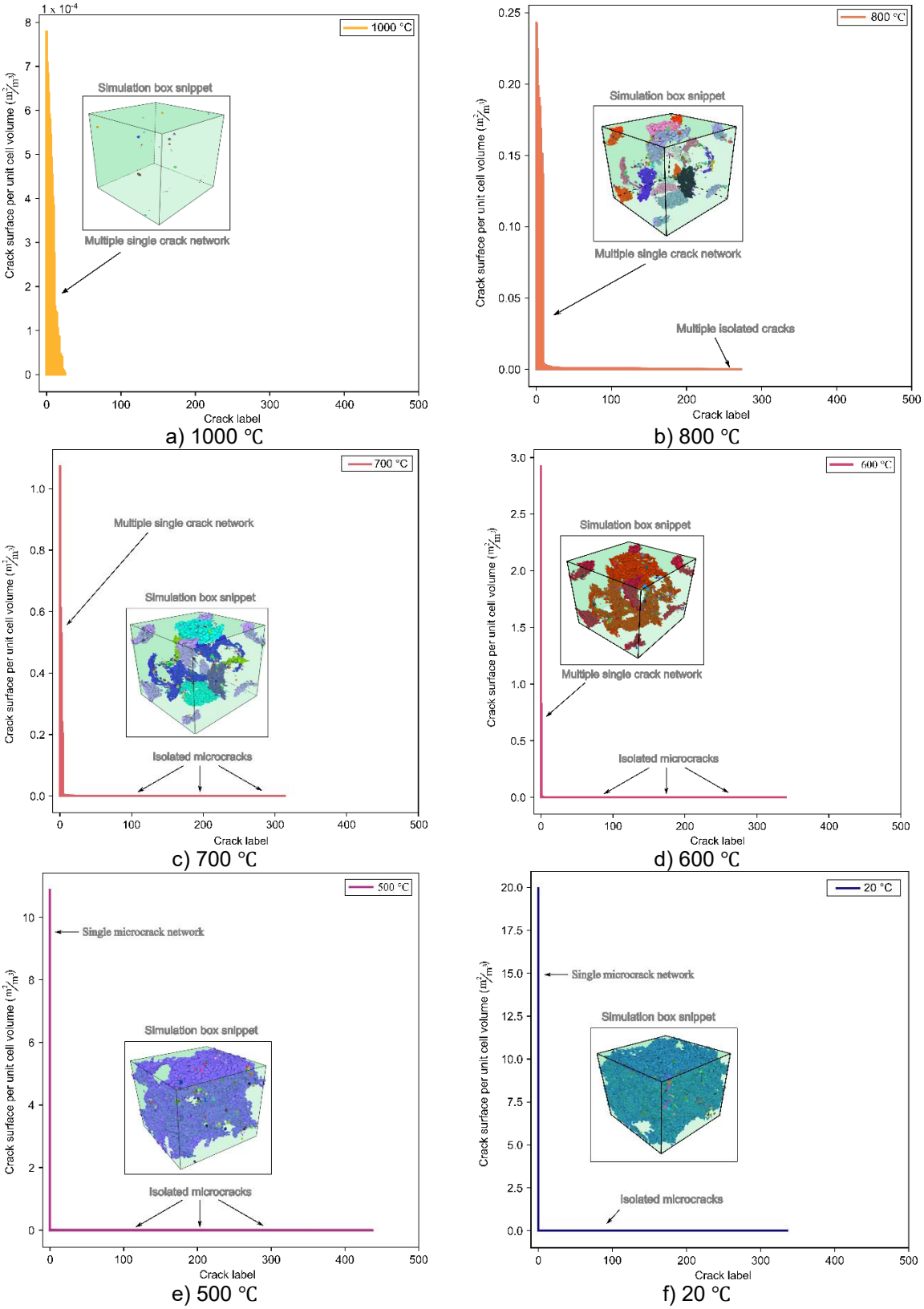

Figure VI-19: Monitoring of crack surface density distribution at different temperature

Thanks for this micromechanics study, which was helpful to understand the evolution of the composite sample during cooling under CTE mismatch, which aligns with the experimental

License CC BY-NC-ND 4.0

observations. Indeed, it is now important to study the impact of composite sample's evolution on the mechanical response of the sample.

VI.5. Mechanical response

The objective of this work is to evaluate the stress-strain response of damaged numerical samples. After cooling, the samples undergo monotonic and cyclic tensile tests, allowing existing microcracks to extend (similar to Ranganathan et al., 2026).

VI.5.1. Monotonic uniaxial tensile loading

The aim of the study is to monitor the apparent stress-strain response of the damaged numerical sample under monotonic uniaxial tensile loading. Recall that, mechanical simulation is performed after each 100 ℃ of cooling. In total, 12 mechanical simulations are performed in this study (Ranganathan et al., 2026). In these simulations, the apparent stress and strain were deduced using the procedure discussed in section II.2.1.3. Figure VI-20 illustrate the mechanical response of the sample across three different temperature ranges. The sample exhibits a brittle response in [1200 - 1100 ℃] range, which is indicated by the sudden initiation and propagation of the cracks in Figure VI-20a and b. In [1000 - 600 ℃] range, the samples show an increasing tendency toward non-linear behavior post the stress-peak region (see Figure VI-20c and d). Conversely, in the [600 - 20 ℃] range, the sample exhibits non-linear behavior in both the pre-stress-peak and post-stress-peak regions, indicating the presence of dense microcracks below 600 ℃ (see Figure VI-20e and f).

Furthermore, the stress-peak decreases with decrease in temperature (see Figure VI-21), which is due to pre-existing cracks and tensile thermal stresses that provide stress concentration. In contrast, the numerical sample exhibits a decrease in strain-peak within the [1200 - 900 ℃] but an increase in strain-peak within the [800 - 20 ℃] range (see Figure VI-21). Accordingly, crack propagation appears to proceed in a stable manner, reflecting a diffuse damage process in the [800 - 20 ℃] range and a concurrent relaxation of internal stresses.

These results suggest a change in the mechanical behaviour (from brittle linear to quasi-brittle non-linear behaviour) as the temperature decreases. At room temperature, the numerical sample exhibits a highly non-linear behaviour, such a feature is expected and significant for thermal shock resistance, as insighted in numerous studies (Grasset-Bourdel et al., 2012; Huger et al., 2011; Kakroudi et al., 2008; Mouiya et al., 2026). A shift in the mechanical response, associated with microstructural evolution and the initiation of microcracks, was also observed in the experimental study by Mouiya et al., 2026.

License CC BY-NC-ND 4.0

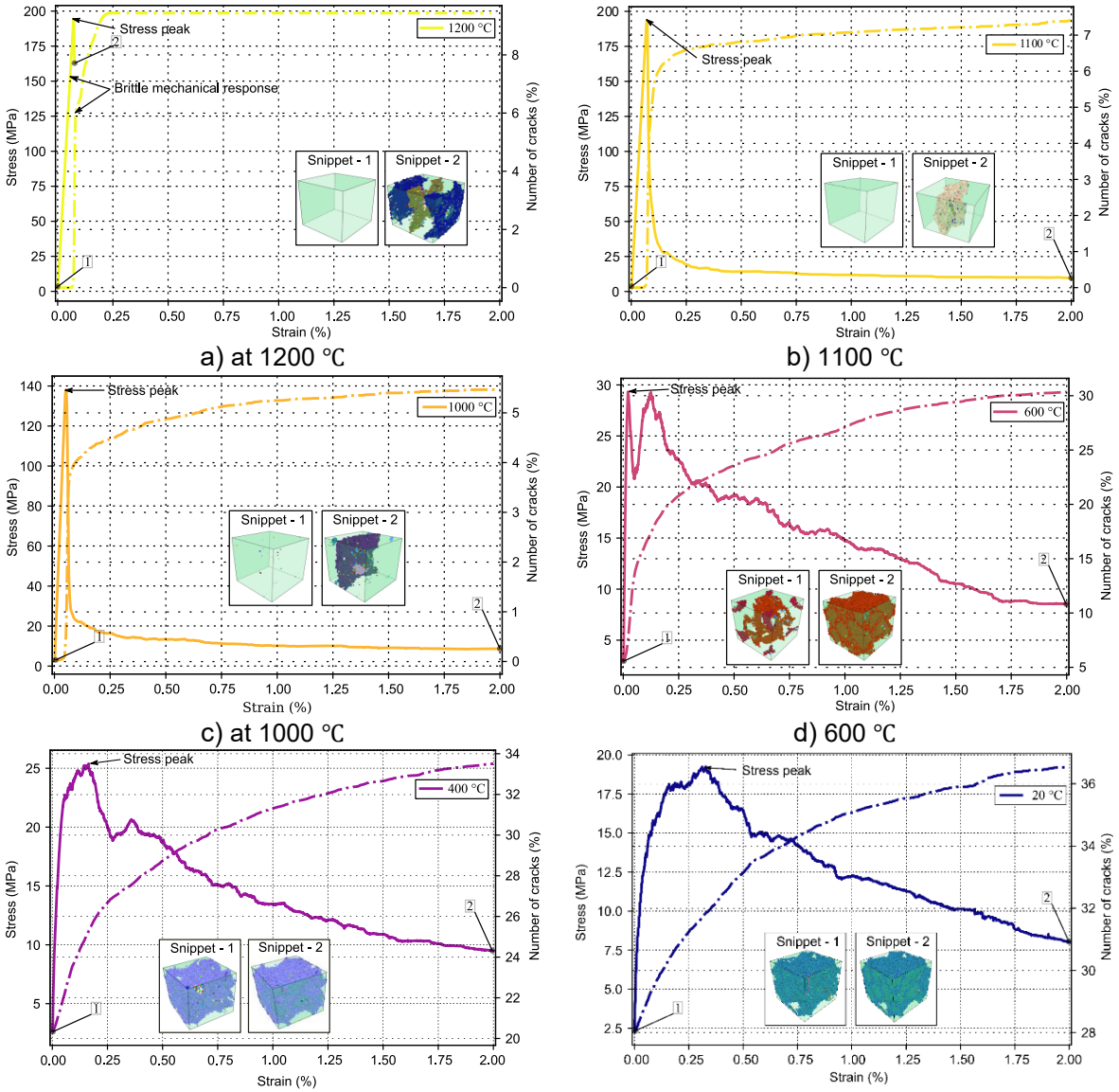

Figure VI-20: Evolution of apparent stress-strain response and cracks in [1200 - 20 °C] range

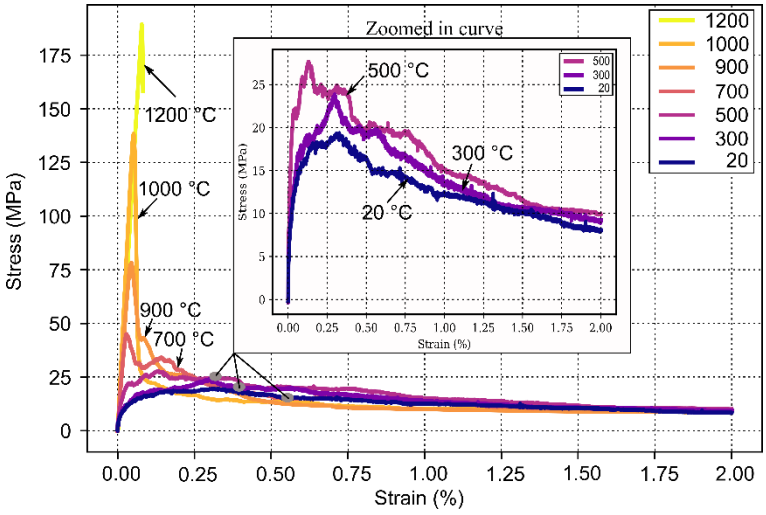

Figure VI-21: Evolution of apparent stress-strain versus the temperature

License CC BY-NC-ND 4.0

Therefore, identifying the required amount of pre-existing thermal stresses combined with the presence of microcracks is crucial for understanding and identifying this change in mechanical behaviour. To evaluate the number of pre-existing microcracks needed to reinforce the numerical sample, the total number of cracks before and after mechanical loading was recorded and is presented in Figure VI-22, in a similar fashion explained in section IV.3.4.1. For reference, the “End of simulation” represents the total number of microcracks following the tensile test, when the sample exhibits minimal rigidity. The “Start of simulation” corresponds to the number of cracks formed during the cooling process. The “Difference” curve is calculated as the difference between these two curves.

The results shown on the Figure VI-22 indicate the presents of two different zones for the “Difference” curve and the 600 ℃ temperature mark seems to be the transition point. Now, on correlating the observation seen in stress-strain response (see Figure VI-21) and Figure VI-22, it is observed that the transition of brittle to (fully) non-linear response happens below 600 ℃ mark.

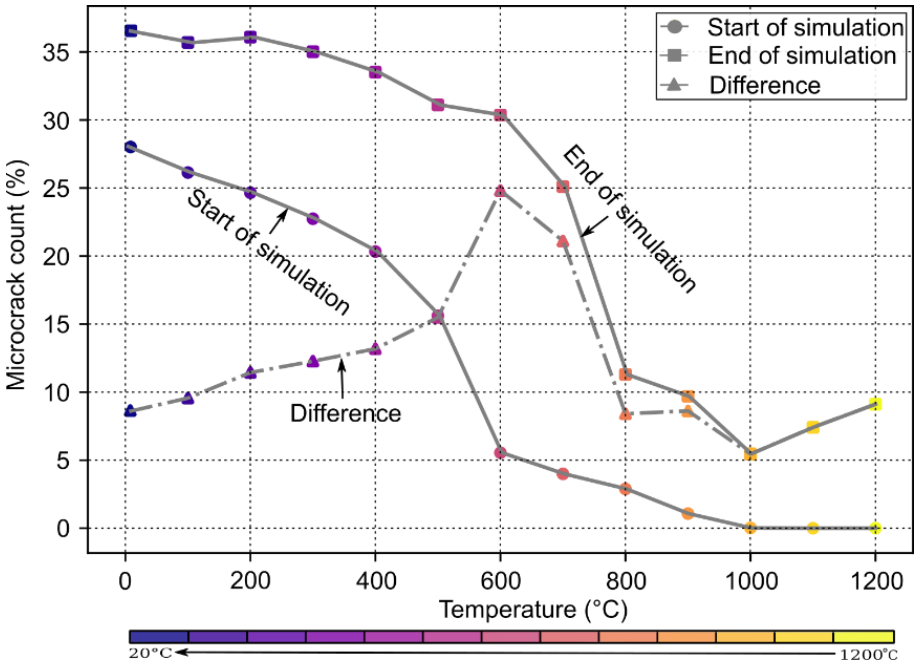

Figure VI-22: Evolution of the microcrack of the modal material versus temperature

So, thanks to this study, which helps to relate the crack statistics with the mechanical response of the material. In the case of the polycrystalline study presented in section IV.3.4.1, a similar transition temperature was observed, corresponding to a change in the sample’s mechanical response from brittle to non-linear behavior (see Figure IV-29). Since this observation was made for the first time, it was initially unclear whether the correlation was genuine or merely coincidental. Therefore, obtaining the same observation with composite sample confirm that, the correlated conclusions is not just a coincident rather an important conclusion to relate the transition of mechanical response with the crack statistics.

VI.5.2. Cyclic uniaxial tensile loading

The present section focuses on monitoring and recording the irreversible strains. After the cooling process, the damaged samples are subjected to cyclic uniaxial tensile loading, following the strategy outlined in section IV.3.4.2. The resulting apparent stress-strain responses as a function of temperature are presented in Figure VI-23.

License CC BY-NC-ND 4.0

Across the entire temperature range of [1200 - 1100 ℃], the mechanical response of the sample evolves progressively with cooling. At high temperatures [1200 - 1100 ℃], the material remains largely intact, with no pre-existing microcracks observed (see snippet-1 in Figure VI-23 (a-b)). The sample at 1200 ℃ shows a fully reversible response, while at 1100 ℃, irreversible strains emerge post the stress peak, indicating the release of internal stresses during crack extension. The unloading behavior in this range remains linear, though the global rigidity gradually decreases with temperature (see Figure VI-23 (a-b)).

As the system cools into the intermediate range [1000 - 600 ℃], pre-existing microcrack networks and internal thermal stresses appear, leading to higher irreversible strains and progressive stiffness loss. These features suggest stable crack extension driven by accumulated thermal stresses (see Figure VI-23 (c-d)).

At lower temperatures [500-20 ℃], the microstructure becomes dominated by dense, interconnected microcrack networks, producing highly non-linear stress-strain responses with substantial irreversible deformation both before and after the stress peak (see Figure VI-23 (e-f)). The unloading/loading phases exhibit hysteresis loops that intensify as temperature decreases, reflecting increased energy dissipation and cracks opening and closure activities. While these hysteresis behaviors closely resemble experimental observations (Figure III-16d), further analysis is needed to determine whether they represent genuine material mechanisms or arise artificially from computational factors (e.g., unloading velocity).

VI.6. Conclusion

The presence of anisotropic inclusions (with single grain) promotes dense microcrack networks and internal compressive stresses (Razavi et al., 2024). These microstructural features lead the material to exhibit a non-linear mechanical response, a key property for enhancing sustainability under thermal shock conditions (Mouiya et al., 2026). This behaviour is further reflected in the material's ability to sustain higher strains at room temperature compared to elevated temperatures. The results also underline the critical role of accumulated internal stresses in driving irreversible strain, while simultaneously intensifying the non-linear stress-strain response through stress redistribution during microcrack propagation. In addition, the present model appears to replicate the hysteresis loop observed in experimental results, during cyclic loading (Mouiya et al., 2026). While this is an encouraging result, it requires further investigation to determine whether the behaviour genuinely reflects the underlying physical mechanisms or is influenced by computational factors.

The DEM tool effectively demonstrates the impact of the CTE mismatch between the matrix and inclusion on promoting fracture behaviour such as crack initiation, propagation, merging, and branching in composite materials. By incorporating crack evolution, the model enhances our understanding of how microstructural features govern the macroscopic thermomechanical properties of composites. Alumina-aluminum titanate was employed as the reference material to explore the limit of the tool, which successfully reproduced the formation of multiple microcrack networks during cooling as a key result.

The iDLSM approach further facilitated the modelling of composite samples with both regular and random inclusion distributions. These samples (with 11.2% of inclusion volume fraction) were first used to examine the influence of microstructural evolution on the apparent Young's modulus. The results reproduced both the quantitative and qualitative aspects of the experimental observations for this case, except that the sudden change in slope was not captured (see Figure VI-10) which is

License CC BY-NC-ND 4.0

not the case for lower volume fraction (5.6%). Despite having reasonable results with both style of arrangement, for subsequent studies, regularly positioned inclusions ("Regular" samples) were used to investigate the impact of inclusion volume fraction on microstructural evolution and apparent Young's modulus. Indeed, "Regular" samples gave acceptable results with easier visualization and are computational efficient. For this study a sample with 5.6% and 11.2% inclusion volume fractions were employed. While quantitative agreement was obtained, some discrepancies remain in the qualitative trends, particularly for the 5.6% inclusion case. Future studies are necessary to address whether the local orientation of inclusions is critical, whether five inclusions per central periodic cell are sufficient, and whether inclusion size also influences Young's modulus.

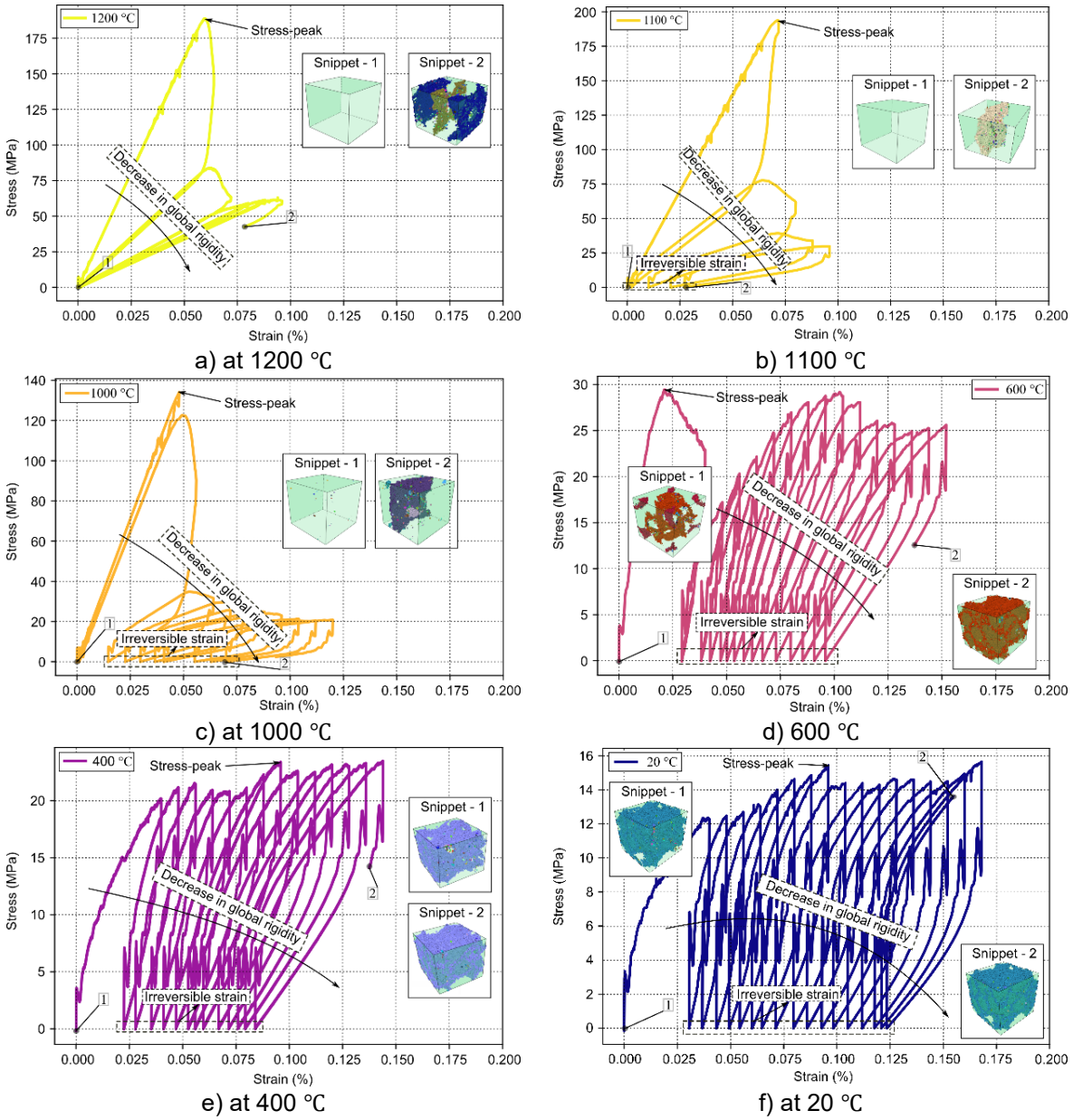

Figure VI-23: Irreversible strain recording during uniaxial cyclic loading in [1200 - 20 °C] range

The "Regular" sample was also used to investigate microstructural evolution during cooling. A key strength of the present tool is its ability to monitor micromechanics evolution separately in the matrix, interface, and inclusions. In this line, the DEM tool was employed to monitor the stresses and this study revealed several important mechanisms in the reference material, including (i) stress relaxation during crack initiation, (ii) the influence of local inclusion orientation on thermal stress

License CC BY-NC-ND 4.0

distribution, and (iii) pseudo-plasticity arising from microcrack extension and internal stress relaxation. Similar to Chapter IV, this study provides insights into preferential crack orientations in relation to the local orientation of inclusions, their origins and trajectories, and whether they remain isolated or evolved into complex crack networks. The results show that microcracks generally initiate as small, isolated networks at the interface at high temperatures. As cooling progresses, these cracks extend into the matrix along preferential orientations before eventually merging into a larger, more random, and complex crack network at lower temperatures.

In addition, the DEM tool was used to monitor the apparent stress-strain response under monotonic and cyclic loading as a function of cooling temperature. Again, the model successfully captured the transition in mechanical behaviour from brittle to quasi-brittle (non-linear) response and highlighted the influence of internal thermal stresses on stress of rupture and crack propagation under monotonic loading. Importantly, the DEM tool was able to correlate the number of microcracks required to exhibit this transition and provide insight into the temperature mark at which it occurs. Furthermore, also tracked irreversible strains (pseudo-plasticity) during cyclic loading. Notably, the model reproduced hysteresis loops similar to those observed experimentally, though further investigation is required to confirm whether this reflects the true underlying physical mechanisms or arises from computational artefacts.

Overall, this work highlights the strong link between microstructural features, such as inclusion position, volume fraction etc. and crack networks, and the resulting macroscopic mechanical response. As a next step, further refinements (as pointed out earlier) are needed to enhance the DEM tool's capabilities for composite materials. Future studies should extend the model to multiphase systems, incorporating secondary phases such as binder deposits at the interface such as CA_6 or inclusions such as WFA (Boateng et al., 2025) in "Regular" samples. Such developments will provide deeper insights into the role of multiple phases and contributes to optimizing microstructural design strategies for improved performance in refractory applications.

License CC BY-NC-ND 4.0

Conclusion and perspective

This PhD project was part of the CESAREF consortium (Huger, 2023) and was carried out in collaboration with the Thermomechanics Ceramic (TMC) Group at IRCER (Limoges) and the Refractory Team at the Imerys Technology Centre (ITC) in Lyon. Building on a long-experiences of thermomechanical characterisation of refractory materials at TMC group, the present project was specifically focused on the development of numerical tools to investigate the relationship between refractory microstructure and thermomechanical properties.

Over the past decades, the TMC group has developed extensive expertise in the evaluation of the thermomechanical behaviour of industrial refractories and in the optimisation of their microstructures for improved high-temperature performance. Notable contributions include the works of Grasset-Bourdel, 2011; Kakroudi, 2007; Peruzzi, 2000; Tessier-Doyen, 2003 and Khlifi, 2019. These studies demonstrated that refractory materials commonly contain pre-existing damage originating from mismatches in the coefficients of thermal expansion (CTE) between their constitutive phases or between two neighbouring grains. This damage manifests either as decohesion, defined as the separation of boundaries between neighbouring grains or at matrix-inclusion interfaces, or as microcracks developed radially around inclusions or grains (Tessier-Doyen et al., 2006). In parallel, the ITC Refractory team has accumulated several years of experimental expertise aimed at improving the sustainability and performance of refractory materials under industrial conditions, by providing pertinent raw minerals to refractory producers.

In addition to these experimental efforts, and leveraging its own rich experimental database together with a forward-looking numerical vision, the TMC group initiated complementary developments in numerical modelling, in which experimental data played a central role in the validation of newly developed simulation methods. These efforts span from the early work of Grasset-Bourdel, 2011 to the more recent contributions of Asadi, 2021, encompassing a total of four PhD projects. Collectively, these studies have significantly advanced the understanding of refractory behaviour across multiple length scales by developing original numerical methods, from the component scale using the Finite Element Method (FEM) to the microstructural scale using the Discrete Element Method (DEM). In this strategical way from FEM to DEM, substantial advances have been already achieved, such as the simulation of microcracking due to CTE mismatch in materials exhibiting isotropic CTE (André et al., 2017; Nguyen, 2019), the introduction of microcracks via Weibull-based distributions to investigate macroscopic response (Asadi, 2021), and the modelling of non-linear mechanical behaviour (Asadi, 2021; Nguyen, 2019). Based on these previous works, the aim of the present PhD was to integrate both aspects: considering firstly the consequences of CTE mismatch (including anisotropy) during cooling in the generation of pre-existing microcracks, and analysing secondly how these microcrack network evolves later with an external load (purely mechanical).

Thus, the objective of the present PhD project was to further investigate the relationship between refractory microstructure and thermomechanical properties. Building on the success of the experimentally driven modelling strategy developed at TMC, the ITC Refractory team adopted and supported the same approach with the aim to better understand the potential effect of their raw minerals. Within the framework of the present PhD project, the specific experimental data from the previous works of Mouiya, 2024 were employed as validation of advanced numerical modelling. In particular, it focuses on simulating microcrack initiation and propagation induced by mismatches in the CTE among multiple constituents within refractory microstructures, using a DEM approach. In particular, existing studies lack robust modelling of anisotropic CTE at the microstructural scale for predicting microcrack evolution under thermal loading (Kakroudi et al., 2008; Mouiya et al., 2026).

License CC BY-NC-ND 4.0

This PhD project aims to address this remaining knowledge gap by developing novel DEM tool that is capable of capturing microstructural micromechanics and linking them to macroscopic thermomechanical behaviour.

In this context, and among the various numerical approaches available to investigate the interplay between microstructure and thermomechanical properties (Huger et al., 2011), DEM was identified as particularly well suited to represent the key physical mechanisms governing refractory behaviour, including CTE mismatch, thermally induced stresses, and microcrack initiation and propagation (André et al., 2017; Asadi, 2021; Longchamp et al., 2024; Nguyen, 2019). Based on the state-of-the-art review presented in **Chapter I**, the DEM, more specifically, the Bonded Particle Element Method (BPEM) combined with an advanced contact law (iDLSM), was selected as the numerical framework for this work (André et al., 2019; André & Celigueta, 2023). This approach enables the explicit introduction of thermal stresses and microcracking at the microstructural scale, thereby allowing the simulation of macroscopic nonlinear mechanical behaviour arising from microstructural damage and crack evolution.

Next, to simulate these microstructural aspects and its corresponding mechanical response, further advancements were required in the iDLSM approach such as anisotropic thermal expansion modelling, crack closure managements and thermomechanical coupling integrated with Periodic Boundary Condition (PBC) (Ranganathan et al., 2025). **Chapter II** provides a detailed description of these enhancements and demonstrates the applicability of the iDLSM approach (André & Celigueta, 2023) for the refractory application by testing these features using hypothetical refractory materials.

With these numerical developments in place, the next step was to verify and validate the DEM tool using experimental data to satisfy the research objectives such as, to evaluate the effect of anisotropic CTE, the role of porosity, and the behavior of composite material embedding anisotropic aggregates. Therefore, appropriate materials have to be chosen as model systems for the simulations. **Chapter III** reviews several industrial refractory systems with the aim of identifying such materials. Based on this assessment, aluminium titanate and alumina-aluminium titanate composites (Mouiya, 2024) were selected as suitable model materials. **Chapter III** also introduces the corresponding thermomechanical framework and outlines the overall research strategy for the PhD.

Once the model materials were identified, the specific research objectives such as effect of anisotropic CTE, the role of porosity, and the behavior of an anisotropic material used as an aggregate were addressed in **Chapter IV** to **Chapter VI**.

Chapter IV introduces the virtual laboratory framework and examines the effect of anisotropic CTE mismatch in polycrystalline microstructures, which constitutes the primary objective of this chapter. This configuration was selected as the most suitable setup for isolating the effects of anisotropic thermal expansion. The study presents the procedure used to generate virtual polycrystalline samples. These samples are then employed to demonstrate the influence of anisotropic CTE mismatch on the formation and propagation of microcrack networks during a thermal treatment process analogous to industrial sintering processes. The samples are subjected to numerical thermo-mechanical tests to assess the impact of microstructural cracks on macroscopic properties such as Dilatometry results, Young’s modulus and stress-strain response. In addition, a micromechanical characterization is conducted using thermal stress and crack statistics related to microstructural characteristics such as crystallographic axes. Furthermore, the study examines preferential crack orientations, the nature of cracking (intergranular versus transgranular), and

License CC BY-NC-ND 4.0

whether cracks occur as isolated events or as interconnected networks, all as functions of temperature (Ranganathan et al., 2025, 2026).

Chapter V then investigates the role of porosity by comparing dense and porous aluminium titanate microstructures. This system was taken to understand the contribution of pores on the macroscopic thermomechanical properties. Similar to **Chapter IV**, this chapter includes a dedicated strategy for embedding pores into the sample and applies the same thermomechanical characterization and micromechanical investigations. Finally, **Chapter VI** extends this comprehensive thermomechanical and micromechanical characterization to a composite model material and systematically investigates the influence of inclusions, taking into account its volume fraction, on microcracks and overall thermomechanical behavior.

Taken together, the studies presented in this thesis highlight both the similarities and the differences in the behaviour of dense polycrystalline, porous polycrystalline, and composite microstructures.

Regarding the similarities, across all microstructures, the iDLSM framework consistently captures microcrack initiation and propagation driven by local CTE mismatch. It is important to note that, in dense and porous polycrystalline samples, these mismatches arise between neighbouring grains (Mouiya, Tessier-Doyen, et al., 2023), whereas in composite systems they occur at the matrix-inclusion interfaces (Mouiya et al., 2026). In all cases, key material parameters such as CTE and failure strength, governs the onset and evolution of microcracking. Grain boundaries systematically act as preferential sites for thermal stress concentration, promoting crack formation due to CTE mismatch. Microcracks are generally oriented perpendicular to directions associated with the largest CTE mismatches (Bruno et al., 2010). Each crack occurrence (initiated by local tension) leads obviously to a gap between two surfaces of this crack, promoting microstructural expansion. In the same way, the release of this local tension when crack propagate during external loading contributes to the development of an irreversible strain (pseudo-plasticity). Furthermore, all samples exhibit a reduction in mechanical strength and an increase in strain to rupture at room temperature. Overall, these results confirm a strong link between microcrack density, microscopic thermal stress distribution, and the macroscopic nonlinear mechanical response, which are essential properties for the material sustainability in front of thermal shocks.

Regarding the differences, one important distinction was observed from the thermal stress statistical study. In polycrystalline systems (see Figure V-8), microcracking relieves both tensile and compressive stresses, whereas in composites the stress release is predominantly compressive (see Figure VI-14). This contrast becomes evident when comparing Figure V-8 and Figure VI-14. Another important point of comparison is the crack statistics. In the polycrystalline samples, cracks were observed in three forms: transgranular (traversing through grains), intergranular (propagating along grain boundaries), and intragranular (forming and propagating within individual grains). In contrast, in the composite microstructures, only intergranular and intragranular cracks were present. Moreover, in composites, the majority of cracks were oriented radially around the inclusions, following specific directions related to the local crystallography of the inclusions, and forming a complex crack network within the matrix (see Figure VI-19). By comparison, the polycrystalline microstructures exhibited anisotropic crack patterns (see Figure IV-24), reflecting directional preferences in crack propagation associated with the local crystallography of the monocrystals. Consequently, both the preferential orientation and the spatial distribution of cracks differed markedly between polycrystalline and composite microstructures.

License CC BY-NC-ND 4.0

Moreover, cracks formed during cooling may exist either as microcracks or as decohesion, as discussed earlier. Distinguishing between microcracks (associated with CTE mismatch, $\Delta\alpha > 0$) and decohesion (associated with CTE mismatch, $\Delta\alpha < 0$) is essential for optimizing refractory microstructures, as these damage modes originate from different mechanisms and have distinct implications for performance and design (Tessier-Doyen et al., 2006). Microcracks, typically intragranular or short intergranular cracks driven by thermal expansion mismatch and crystallographic anisotropy, can, in some cases, be beneficial. They may help relieve thermal stresses and improve thermal shock resistance, albeit at the expense of stiffness and strength (Kakroudi et al., 2008; M. G. Kakroudi et al., 2009; Mouiya et al., 2026). In contrast, decohesion refers to debonding at grain boundaries, matrix-aggregate interfaces, or phase boundaries. It primarily reflects weak interfaces, directly impairs load transfer, promotes crack coalescence into macrocracks, and significantly facilitates slag penetration (Boccaccini et al., 2005; Chotard et al., 2008).

If these damage modes are not distinguished in the analysis, it becomes impossible to determine whether failure is governed by bulk phase properties or by interface quality, and appropriate design strategies cannot be identified. Microcrack-dominated behaviour calls for control of phase composition (Chotard et al., 2019), CTE matching (Grasset-Bourdel et al., 2012), grain size (Boateng et al., 2025), texture, and the development of microcrack-tolerant matrices (Mouiya, 2024). By contrast, decohesion-dominated behaviour requires improvements in interface chemistry, bonding strength, and microstructural gradation (Chen et al., 2021; Sarkar, 2020). Therefore, separating crack statistics into microcracks and decohesion is a prerequisite for the rational microstructural optimization of refractory materials subjected to thermal cycling.

With this in mind, crack statistics analysed in relation to local crystallography (see Figure IV-21 and Figure VI-17) can be employed to distinguish between microcracking and decohesion. In composite microstructures, this distinction is relatively straightforward due to the clear separation of crack statistics associated with the matrix, inclusions, and interfaces, as well as the known driving CTE mismatch ($\Delta\alpha > 0$ or $\Delta\alpha < 0$) governing crack development. In contrast, in polycrystalline samples, segregating crack statistics into microcracks and decohesion is considerably more challenging, owing to the presence of multiple randomly oriented grains, which makes it difficult to determine whether crack initiation is driven by $\Delta\alpha > 0$ or $\Delta\alpha < 0$.

It is therefore of interest to compare the evolution of the macroscopic Young's modulus (see Figure V-6 and Figure VI-10) with temperature for the three microstructures in the presence of microcracking. As discussed earlier, all samples develop microcracks during cooling as a result of CTE mismatch. However, the volume of microcracks plays a key role in governing the macroscopic Young's modulus. In the composite samples, results from the study on the effect of inclusion volume fraction (see Figure VI-10) show that the inclusion content strongly influences the volume of microcracks, which in turn affects the evolution of the macroscopic Young's modulus with temperature. Consequently, both the inclusion volume fraction and the associated microcrack volume contribute to the observed changes in Young's modulus. By contrast, in the polycrystalline samples, although the pore volume fraction affects the macroscopic Young's modulus (see Figure V-6) in the undamaged state, its influence becomes negligible once microcracking develops. In this regime, the macroscopic Young's modulus is governed primarily by the volume of microcracks, which becomes the dominant controlling parameter.

These trends are also reflected in the macroscopic stress-strain responses of the three microstructural models. For this purpose, the results obtained in cyclic loading is being employed. Microcrack accumulation during the mechanical test promotes nonlinear behaviour in all cases. It

License CC BY-NC-ND 4.0

seems that porous samples exhibit higher nonlinearity than dense samples (see Figure V-14). This probably indicates that pores introduce additional flexibility in porous sample. In addition, the composite sample exhibits non-linearity (see Figure VI-23) but regarding which is much flexible, whether a porous or composite, could not be addressed from these results. In addition, the unloading path differs between material systems: the polycrystalline samples unload almost linearly (Figure V-14), whereas composite samples show a nonlinear unloading trajectory at room temperature (Figure VI-23). Lastly, it is observed that the porous sample exhibits irreversible strain much earlier than dense samples, especially at 1200 °C (see Figure V-14a).

In summary, the studies carried out within this PhD project have improved understanding of the relationship between microstructure and thermomechanical properties in selected model materials. The same methodological principles established here can be now extended to analyse more complex industrial refractories (Huger et al., 2011).

Despite the significant advances achieved in this PhD project, substantial opportunities remain for further improvement and extension of the proposed framework. Several promising perspectives can be envisaged at this stage. As a priority for future work, further developments should focus on the following key directions:

- **Integration of more realistic microstructural features and geometries**
  A major perspective concerns the incorporation of more realistic microstructural features and geometries. The current framework relies on simplified representations, including equiaxed grains and spherical pores or inclusions, which do not fully capture the complexity of real refractory microstructures. Enhancing microstructural realism through high-fidelity reconstructions, using direct digitisation from tomography (a scale above 1µm) (Razavi et al., 2024)or FIB-SEM images (for a scale below 1µm) (Longchamp et al., 2024), would significantly strengthen the link between numerical simulations and actual material behaviour. In addition, AI-based synthetic microstructure generation could be today considered as an interesting new route to move a step forward in achieving more ideal microstructure designs. In addition, integrating experimentally derived crystallographic information, particularly local grain orientations obtained from EBSD (Mouiya et al., 2024), would allow more accurate prediction of anisotropic thermomechanical responses. Future studies should also consider non-equiaxed grain morphologies, non-spherical pore shapes, polydisperse inclusion sizes, and multiscale pore architectures in which micro- and meso-sized pores coexist. Together, these improvements would substantially enhance the applicability of the iDLSM framework for microstructure-driven optimisation and predictive design of refractory materials.

  It is also extremely important to mention that, despite the present numeral study was based on aluminum titanate model materials (polycrystalline system or aluminum titanate monocrystals embedded in fine alumina matrix), this work should now be transposed to other raw minerals which could be advantageously used to improve thermomechanical property of other industrial refractory materials. In that perspective, as already mentioned in the **Chapter III**, andalusite-based refractory materials, polycrystalline alumina with large grains or white fused alumina aggregates (constituted of large monocrystals) have already been documented to exhibit interesting thermomechanical properties to face thermal shocks (Boateng et al., 2025; M. G. Kakroudi et al., 2009). The very interesting iDLSM framework developed during the present work could be here advantageously used to revisit the microstructure design of these materials in order to optimize a step further their thermomechanical properties.

License CC BY-NC-ND 4.0

- **Enhancement of material modelling through mechanical anisotropy**
  Although anisotropic thermal expansion is already incorporated into the current model, the mechanical behaviour is still assumed to be isotropic. A natural extension of the framework is therefore the introduction of mechanical elastic anisotropy. Representing elastic properties in tensorial form, for example, using an orthorhombic stiffness tensor for aluminium titanate, would provide a more faithful description of crystallographic anisotropy. Such an enhancement would allow a more accurate assessment of its influence on crack initiation, crack trajectory, and macroscopic thermomechanical behaviour.

  The macroscopic apparent elastic stiffness tensor can be determined experimentally using techniques such as ultrasonic wave-velocity measurements(Tessier-Doyen et al., 2006). In fact, at the local scale of individual crystals, the elastic stiffness tensor is quite difficult to determine, particularly at high temperatures. As soon as the crystal structure is well known, sophisticated computational methods (such as VASP) can, in principle, be employed to estimate this tensor. Nevertheless, for aluminium titanate, the elastic stiffness tensor has not yet been unambiguously determined. Consequently, its precise definition lies beyond the scope of this thesis.
- **Grain boundary specific tensile strengths to represent microstructural heterogeneity**
  Another important perspective involves improving the representation of microstructural heterogeneity by assigning grain-boundary-specific tensile strengths within the enhanced iDLSM framework. In real polycrystalline materials, grain boundaries exhibit widely varying mechanical resistance depending on factors such as crystallographic misorientation, boundary character, local chemistry, and defect content (Boateng et al., 2025; Mouiya, 2024). In contrast, current iDLSM implementations typically assign uniform tensile strengths to all interface bonds, which does not reflect this intrinsic variability. A natural extension of the model would be to introduce microstructure-informed bond strength assignments along grain boundaries. This could be achieved either by directly mapping experimentally measured or synthetic microstructures, such as EBSD-based grain maps (Boateng et al., 2025; Mouiya, 2024), onto the lattice and correlating boundary character with tensile strength, or by prescribing statistically distributed tensile strengths drawn from calibrated probability distributions that reflect experimentally observed scatter in grain-boundary strength (Asadi, André, Emam, Doumalin, & Huger, 2022). Such an approach would improve the model's ability to capture preferential crack paths, mixed intergranular-transgranular fracture modes, and size effects arising from microstructural heterogeneity.

  However, incorporating grain-boundary-specific tensile strengths into the iDLSM framework induce experimental challenges. In fact, direct measurement of the mechanical resistance of individual grain boundaries requires sophisticated small-scale testing techniques (e.g., micro-cantilever (Shimada & Tatami, 2025), micro-pillar (Basak et al., 2019), or bicrystal fracture (Grosso et al., 2020) experiments) combined with high-resolution EBSD to characterize boundary misorientation, plane orientation, and local chemistry (Callister Jr & Rethwisch, 2020). Such measurements are time-consuming, highly sensitive to specimen preparation, and typically limited to a small subset of boundary types, making it difficult to obtain statistically representative strength distributions.
- **Improved representation of energy dissipation mechanisms**
  To date, limited attention has been paid to how energy is physically dissipated during crack initiation and propagation within iDLSM simulations. From a theoretical standpoint, fracture is governed by an energy balance between the elastic strain energy stored in the material and the energy required to nucleate and propagate cracks. This energy consumption

License CC BY-NC-ND 4.0

includes the creation of new free surfaces (thermodynamic fracture surface energy) as well as additional irreversible processes such as pseudo-plasticity, microcracking, heat dissipation, and frictional sliding along crack faces (Rice & Pohanka, 1979; Sakai & Bradt, 1986). While ideally brittle materials are dominated by surface creation, real materials exhibit substantial additional dissipation, leading to an effective macroscopic fracture energy. In current iDLSM formulations, however, the surface energy associated with bond rupture is not explicitly isolated and is often entangled with artificial numerical damping introduced to control dynamic oscillations. In contrast, frictional dissipation along crack surfaces can be treated more transparently through local Coulomb-type friction laws. A key perspective for future work is therefore to refine the enhanced iDLSM framework such that numerical damping is minimised and treated purely as a numerical stabilisation tool, while all physically meaningful energy losses, bond breaking, frictional sliding, and other irreversible mechanisms, are explicitly computed and stored during simulations. With such improvements, cyclic loading-unloading strategies could be used to compute macroscopic fracture energy directly from the simulated energy balance and to relate iDLSM parameters more directly to experimentally measured fracture toughness (Sakai & Bradt, 1986).

- **Energy-based fracture criteria for bond failure**
  Finally, the local fracture criterion in the enhanced iDLSM framework could be reformulated using an energy-based approach at the bond level. In existing implementations, bond failure is typically governed by stress-based thresholds (primarily mode-I), whereby a bond breaks once a critical tensile stress or opening displacement is exceeded. While computationally convenient, such criteria do not provide a direct link between local failure and macroscopic fracture energy. A more physically transparent alternative would be to assign each bond a critical fracture energy and to trigger rupture when the elastic energy stored in the bond, computed from its force-displacement response, reaches this critical value. Within this framework, grain-interior and grain-boundary bonds could be assigned distinct critical energies consistent with their respective mechanical roles and target fracture energies. The energy dissipated by bond breaking could then be directly interpreted as a contribution to macroscopic fracture energy. When coupled with explicit tracking of frictional dissipation, this approach would establish a clearer and more direct connection between local failure mechanisms in the enhanced iDLSM and experimentally measured fracture toughness.

These improvements in the iDLSM approach with two-scale analysis will lead to more accurate refractory models. This will help to better understand how microstructure influences thermomechanical macroscopic behaviour. The modelling tools can be used to optimise material microstructure design. They can also provide useful guidance for experimental investigations. This approach can reduce raw material use and experimental effort. It can also speed up decision-making compared to current practices and promote more efficient use of natural resources.

License CC BY-NC-ND 4.0

Bibliography

A. Oliveira Mendes, H. Leão, S. Castro, & R. Pitangueira. (2024). Machine Learning aided Phase-Field Method in Constitutive Modeling of Concrete Structures. *Ibero-Latin American Congress on Computational Methods in Engineering (CILAMCE)*. https://doi.org/10.55592/cilamce.v6i06.10405

Adibaskoro, T., Bordas, S., Sołowski, W. T., & Hostikka, S. (2024). Multiple discrete crack initiation and propagation in Material Point Method. *Engineering Fracture Mechanics*, *301*, 109918. https://doi.org/10.1016/j.engfracmech.2024.109918

Aksel, C., & Warren, P. D. (2003). Work of fracture and fracture surface energy of magnesia-spinel composites. *Composites Science and Technology*, *63*(10), 1433–1440. https://doi.org/10.1016/S0266-3538(03)00085-X

Alekseeva, L. S., Nokhrin, A. V., Karazanov, K. O., Orlova, A. I., Boldin, M. S., Lantsev, E. A., Murashov, A. A., & Chuvil'deev, V. N. (2022). Mechanical Properties and Thermal Shock Resistance of Fine-Grained Nd:YAG/SiC Ceramics. *Inorganic Materials*, *58*(2), 199–204. https://doi.org/10.1134/S0020168522020017

Alhajj Hassan, G., Leclerc, W., Pélegris, C., Guessasma, M., & Bellenger, E. (2020). On the suitability of a 3D discrete element method to model the composite damage induced by thermal expansion mismatch. *Computational Particle Mechanics*, *7*(4), 679–698. https://doi.org/10.1007/s40571-019-00298-1

Aliabadi, M. H., & Brebbia, C. A. (2025). Boundary element formulations in fracture mechanics: a review. *WIT Transactions on Engineering Sciences*.

Ambati, M., Gerasimov, T., & De Lorenzis, L. (2015). A review on phase-field models of brittle fracture and a new fast hybrid formulation. *Computational Mechanics*, *55*(2), 383–405. https://doi.org/10.1007/s00466-014-1109-y

Andersson, C. A. (1996). Derivation of the Exponential Relation for the Effect of Ellipsoidal Porosity on Elastic Modulus. *Journal of the American Ceramic Society*, *79*(8), 2181–2184. https://doi.org/10.1111/j.1151-2916.1996.tb08955.x

André, D., & Celigueta, M. A. (2023). A DEM bonded particle model compatible with stress/strain constitutive relations. *International Journal of Rock Mechanics and Mining Sciences*, *170*, 105437. https://doi.org/10.1016/j.ijrmms.2023.105437

André, D., Charles, J., & Iordanoff, I. (2015). *3D Discrete Element Workbench for Highly Dynamic Thermo-Mechanical Analysis: GranOO*. Wiley. https://doi.org/10.1002/9781119116356

André, D., Girardot, J., & Hubert, C. (2019). A novel DEM approach for modeling brittle elastic media based on distinct lattice spring model. *Computer Methods in Applied Mechanics and Engineering*, *350*, 100–122. https://doi.org/10.1016/j.cma.2019.03.013

André, D., Iordanoff, I., Charles, J., & Néauport, J. (2012). Discrete element method to simulate continuous material by using the cohesive beam model. *Computer Methods in Applied Mechanics and Engineering*, *213–216*, 113–125. https://doi.org/10.1016/j.cma.2011.12.002

André, D., Levraut, B., Tessier-Doyen, N., & Huger, M. (2017). A discrete element thermo-mechanical modelling of diffuse damage induced by thermal expansion mismatch of two-phase materials. *Computer Methods in Applied Mechanics and Engineering*, *318*, 898–916. https://doi.org/10.1016/j.cma.2017.01.029

License CC BY-NC-ND 4.0

Angenault, J. (2001). *Symétrie [et] structure: cristallochimie du solide: cours & exercices corrigés: premier et deuxième cycles universitaires*.

Asadi, F. (2021). *Micro-mechanical modelling of heterogeneous materials containing microcracks with Discrete Element Method (DEM)*. http://www.theses.fr/2021LIMO0046/document

Asadi, F., André, D., Emam, S., Doumalin, P., & Huger, M. (2022). Numerical modelling of the quasi-brittle behaviour of refractory ceramics by considering microcracks effect. *Journal of the European Ceramic Society*, *42*(3), 1149–1161. https://doi.org/10.1016/j.jeurceramsoc.2021.11.016

Asadi, F., André, D., Emam, S., Doumalin, P., & Huger, M. (2023). Advances in micro-mechanical modeling using a bonded-particle model and periodic homogenization within discrete element framework applied to heterogeneous ceramics. *Journal of the European Ceramic Society*, *43*(3), 1205–1219. https://doi.org/10.1016/j.jeurceramsoc.2022.10.073

Asadi, F., André, D., Emam, S., Doumalin, P., Khlifi, I., & Huger, M. (2022). Investigation of different discrete modeling strategies to mimic microstructural aspects that influence the fracture energy of refractory materials. *Open Ceramics*, *11*, 100288. https://doi.org/10.1016/j.oceram.2022.100288

Asbury, J. J. (1975). *Aluminum titanate crucible for molten uranium*.

Ashizuka, M., Ishida, E., Matsushita, T., & Hisanaga, M. (2002). Elastic Modulus, Strength and Fracture Toughness of Alumina Ceramics Containing Pores. *Journal of the Ceramic Society of Japan*, *110*(1282), 554–559. https://doi.org/10.2109/jcersj.110.554

Austin, A. E., & Schwartz, C. M. (1953). The crystal structure of aluminium titanate. *Acta Crystallographica*, *6*(10), 812–813. https://doi.org/10.1107/S0365110X53002374

Babelot, C., Guignard, A., Huger, M., Gault, C., Chotard, T., Ota, T., & Adachi, N. (2011). Preparation and thermomechanical characterisation of aluminum titanate flexible ceramics. *Journal of Materials Science*, *46*(5), 1211–1219. https://doi.org/10.1007/s10853-010-4897-2

Backhaus-Ricoult, M., Glose, C., Tepesch, P., Wheaton, B., & Zimmermann, J. (2010). *Aluminum Titanate Composites for Diesel Particulate Filter Applications* (pp. 147–164). https://doi.org/10.1002/9780470944028.ch15

Bae, I., & Baik, S. (1997). Abnormal Grain Growth of Alumina. *Journal of the American Ceramic Society*, *80*(5), 1149–1156. https://doi.org/10.1111/j.1151-2916.1997.tb02957.x

Barclay, P. L., & Zhang, D. Z. (2021). Periodic boundary conditions for arbitrary deformations in molecular dynamics simulations. *Journal of Computational Physics*, *435*, 110238. https://doi.org/10.1016/j.jcp.2021.110238

Barenblatt, G. I. (1962). *The Mathematical Theory of Equilibrium Cracks in Brittle Fracture* (pp. 55–129). https://doi.org/10.1016/S0065-2156(08)70121-2

Basak, A. K., Pramanik, A., & Prakash, C. (2019). Deformation and strengthening of SiC reinforced Al-MMCs during in-situ micro-pillar compression. *Materials Science and Engineering: A*, *763*, 138141. https://doi.org/10.1016/j.msea.2019.138141

Bauer, W. F. (1958). The Monte Carlo Method. *Journal of the Society for Industrial and Applied Mathematics*, *6*(4), 438–451. https://doi.org/10.1137/0106028

Bayer, G. (1971). Thermal expansion characteristics and stability of pseudobrookite-type compounds, Me3O5. *Journal of the Less Common Metals*, *24*(2), 129–138. https://doi.org/10.1016/0022-5088(71)90091-9

License CC BY-NC-ND 4.0

Bazazzadeh, S., Mossaiby, F., & Shojaei, A. (2020). An adaptive thermo-mechanical peridynamic model for fracture analysis in ceramics. *Engineering Fracture Mechanics*, *223*, 106708. https://doi.org/10.1016/j.engfracmech.2019.106708

Becher, P. F., Fuller, E. R., & Angelini, P. (1991). Journal. Matrix-Grain-Bridging Contributions to the Toughness of Whisker-Reinforced Ceramics. *Journal of the American Ceramic Society*, *74*(9), 2131–2135. https://doi.org/10.1111/j.1151-2916.1991.tb08271.x

Belytschko, T., & Black, T. (1999). Elastic crack growth in finite elements with minimal remeshing. *International Journal for Numerical Methods in Engineering*, *45*(5), 601–620. https://doi.org/10.1002/(SICI)1097-0207(19990620)45:5<601::AID-NME598>3.0.CO;2-S

Benedetti, I. (2023). An integral framework for computational thermo-elastic homogenization of polycrystalline materials. *Computer Methods in Applied Mechanics and Engineering*, *407*, 115927. https://doi.org/10.1016/j.cma.2023.115927

Benedetti, I., & Aliabadi, M. H. (2013). A three-dimensional cohesive-frictional grain-boundary micromechanical model for intergranular degradation and failure in polycrystalline materials. *Computer Methods in Applied Mechanics and Engineering*, *265*, 36–62. https://doi.org/10.1016/j.cma.2013.05.023

Benedetti, I., & Aliabadi, M. H. (2015). Multiscale modeling of polycrystalline materials: A boundary element approach to material degradation and fracture. *Computer Methods in Applied Mechanics and Engineering*, *289*, 429–453. https://doi.org/10.1016/j.cma.2015.02.018

Biswas, S., & Sarkar, D. (2020). *Introduction to Refractories for Iron- and Steelmaking*. Springer International Publishing. https://doi.org/10.1007/978-3-030-43807-4

Boateng, K. A., Kaczmarek, R. P., Auvray, J.-M., Wöhrmeyer, C., Thune, E., Tessier-Doyen, N., & Huger, M. (2025). Influence of tabular and white fused alumina aggregates on Young's modulus evolution versus temperature in refractory castables. *Journal of the European Ceramic Society*, *45*(15), 117583. https://doi.org/10.1016/j.jeurceramsoc.2025.117583

Boccaccini, D. N., Leonelli, C., Rivasi, M. R., Romagnoli, M., & Boccaccini, A. R. (2005). Microstructural investigations in cordierite–mullite refractories. *Ceramics International*, *31*(3), 417–432. https://doi.org/10.1016/j.ceramint.2004.06.005

Bolander, J. E., Shiraishi, T., & Isogawa, Y. (1996). An adaptive procedure for fracture simulation in extensive lattice networks. *Engineering Fracture Mechanics*, *54*(3), 325–334. https://doi.org/10.1016/0013-7944(95)00200-6

Branko Savija, & Erik Schlangen. (2015). *On the Use of a Lattice Model for Analyzing of In-Plane Vibration of Thin Plates* (Vol. 48). Tech Science Press.

Braulio, M. A. L., Bittencourt, L. R. M., & Pandolfelli, V. C. (2008). Magnesia grain size effect on in situ spinel refractory castables. *Journal of the European Ceramic Society*, *28*(15), 2845–2852. https://doi.org/10.1016/j.jeurceramsoc.2008.05.014

Brisard, S., Bertin, M., & Legoll, F. (2023). A variance reduction strategy for numerical random homogenization based on the equivalent inclusion method. *Computer Methods in Applied Mechanics and Engineering*, *417*, 116389. https://doi.org/10.1016/j.cma.2023.116389

Brown, W. F., & Srawley, J. E. (1966). Plane Strain Crack Toughness Testing of High Strength Metallic Materials. In *Plane Strain Crack Toughness Testing of High Strength Metallic Materials* (pp. 1–129). ASTM International100 Barr Harbor Drive, PO Box C700, West Conshohocken, PA 19428-2959. https://doi.org/10.1520/STP44663S

License CC BY-NC-ND 4.0

Bruno, G., Efremov, A. M., Wheaton, B. R., & Webb, J. E. (2010). Microcrack orientation in porous aluminum titanate. *Acta Materialia*, *58*(20), 6649–6655. https://doi.org/10.1016/j.actamat.2010.08.027

Bruno, G., & Kachanov, M. (2013). On modeling of microstresses and microcracking generated by cooling of polycrystalline porous ceramics. *Journal of the European Ceramic Society*, *33*(10), 1995–2005. https://doi.org/10.1016/j.jeurceramsoc.2013.02.023

Bruno, G., & Kachanov, M. (2016). Microstructure–Property Connections for Porous Ceramics: The Possibilities Offered by Micromechanics. *Journal of the American Ceramic Society*, *99*(12), 3829–3852. https://doi.org/10.1111/jace.14624

Buessem, W. R., Thielke, N. R., & Sarakauskas, R. V. (1952). Thermal expansion hysteresis of aluminum titanate. *Ceram.*, 38–40.

Buljak, V., & Bruno, G. (2018). Numerical modeling of thermally induced microcracking in porous ceramics: An approach using cohesive elements. *Journal of the European Ceramic Society*, *38*(11), 4099–4108. https://doi.org/10.1016/j.jeurceramsoc.2018.03.041

Buscaglia, V., Nanni, P., Battilana, G., Aliprandi, G., & Carry, C. (1994). Reaction sintering of aluminium titanate: I—Effect of MgO addition. *Journal of the European Ceramic Society*, *13*(5), 411–417. https://doi.org/10.1016/0955-2219(94)90018-3

Cabezas-Rodriguez, R., Ciria, D., Martinez-Fernandez, J., Dezanneau, G., Karolak, F., & Ramirez-Rico, J. (2022). High temperature mechanical properties of polycrystalline Y2SiO5. *Boletín de La Sociedad Española de Cerámica y Vidrio*, *61*, S60–S68. https://doi.org/10.1016/j.bsecv.2021.09.008

Callister Jr, W. D., & Rethwisch, D. G. (2020). *Materials science and engineering: an introduction*. John wiley & sons.

Cascio, M. Lo, Gulizzi, V., Milazzo, A., & Benedetti, I. (2024). A Model for Polycrystalline Thermo-Mechanical Homogenisation and Micro-Cracking. *Procedia Structural Integrity*, *52*, 618–624. https://doi.org/10.1016/j.prostr.2023.12.063

Case, E. D., Smyth, J. R., & Hunter, O. (1981). Microcracking in Large-grain Al2O3. *Materials Science and Engineering*, *51*(2), 175–179. https://doi.org/10.1016/0025-5416(81)90193-2

Cavuoto, R., Lenarda, P., Tampieri, A., Bigoni, D., & Paggi, M. (2024). Phase-field modelling of failure in ceramics with multiscale porosity. *Materials & Design*, *238*, 112708. https://doi.org/10.1016/j.matdes.2024.112708

Celigueta, M. A., Latorre, S., Arrufat, F., & Oñate, E. (2017). Accurate modelling of the elastic behavior of a continuum with the Discrete Element Method. *Computational Mechanics*, *60*(6), 997–1010. https://doi.org/10.1007/s00466-017-1453-9

Chaudhuri, S. P., & Sircar, N. R. (1981). Design Criteria of Efficient Refractories for Energy Conservation. *Transactions of the Indian Ceramic Society*, *40*(1), 12–20. https://doi.org/10.1080/0371750X.1981.10822512

Chen, C., Müller, B. R., Prinz, C., Stroh, J., Feldmann, I., & Bruno, G. (2020). The correlation between porosity characteristics and the crystallographic texture in extruded stabilized aluminium titanate for diesel particulate filter applications. *Journal of the European Ceramic Society*, *40*(4), 1592–1601. https://doi.org/10.1016/j.jeurceramsoc.2019.11.076

Chen, C.-H., & Awaji, H. (2007). Temperature dependence of mechanical properties of aluminum titanate ceramics. *Journal of the European Ceramic Society*, *27*(1), 13–18. https://doi.org/10.1016/j.jeurceramsoc.2006.04.182

License CC BY-NC-ND 4.0

Chen, H., Jiao, Y., & Liu, Y. (2016). A nonlocal lattice particle model for fracture simulation of anisotropic materials. *Composites Part B: Engineering*, *90*, 141–151. https://doi.org/10.1016/j.compositesb.2015.12.028

Chen, H., Lin, E., Jiao, Y., & Liu, Y. (2014). A generalized 2D non-local lattice spring model for fracture simulation. *Computational Mechanics*, *54*(6), 1541–1558. https://doi.org/10.1007/s00466-014-1075-4

Chen, L.-Q., & Wang, Y. (1996). The continuum field approach to modeling microstructural evolution. *JOM*, *48*(12), 13–18. https://doi.org/10.1007/BF03223259

Chen, W., Shui, A., Shan, Q., Lian, J., Wang, C., & Li, J. (2021). The influence of different additives on microstructure and mechanical properties of aluminum titanate ceramics. *Ceramics International*, *47*(1), 1169–1176. https://doi.org/10.1016/j.ceramint.2020.08.234

Chen, Z., Yan, W., Schafföner, S., Dai, Y., Wang, Q., & Li, G. (2020). A novel approach to lightweight alumina-carbon refractories for flow control of molten steel. *Journal of the American Ceramic Society*, *103*(8), 4713–4724. https://doi.org/10.1111/jace.17137

Cheon, Y., & Kim, H. (2019). An adaptive material point method coupled with a phase-field fracture model for brittle materials. *International Journal for Numerical Methods in Engineering*, *120*(8), 987–1010. https://doi.org/10.1002/nme.6167

Chotard, T., Arbelaez Morales, L., Bouchetou, M.-L., & Poirier, J. (2019). Thermomechanical Characterisation of Mullite Zirconia Composites Sintered from Andalusite for High Temperature Applications. *Ceramics*, *2*(4), 587–601. https://doi.org/10.3390/ceramics2040046

Chotard, T., Soro, J., Lemercier, H., Huger, M., & Gault, C. (2008). High temperature characterisation of cordierite–mullite refractory by ultrasonic means. *Journal of the European Ceramic Society*, *28*(11), 2129–2135. https://doi.org/10.1016/j.jeurceramsoc.2008.02.029

Christian, M., Françoise, L. P., & Ludovic, A. (2015). A least-squares coupling method between a finite element code and a discrete element code. *International Journal for Numerical Methods in Engineering*, *101*(10), 731–743. https://doi.org/10.1002/nme.4822

Clayton, J. D., & Knap, J. (2015). Phase field modeling of directional fracture in anisotropic polycrystals. *Computational Materials Science*, *98*, 158–169. https://doi.org/10.1016/j.commatsci.2014.11.009

Cleveland, J. J., & Bradt, R. C. (1978). Grain Size/Microcracking Relations for Pseudobrookite Oxides. *Journal of the American Ceramic Society*, *61*(11–12), 478–481. https://doi.org/10.1111/j.1151-2916.1978.tb16121.x

Coble, R. L., & Kingery, W. D. (1955). Effect of Porosity on Thermal Stress Fracture. *Journal of the American Ceramic Society*, *38*(1), 33–37. https://doi.org/10.1111/j.1151-2916.1955.tb14549.x

Coetzee, C., & Katterfeld, A. (2023). Calibration of <scp>DEM</scp> Parameters. In *Simulations in Bulk Solids Handling* (pp. 1–40). Wiley. https://doi.org/10.1002/9783527835935.ch1

Cundall, P. A. (1988). *Computer Simulations of Dense Sphere Assemblies* (pp. 113–123). https://doi.org/10.1016/B978-0-444-70523-5.50021-7

Cundall, P. A., & Strack, O. D. L. (1979). A discrete numerical model for granular assemblies. *Géotechnique*, *29*(1), 47–65. https://doi.org/10.1680/geot.1979.29.1.47

Cunha-Duncan, F. N., & Bradt, R. C. (2003). Fratura de refratários. *Cerâmica*, *49*(312), 199–215. https://doi.org/10.1590/S0366-69132003000400003

License CC BY-NC-ND 4.0

Cusatis, G., Bažant, Z. P., & Cedolin, L. (2003). Confinement-Shear Lattice Model for Concrete Damage in Tension and Compression: I. Theory. *Journal of Engineering Mechanics*, *129*(12), 1439–1448. https://doi.org/10.1061/(ASCE)0733-9399(2003)129:12(1439)

Cusatis, G., Mencarelli, A., Pelessone, D., & Baylot, J. T. (2008). Lattice Discrete Particle Model (LDPM) for Fracture Dynamics and Rate Effect in Concrete. *Structures Congress 2008*, 1–11. https://doi.org/10.1061/41000(315)42

da Luz A, Braulio M, & Pandolfelli V. (2015). *Refractory castable engineering*. Göller Verlag is publisher of Refractories Worldforum and Journal of Ceramic Science and Technology.

Daux, C., Moes, N., Dolbow, J., Sukumar, N., & Belytschko, T. (2000). Arbitrary branched and intersecting cracks with the extended finite element method. *International Journal for Numerical Methods in Engineering*, *48*(12), 1741–1760. https://doi.org/10.1002/1097-0207(20000830)48:12<1741::AID-NME956>3.0.CO;2-L

de Carvalho Bonaldo, J. C. (2022). *Modélisation du lien entre microstructure, traitement thermomécanique et performance mécanique de produits réfractaires*. http://www.theses.fr/2022GRALI008/document

De Meo, D., Zhu, N., & Oterkus, E. (2016). Peridynamic Modeling of Granular Fracture in Polycrystalline Materials. *Journal of Engineering Materials and Technology*, *138*(4). https://doi.org/10.1115/1.4033634

dell'Isola, F., Della Corte, A., Esposito, R., & Russo, L. (2016). *Some Cases of Unrecognized Transmission of Scientific Knowledge: From Antiquity to Gabrio Piola's Peridynamics and Generalized Continuum Theories* (pp. 77–128). https://doi.org/10.1007/978-3-319-31721-2_5

Doncieux, A., Ninomiya, K., Ishizawa, N., & Ota, T. (2017). *Structural Basis for the Anisotropic Thermal Expansion of Aluminum Titanate, Al2TiO5, at Elevated Temperatures*. Nagoya Institute of Technology.

Doncieux, A., Stagnol, D., Huger, M., Chotard, T., Gault, C., Ota, T., & Hashimoto, S. (2008). Thermo-elastic behaviour of a natural quartzite: itacolumite. *Journal of Materials Science*, *43*(12), 4167–4174. https://doi.org/10.1007/s10853-007-2414-z

Drago, A., & Pindera, M. (2007). Micro-macromechanical analysis of heterogeneous materials: Macroscopically homogeneous vs periodic microstructures. *Composites Science and Technology*, *67*(6), 1243–1263. https://doi.org/10.1016/j.compscitech.2006.02.031

Du, Q., Faber, V., & Gunzburger, M. (1999). Centroidal Voronoi Tessellations: Applications and Algorithms. *SIAM Review*, *41*(4), 637–676. https://doi.org/10.1137/S0036144599352836

Du, W., & Jin, S. (2022). Discrete Element Modelling of Cold Crushing Tests Considering Various Interface Property Distributions in Ordinary Refractory Ceramics. *Materials*, *15*(21), 7650. https://doi.org/10.3390/ma15217650

Du, W., Jin, S., & Gruber, D. (2024). Determination of the influence of particle spatial distribution and interface heterogeneity on tensile fracture of ordinary refractory ceramics by applying discrete element modelling. *Computational Particle Mechanics*, *11*(5), 1887–1901. https://doi.org/10.1007/s40571-024-00716-z

Dugdale, D. S. (1960). Yielding of steel sheets containing slits. *Journal of the Mechanics and Physics of Solids*, *8*(2), 100–104. https://doi.org/10.1016/0022-5096(60)90013-2

Eshelby, J. D. (1957). The determination of the elastic field of an ellipsoidal inclusion, and related problems. *Proceedings of the Royal Society of London. Series A. Mathematical and Physical Sciences*, *241*(1226), 376–396. https://doi.org/10.1098/rspa.1957.0133

License CC BY-NC-ND 4.0

Espinosa, H., & Zavattieri, P. (2003a). A grain level model for the study of failure initiation and evolution in polycrystalline brittle materials. Part I: Theory and numerical implementation. *Mechanics of Materials*, *35*(3–6), 333–364. https://doi.org/10.1016/S0167-6636(02)00285-5

Espinosa, H., & Zavattieri, P. (2003b). A grain level model for the study of failure initiation and evolution in polycrystalline brittle materials. Part II: Numerical examples. *Mechanics of Materials*, *35*(3–6), 365–394. https://doi.org/10.1016/S0167-6636(02)00287-9

Evans, A. G. (1978). Microfracture from thermal expansion anisotropy—I. Single phase systems. *Acta Metallurgica*, *26*(12), 1845–1853. https://doi.org/10.1016/0001-6160(78)90097-4

Farukh, F., Zhao, L. G., Jiang, R., Reed, P., Proprentner, D., & Shollock, B. A. (2016). Realistic microstructure-based modelling of cyclic deformation and crack growth using crystal plasticity. *Computational Materials Science*, *111*, 395–405. https://doi.org/10.1016/j.commatsci.2015.09.054

Fasching, C., Gruber, D., & Harmuth, H. (2015). Simulation of micro-crack formation in a magnesia spinel refractory during the production process. *Journal of the European Ceramic Society*, *35*(16), 4593–4601. https://doi.org/10.1016/j.jeurceramsoc.2015.08.012

Fei, Y. (2013). *Thermal Expansion* (pp. 29–44). https://doi.org/10.1029/RF002p0029

Fertig, R. S., & Nickerson, S. T. (2016). Towards Prediction of Thermally Induced Microcrack Initiation and Closure in Porous Ceramics. *Journal of the American Ceramic Society*, *99*(2), 581–588. https://doi.org/10.1111/jace.13981

Firooz, S., Saeb, S., Chatzigeorgiou, G., Meraghni, F., Steinmann, P., & Javili, A. (2019). Systematic study of homogenization and the utility of circular simplified representative volume element. *Mathematics and Mechanics of Solids*, *24*(9), 2961–2985. https://doi.org/10.1177/1081286518823834

Freudenberg, B., & Mocellin, A. (1988). Aluminum Titanate Formation by Solid-State Reaction of Coarse Al2O3 and TiO2 Powders. *Journal of the American Ceramic Society*, *71*(1), 22–28. https://doi.org/10.1111/j.1151-2916.1988.tb05755.x

Fruhstorfer, J., & Gruber, D. (2023). A methodology for performing and evaluating miniaturized wedge splitting tests accompanied by digital image correlation. *Engineering Fracture Mechanics*, *288*, 109357. https://doi.org/10.1016/j.engfracmech.2023.109357

Fu, L., Zou, Y., Huang, A., Gu, H., & Ni, H. (2019). Corrosion mechanism of lightweight microporous alumina-based refractory by molten steel. *Journal of the American Ceramic Society*, *102*(6), 3705–3714. https://doi.org/10.1111/jace.16205

Fu, M., & Zhao, G.-F. (2022). A micro-macro constitutive model for compressive failure of rock by using 4D lattice spring model. *International Journal of Rock Mechanics and Mining Sciences*, *160*, 105261. https://doi.org/10.1016/j.ijrmms.2022.105261

Gabriela Rezende Fernandes, Guilherme Bassi da Silva Pontes, & Vitor Nascimento Oliveira. (2024). Multiscale Modelling of the Two-Dimensional Problem Using the Boundary Element Method. *Ibero-Latin American Congress on Computational Methods in Engineering (CILAMCE)*. https://doi.org/10.55592/cilamce.v6i06.8176

Gao, Z., Zimmerman, J. W., & Kachanov, M. (2013). On microstructural mechanisms causing non-linear stress-strain behavior of porous ceramics under tension. *International Journal of Fracture*, *183*(2), 283–288. https://doi.org/10.1007/s10704-013-9892-6

License CC BY-NC-ND 4.0

Garrard, J. M., & Abedi, R. (2020). Statistical volume element averaging scheme for fracture of quasi-brittle materials. *Computers and Geotechnics*, *117*, 103229. https://doi.org/10.1016/j.compgeo.2019.103229

Geraci, G., & Aliabadi, M. H. (2017). Micromechanical boundary element modelling of transgranular and intergranular cohesive cracking in polycrystalline materials. *Engineering Fracture Mechanics*, *176*, 351–374. https://doi.org/10.1016/j.engfracmech.2017.03.016

Geraci, G., & Aliabadi, M. H. (2018). Micromechanical modelling of cohesive thermoelastic cracking in orthotropic polycrystalline materials. *Computer Methods in Applied Mechanics and Engineering*, *339*, 567–590. https://doi.org/10.1016/j.cma.2018.05.011

Geraci, G., & Aliabadi, M. H. (2019). Micromechanical modeling of cohesive thermoelastic steady-state and transient cracking in polycrystalline materials. *International Journal for Numerical Methods in Engineering*, *117*(12), 1205–1233. https://doi.org/10.1002/nme.5997

Gilman, J. J. (1960). Direct Measurements of the Surface Energies of Crystals. *Journal of Applied Physics*, *31*(12), 2208–2218. https://doi.org/10.1063/1.1735524

Glandus, J. C., & Boch, P. (1984). Main testing methods for thermal shock. *Interceram*, *33*(5), 33–37.

Gostick, J., Khan, Z., Tranter, T., Kok, M., Agnaou, M., Sadeghi, M., & Jervis, R. (2019). PoreSpy: A Python Toolkit for Quantitative Analysis of Porous Media Images. *Journal of Open Source Software*, *4*(37), 1296. https://doi.org/10.21105/joss.01296

Grasset-Bourdel, R. (2011). *Structure/property relations of magnesia-spinel refractories : experimental determination and simulation*. http://www.theses.fr/2011LIMO4050

Grasset-Bourdel, R., Alzina, A., Huger, M., Chotard, T., Emler, R., Gruber, D., & Harmuth, H. (2013). Tensile behaviour of magnesia-spinel refractories: Comparison of tensile and wedge splitting tests. *Journal of the European Ceramic Society*, *33*(5), 913–923. https://doi.org/10.1016/j.jeurceramsoc.2012.10.031

Grasset-Bourdel, R., Alzina, A., Huger, M., Gruber, D., Harmuth, H., & Chotard, T. (2012). Influence of thermal damage occurrence at microstructural scale on the thermomechanical behaviour of magnesia–spinel refractories. *Journal of the European Ceramic Society*, *32*(5), 989–999. https://doi.org/10.1016/j.jeurceramsoc.2011.10.048

Griffith, A. A. (1921). VI. The phenomena of rupture and flow in solids. *Philosophical Transactions of the Royal Society of London. Series A, Containing Papers of a Mathematical or Physical Character*, *221*(582–593), 163–198. https://doi.org/10.1098/rsta.1921.0006

Grosso, R. L., Muccillo, E. N. S., Muche, D. N. F., Jawaharram, G. S., Barr, C. M., Monterrosa, A. M., Castro, R. H. R., Hattar, K., & Dillon, S. J. (2020). In Situ Transmission Electron Microscopy for Ultrahigh Temperature Mechanical Testing of ZrO_2. *Nano Letters*, *20*(2), 1041–1046. https://doi.org/10.1021/acs.nanolett.9b04205

Gu, X., Li, X., Xia, X., Madenci, E., & Zhang, Q. (2023). A robust peridynamic computational framework for predicting mechanical properties of porous quasi-brittle materials. *Composite Structures*, *303*, 116245. https://doi.org/10.1016/j.compstruct.2022.116245

Guéguen, Y., & Kachanov, M. (2011). *Effective Elastic Properties of Cracked Rocks — An Overview* (pp. 73–125). https://doi.org/10.1007/978-3-7091-0939-7_3

Gulizzi, V., & Benedetti, I. (2016). Micro-cracking of brittle polycrystalline materials with initial damage. *European Journal of Computational Mechanics*, *25*(1–2), 38–53. https://doi.org/10.1080/17797179.2016.1181032

License CC BY-NC-ND 4.0

Gulizzi, V., Milazzo, A., & Benedetti, I. (2015). An enhanced grain-boundary framework for computational homogenization and micro-cracking simulations of polycrystalline materials. *Computational Mechanics*, *56*(4), 631–651. https://doi.org/10.1007/s00466-015-1192-8

Gulizzi, V., Rycroft, C. H., & Benedetti, I. (2018). Modelling intergranular and transgranular micro-cracking in polycrystalline materials. *Computer Methods in Applied Mechanics and Engineering*, *329*, 168–194. https://doi.org/10.1016/j.cma.2017.10.005

Guthrie, R. I. L., & Isac, M. M. (2022). Continuous Casting Practices for Steel: Past, Present and Future. *Metals*, *12*(5), 862. https://doi.org/10.3390/met12050862

Harmuth, H. (1995). Stability of crack propagation associated with fracture energy determined by wedge splitting specimen. *Theoretical and Applied Fracture Mechanics*, *23*(1), 103–108. https://doi.org/10.1016/0167-8442(95)00008-3

Hashin, Z., & Shtrikman, S. (1963). A variational approach to the theory of the elastic behaviour of multiphase materials. *Journal of the Mechanics and Physics of Solids*, *11*(2), 127–140. https://doi.org/10.1016/0022-5096(63)90060-7

Hasselman, D. P. H. (1963). Elastic Energy at Fracture and Surface Energy as Design Criteria for Thermal Shock. *Journal of the American Ceramic Society*, *46*(11), 535–540. https://doi.org/10.1111/j.1151-2916.1963.tb14605.x

Hasselman, D. P. H. (1967). Approximate Theory of Thermal Stress Resistance of Brittle Ceramics Involving Creep. *Journal of the American Ceramic Society*, *50*(9), 454–457. https://doi.org/10.1111/j.1151-2916.1967.tb15160.x

Hasselman, D. P. H. (1969). Unified Theory of Thermal Shock Fracture Initiation and Crack Propagation in Brittle Ceramics. *Journal of the American Ceramic Society*, *52*(11), 600–604. https://doi.org/10.1111/j.1151-2916.1969.tb15848.x

Hasselman, D. P. H. (1985). Thermal stress resistance of engineering ceramics. *Materials Science and Engineering*, *71*, 251–264. https://doi.org/10.1016/0025-5416(85)90235-6

Herrmann, H. J., Hansen, A., & Roux, S. (1989). Fracture of disordered, elastic lattices in two dimensions. *Physical Review B*, *39*(1), 637–648. https://doi.org/10.1103/PhysRevB.39.637

Hill, R. (1952). The Elastic Behaviour of a Crystalline Aggregate. *Proceedings of the Physical Society. Section A*, *65*(5), 349–354. https://doi.org/10.1088/0370-1298/65/5/307

Hill, R. (1963). Elastic properties of reinforced solids: Some theoretical principles. *Journal of the Mechanics and Physics of Solids*, *11*(5), 357–372. https://doi.org/10.1016/0022-5096(63)90036-X

Hillerborg, A., Modéer, M., & Petersson, P.-E. (1976). Analysis of crack formation and crack growth in concrete by means of fracture mechanics and finite elements. *Cement and Concrete Research*, *6*(6), 773–781. https://doi.org/10.1016/0008-8846(76)90007-7

Hirata, Y., Itoh, S., Shimonosono, T., & Sameshima, S. (2016). Theoretical and experimental analyses of Young's modulus and thermal expansion coefficient of the alumina-mullite system. *Ceramics International*, *42*(15), 17067–17073. https://doi.org/10.1016/j.ceramint.2016.07.216

Hirata, Y., Takehara, K., & Shimonosono, T. (2017). Analyses of Young's modulus and thermal expansion coefficient of sintered porous alumina compacts. *Ceramics International*, *43*(15), 12321–12327. https://doi.org/10.1016/j.ceramint.2017.06.095

License CC BY-NC-ND 4.0

Honda, S., Ogihara, Y., Kishi, T., Hashimoto, S., & Iwamoto, Y. (2009). Estimation of thermal shock resistance of fine porous alumina by infrared radiation heating method. *Journal of the Ceramic Society of Japan*, *117*(1371), 1208–1215. https://doi.org/10.2109/jcersj2.117.1208

Hou, Q., Luo, X., An, D., & Xie, Z. (2022). Fabrication and analysis of lightweight magnesia refractories with micro-nanometer double pore size structure. *Journal of the Australian Ceramic Society*, *58*(2), 627–636. https://doi.org/10.1007/s41779-021-00680-4

Hrennikoff, A. (1941). Solution of Problems of Elasticity by the Framework Method. *Journal of Applied Mechanics*, *8*(4), A169–A175. https://doi.org/10.1115/1.4009129

Huger, M. (2019). *Deliverable D1. 3 Devices for Thermo-Physical Properties Characterisation*.

Huger, M. (2023). *CESAREF - Concerted European action on Sustainable Applications of REFractories*. EU Horizon Industrial Doctoral Network.

Huger, M., Derrick, G., Mouiya, M., Salerno, A., Boateng, K. A., Ranganathan, H., & Gope, A. (2024). How Marie Sklodowska-Curie Doctoral Networks Can Support European Refractory Ecosystem in Context of The European Green Deal. *China's Refractories*, *33*(2).

Huger, M., Ota, T., Tessier-Doyen, N., Michaud, P., & Chotard, T. (2011). Microstructural effects associated to CTE mismatch for enhancing the thermal shock resistance of refractories. *IOP Conference Series: Materials Science and Engineering*, *18*(22), 222002. https://doi.org/10.1088/1757-899X/18/22/222002

Huger, M., Tessier-Doyen, N., Chotard, T., & Gault, C. (2007). Microstructural effects associated to CTE mismatch for enhancing the thermal shock resistance of refractories: investigation by high temperature ultrasounds. *Ceramic Forum International*, *84*(9).

Hütter, M., & Tervoort, T. A. (2008). Continuum damage mechanics: combining thermodynamics with a thoughtful characterization of the microstructure. *Acta Mechanica*, *201*(1–4), 297–312. https://doi.org/10.1007/s00707-008-0064-0

Irving, W. R. (2024). *Continuous Casting of Steel*. CRC Press. https://doi.org/10.1201/9781003575849

Irwin, G. R. (1958). *Fracture* (pp. 551–590). https://doi.org/10.1007/978-3-642-45887-3_5

Jacques, S., De Baere, I., & Van Paepegem, W. (2014). Application of periodic boundary conditions on multiple part finite element meshes for the meso-scale homogenization of textile fabric composites. *Composites Science and Technology*, *92*, 41–54. https://doi.org/10.1016/j.compscitech.2013.11.023

Jain, A., Ong, S. P., Hautier, G., Chen, W., Richards, W. D., Dacek, S., Cholia, S., Gunter, D., Skinner, D., Ceder, G., & Persson, K. A. (2013). Commentary: The Materials Project: A materials genome approach to accelerating materials innovation. *APL Materials*, *1*(1). https://doi.org/10.1063/1.4812323

Janati, K. I. (2020). Thermo-elastic behavior study of rotary kilns for cement plants. *Engineering Failure Analysis*, *118*, 104896. https://doi.org/10.1016/j.engfailanal.2020.104896

Javili, A., Morasata, R., Oterkus, E., & Oterkus, S. (2019). Peridynamics review. *Mathematics and Mechanics of Solids*, *24*(11), 3714–3739. https://doi.org/10.1177/1081286518803411

Jebahi, M., André, D., Terreros, I., & Iordanoff, I. (2015). *Discrete Element Method to Model 3D Continuous Materials*. Wiley. https://doi.org/10.1002/9781119103042

License CC BY-NC-ND 4.0

Jiang, W. H., Jiang, Q. M., Liu, J. M., Zhu, Q. X., & Zhang, Q. (2012). Prepartion of Stabilized Aluminum Titanate Film via Nonhydrolytic Sol-Gel Route. *Advanced Materials Research*, *538–541*, 96–100. https://doi.org/10.4028/www.scientific.net/AMR.538-541.96

Joliff, Y., Absi, J., Glandus, J. C., Huger, M., & Tessier-Doyen, N. (2007). Experimental and numerical study of the thermomechanical behaviour of refractory model materials. *Journal of the European Ceramic Society*, *27*(2–3), 1513–1520. https://doi.org/10.1016/j.jeurceramsoc.2006.04.031

Kachanov, M. (1992). Effective Elastic Properties of Cracked Solids: Critical Review of Some Basic Concepts. *Applied Mechanics Reviews*, *45*(8), 304–335. https://doi.org/10.1115/1.3119761

Kakouris, E. G., & Triantafyllou, S. P. (2017). Phase-field material point method for brittle fracture. *International Journal for Numerical Methods in Engineering*, *112*(12), 1750–1776. https://doi.org/10.1002/nme.5580

Kakroudi, M. G. (2007). *Comportement thermomécanique en traction de bétons réfractaires: influence de la nature des agrégats et de l'histoire thermique*.

Kakroudi, M. G., Huger, M., Gault, C., & Chotard, T. (2009). Anisotropic behaviour of andalusite particles used as aggregates on refractory castables. *Journal of the European Ceramic Society*, *29*(4), 571–579. https://doi.org/10.1016/j.jeurceramsoc.2008.07.043

Kakroudi, M. G., Yeugo-Fogaing, E., Gault, C., Huger, M., & Chotard, T. (2008). Effect of thermal treatment on damage mechanical behaviour of refractory castables: Comparison between bauxite and andalusite aggregates. *Journal of the European Ceramic Society*, *28*(13), 2471–2478. https://doi.org/10.1016/j.jeurceramsoc.2008.03.048

Kakroudi, Yeugo-Fogaing, E., Huger, M., Gault, C., & Chotard, T. (2009). Influence of the thermal history on the mechanical properties of two alumina based castables. *Journal of the European Ceramic Society*, *29*(15), 3197–3204. https://doi.org/10.1016/j.jeurceramsoc.2009.05.052

Kappmeyer, K. K., Russell, C. K., & Hubble, D. H. (1974). Refractories for continuous casting. *JOM*, *26*(7), 29–36. https://doi.org/10.1007/BF03355891

Kazemi, N. (2019). Reasons for crack propagation and strength loss in refractory castables based on changes in their chemical compositions and micromorphologies with heating: special focus on the large blocks. *Journal of Asian Ceramic Societies*, *7*(2), 109–126. https://doi.org/10.1080/21870764.2019.1597957

Khlifi, I. (2019). *Optimisation of optical methods for strain field measurements dedicated to the characterisation of the fracture behaviour of refractories : Application to magnesia based materials*. http://www.theses.fr/2019LIMO0123/document

Khoei, A. R. (2014). Extended finite element method: theory and applications. *John Wiley & Sons*.

Kikuchi, A., Kawai, T., & Suzuki, N. (1992). The rigid bodies—spring models and their applications to three-dimensional crack problems. *Computers & Structures*, *44*(1–2), 469–480. https://doi.org/10.1016/0045-7949(92)90269-6

Kim, I. J., Lee, K. S., & Aneziris, C. G. (2007). Crack Healing, Reopening and Thermal Expansion Behavior of Al2TiO5 Ceramics at High Temperature. *Key Engineering Materials*, *336–338*, 2448–2450. https://doi.org/10.4028/www.scientific.net/KEM.336-338.2448

Kim, K., Forest, B., & Geringer, J. (2011). Two-dimensional finite element simulation of fracture and fatigue behaviours of alumina microstructures for hip prosthesis. *Proceedings of the Institution of Mechanical Engineers, Part H: Journal of Engineering in Medicine*, *225*(12), 1158–1168. https://doi.org/10.1177/0954411911422843

License CC BY-NC-ND 4.0

Kingery, W. D. (1955). Factors Affecting Thermal Stress Resistance of Ceramic Materials. *Journal of the American Ceramic Society*, *38*(1), 3–15. https://doi.org/10.1111/j.1151-2916.1955.tb14545.x

Kingery, W. D., Bowen, H. K., Uhlmann, D. R., & Frieser, R. (1977). Introduction to Ceramics. *Journal of The Electrochemical Society*, *124*(3), 152C-152C. https://doi.org/10.1149/1.2133296

Kruggel-Emden, H., Simsek, E., Rickelt, S., Wirtz, S., & Scherer, V. (2007). Review and extension of normal force models for the Discrete Element Method. *Powder Technology*, *171*(3), 157–173. https://doi.org/10.1016/j.powtec.2006.10.004

Kuna, M. (2013). *Finite Elements in Fracture Mechanics* (Vol. 201). Springer Netherlands. https://doi.org/10.1007/978-94-007-6680-8

Kuna, M., & Roth, S. (2015). General remarks on cyclic cohesive zone models. *International Journal of Fracture*, *196*(1–2), 147–167. https://doi.org/10.1007/s10704-015-0053-y

Ladányi, G., & Gonda, V. (2021). Review of Peridynamics: Theory, Applications, and Future Perspectives. *Strojniški Vestnik – Journal of Mechanical Engineering*, *67*(12), 666–681. https://doi.org/10.5545/sv-jme.2021.7289

Lang, S. M., Fillmore, C. L., & Maxwell, L. H. (1952). The system beryllia-alumina-titania: phase relations and general physical properties of three-component porcelains. *Journal of Research of the National Bureau of Standards*, *48*(4), 298. https://doi.org/10.6028/jres.048.038

Leclerc, W., Haddad, H., & Guessasma, M. (2018). On a discrete element method to simulate thermal-induced damage in 2D composite materials. *Computers & Structures*, *196*, 277–291. https://doi.org/10.1016/j.compstruc.2017.10.008

Lee, W. E., & Moore, R. E. (1998). Evolution of in Situ Refractories in the 20th Century. *Journal of the American Ceramic Society*, *81*(6), 1385–1410. https://doi.org/10.1111/j.1151-2916.1998.tb02497.x

Lemaistre, H. (1998). *Etude des propriétés thermomécaniques de divers réfractaires*. http://www.theses.fr/1998ISAL0080

Lemaitre, S., Salnikov, V., Choi, D., & Karamian-Surville, P. (2016). *Influence of morphological parameters in 3D composite materials on their effective thermal properties and comparison with effective mechanical properties*.

Li, H., Zhang, H., Zhang, Y., Bai, X., Shao, X., & Wu, B. (2024). Coupled Non-Ordinary State-Based Peridynamics Model for Ductile and Brittle Solids Subjected to Thermal Shocks. *Applied Sciences*, *14*(16), 6927. https://doi.org/10.3390/app14166927

Li, X. F., Li, H. B., & Zhao, J. (2017). 3D polycrystalline discrete element method (3PDEM) for simulation of crack initiation and propagation in granular rock. *Computers and Geotechnics*, *90*, 96–112. https://doi.org/10.1016/j.compgeo.2017.05.023

Liang, Y., Zhang, X., & Liu, Y. (2021). Extended material point method for the three-dimensional crack problems. *International Journal for Numerical Methods in Engineering*, *122*(12), 3044–3069. https://doi.org/10.1002/nme.6653

Lilliu, G., & van Mier, J. G. M. (2003). 3D lattice type fracture model for concrete. *Engineering Fracture Mechanics*, *70*(7–8), 927–941. https://doi.org/10.1016/S0013-7944(02)00158-3

Lin, L., Wang, X., & Zeng, X. (2017). The role of cohesive zone properties on intergranular to transgranular fracture transition in polycrystalline solids. *International Journal of Damage Mechanics*, *26*(3), 379–394. https://doi.org/10.1177/1056789515618732

License CC BY-NC-ND 4.0

Litovsky, E., Gambaryan-Roisman, T., Shapiro, M., & Shavit, A. (1999). Effect of Grain Thermal Expansion Mismatch on Thermal Conductivity of Porous Ceramics. *Journal of the American Ceramic Society*, *82*(4), 994–1000. https://doi.org/10.1111/j.1151-2916.1999.tb01865.x

Liu, B., Li, P., Qi, J., Li, M., Chen, R., Li, S., Qi, G., & Ding, Y. (2024). Additive manufacturing of oriented steel fiber-reinforced mullite refractories for enhanced mechanical properties. *Construction and Building Materials*, *456*, 139301. https://doi.org/10.1016/j.conbuildmat.2024.139301

Liu, B., Wang, Y., & Li, C. (2023). Simulation of microscopic interface damage of ZrB2 based ceramics based on cohesive zone model. *Mechanics of Advanced Materials and Structures*, *30*(7), 1417–1425. https://doi.org/10.1080/15376494.2022.2033368

Liu, G., Zhou, D., Guo, J., Bao, Y., Han, Z., & Lu, J. (2018). Numerical simulation of fatigue crack propagation interacting with micro-defects using multiscale XFEM. *International Journal of Fatigue*, *109*, 70–82. https://doi.org/10.1016/j.ijfatigue.2017.12.012

Liu, J. X., Zhao, Z. Y., Deng, S. C., & Liang, N. G. (2008). Modified generalized beam lattice model associated with fracture of reinforced fiber/particle composites. *Theoretical and Applied Fracture Mechanics*, *50*(2), 132–141. https://doi.org/10.1016/j.tafmec.2008.07.006

Liu, T. S., & Perera, D. S. (1998). Long-term thermal stability and mechanical properties of aluminium titanate at 1000–1200°C. *Journal of Materials Science*, *33*(4), 995–1001. https://doi.org/10.1023/A:1004368029554

Liu, Y., Han, B., Zhang, T., Yu, H., Yan, W., Wei, Y., & Li, N. (2016). Effect of zirconia particle size on the properties of alumina-spinel castables. *Ceramics International*, *42*(15), 16961–16968. https://doi.org/10.1016/j.ceramint.2016.07.201

Liu, Y. J., Mukherjee, S., Nishimura, N., Schanz, M., Ye, W., Sutradhar, A., Pan, E., Dumont, N. A., Frangi, A., & Saez, A. (2011). Recent Advances and Emerging Applications of the Boundary Element Method. *Applied Mechanics Reviews*, *64*(3). https://doi.org/10.1115/1.4005491

Liu, Y., Wu, X., Guo, Q., Jiang, C., Song, F., & Li, J. (2015a). Experiments and numerical simulations of thermal shock crack patterns in thin circular ceramic specimens. *Ceramics International*, *41*(1), 1107–1114. https://doi.org/10.1016/j.ceramint.2014.09.036

Liu, Y., Wu, X., Guo, Q., Jiang, C., Song, F., & Li, J. (2015b). Experiments and numerical simulations of thermal shock crack patterns in thin circular ceramic specimens. *Ceramics International*, *41*(1), 1107–1114. https://doi.org/10.1016/j.ceramint.2014.09.036

Longchamp, V., Girardot, J., André, D., Malaise, F., Quet, A., Carles, P., & Iordanoff, I. (2024). Discrete 3D modeling of porous-cracked ceramic at the microstructure scale. *Journal of the European Ceramic Society*, *44*(4), 2522–2536. https://doi.org/10.1016/j.jeurceramsoc.2023.11.026

Luo, Y., Gu, H., Zhang, M., Huang, A., Li, H., Yu, C., Li, T., & Yan, P. (2020). Research on thermal shock resistance of porous refractory material by strain-life fatigue approach. *Ceramics International*, *46*(10), 14884–14893. https://doi.org/10.1016/j.ceramint.2020.03.015

Ma, Q., Liu, X., Song, D., Wang, E., Zhang, J., Yao, W., & Wang, M. (2023). Thermal damage evolution of granite under different thermal conditions based on two-scale tessellation via discrete element method. *Geomechanics and Geophysics for Geo-Energy and Geo-Resources*, *9*(1), 169. https://doi.org/10.1007/s40948-023-00711-3

License CC BY-NC-ND 4.0

Mahéo, L., Grolleau, V., & Rio, G. (2009). Damping efficiency of the Tchamwa–Wielgosz explicit dissipative scheme under instantaneous loading conditions. *Comptes Rendus. Mécanique*, *337*(11–12), 722–732. https://doi.org/10.1016/j.crme.2009.10.005

Mariotti, C., Michaut, V., & Molinari, J. F. (2009). Modeling of the fragmentation by Discrete Element Method. *DYMAT 2009 - 9th International Conferences on the Mechanical and Physical Behaviour of Materials under Dynamic Loading*, 1523–1528. https://doi.org/10.1051/dymat/2009215

Merlani, E., Schmid, C., & Sergo, V. (2001). Residual Stresses in Alumina/Zirconia Composites: Effect of Cooling Rate and Grain Size. *Journal of the American Ceramic Society*, *84*(12), 2962–2968. https://doi.org/10.1111/j.1151-2916.2001.tb01121.x

Miehe, C., Schänzel, L.-M., & Ulmer, H. (2015). Phase field modeling of fracture in multi-physics problems. Part I. Balance of crack surface and failure criteria for brittle crack propagation in thermo-elastic solids. *Computer Methods in Applied Mechanics and Engineering*, *294*, 449–485. https://doi.org/10.1016/j.cma.2014.11.016

Mityushev, V. (2015a). Random 2D Composites and the Generalized Method of Schwarz. *Advances in Mathematical Physics*, *2015*, 1–15. https://doi.org/10.1155/2015/535128

Mityushev, V. (2015b). *Random composites and the generalized method of Schwarz I. Conductivity problems*.

Miyaji, D. Y., Tonnesen, T., & Rodrigues, J. A. (2014). Fracture energy and thermal shock damage resistance of refractory castables containing eutectic aggregates. *Ceramics International*, *40*(9), 15227–15239. https://doi.org/10.1016/j.ceramint.2014.06.112

Mocciaro, A., Cimas, A., Rendtorff, N. M., & Scian, A. N. (2022). Mullite macro-needles for reinforcement of refractory castables. *Cerâmica*, *68*(388), 420–426. https://doi.org/10.1590/0366-69132022683883342

Moes, N., Dolbow, J., & Belytschko, T. (1999). A finite element method for crack growth without remeshing. *International Journal for Numerical Methods in Engineering*, *46*(1), 131–150. https://doi.org/10.1002/(SICI)1097-0207(19990910)46:1<131::AID-NME726>3.0.CO;2-J

Morosin, B., & Lynch, R. W. (1972). Structure studies on Al2TiO5 at room temperature and at 600°C. *Acta Crystallographica Section B Structural Crystallography and Crystal Chemistry*, *28*(4), 1040–1046. https://doi.org/10.1107/S0567740872003681

Morrison, C. N., Jivkov, A. P., Vertyagina, Ye., & Marrow, T. J. (2016). Multi-scale modelling of nuclear graphite tensile strength using the site-bond lattice model. *Carbon*, *100*, 273–282. https://doi.org/10.1016/j.carbon.2015.12.100

Morrison, C. N., Zhang, M., Jivkov, A. P., & Yates, J. R. (2014). Discrete Lattice Model of Quasi-Brittle Fracture in Porous Graphite. *Materials Performance and Characterization*, *3*(3), 414–428. https://doi.org/10.1520/MPC20130077

Mouiya, M. (2024). *Thermomechanical properties of refractory materials, influence of the diffuse microcracking*. http://www.theses.fr/2024LIMO0066/document

Mouiya, M., Bouazizi, A., Abourriche, A., El Khessaimi, Y., Benhammou, A., El hafiane, Y., Taha, Y., Oumam, M., Abouliatim, Y., Smith, A., & Hannache, H. (2019). Effect of sintering temperature on the microstructure and mechanical behavior of porous ceramics made from clay and banana peel powder. *Results in Materials*, *4*, 100028. https://doi.org/10.1016/j.rinma.2019.100028

License CC BY-NC-ND 4.0

Mouiya, M., Martynyuk, M., Kupsch, A., Laquai, R., Müller, B. R., Tessier Doyen, N., Tamraoui, Y., Serrano-Munoz, I., Huger, M., Kachanov, M., & Bruno, G. (2023). The stress–strain behavior of refractory microcracked aluminum titanate: The effect of zigzag microcracks and its modeling. *Journal of the American Ceramic Society*, *106*(11), 6995–7008. https://doi.org/10.1111/jace.19325

Mouiya, M., Tessier-Doyen, N., Tamraoui, Y., Alami, J., & Huger, M. (2023). High temperature thermomechanical properties of a microcracked model refractory material: A silica-doped aluminium titanate. *Ceramics International*, *49*(14), 24572–24580. https://doi.org/10.1016/j.ceramint.2023.01.027

Mouiya, M., Tessier-Doyen, N., Tamraoui, Y., Gruber, D., Dupré, J.-C., Doumalin, P., Alami, J., & Huger, M. (2026). Engineered microcracking in alumina/aluminum titanate composites: A pathway to enhance nonlinear mechanical behavior and fracture energy. *Journal of the European Ceramic Society*, *46*(5), 118046. https://doi.org/10.1016/j.jeurceramsoc.2025.118046

Mouiya, M., Tingaud, D., Tamraoui, Y., Thune, E., Tessier-Doyen, N., Guinebretière, R., Alami, J., & Huger, M. (2024). Crystallography and anisotropy of crystals shape in dense aluminum titanate ceramics. *Journal of the European Ceramic Society*, *44*(7), 4761–4771. https://doi.org/10.1016/j.jeurceramsoc.2024.01.090

Mubashar, A., Ashcroft, I. A., & Crocombe, A. D. (2014). Modelling Damage and Failure in Adhesive Joints Using A Combined XFEM-Cohesive Element Methodology. *The Journal of Adhesion*, *90*(8), 682–697. https://doi.org/10.1080/00218464.2013.826580

Mukhopadhyay, S., & Das Poddar, P. K. (2004). Effect of preformed and in situ spinels on microstructure and properties of a low cement refractory castable. *Ceramics International*, *30*(3), 369–380. https://doi.org/10.1016/S0272-8842(03)00117-2

Muneton Lopez, R. A. (2023). *A phase-field formulation for fracture modeling of quasi-brittle and rate-and temperature-dependent materials*.

Munro, R. G. (2004). Analytical representations of elastic moduli data with simultaneous dependence on temperature and porosity. *Journal of Research of the National Institute of Standards and Technology*, *109*(5), 497. https://doi.org/10.6028/jres.109.036

Nakayama, J. (1965). Direct Measurement of Fracture Energies of Brittle Heterogeneous Materials. *Journal of the American Ceramic Society*, *48*(11), 583–587. https://doi.org/10.1111/j.1151-2916.1965.tb14677.x

napari Work, H. D. (2019). *napari: A Multidimensional Image Viewer for Python A guide to some of the key concepts of napari*.

Nemaleu, J. G. D., à Moungam, L. M. B., Kamga Samen, V. E. L., Zenabou, N. Ndayou. M., Venyite, P., Kamseu, E., & Sglavo, V. M. (2023). Low-temperature high-strength lightweight refractory composites: Pore structures and insulating properties. *Ceramics International*, *49*(14), 23510–23521. https://doi.org/10.1016/j.ceramint.2023.04.184

Nguyen, C. T., Oterkus, S., & Oterkus, E. (2023). A peridynamic-based machine learning model for one-dimensional and two-dimensional structures. *Continuum Mechanics and Thermodynamics*, *35*(3), 741–773. https://doi.org/10.1007/s00161-020-00905-0

Nguyen, T. K., Combe, G., Caillerie, D., & Desrues, J. (2014). FEM × DEM modelling of cohesive granular materials: Numerical homogenisation and multi-scale simulations. *Acta Geophysica*, *62*(5), 1109–1126. https://doi.org/10.2478/s11600-014-0228-3

License CC BY-NC-ND 4.0

Nguyen, T. T. (2019). *Numerical modeling of microstructure-properties relationships of refractories : micro-mechanical approach with the discrete element method*. http://www.theses.fr/2019LIMO0089/document

Nguyen, T.-T., Réthoré, J., Yvonnet, J., & Baietto, M.-C. (2017). Multi-phase-field modeling of anisotropic crack propagation for polycrystalline materials. *Computational Mechanics*, *60*(2), 289–314. https://doi.org/10.1007/s00466-017-1409-0

Nikolić, M., Karavelić, E., Ibrahimbegovic, A., & Miščević, P. (2018). Lattice Element Models and Their Peculiarities. *Archives of Computational Methods in Engineering*, *25*(3), 753–784. https://doi.org/10.1007/s11831-017-9210-y

Nishikawa, T., Nakahima, A., Honda, S., & Awaji, H. (2001). Ceramic Materials. Effects of Porosity and Pore Morphology on Mechanical Properties of Porous Alumina. *Journal of the Society of Materials Science, Japan*, *50*(6), 625–629. https://doi.org/10.2472/jsms.50.625

Nitka, M., & Tejchman, J. (2020). Meso-mechanical modelling of damage in concrete using discrete element method with porous ITZs of defined width around aggregates. *Engineering Fracture Mechanics*, *231*, 107029. https://doi.org/10.1016/j.engfracmech.2020.107029

Nosewicz, S., Rojek, J., & Chmielewski, M. (2020). Discrete Element Framework for Determination of Sintering and Postsintering Residual Stresses of Particle Reinforced Composites. *Materials*, *13*(18), 4015. https://doi.org/10.3390/ma13184015

Öchsner, A. (2016). Continuum Damage Mechanics. In *Continuum Damage and Fracture Mechanics* (pp. 65–84). Springer Singapore. https://doi.org/10.1007/978-981-287-865-6_4

Ohin Mensan Daniel, Alexandra Doncieux, Carole Babelot, Alexandre Guignard, Toshitaka Ota, Nicolas Pradeilles, Marc Huger, & Thierry Chotard. (2014). Study of aluminum titanate (TiAl2O5) sintering and characterization of thermomechanical properties. *Matériaux*.

Ohya, Y., KAWAUCHI, Y., & BAN, T. (2017). Cation distribution of pseudobrookite-type titanates and their phase stability. *Journal of the Ceramic Society of Japan*, *125*(9), 695–700. https://doi.org/10.2109/jcersj2.17086

Ohya, Y., Nakagawa, Z., & Hamano, K. (1987). Grain-Boundary Microcracking Due to Thermal Expansion Anisotropy in Aluminum Titanate Ceramics. *Journal of the American Ceramic Society*, *70*(8). https://doi.org/10.1111/j.1151-2916.1987.tb05720.x

Ohya, Y., Nakagawa, Z., & Hamano, K. (1988). Crack Healing and Bending Strength of Aluminum Titanate Ceramics at High Temperature. *Journal of the American Ceramic Society*, *71*(5). https://doi.org/10.1111/j.1151-2916.1988.tb05064.x

Ortiz, M., & Suresh, S. (1993). Statistical Properties of Residual Stresses and Intergranular Fracture in Ceramic Materials. *Journal of Applied Mechanics*, *60*(1), 77–84. https://doi.org/10.1115/1.2900782

Pan, Z., Ma, R., Wang, D., & Chen, A. (2018). A review of lattice type model in fracture mechanics: theory, applications, and perspectives. *Engineering Fracture Mechanics*, *190*, 382–409. https://doi.org/10.1016/j.engfracmech.2017.12.037

Pandey, A., Shyam, A., Watkins, T. R., Lara-Curzio, E., Stafford, R. J., & Hemker, K. J. (2014). The Uniaxial Tensile Response of Porous and Microcracked Ceramic Materials. *Journal of the American Ceramic Society*, *97*(3), 899–906. https://doi.org/10.1111/jace.12720

Papanicolau, G., Bensoussan, A., & Lions, J. L. (1978). *Asymptotic analysis for periodic structures* (Vol. 5).

License CC BY-NC-ND 4.0

Park, K., & Paulino, G. H. (2011). Cohesive Zone Models: A Critical Review of Traction-Separation Relationships Across Fracture Surfaces. *Applied Mechanics Reviews*, *64*(6). https://doi.org/10.1115/1.4023110

Peray K. E, & Waddell J. J. (1986). *The rotary cement kiln*. Edward Arnold.

Peruzzi, S. (2000). *Simulation numerique du comportement thermomechanique de pieces refractaires due coulee continue*. University of limoges.

Phani, K. K., & Sanyal, D. (2008). The relations between the shear modulus, the bulk modulus and Young's modulus for porous isotropic ceramic materials. *Materials Science and Engineering: A*, *490*(1–2), 305–312. https://doi.org/10.1016/j.msea.2008.01.030

Pilli, V., & Sarkar, R. (2020). Carbon Sources for Alumina-Carbon Functional Refractories: An Overview. *Emerging Materials Research*, *9*(2), 1–10. https://doi.org/10.1680/jemmr.19.00118

Pöschel, T., & Schwager, T. (2005). (2005). *Pöschel, T., & Schwager, T. (2005). Computational granular dynamics: models and algorithms. Berlin, Heidelberg: Springer Berlin Heidelberg.* Springer-Verlag. https://doi.org/10.1007/3-540-27720-X_3

Potyondy, D. O. (2011). Parallel-bond refinements to match macroproperties of hard rock. *Continuum and Distinct Element Numerical Modeling in Geomechanics*, 459–465.

Potyondy, D. O., & Cundall, P. A. (2004). A bonded-particle model for rock. *International Journal of Rock Mechanics and Mining Sciences*, *41*(8), 1329–1364. https://doi.org/10.1016/j.ijrmms.2004.09.011

Prakash, V., Behera, A. K., & Rahaman, M. M. (2023). A phase-field model for thermo-mechanical fracture. *Mathematics and Mechanics of Solids*, *28*(2), 533–561. https://doi.org/10.1177/10812865221085198

Ranganathan, H., André, D., Mouiya, M., Huger, M., Soth, R., & Wöhrmeyer, C. (2025). A multiscale discrete element thermomechanical modeling approach of microcracking generated at high temperature by anisotropic thermal expansion in an elastic brittle polycrystalline ceramic material. *Engineering Fracture Mechanics*, *320*, 111088. https://doi.org/10.1016/j.engfracmech.2025.111088

Ranganathan, H., André, D., Mouiya, M., Huger, M., Soth, R., & Wöhrmeyer, C. (2026). Application of discrete element modelling to investigate microstructural effects of anisotropic thermal expansion in polycrystalline ceramics at high temperatures. *Journal of the European Ceramic Society*, *46*(4), 117985. https://doi.org/10.1016/j.jeurceramsoc.2025.117985

Rangel, R. L., Franci, A., Oñate, E., & Gimenez, J. M. (2024). Multiscale data-driven modeling of the thermomechanical behavior of granular media with thermal expansion effects. *Computers and Geotechnics*, *176*, 106789. https://doi.org/10.1016/j.compgeo.2024.106789

Razavi, A., Hopp, V., Hahn, D., Sax, A., & Quirmbach, P. (2024). Microstructural X-Ray Computed Tomography Investigation of the Defect Evolution in Refractory Castings Based on Andalusite. *Ceramics*, *7*(4), 1867–1879. https://doi.org/10.3390/ceramics7040117

Reuss, A. (1929). Berechnung der Fließgrenze von Mischkristallen auf Grund der Plastizitätsbedingung für Einkristalle . *ZAMM - Journal of Applied Mathematics and Mechanics / Zeitschrift Für Angewandte Mathematik Und Mechanik*, *9*(1), 49–58. https://doi.org/10.1002/zamm.19290090104

Ribeiro Gomes, M., Leber, T., Tillmann, T., Kenn, D., Gavagnin, D., Tonnesen, T., & Gonzalez-Julian, J. (2024). Towards H2 implementation in the iron- and steelmaking industry: State of

License CC BY-NC-ND 4.0

the art, requirements, and challenges for refractory materials. *Journal of the European Ceramic Society*, *44*(3), 1307–1334. https://doi.org/10.1016/j.jeurceramsoc.2023.10.044

Rice, R. W., & Pohanka, R. C. (1979). Grain-Size Dependence of Spontaneous Cracking in Ceramics. *Journal of the American Ceramic Society*, *62*(11–12), 559–563. https://doi.org/10.1111/j.1151-2916.1979.tb12730.x

Rigaud, M., Gault, C., Poirier, J., & Pirker, S. (2006). *FEDERATION FOR INTERNATIONAL REFRACTORY RESEARCH AND EDUCATION (FIRE)*. *1006*, 63-66.

Roesler, F. C. (1956). Brittle Fractures near Equilibrium. *Proceedings of the Physical Society. Section B*, *69*(10), 981–992. https://doi.org/10.1088/0370-1301/69/10/303

Roy, S. (2025). Thermal properties of porous ceramics. *Open Ceramics*, *24*, 100867. https://doi.org/10.1016/j.oceram.2025.100867

Rui, F., & Zhao, G.-F. (2022). Development of the four-dimensional lattice spring model for thermo-mechanical fracturing and large deformation of solids. *Engineering Analysis with Boundary Elements*, *138*, 390–406. https://doi.org/10.1016/j.enganabound.2022.03.011

Rycroft, C. (2009). *VORO++: A three-dimensional Voronoi cell library in C++*.

Sadd, M. H. (2019). *Continuum Mechanics Modeling of Material Behavior*. Elsevier. https://doi.org/10.1016/C2016-0-01495-X

Sakai, M., & Bradt, R. C. (1986). Graphical Methods for Determining the Nonlinear Fracture Parameters of Silica and Graphite Refractory Composites. In *Fracture Mechanics of Ceramics* (pp. 127–142). Springer US. https://doi.org/10.1007/978-1-4615-7023-3_10

Sakai, M., & Bradt, R. C. (1993). Fracture toughness testing of brittle materials. *International Materials Reviews*, *38*(2), 53–78. https://doi.org/10.1179/imr.1993.38.2.53

Sarkar, R. (2020). Binders for Refractory Castables: An Overview. *Interceram - International Ceramic Review*, *69*(4–5), 44–53. https://doi.org/10.1007/s42411-020-0112-x

Sarkar, R. (2023). *Refractory Technology*. CRC Press. https://doi.org/10.1201/9781003227854

Savchenko, N., Sevostyanova, I., Sablina, T., Gömze, L., & Kulkov, S. (2014). *The influence of porosity on the elasticity and strength of alumina and zirconia ceramics*. 547–550. https://doi.org/10.1063/1.4899003

Schlangen, E., & Garboczi, E. J. (1996). New method for simulating fracture using an elastically uniform random geometry lattice. *International Journal of Engineering Science*, *34*(10), 1131–1144. https://doi.org/10.1016/0020-7225(96)00019-5

Schneider, M., Josien, M., & Otto, F. (2021). *Representative volume elements for matrix-inclusion composites -- a computational study on periodizing the ensemble*.

Sfantos, G. K., & Aliabadi, M. H. (2007). A boundary cohesive grain element formulation for modelling intergranular microfracture in polycrystalline brittle materials. *International Journal for Numerical Methods in Engineering*, *69*(8), 1590–1626. https://doi.org/10.1002/nme.1831

Shan, Q., Chen, C., Xu, Q., Xue, Y., Ma, Q., Zhou, Y., & Shui, A. (2022). The influence of sintering temperature on the mechanical evolution of Al2TiO5 flexible ceramics based on the acoustic emission. *Journal of Alloys and Compounds*, *898*, 163004. https://doi.org/10.1016/j.jallcom.2021.163004

Shao, Y., Zhang, Y., Xu, X., Zhou, Z., Li, W., & Liu, B. (2011). Effect of Crack Pattern on the Residual Strength of Ceramics After Quenching. *Journal of the American Ceramic Society*, *94*(9), 2804–2807. https://doi.org/10.1111/j.1551-2916.2011.04728.x

License CC BY-NC-ND 4.0

Shiah, Y. C., & Tan, C. L. (2016). Thermoelastic analysis of 3D generally anisotropic bodies by the boundary element method. *European Journal of Computational Mechanics*, *25*(1–2), 91–108. https://doi.org/10.1080/17797179.2016.1181038

Shimada, K., & Tatami, J. (2025). Grain and grain boundary strength of silicon nitride ceramics with different thermal conductivities and microstructures. *Ceramics International*, *51*(17), 24306–24313. https://doi.org/10.1016/j.ceramint.2025.03.119

Shubin, V. I. (2001). Mechanical Effects on the Lining of Rotary Cement Kilns. *Refractories and Industrial Ceramics*, *42*(5–6), 245–250. https://doi.org/10.1023/A:1012354919912

Shyam, A., Bruno, G., Watkins, T. R., Pandey, A., Lara-Curzio, E., Parish, C. M., & Stafford, R. J. (2015). The effect of porosity and microcracking on the thermomechanical properties of cordierite. *Journal of the European Ceramic Society*, *35*(16), 4557–4566. https://doi.org/10.1016/j.jeurceramsoc.2015.08.014

Silling, S. A. (2000). Reformulation of elasticity theory for discontinuities and long-range forces. *Journal of the Mechanics and Physics of Solids*, *48*(1), 175–209. https://doi.org/10.1016/S0022-5096(99)00029-0

Sinaie, S., Heidarpour, A., & Zhao, X. L. (2016). A micro-mechanical parametric study on the strength degradation of concrete due to temperature exposure using the discrete element method. *International Journal of Solids and Structures*, *88–89*, 165–177. https://doi.org/10.1016/j.ijsolstr.2016.03.009

Skala, R. D., Li, D., & Low, I. M. (2009). Diffraction, structure and phase stability studies on aluminium titanate. *Journal of the European Ceramic Society*, *29*(1), 67–75. https://doi.org/10.1016/j.jeurceramsoc.2008.05.037

Smith, D. S., Alzina, A., Bourret, J., Nait-Ali, B., Pennec, F., Tessier-Doyen, N., Otsu, K., Matsubara, H., Elser, P., & Gonzenbach, U. T. (2013). Thermal conductivity of porous materials. *Journal of Materials Research*, *28*(17), 2260–2272. https://doi.org/10.1557/jmr.2013.179

Sridhar, N., Yang, W., Srolovitz, D. J., & Fuller, E. R. (1994). Microstructural Mechanics Model of Anisotropic-Thermal-Expansion-Induced Microcracking. *Journal of the American Ceramic Society*, *77*(5), 1123–1138. https://doi.org/10.1111/j.1151-2916.1994.tb05384.x

Steinbrech, R. W. (1992). Toughening mechanisms for ceramic materials. *Journal of the European Ceramic Society*, *10*(3), 131–142. https://doi.org/10.1016/0955-2219(92)90026-A

Studart, A. R., Gonzenbach, U. T., Tervoort, E., & Gauckler, L. J. (2006). Processing Routes to Macroporous Ceramics: A Review. *Journal of the American Ceramic Society*, *89*(6), 1771–1789. https://doi.org/10.1111/j.1551-2916.2006.01044.x

Sukumar, N., & Srolovitz, D. J. (2004). Finite element-based model for crack propagation in polycrystalline materials. *Computational & Applied Mathematics*, *23*, 363-380.

Sukumar, N., Srolovitz, D. J., Baker, T. J., & Prévost, J. -H. (2003). Brittle fracture in polycrystalline microstructures with the extended finite element method. *International Journal for Numerical Methods in Engineering*, *56*(14), 2015–2037. https://doi.org/10.1002/nme.653

Sulsky, D., Chen, Z., & Schreyer, H. L. (1994). A particle method for history-dependent materials. *Computer Methods in Applied Mechanics and Engineering*, *118*(1–2), 179–196. https://doi.org/10.1016/0045-7825(94)90112-0

License CC BY-NC-ND 4.0

Sun, F., Wang, G., Liu, D., Wang, R., Cao, C., Zhang, J., & Qing, Y. (2024). Explicit phase-field material point method for thermally induced fractures. *Theoretical and Applied Fracture Mechanics*, *133*, 104618. https://doi.org/10.1016/j.tafmec.2024.104618

Sun, F., Wang, G., Zhang, L., Wang, R., Cao, T., & Ouyang, X. (2021). Material point method for the propagation of multiple branched cracks based on classical fracture mechanics. *Computer Methods in Applied Mechanics and Engineering*, *386*, 114116. https://doi.org/10.1016/j.cma.2021.114116

Szczerba, J., Śnieżek, E., & Antonovič, V. (2017). Evolution of Refractory Materials for Rotary Cement Kiln Sintering Zone. *Refractories and Industrial Ceramics*, *58*(4), 426–433. https://doi.org/10.1007/s11148-017-0123-y

Taghizadeh, K., Luding, S., & Magnanimo, V. (2017). *DEM applied to soil mechanics: 129.* ALERT Doctoral School.

Tangella, R. G., Kumbhar, P., & Annabattula, R. K. (2022). Hybrid phase-field modeling of thermo-elastic crack propagation. *International Journal for Computational Methods in Engineering Science and Mechanics*, *23*(1), 29–44. https://doi.org/10.1080/15502287.2021.1904462

Taylor, D. J. (1987). *Thermal Expansion Data. XI. Complex Oxides, A2BO5, and the Garnets* (pp. 1–16).

Teichtmeister, S., Kienle, D., Aldakheel, F., & Keip, M.-A. (2017). Phase field modeling of fracture in anisotropic brittle solids. *International Journal of Non-Linear Mechanics*, *97*, 1–21. https://doi.org/10.1016/j.ijnonlinmec.2017.06.018

Terzić, A., & Pavlović, L. (2009). Correlation among sintering process, porosity, and creep deformation of refractory concrete. *Journal of Materials Science*, *44*(11), 2844–2850. https://doi.org/10.1007/s10853-009-3376-0

Tessier-Doyen, N. (2003). *Etude expérimentale et numérique du comportement thermomécanique de matériaux réfractaires modèles*. http://www.theses.fr/2003LIMO0030

Tessier-Doyen, N., Glandus, J. C., & Huger, M. (2006). Untypical Young's modulus evolution of model refractories at high temperature. *Journal of the European Ceramic Society*, *26*(3), 289–295. https://doi.org/10.1016/j.jeurceramsoc.2004.10.028

THOMAS, H. J., & Stevens, R. (1989). Aluminium titanate: a literature review. II: Engineering properties and thermal stability. *British Ceramic. Transactions and Journal*, *88*(5), 184–190.

Trostel, L. J. (1962). Strength and Structure of Refractories as a Function of Pore Content. *Journal of the American Ceramic Society*, *45*(11), 563–564. https://doi.org/10.1111/j.1151-2916.1962.tb11057.x

Tschegg, E. K. (1986). Equipment and appropriate specimen shapes for tests to measure fracture values. *Patent AT-390328.*

Tvergaard, V., & Hutchinson, J. W. (1988). Microcracking in Ceramics Induced by Thermal Expansion or Elastic Anisotropy. *Journal of the American Ceramic Society*, *71*(3), 157–166. https://doi.org/10.1111/j.1151-2916.1988.tb05022.x

Vakhrushev, A., Kharicha, A., Wu, M., Ludwig, A., Tang, Y., Hackl, G., Nitzl, G., Watzinger, J., & Bohacek, J. (2021). On Modelling Parasitic Solidification Due to Heat Loss at Submerged Entry Nozzle Region of Continuous Casting Mold. *Metals*, *11*(9), 1375. https://doi.org/10.3390/met11091375

Verbanac, D. (2023). *Marie Skłodowska-Curie actions: Cluster Event with European Industrial Doctorates-workshop rapporteur.*

License CC BY-NC-ND 4.0

Violini, M. A., Hernández, M. F., Gauna, M., Suarez, G., Conconi, M. S., & Rendtorff, N. M. (2018). Low (and negative) thermal expansion Al2TiO5 materials and Al2TiO5 - 3Al2O3.2SiO2 - ZrTiO4 composite materials. Processing, initial zircon proportion effect, and properties. *Ceramics International*, *44*(17), 21470–21477. https://doi.org/10.1016/j.ceramint.2018.08.208

Voigt, W. (1889). Ueber die Beziehung zwischen den beiden Elasticitätsconstanten isotroper Körper. *Annalen Der Physik*, *274*(12), 573–587. https://doi.org/10.1002/andp.18892741206

Wang, D., Zhao, J., Zhou, Y., Chen, X., Li, A., & Gong, Z. (2013). Extended finite element modeling of crack propagation in ceramic tool materials by considering the microstructural features. *Computational Materials Science*, *77*, 236–244. https://doi.org/10.1016/j.commatsci.2013.04.045

Wang, T., Han, H., Wang, Y., Ye, X., Huang, G., Liu, Z., & Zhuang, Z. (2022). Simulation of crack patterns in quasi-brittle materials under thermal shock using phase field and cohesive zone models. *Engineering Fracture Mechanics*, *276*, 108889. https://doi.org/10.1016/j.engfracmech.2022.108889

Wang, T., Zhou, M., Li, Y., Yu, Y., & He, H. (2020). Lattice spring model with angle spring and its application in fracture simulation of elastic brittle materials. *Theoretical and Applied Fracture Mechanics*, *106*, 102469. https://doi.org/10.1016/j.tafmec.2019.102469

Wciślik, W., & Pała, T. (2021). Selected Aspects of Cohesive Zone Modeling in Fracture Mechanics. *Metals*, *11*(2), 302. https://doi.org/10.3390/met11020302

Wei, X., Li, Z., & Zhao, G. (2024). Implementation of the Zienkiewicz–Pande Model into a Four-Dimensional Lattice Spring Model for Plasticity and Fracture. *International Journal for Numerical and Analytical Methods in Geomechanics*, *48*(18), 4506–4519. https://doi.org/10.1002/nag.3860

Willis, M. J. (1999). *Proportional-integral-derivative control*. University of Newcastle.

Wlodzimierz Bryc. (1995). *The Normal Distribution: Characterizations with Applications (Lecture Notes in Statistics, 100)* (1st ed.). Springer.

Wretborn, J. (2016). *Modelling cracks in solid materials using the Material Point Method*. Linköping University, Department of Physics, Chemistry and Biology.

Yang, J., Ohji, T., Kanzaki, S., Díaz, A., & Hampshire, S. (2002). Microstructure and Mechanical Properties of Silicon Nitride Ceramics with Controlled Porosity. *Journal of the American Ceramic Society*, *85*(6), 1512–1516. https://doi.org/10.1111/j.1151-2916.2002.tb00305.x

Yang, L., Ma, X., Liu, J., Hu, X., Wu, Z., & Shi, C. (2022). Improving the effectiveness of internal curing through engineering the pore structure of lightweight aggregates. *Cement and Concrete Composites*, *134*, 104773. https://doi.org/10.1016/j.cemconcomp.2022.104773

Yang, Z., Zheng, S., Shen, S., & Han, F. (2022). *An efficient peridynamics-based statistical multiscale method for fracture in composite structure with randomly distributed particles*.

Yousef, S. G., Rödel, J., Fuller, E. R., Zimmermann, A., & El-Dasher, B. S. (2005). Microcrack Evolution in Alumina Ceramics: Experiment and Simulation. *Journal of the American Ceramic Society*, *88*(10), 2809–2816. https://doi.org/10.1111/j.1551-2916.2005.00312.x

Yuan, S., Zhu, Q., Zhang, W., Zhang, J., & Zhao, L. (2021). A Micromechanical Anisotropic Damage Model for Brittle Rocks With Non-Associated Plastic Flow Rule Under True Triaxial Compressive Stresses. *Frontiers in Physics*, *9*. https://doi.org/10.3389/fphy.2021.808375

License CC BY-NC-ND 4.0

Zhang, H., Liu, L., Lai, X., Mei, H., & Liu, X. (2022). Thermo-Mechanical Coupling Model of Bond-Based Peridynamics for Quasi-Brittle Materials. *Materials*, *15*(20), 7401. https://doi.org/10.3390/ma15207401

Zhang, J., Liu, Q., Yang, S., Chen, Z., Li, J., & Jiang, Z. (2019). Advances in Ladle Shroud as A Functional Device in Tundish Metallurgy: A Review. *ISIJ International*, *59*(7), 1167–1177. https://doi.org/10.2355/isijinternational.ISIJINT-2019-044

Zhang, J., Mei, G., Xie, Z., & Zhao, S. (2018). Firing mechanism of oxide-carbon refractories with phenolic resin binder. *Ceramics International*, *44*(5), 5594–5600. https://doi.org/10.1016/j.ceramint.2017.12.206

Zhang, L., Wang, Y., Fan, W., Gao, Y., Sun, Y., & Bai, Y. (2020). A Simulation Study on the Crack Propagation Behavior of Nanostructured Thermal Barrier Coatings with Tailored Microstructure. *Coatings*, *10*(8), 722. https://doi.org/10.3390/coatings10080722

Zhao, G., Fang, J., & Zhao, J. (2011). A 3D distinct lattice spring model for elasticity and dynamic failure. *International Journal for Numerical and Analytical Methods in Geomechanics*, *35*(8), 859–885. https://doi.org/10.1002/nag.930

Zhao, G.-F., Rui, F., Chen, H., & Li, Q. (2020). Parallel implementation of the four-dimensional lattice spring model on heterogeneous CPU-GPU systems. *International Journal of Rock Mechanics and Mining Sciences*, *133*, 104361. https://doi.org/10.1016/j.ijrmms.2020.104361

Zhou, M.-J. (2021). A crack theory-based bonded-particle model for rock particles considering size effects. *Géotechnique Letters*, *11*(4), 340–349. https://doi.org/10.1680/jgele.21.00022

License CC BY-NC-ND 4.0

Résumé

Les matériaux réfractaires industriels sont régulièrement exposés à des gradients thermiques importants pendant leur utilisation, ce qui fait du choc thermique un facteur majeur limitant leur durée de vie opérationnelle. Des études approfondies ont permis d'identifier les paramètres clés qui régissent la résistance aux chocs thermiques : la conductivité thermique, la dilatation thermique, la rigidité élastique et les propriétés de rupture. Parmi les approches établies, la stratégie basée sur les microfissures de Hasselman, qui découle des incompatibilités entre les coefficients de dilatation thermique (CTE) des différents composants, s'est avérée à la fois pratique et efficace. Les réseaux de microfissures peuvent réduire le CTE macroscopique et le module d'Young tout en augmentant l'énergie de rupture et la déformation à la rupture, améliorant ainsi la résistance aux chocs thermiques. Du point de vue de la conception microstructurale, Kakroudi (2007) a montré que les agrégats monocristallins grossiers tels que l'andalousite, en raison de leur forte anisotropie CTE, favorisent la formation de réseaux de microfissures denses et complexes à petite échelle, ajustant efficacement ces paramètres. Ces effets microstructuraux sont généralement associés à une hystérésis prononcée du module d'Young et des réponses dilatométriques à la température, ainsi qu'à une forte non-linéarité du comportement contrainte-déformation en traction, ce qui favorise une augmentation de l'énergie de rupture et de la déformation à la rupture. Bien que ces phénomènes aient été largement documentés expérimentalement au cours des deux dernières décennies, leur simulation numérique reste difficile. Dans ce contexte, cette thèse de doctorat développe un cadre numérique pour étudier la microfissuration induite thermiquement dans les matériaux réfractaires contenant des agrégats anisotropes. Une approche de modélisation par éléments discrets basée sur le modèle amélioré Distinct Lattice Spring Model (iDLSM), implémentée dans l'atelier GranOO, est améliorée pour simuler explicitement la dilatation thermique anisotrope, l'initiation, la propagation et l'interaction des fissures, ainsi que l'ouverture et la fermeture des fissures sous charge thermomécanique. Des matériaux polycristallins à base de titanate d'aluminium sont d'abord utilisés pour valider le modèle par rapport aux données expérimentales, après quoi le cadre est étendu aux systèmes poreux et composites. Ces applications mettent en évidence le rôle central de la dilatation thermique anisotrope dans le développement du réseau de microfissures et le comportement thermomécanique non linéaire et hystérétique qui en résulte. Dans l'ensemble, le cadre proposé fournit un laboratoire virtuel pour l'optimisation basée sur la microstructure des matériaux réfractaires soumis à des chocs thermiques.

Mots-clés : Comportement thermomécanique, Méthode des éléments discrets (DEM), Microstructure réfractaire, Microfissures

Abstract

Industrial refractory materials are routinely exposed to severe thermal gradients during service, making thermal shock a major factor limiting their operational lifetime. Extensive studies have identified key governing parameters, thermal conductivity, thermal expansion, elastic stiffness, and rupture properties, that control thermal shock resistance. Among established approaches, Hasselman's microcrack-based strategy, arising from mismatches in the CTE between constituents, has proven both practical and effective. Microcrack networks can reduce macroscopic CTE and Young's modulus while increasing fracture energy and strain to rupture, thereby improving thermal shock resistance. From a microstructural design standpoint, Kakroudi (2007) showed that coarse monocrystalline aggregates such as andalusite, due to their strong CTE anisotropy, promote the formation of dense and complex fine-scale microcrack networks, effectively tuning these parameters. These microstructural effects are commonly associated with pronounced hysteresis in Young's modulus and dilatometric responses with temperature, as well as strong nonlinearity in tensile stress-strain behaviour, which favours increased fracture energy and strain to rupture. Although such phenomena have been extensively documented experimentally over the past two decades, their numerical simulation remains challenging. In this context, this PhD thesis develops a numerical framework to investigate thermally induced microcracking in refractory materials containing anisotropic aggregates. A discrete element modelling approach based on the improved Distinct Lattice Spring Model (iDLSM), implemented in the GranOO workbench, is enhanced to explicitly simulate anisotropic thermal expansion, crack initiation, propagation, interaction, and crack opening–closure under thermomechanical loading. Polycrystalline aluminium titanate materials are first used to validate the model against experimental data, after which the framework is extended to porous and composite systems. These applications highlight the central role of anisotropic thermal expansion in microcrack network development and the resulting nonlinear and hysteretic thermomechanical behaviour. Overall, the proposed framework provides a virtual laboratory for microstructure-based optimisation of refractory materials subjected to thermal shock.

Keywords: Thermomechanical behavior, Discrete Element Method (DEM), Refractory microstructure, Microcracks

License CC BY-NC-ND 4.0

License CC BY-NC-ND 4.0